

Performance Improvement of Synchronous Generators through Accurate Modelling and Integration of Power Electronics

Al-Hussein Mohammed Abu-Jalala, Bhc, MSc

Student ID: 4202108

Submitted to the University of Nottingham for the degree of Master of Philosophy, 2021

To my father's soul,

my beloved mother and

My Family

Abstract

In this thesis, an active power filters (Shunt and series) are considered as an alternative to traditional methods (such as distributed winding, short pitch winding and skewing the stator) to improve the output power quality of synchronous generators. Instead of short pitching the winding, using different slot/pole combinations and/or skewing the stator, a power electronics device (active power filters) are used to improve the output power quality and the dynamic response of synchronous generators. A large amount of published work in the area of synchronous generator design has focused on traditional methods to improve the output power quality, but these methods complicate the synchronous generator, decrease generator rating and increase the manufacturing cost. In addition, the active power filters have been widely used in a power system to eliminate nonlinear load harmonics and reactive power compensation.

The aim of this project is, therefore, to investigate using active power filters to improve the output power of a simple design of synchronous generator and improve the dynamic response of the synchronous generator without damper bars. Using an active power filters in parallel and series with a simplified synchronous generator allows the use of simple generator designs with reduced complexity and manufacturing cost, without compromising the quality of power delivered to the load.

A simplified synchronous generator is proposed in this thesis to investigate the project idea, this generator has a full pitch-winding configuration and unskewed stator to increase generator power and simplify the manufacturing process. A two converters are connected

one in parallel and one in series with the proposed generator to achieve IEEE standards for current harmonics. This thesis describes the derivation of the proposed synchronous generator model and active power filters control as well as experimental results from the proposed generator.

Simulation and experimental results are provided to validate the approach and to demonstrate the feasibility of the proposed synchronous generator with active power filters modelling approach and control strategy. A good correlation between simulation and experimental results was obtained.

Thesis Contribution

Different methods have been used by synchronous generator designer to get good quality output power, such as stator skewing, pole/slot combination and winding configuration. This work used a new approach to improve the output power quality of the synchronous generator which is using the power electronics devices.

The first contribution of this work is developing a novel and accurate synchronous generator model able to include synchronous generator harmonics. This model uses the FEA model result to build the model with Matlab Simulink.

The second contribution of this thesis is using the active power filters (shunt and series) to improve the power quality of simplified synchronous generator. The simplified synchronous generator has simple design to decrease the production cost and faster in manufacturing process.

The final contribution is using the active power filters to improve the dynamic response of the synchronous generator without damper bars. Removing the damper bars from the rotor of the generator decrease the rotor losses and simplify the manufacturing process.

The work presented in this thesis has resulted in one conference and one journal publications. The published papers are as listed:

- A. Abu-Jalala, T. Cox, C. Gerada, M. Rashed, T. Hamiti, and N. Brown, "Power quality improvement of synchronous generators using an active power filter," IEEE Transactions on Industry Applications, pp. 1–1, 2018.

- A. Abu-Jalala, T. Cox, C. Gerada, M. Rashed, T. Hamiti, and N. Brown, "Performance improvement of simplified synchronous generators using an active power filter," in IEEE Energy Conversion Congress and Exposition (ECCE), Oct 2017, pp. 1845–1849.

Acknowledgement

I would like to express my deep appreciation and gratitude to my supervisors Prof. Chris Gerada, Dr. Tom Cox, Dr. Mohammed Rashed ,and Dr. Tahar Hamiti for their encouragement, valuable advice, guidance, supervision and support throughout my years of study at the University of Nottingham

I would like to thank all my colleagues and friends in the Power Electronics, Control and Machine Group at the University of Nottingham for the support and valuable discussions over the last few years.

I also wish to thank the all the technical teams (electrical and mechanical) in the group for their help, support, and valuable advices during the experimental setup and the experimental testing.

Last but not least, I owe the greatest debt of gratitude to my mother, my wife, my sons, my brothers, my sisters, and all other family members and friends for their love, support and encouragement throughout my studies.

Thank you all.

Contents

Abstract ii

Thesis Contribution iv

Acknowledgement vi

Contents vii

Chapter-1 Introduction 2

1.1 Background 2

1.2 Project objectives 9

1.3 Thesis outline 9

Chapter-2 Modelling of the Synchronous Generator 13

2.1 Introduction 13

2.2 Synchronous Machine dq Model 14

2.2.1 Assumption 15

2.2.2 SM Equations in the Phase Variable or abc Reference Frame 15

2.2.3 Stator Equation in Synchronous Reference dq Frame 18

2.2.4 Matlab Simulink Model: 29

2.2.5 Simulation Result: 34

2.3 Finite Element Modelling of the Synchronous Generator 36

2.3.1 The Original Generator: 37

2.3.2 The Proposed Generator 37

2.3.3 2DFEA Model for the Proposed Generator 40

2.3.4 Inductance Matrix of the Proposed Generator: 44

2.4 Accurate Modelling of Synchronous Generator in Matlab Simulink 46

2.4.1 Model Description and Operation Principle: 47

2.5 Comparison between FEA and Matlab Simulink Models 52

2.5.1 The back-EMF Voltage and Open Circuit Test: . 52

2.5.2 Loaded Generator..... 54

2.6 Experimental Validation..... 57

2.6.1 Open-Circuit Test: 58

2.6.2 Loaded Generator: 59

2.7 Conclusion..... 61

Chapter-3 Active power Filters 64

3.1 Introduction..... 64

3.2 Active Power Filter Topologies 66

3.3 Shunt Active Power Filter: 67

3.4 Series Active Power Filter: 69

3.5 Grid Synchronization Methods 70

3.5.1 Conventional SRF-PLL..... 70

3.5.2 Decoupled Double Synchronous Reference Frame PLL (DDSRF-PLL) 76

3.5.3 Dual Second Order Generalised integrator (DSOGI-PLL) 85

3.6 Current/Voltage Harmonics Extraction Techniques 90

3.6.1 Current Reference Extraction: P-Q Method..... 91

3.6.2 Current/voltage Reference Extraction: Synchronous Reference (d-q) Method 95

3.7 Shunt APF Current Control Techniques 97

3.7.1 Hysteresis Current Control..... 98

3.7.2 Synchronous Reference PI Controller (SRF-PI) 100

3.7.3 Proportional Resonant Current Controller (PR) 107

3.8 Modulation technique 114

3.9 DC-link Voltage Control 115

3.10 Passive Elements Design: 118

3.10.1 Filter Inductance 118

3.10.2 DC-link Capacitor 119

3.11 APF Design Validation 120

3.12 Conclusion 122

Chapter-4 Synchronous Generator Power Quality Improvements 125

4.1 System Configuration..... 125

4.2 Shunt Active Filter: 126

4.2.1 Output Power Quality Improvements of Synchronous Generator with Linear Load 126

4.2.2 Current Harmonics Compensation of Nonlinear Loads 129

4.2.3 Synchronous Generator Load Balancing..... 132

4.3 Series Active Filter:..... 139

4.3.1 Control Method of Series Active Filter..... 140

4.3.2 Output Power Quality Improvements of Synchronous Generator with Linear Load 143

4.3.3 Output Power Quality Improvements of Synchronous Generator with Nonlinear Load..... 145

4.4 The Proposed Generator with Shunt and Series Active Filters Simulation: 149

4.4.1 Output Power Quality Improvements of the proposed Generator with Linear Load..... 149

4.4.2 Output Power Quality Improvements of the proposed Generator with Nonlinear Load 151

4.5 Conclusion 154

Chapter-5 Dynamics Performance Improvements of Synchronous Generator without Damper Bars..... 157

5.1 Introduction 157

5.2 Study of Dynamic Performance of Synchronous Generator with and without Damper Bars..... 158

5.2.1 Swing Equation without Damper Torque:..... 158

5.2.2 Swing Equation with Damper Torque: 161

5.3 Proposed Control Approach of APF for Dynamic Performance Improvements of Synchronous Generator..... 163

5.4 Simulation Procedure and Results 164

5.4.1 Speed Controller and Diesel Engine Dynamic model 165

5.4.2 Exciter Model 166

5.4.3 Simulation Results..... 167

5.5 Conclusion 172

Chapter-6 Experimental Setup and Experimental Results.. 174

6.1 Test Rig Setup: 174

6.2 Experimental Active Power Filter Implementation 175

6.3 Interface Inductance and DC-link Capacitor Bank. 176

6.4 FPGA/DSP Control Platform 177

6.5 Measurement Boards 178

6.6 APF Test 179

6.7 Balanced Linear Load 179

6.8 Balanced Nonlinear Load 182

6.9 Unbalanced Nonlinear Load (type-2) 185

6.10 Comparison Between the Simulation and the Experimental Results: 189

6.11 Conclusion 190

Chapter-7 Conclusion and Future Work 192

7.1 Conclusion 192

7.2 Future Work 194

References: 195

A. Appendix-A 201

B. Appendix-B 202

C. Appendix-C 203

D. Appendix D 207

List of Figures

Figure 1-1 Amortisseur winding or damper winding,(a) connected and (b) not connected [4] 3

Figure 2-1 Synchronous machine rotor type [39] 14

Figure 2-2 Schematic representation of synchronous machine windings 16

Figure 2-3 Equivalent circuit of synchronous machine in the rotor reference frame 22

Figure 2-4 Equivalent circuit of synchronous machine after referring the rotor quantities to the stator 25

Figure 2-5 Matlab Simulink SG Model 34

Figure 2-6 comparison between dq-model and the commercial generator OCT 35

Figure 2-7 comparison between dq-model and the commercial generator SCT 36

Figure 2-8 Full pitch skewless generator (a)2D finite element analysis (FEA) model (b) Experimental prototype (the proposed generator) (c) Stator coils connection diagram 37

Figure 2-9 The proposed generator phase-A winding layout 38

Figure 2-10 Phasor diagram of the resultant EMF of short and full pitched coil 39

Figure 2-11 2DFEA model for the proposed generator . 40

Figure 2-12 (a) Flux distribution inside the proposed generator (If=11.2A), (b) B-H curve of the core material .. 41

Figure 2-13 The no load voltage of the proposed generator (If=11.2A) 42

Figure 2-14 FFT analysis for the back-EMF voltage of the proposed generator 42

Figure 2-15 Line-to-line voltage of the proposed generator 43

Figure 2-16 FFT analysis for the line voltage of the proposed generator 43

Figure 2-17 Phase-A inductance waveforms 45

Figure 2-18 the mutual and self-inductance of the field winding 46

Figure 2-19 Block diagram of the generator Simulink Matlab model 47

Figure 2-20 Matlab Simulink Block diagram for implementing Phase-A 48

Figure 2-21 Matlab Simulink Block diagram for stator and field winding inductances 49

Figure 2-22 Matlab Simulink Block diagram for the back-EMF of the stator winding 50

Figure 2-23 Matlab Simulink Block diagram for the proposed generator 51

Figure 2-24 Comparison between 2DFEA (FEA) and Matlab Simulink (MS) models of the proposed generator ... 53

Figure 2-25 Open-circuit test form 2DFEA model and the Matlab Simulink (MS) model 54

Figure 2-26 The simulation results for a balanced linear load from Simulink Matlab model, (a) Generator output voltage (b) Generator output current 55

Figure 2-27 The simulation results for a balanced linear load from 2DFEA model, (a) Generator output voltage (b) Generator output current 56

Figure 2-28 The stator of the prototype generator 57

Figure 2-29 The proposed generator test rig 58

Figure 2-30 Open circuit test for the proposed generator and the standard commercial generator 59

Figure 2-31 The simulation and experimental results for balanced linear load 60

Figure 2-32 The simulation and experimental results for balanced nonlinear load 61

Figure 3-1 Block diagram of the propose system 65

Figure 3-2 Subdivision of power system filters according to power circuit configuration and connection (AF: Active Filter, PF: Passive Filter) 66

Figure 3-3 Three-Phase four-wire APF topologies 67

Figure 3-4 Active series filter control circuit 69

Figure 3-5 SRF-PLL block diagram 71

Figure 3-6 PLL control circuit diagram 73

Figure 3-7 Control block diagram of the SRF-PLL 73

Figure 3-8 SRF-PLL performance under ideal voltage source and different values for KP 75

Figure 3-9 SRF-PLL performance under Unbalanced voltage source and different values for KP 76

Figure 3-10 Block diagram of decoupling terms, (a) for (dq+) reference frame (b) for (dq-) reference 80

Figure-3-11 Block diagram of decoupling network of DDSRF-PLL 81

Figure-3-12 The block diagram of the decoupling double synchronous reference frame (DDSRF_PLL) 82

Figure-3-13 DDSRF-PLL performance under Unbalanced voltage source 83

Figure-3-14 DDSRF-PLL performance under Unbalanced and distorted voltage source 84

Figure-3-15 SOGI-QSG block diagram 85

Figure-3-16 block diagram SOGI-QSG and PSC 88

Figure-3-17 block diagram DSOGI-PLL 89

Figure-3-18 DSOGI-PLL performance under Unbalanced and distorted voltage source 90

Figure-3-19 Calculation block diagram of P-Q method . 92

Figure-3-20 The block diagram for SRF reference current calculation 97

Figure 3-21 The block diagram of the hysteresis current controller 98

Figure 3-22 The basic concept of the hysteresis current controller 99

Figure 3-23 APF connection to the grid through interface L-filter 100

Figure 3-24 Block diagram of SRF PI controller with decoupling between the axes 103

Figure 3-25 Block diagram of the SRF-PI controller for PI parameter calculation 103

Figure 3-26 the simulation results for SRF-PI controller for different current references 106

Figure 3-27 Bode blot of ideal PR current controller .. 108

Figure 3-28 Bode blot of non-ideal PR current controller with different ωc 109

Figure 3-29 Block diagram of PR+HC controller 111

Figure 3-30 Bode blot of non-ideal PR+HC current controller 112

Figure 3-31 the simulation results for PR+HC controller for different current references 113

Figure-3-32: The block diagram of carrier-based PWM current control 114

Figure-3-33: The basic concept of carrier-based PWM current control 115

Figure-3-34: The block diagram of the DC-link voltage controller 116

Figure 3-35 DC-link regulator and the transfer function derivation 116

Figure 3-36 Block diagram for DC-link voltage control circuit 117

Figure 3-37 APF system test with nonlinear load 121

Figure 3-38 FFT Analysis for generator current 122

Figure 4-1 Block diagram of the proposed system 126

Figure 4-2 Simulation circuit for balanced linear load 128

Figure 4-3 simulation results for harmonic compensation for balanced linear load (a) generator and load currents before enabling the APF (b) load currents after enabling the APF (c) the APF currents 129

Figure 4-4 Simulation circuit for balanced nonlinear load 131

Figure 4-5 Simulation results for balanced nonlinear load (a) generator and load currents before enabling the APF (b) generator currents after enabling the APF (c) the APF currents 132

Figure 4-6 Simulation circuit for type-1 of unbalanced nonlinear load 134

Figure 4-7 System currents after enabling the APF with nonlinear and unbalanced load type-1 136

Figure 4-8 Simulation circuit for type-2 of unbalanced nonlinear load 137

Figure 4-9 System currents after enabling the APF with nonlinear and unbalanced load type-2 138

Figure 4-10 Series active filter simulation circuit 140

Figure 4-11 Block diagram showing control method of the series ASF 142

Figure 4-12 The Proposed Generator Output Voltage with and without Active Series Filter feeding Linear Load 144

Figure 4-13 The Proposed Generator Output Voltage with Active Series Filter feeding Nonlinear Load 148

Figure 4-14 The Proposed Generator Output Voltage and Output current with both Filters for Linear Load 150

Figure 4-15 The Proposed Generator Output Voltage with both Filters feeding Nonlinear Load 153

Figure 5-1 Proposed filter, load, and generator currents during a step load change for the generator without damper bars and APF..... 164

Figure 5-2 Block diagram of the proposed system 165

Figure 5-3 Block Diagram of Speed Controller..... 166

Figure 5-4 IEEE Type 1 (Type DC1A) excitation system 167

Figure 5-5 Generator current with and without APF during sudden load change 169

Figure 5-6 APF current and power 170

Figure 5-7 Speed response to sudden change in the generator loading with and without APF..... 171

Figure 5-8 Developed electromagnetic torque at sudden change in the generator loading with and without APF.... 172

Figure 6-1 The test rig 175

Figure 6-2 The active power filter 176

Figure 6-3 SKAI Modules..... 176

Figure 6-4 the Capacitor bank and the interface filter 177

Figure 6-5 FPGA and DSP platform controller..... 178

Figure 6-6 Measurement Boards, (A) and (B) current transducers, and (C) voltage transducers 179

Figure 6-7 Generator/ load current at 35 kW loading 180

Figure 6-8 Frequency spectrum for the phase-A current 181

Figure 6-9 Load current with enabled APF 182

Figure 6-10 Spectrum analysis of the phase-A load current with and without APF 182

Figure 6-11 Generator/ load current with nonlinear load 183

Figure 6-12 Frequency spectrum for the generator/load phase-A current with nonlinear load 183

Figure 6-13 Generator current with balanced nonlinear load with enabled APF 184

Figure 6-14 Frequency Spectrum analysis of the phase-A generator current with nonlinear load, with and without APF 185

Figure 6-15 Generator/ load current with unbalanced nonlinear load before enabling the APF 186

Figure 6-16 Frequency spectrum for Generator/ load current with unbalanced nonlinear load before enabling the APF 187

Figure 6-17 Generator current with unbalanced nonlinear load and with enabled APF 188

Figure 6-18 Frequency Spectrum analysis of the generator current and the load current with nonlinear unbalanced load with APF 189

Figure C-1 current ripple and symmetrical-aligned modulation signal 203

List of Tables

Table 1-1 Current Distortion Limits for General Distribution Systems (120 V Through 69 000 V).....6

Table 1-2 Voltage Distortion Limits.....7

Table 3-1 the numerical values of unideal voltage source 83

Table 3-2 The specification of the shunt APF filter.....123

Table 3-3 The specification of the series APF filter 123

Table 4-1 The simulation results for the THD and currents values before and after enabling the APF for unbalanced nonlinear load with just negative sequence.....135

Table 4-2 The simulation results for the THD and currents values before and after enabling the APF for unbalanced nonlinear load type-2.....139

Table 4-3 The Total Harmonic Distortion (THD) in the output voltage of the proposed generator feeding linear load 144

Table 4-4 The Total Harmonic Distortion (THD) in the output voltage in the proposed generator feeding non-linear load for different operation condition 146

Table 4-5 The THD of the output voltage of the proposed generator for different values of loading 147

Table 4-6 The Total Harmonic Distortion (THD) in the output voltage in the proposed generator feeding non-linear load for different Connected filters 152

Table 5-1 Speed controller time constants and their values 166

Table 5-2 Typical per unit data for an IEEE Type 1 DC exciter 167

Table 6-1 The RMS value and the THD of the unbalanced nonlinear load.....186

Table 6-2 the RMS value and the THD value of the generator and the load current before and after enabling the APF 188

Table 6-3 Comparison between the simulation results and the experimental results for the THD in the load/generator current.....190

Table B-1 dq-model parameters.....202

Chapter-1 Introduction

Chapter-1 **Introduction**

This chapter presents a brief introduction about the background and motivation of the research work presented in this thesis, combined with a review of synchronous generators and the traditional methods used to design them. Moreover, the active power filter usage with the synchronous generator is presented in section 1.1. Then the thesis objectives and aims are presented in section 1.2 , the thesis outline in section 1.3.

1.1 **Background**

Synchronous generators play an important role in power generation, and their rated power can reach hundreds megawatts. Synchronous generators consist of two main parts, a stator which contains the windings which are usually placed in three-phase layout, and a rotor which contains the field winding and is fed by a DC voltage.

Synchronous generator designers' use different approaches to improve the output power quality of the generator, such as, short pitch windings, different slot-pole combinations, and skewed stator [1-3]. However, these approaches decrease the back-EMF voltage and complicate the manufacturing process. Therefore, this work, which is titled "*Performance Improvement of Synchronous Generators through accurate modelling and integration of power electronics*", adopts different approach to improve the performance of the synchronous generator, using power electronics, (an active power filter) to improve the output power quality of the generator. The proposed generator has a simple design with full pitch winding to get maximum induced back-EMF and an unskewed stator to simplify the manufacture process.

Furthermore, the synchronous generators contain damper bars, also called amortisseur windings. In the synchronous generator these damper bars play an important role in synchronous generator dynamics. The damper bar is made from copper or aluminium bars installed in the rotor pole surface and short-circuited at both ends by arcs (there is no connection between poles) or rings (as in squirrel cage induction motor) or sometimes end lamination. Figure 1-1 shows the damper bar types in synchronous machines [4].

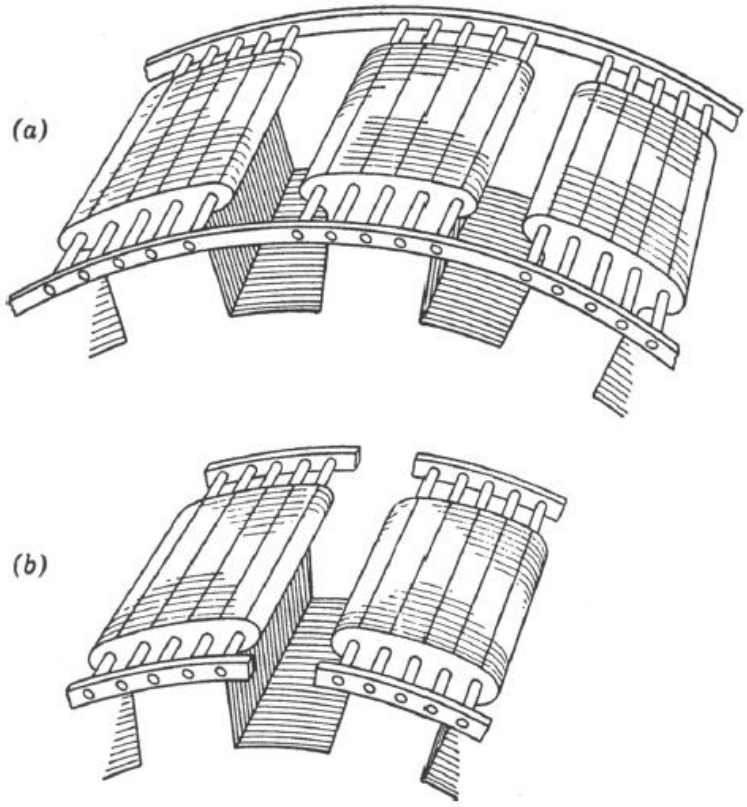


Figure 1-1 Amortisseur winding or damper winding,(a) connected and (b) not connected [4]

However, the damper bars complicate the synchronous generator manufacturing and the current that is induced in the damper bar increase the power losses in the generator, heats up the machine and reduces generator efficiency.

During the steady state condition, the relative speed between the fundamental component of the rotating air-gap magnetic field and the damper bars cage is zero, i.e. there is no voltage induced in the damper bar. However, when there is a sudden change in the generator loading, there will be a relative speed between the damper cage and the rotating air-gap magnet field. This relative motion induces voltage in the damper bar circuit and this voltage is proportional to the speed difference between the rotor and the air-gap field and produces current in the damper bars. The produced current develops a torque called the damping torque which interacts with the air-gap magnetic field to help bring back synchronisation between the rotor and the air-gap field [5].

The operation of a power converter as synchronous generator is widely discussed in literature [6-9]. in [6] they introduced the VSYNC project [10] where the concept of a virtual Synchronous generator (VSG) is demonstrated to overcome the grid instability problem that might be caused by renewable resources due to decreasing the total rotating inertia. In this control algorithm (VSG), virtual inertia is added by adding short-term energy storage to the system. By this configuration, the generator that is used in renewables can behave like a "Virtual synchronous Generator" during short time intervals and improve grid stability.

In addition, the power converters in renewable energy may be controlled to mimic a synchronous generator and they are called "*synchronverters*" [11, 12]. This type of controller facilitates integrating various types of green energy sources, electric vehicles and energy system to the smart grid.

Therefore, another application of active power filters is investigated, which is using the active power filter to improve the dynamic response of a synchronous generator without damper bars.

The impact of current harmonics on synchronous generators will be apparent both mechanically and electrically. The mechanical effect will appear as vibration on the generator shaft with electromagnetic torque pulsation, and will shorten the lifetime of the generator. The electrical effect will result in distorted current and voltage waveforms in both stator and rotor windings and this will cause excess heating and increase generator losses, lowering efficiency of power conversion [13, 14]. In addition, the impact of current harmonics on the voltage regulation and stability of synchronous generator were studied in [15, 16].

The total harmonic distortion (THD) is calculated from equation (1-1) [17]

$$THD\ \% = 100 * \sqrt{\sum_{n=2}^{\infty} \left(\frac{X_n}{X_1}\right)^2} \qquad (1\text{-}1)$$

Where X_1 is the amplitude of the fundamental component of the waveform and X_n is the amplitude of the n harmonic waveform.

The current harmonic content in power system should comply with the limit in IEEE Std 519 [18] and it shown in Table 1-1.

Table 1-1 Current Distortion Limits for General Distribution Systems (120 V Through 69 000 V)

Maximum Harmonic Current Distortion in Percent of I_L						
Individual Harmonic Order (Odd Harmonic)						
I_{sc}/I_L	11	$11 \leq h < 17$	$17 \leq h < 23$	$23 \leq h < 35$	$35 \leq h$	TDD
<20	4.0	2.0	1.5	0.6	0.3	5.0
20<50	7.0	3.5	2.5	1.0	0.5	8.0
50<100	10.0	4.5	4.0	1.5	0.7	12.0
100<1000	12.0	5.5	5.0	2.0	10	15.0
>1000	15.0	7.0	6.0	2.5	1.4	20.0

Where I_{sc} is the maximum short-circuit current at PCC (i.e. short-circuit level), I_L is the maximum demand fundamental load current at PCC and TDD is the total demand distortion and it is given by equation (1-2) [17]

$$TDD\ \% = 100 * \sqrt{\sum_{n=2}^{40} \left(\frac{I_n}{I_L}\right)^2} \qquad (1\text{-}2)$$

From equation (1-1) and equation (1-2) at the full load THD equals TDD. At lower loads the TDD will be lower than THD and the ratio between TDD and THD is the same load ratio, for example at 50% of the load the TDD will be half the THD.

In addition, the voltage harmonic content in power system for normal operation (more than hour) should comply with the limit in IEEE Std 519 [18] and it shown in Table 1-2, while during start-up or unusual condition, the limits may be exceeded by 50%.

Table 1-2 Voltage Distortion Limits

Bus Voltage at PCC	Individual Voltage Distortion (%)	Total Voltage Distortion THD (%)
69 kV and below	3.0	5.0
69.001 kV through 161kV	1.5	2.5
161.001 and above	1.0	1.5

The power electronic converter have been widely used with distributed power generators and renewable energy resources [19-24]. They are used as an interface between the source and the grid, for active and reactive power control, and harmonic mitigation.

Shunt active power filter topologies and control algorithms have been widely discussed in the literature [25-29]. In [30-33] the APF is used in cases with distorted mains voltages and the results showed a high capability for the proposed control techniques in these papers to eliminate the harmonics in the source current and balance them, regardless of the load condition and the source voltage.

Using active power filter (APF) and series filters with synchronous generator has not gained significant attention in recent research. The APF is used with stand-alone generators to improve their dynamic performance, where in [34] an APF is used with an isolated synchronous generator feeding a nonlinear load to compensate current harmonics and regulate the generator terminal voltages. In addition, APF is used to regulate the output voltage of a variable speed interior permanent magnet synchronous generator (IPMSG) with nonlinear load while controlling the reactive power and compensate any current harmonics [35].

This work develops and validates the use of active power filters (parallel filter) and active series filter specifically with simplified synchronous generators. The simplified generators described are less complex and so both simpler and less expensive to produce. However, the simplified generator design also produce significantly more harmonics and hence another approach, in this case an combination from active parallel filter and active series filter, will be used to mitigate these harmonics and ensure the level of harmonics seen at the load remains acceptable. In addition, this work investigates the use of just active power filters to improve the dynamic response of synchronous generators without damper bars, where the active power filter is used to decrease speed fluctuation during sudden load change.

The additional costs that would be introduced by adding the active filters may be compensated by the practical benefits can be gained. As well as the direct benefits of increased generator capability and reduced construction cost and complexity outlined above, APF also has established benefits in terms of improving the transient response of the generator [36] and its ride-through capability, as well as the potential to allow reduced three-phase output power in fault conditions.

In addition, it well known that the cost of semiconductor devices is in a decreasing trend. For example, for a traction drive systems (55 kW peak power for 18 sec; 30 kw continuous power) the cost of power electronics in 2010 was 7.9 $/kW and in 2020, this is estimated to drop to 3.3 $/kW , i.e. the cost will be 58% less in ten years [37].

Active filtering (both the active parallel and the active series compensators) will be used to improve the power quality (voltage and current) of the proposed generator.

1.2 **Project objectives**

The purpose of this work is to improve the performance and the dynamic response of simplified synchronous generators by using two active power filters. This will done by:

- Development of an effective dynamic model of the SG for analysis and design optimisation purposes
- Review of power converters and selecting a suitable configurations for integration within the SG
- Modelling, simulation and optimization of the selected converter topologies and its integration within the SG
- Experimental setup of the SG with the associated power converter
- Experimental evaluation

Although use of the active power filter to compensate load harmonics is widely discussed in the literature [25-28], using it with an active series filter to simplify the design of synchronous generator and improve the dynamic response, according to my knowledge, is a new subject and has not been presented. The originality of the research is shown by the publications listed under the title 'Thesis contribution' as shown in page iv.

1.3 **Thesis outline**

The thesis is structured as follows:

- **Chapter 2**: presents synchronous generator models, where the dq model explained in details in section 2.2. In section 2.3, a finite element analysis model FEA was

introduced for the proposed generator by using MagNet software. A MatLab Simulink model based on the inductance matrix from FEA model was proposed in section 2.4, followed by a comparison between the FEA model and the Simulink model in section 2.5. Experimental validation for the proposed generator models were presented in section 2.6, finally the chapter concluded in section 2.7

- **Chapter 3**: discusses active power filters topology and control. This chapter started with an introduction about active power filters, and then followed by active power filter topologies in section 3.2. Shunt and series active filter presented in sections 3.3 and 3.4 respectively. The synchronisation (phase angle tracking) methods and current and voltage reference generation techniques are presented in sections 3.43.5 and 3.63.6 respectively. Section 3.7 explains three different current control methods. Section 3.8 represent the modulation technique and sections 3.9 and 3.10 present the DC-link voltage control and Passive element design (filter inductance and DC-link capacitance). Finally, a conclusion of this chapter is given in section 3.12.

- **Chapter 4**: presents the power quality improvement of the proposed synchronous generator. The introduction of this chapter and the proposed system configuration are presented in section 4.1, after that in section 4.2 proposes power quality improvement of the simplified generator by using the shunt active power filter. Section 4.3 proposes power quality improvement of the simplified generator by using the series active power filter and using both filter is

presented in section 04.4. Finally, a chapter conclusion is given in section 4.5.

- **Chapter 5**: explains the dynamic response improvement of synchronous generator without damper bars by using an active power filter, section 5.1 presents an introduction about the damper bar function in synchronous generators and their drawbacks, and section 5.2 explains the dynamic performance and the swing equation of synchronous generator with and without damper bars. The proposed control algorithm is presented in section 5.3 and the simulation results are shown in section 5.4. Finally, a conclusion of this chapter is presented in section 5.5

- **Chapter 6**: gives a description of the experimental work including the proposed generator and the active filters implementation and testing, and present the experimental results for different kind of loads

- **Chapter 7:** presented a general conclusion and discussion the possible further developments.

Chapter-2 Modelling of the Synchronous Generator

Chapter-2 **Modelling of the Synchronous Generator**

This chapter provides an introduction to wound field synchronous generator modelling. Section 2.1 presents a general introduction about the synchronous generator and an overview about traditional methods of designing synchronous generators. Then the dq model is presented in section 2.2 followed by the two dimensional finite element model (2DFEA) of the proposed generator, presented in section 2.3. Accurate modelling of the synchronous generator in Matlab Simulink based on 2DFEA is presented in section 2.4 followed by a comparison between the Matlab Simulink model and the 2DFEA model presented in section 2.5. An experimental validation is presented in section 0, finally the conclusion of this chapter is presented in section 2.7.

2.1 **Introduction**

A good model is essential to study the SG dynamic behaviour, test a new excitation system or develop a new SG design. Synchronous machine modelling is a very important subject and has been widely discussed in the literature [38-41], where in [38, 39] a detailed analysis of d-q model was presented. In [40] a new modelling approach based on a stator-oriented magnetic circuit was proposed for electrically excited synchronous machines, this model considers the nonlinearity and multiple saliencies, but did not consider the harmonic effect. Ref [41] presented a solid rotor machine model in d-q axis frames, however, this model increased machine model order and did not consider the saturation effect.

The synchronous machine consists of two main parts, a stator and a rotor. The stator windings are distributed in slots and wound in three-phases, and may be connected in star or delta. The rotor, which is the moving part, contains the field winding and it is supplied by a DC current to produce the rotor magnetic field. In terms of rotor shape, there are two types of synchronous machines. The first one is the salient pole synchronous machine and the second one is the non-salient (cylindrical) rotor synchronous machine and used in high speed generators. Figure 2-1 shows the two types of synchronous machine [39].

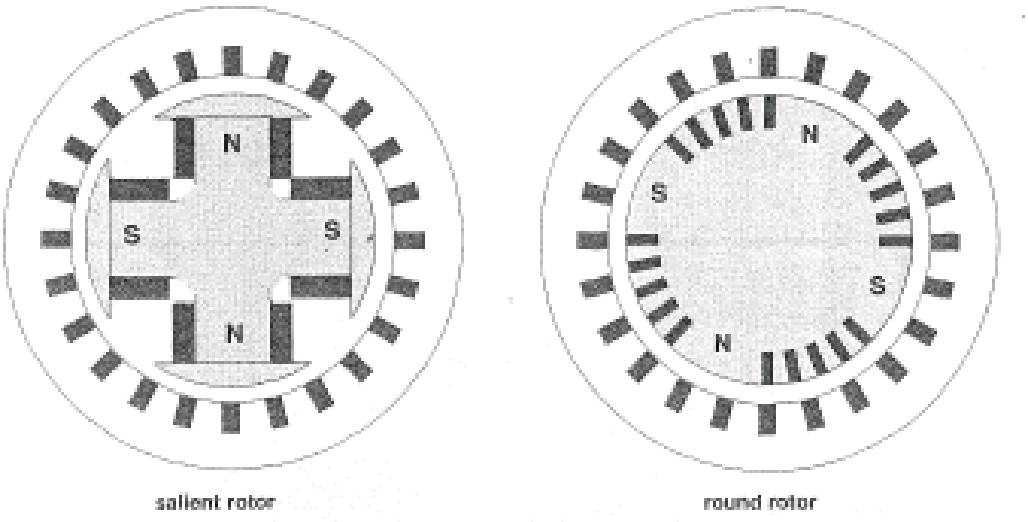


Figure 2-1 Synchronous machine rotor type [39]

2.2 **Synchronous Machine dq Model**

The synchronous machine dq model is based on the Park transformation for the $\boldsymbol{abc}$ machine equation, where all machine parameters are presented in the synchronous reference dq frame. The machine equivalent circuit is implemented as d-axis and q-axis equivalent circuits. The d-axis equivalent circuit contains the equivalent inductance of the stator windings in the direct axis, field winding and the equivalent inductance of the damper bars in the

direct axis, while the q-axis equivalent circuit contains the equivalent inductance of the stator windings in the quadrature axis and the equivalent inductance of the dampers bar in the quadrature axis.

2.2.1 Assumption

Before starting with machine modelling the following assumption were made;

- The stator winding is distributed in balanced three phase and displayed by 120 electrical degree and in sinusoidal distribution.
- The machine has silent rotor with a single pole pare (p=1, $\theta_e=\theta_r=\theta$. i.e. electrical speed =mechanical speed)
- The damper cage is represented with two winding and displayed by 90 electrical degree.
- The field is represented with a single coil and supplied by a constant current

2.2.2 SM Equations in the Phase Variable or abc Reference Frame

In order to model the machine, firstly the equations that describe the machine variables should be written. The stator has three-phase windings placed in slots displayed by 120° (electrical degree). The rotor will be arranged in two phase configurations (direct and quadratic axes) with a rotating angle θ. There are three windings in the rotor circuit, two windings in the direct axis (field and one damper bar windings) and the other damping bar winding in quadratic axis. Figure 2-2 shows a schematic representation of synchronous machine with three phase winding windings [38]

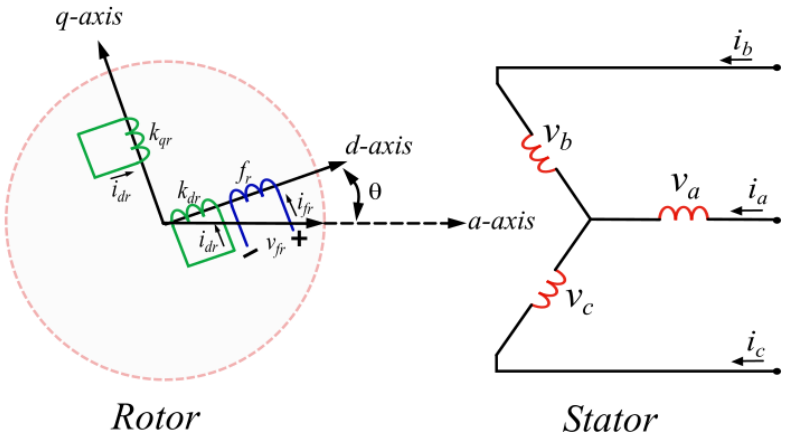


Figure 2-2 Schematic representation of synchronous machine windings

Note: All the following Equations represent SM in motoring mode (for generating mode we just need to inverse the sign of current)

The stator equation is given as:

$$v_{abcs} = r_s i_{abcs} + \frac{d}{dt}(\lambda_{abcs}) \tag{2-1}$$

Where v_{abcs} is the stator phases voltage, r_s is the stator phase resistance, i_{abcs} is the phase current and λ_{abcs} is the stator flux linkage. The matrix form of these variables are:

$$v_{abcs} = \begin{bmatrix} v_{as} \\ v_{bs} \\ v_{cs} \end{bmatrix} \quad , \quad i_{abcs} = \begin{bmatrix} i_{as} \\ i_{bs} \\ i_{cs} \end{bmatrix} \quad , \quad \lambda_{abcs} = \begin{bmatrix} \lambda_{as} \\ \lambda_{bs} \\ \lambda_{cs} \end{bmatrix} \text{ and } r_s = \begin{bmatrix} r_s & 0 & 0 \\ 0 & r_s & 0 \\ 0 & 0 & r_s \end{bmatrix}$$

The rotor equation is given as:

$$v_{fdqr} = r_r i_{fdqr} + \frac{d}{dt}(\lambda_{fdqr}) \tag{2-2}$$

Where v_{fdqr} is the rotor windings voltages (damper bars windings in the direct and quadrature axis and the field winding), r_r is the resistance of the rotor windings, i_{fdqr} is the currents in the

rotor windings and λ_{fdqr} is the flux linkage in the rotor circuit. The matrix form of these variables are:

$$v_{fdqr} = \begin{bmatrix} v_{fr} \\ v_{dr} \\ v_{qr} \end{bmatrix}, \quad i_{fdqr} = \begin{bmatrix} i_{fr} \\ i_{dr} \\ i_{qr} \end{bmatrix}, \quad \lambda_{fdqr} = \begin{bmatrix} \lambda_{fr} \\ \lambda_{dr} \\ \lambda_{qr} \end{bmatrix} \quad \text{and } r_r = \begin{bmatrix} r_{fr} & 0 & 0 \\ 0 & r_{dr} & 0 \\ 0 & 0 & r_{qr} \end{bmatrix}$$

All the windings in the machine are mutually coupled, and the flux linkage of the machine windings is given as:

$$\lambda_{abcs} = L_{abcs} i_{abcs} + L_{abcsr}\, i_{fdqr} \tag{2-3}$$

$$\lambda_{fdqf} = L^{t}_{abcsr} i_{abcs} + L_{fdqr}\, i_{fdqr} \tag{2-4}$$

Where L_{abcs} is the self and mutual inductance matrix of the stator windings, L_{abcsr} is mutual inductance matrix between the stator windings and the rotor windings and L_{fdqr} is the self and mutual inductance matrix of the rotor windings. The matrix form of these variables are:

$$L_{abcs} = \begin{bmatrix} L_{aa} & L_{ab} & L_{ac} \\ L_{ba} & L_{bb} & L_{bc} \\ L_{ca} & L_{cb} & L_{cc} \end{bmatrix}, \quad L_{abcsr} = \begin{bmatrix} L_{afr} & L_{adr} & L_{aqr} \\ L_{bfr} & L_{bdr} & L_{bqr} \\ L_{cfr} & L_{cdr} & L_{cqr} \end{bmatrix}, \text{ and}$$

$$L_{fdqr} = \begin{bmatrix} L_{frfr} & L_{frdr} & 0 \\ L_{drfr} & L_{drdr} & 0 \\ 0 & 0 & L_{qrqr} \end{bmatrix}$$

By assuming that the machine stator windings have sinusoidal distribution (harmonic free), these inductance matrices are given as follows

$$L_{abcs} = \begin{bmatrix} L_{ls} + L_0 - L_{ms}\cos 2\theta & -\frac{L_0}{2} - L_{ms}\cos 2\left(\theta - \frac{\pi}{3}\right) & -\frac{L_0}{2} - L_{ms}\cos 2\left(\theta + \frac{\pi}{3}\right) \\ -\frac{L_0}{2} - L_{ms}\cos 2\left(\theta - \frac{\pi}{3}\right) & L_{ls} + L_0 - L_{ms}\cos 2\left(\theta - \frac{2\pi}{3}\right) & -\frac{L_0}{2} - L_{ms}\cos 2(\theta - \pi) \\ -\frac{L_0}{2} - L_{ms}\cos 2\left(\theta + \frac{\pi}{3}\right) & -\frac{L_0}{2} - L_{ms}\cos 2(\theta - \pi) & L_{ls} + L_0 - L_{ms}\cos 2\left(\theta + \frac{2\pi}{3}\right) \end{bmatrix} \tag{2-5}$$

$$L_{abcsr} = \begin{bmatrix} L_{sfr}\cos\theta & L_{sdr}\cos\theta & L_{sqr}\sin\theta \\ L_{sfr}\cos\left(\theta - \frac{2\pi}{3}\right) & L_{sdr}\cos\left(\theta - \frac{2\pi}{3}\right) & L_{sqr}\sin\left(\theta - \frac{2\pi}{3}\right) \\ L_{sfr}\cos\left(\theta + \frac{2\pi}{3}\right) & L_{sdr}\cos\left(\theta + \frac{2\pi}{3}\right) & L_{sqr}\sin\left(\theta + \frac{2\pi}{3}\right) \end{bmatrix} \quad (2\text{-}6)$$

$$L_{fdqr} = \begin{bmatrix} L_{lfr} + L_{mfr} & L_{frdr} & 0 \\ L_{drfr} & L_{ldr} + L_{mdr} & 0 \\ 0 & 0 & L_{lqr} + L_{mqr} \end{bmatrix} \quad (2\text{-}7)$$

Where θ is the rotating speed, L_{ls} is stator winding leakage inductance, L_{sfr} is mutual inductance between the stator and the field winding, L_{sdr} is mutual inductance between the stator and the d-axis damper bar winding, L_{sqr} is mutual inductance between the stator and the q-axis damper bar winding, L_{lfr} is d-axis field winding leakage inductance, L_{mfr} is d-axis field winding self-inductance, L_{frdr} is the mutual inductance between d-axis field winding and d-axis damper bar winding, L_{drfr} is the mutual inductance between d-axis damper bar winding and d-axis field winding L_{ldr} is d-axis damper winding leakage inductance, L_{mdr} is d-axis damper bar winding self-inductance, L_{mqr} is q-axis damper bar winding self-inductance L_{lqr} is q-axis damper winding leakage inductance.

As can be seen from the machine equations, the machine inductances are time-variant and depend on rotor positions and this increases the computation time and complexity of machine model. In the next section, the machine parameters are transformed to the synchronous reference dq frame to make the machine inductance matrices time-invariant and simplify the model.

2.2.3 Stator Equation in Synchronous Reference dq Frame

As discussed in the previous section the machine inductance matrix is time dependent and this makes the machine equations complex. To simplify the machine equations, the Park transformation is used to transform the stator equations from the stationary reference frame to the rotating reference frame rotating at P*theta,

where P are the pole pairs. Applying Park transformation on equation (2-1) yields:

$$[T_{dq0}]v_{abcs} = r_s[T_{dq0}]i_{abcs} + [T_{dq0}]\frac{d}{dt}(\lambda_{abcs}) \tag{2-8}$$

Where $[T_{dq0}]$ is the transformation matrix and given as:

$$[T_{dq0}] = \frac{2}{3}\begin{bmatrix} \cos\theta & \cos\left(\theta - \frac{2\pi}{3}\right) & \cos\left(\theta + \frac{2\pi}{3}\right) \\ -\sin\theta & -\sin\left(\theta - \frac{2\pi}{3}\right) & -\sin\left(\theta + \frac{2\pi}{3}\right) \\ \frac{1}{2} & \frac{1}{2} & \frac{1}{2} \end{bmatrix} \tag{2-9}$$

$$[T_{dq0}]^{-1} = \begin{bmatrix} \cos\theta & -\sin\theta & \frac{1}{2} \\ \cos\left(\theta - \frac{2\pi}{3}\right) & -\sin\left(\theta - \frac{2\pi}{3}\right) & \frac{1}{2} \\ \cos\left(\theta + \frac{2\pi}{3}\right) & -\sin\left(\theta + \frac{2\pi}{3}\right) & \frac{1}{2} \end{bmatrix} \tag{2-10}$$

From equation (2-8), the left-hand side of the equation becomes:

$$[T_{dq0}]v_{abcs} = v_{dq0s} \tag{2-11}$$

Where the v_{dq0s} is the direct, quadratic and zero sequence voltages of the stator, and the currents term in the right-hand side of the equation become:

$$[T_{dq0}]i_{abcs} = i_{dq0s} \tag{2-12}$$

Where the i_{dq0s} is the direct, quadratic and zero sequence currents of the stator. For the fluxes term, it can be calculated from the formula of derivative of product two function which given as:

$$\frac{d}{dt}x(t)y(t) = x(t)\frac{d}{dt}y(t) + y(t)\frac{d}{dt}x(t) \tag{2-13}$$

Then from equation (2-13) the fluxes term in equation (2-8) can be calculated as:

$$\left[T_{dq0}\right]\frac{d}{dt}(\lambda_{abcs}) = \frac{d}{dt}\left(\left[T_{dq0}\right](\lambda_{abcs})\right) - \left(\frac{d}{dt}\left[T_{dq0}\right]\right)\lambda_{abcs} \quad (2\text{-}14)$$

After simplification of equation (2-14), yields

$$\left[T_{dq0}\right]\frac{d}{dt}(\lambda_{abcs}) = \frac{d}{dt}\lambda_{dq0s} + \omega\begin{bmatrix}0 & -1 & 0\\ 1 & 0 & 0\\ 0 & 0 & 0\end{bmatrix}\lambda_{dq0s} \quad (2\text{-}15)$$

Where the λ_{dq0s} is the direct, quadratic and zero sequence fluxes of the stator, ω is the rotor speed in rad/esc and equal to $\frac{d\theta}{dt}$.

Then the stator equation in the rotating reference frame (dq) can be written as:

$$v_{ds} = r_s i_{ds} + \rho\lambda_{ds} - \omega\lambda_{qs} \quad (2\text{-}16)$$

$$v_{qs} = r_s i_{qs} + \rho\lambda_{qs} + \omega\lambda_{ds} \quad (2\text{-}17)$$

$$v_{0s} = r_s i_{0s} + \rho\lambda_{0s} \quad (2\text{-}18)$$

Where $\rho = \frac{d}{dt}$.

2.2.3.1 Flux Linkage Equations

The flux linkage equation (equation (2-3)) can be transformed to dq frame and only the stator quantities are transformed and given as:

$$[T_{dq0}]\,\lambda_{abcs} = [T_{dq0}]L_{abcs}[T_{dq0}]^{-1}i_{dq0s} + [T_{dq0}]L_{abcsr}\,i_{fdqr} \quad (2\text{-}19)$$

After simplifying the right-hand side, the equation (2-19) can be simplified as:

$$\begin{aligned}\lambda_{ds} &= \left\{ L_{ls} + \frac{3}{2}(L_0 + L_{ms}) \right\} i_{ds} + L_{sfr} i_{fr} \\ &\quad + L_{sdr} i_{dr} \\ \lambda_{qs} &= \left\{ L_{ls} + \frac{3}{2}(L_0 - L_{ms}) \right\} i_{qs} + L_{sqr} i_{dr} \\ \lambda_{0s} &= L_{ls} i_{0s}\end{aligned} \tag{2-20}$$

$$\begin{aligned}\lambda_{ds} &= \{ L_{ls} + L_{md} \} i_{ds} + L_{sfr} i_{fr} + L_{sdr} i_{dr} \\ \lambda_{qs} &= \{ L_{ls} + L_{mq} \} i_{qs} + L_{sqr} i_{qr} \\ \lambda_{0s} &= L_{ls} i_{0s}\end{aligned} \tag{2-21}$$

Where the d-axis magnetising inductance $L_{md} = \frac{3}{2}(L_0 + L_{ms})$ and the q-axis magnetising inductance $L_{mq} = \frac{3}{2}(L_0 - L_{ms})$

The flux linkage of rotor quantities are given in the following equation:

$$\begin{aligned}\lambda_{fr} &= \frac{3}{2} L_{sfr} i_{ds} + L_{frfr} i_{fr} + L_{frdr} i_{dr} \\ \lambda_{dr} &= \frac{3}{2} L_{sdr} i_{ds} + L_{drfr} i_{fr} + L_{drdr} i_{dr} \\ \lambda_{qr} &= \frac{3}{2} L_{sqr} i_{qs} + L_{qrqr} i_{qr}\end{aligned} \tag{2-22}$$

Figure 2-3 shows the equivalent circuit of the synchronous machine in the rotor reference frame.

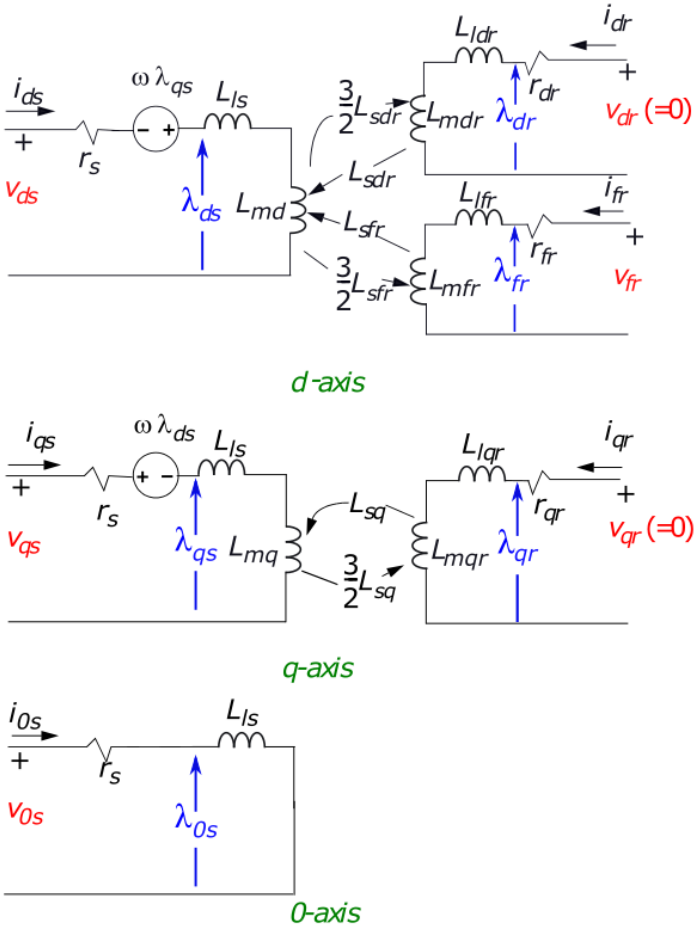


Figure 2-3 Equivalent circuit of synchronous machine in the rotor reference frame

The equivalent circuit is still complicated, and the inductance matrix of the d and q component is not symmetric. To simplify more, the rotor quantities are referred to the stator side by using the turns ratio between the stator windings and rotor windings. All the rotor variables that are referred to the stator are denoted by a prime superscript as

$$i'_{fr} = \frac{2}{3}\frac{N_{fr1}}{N_{s1}} i_{fr} \tag{2-23}$$

$$i'_{dr} = \frac{2}{3}\frac{N_{dr1}}{N_{s1}} i_{dr} \tag{2-24}$$

$$i'_{qr} = \frac{2}{3}\frac{N_{qr1}}{N_{s1}} i_{qr} \tag{2-25}$$

$$r'_{fr} = \frac{3}{2}\left(\frac{N_{s1}}{N_{fr1}}\right)^2 r_{fr} \quad (2\text{-}26)$$

$$r'_{dr} = \frac{3}{2}\left(\frac{N_{s1}}{N_{dr1}}\right)^2 r_{dr} \quad (2\text{-}27)$$

$$r'_{qr} = \frac{3}{2}\left(\frac{N_{s1}}{N_{qr1}}\right)^2 r_{qr} \quad (2\text{-}28)$$

$$\lambda'_{fr} = \frac{N_{s1}}{N_{fr1}}\lambda_{fr} \quad (2\text{-}29)$$

$$\lambda'_{dr} = \frac{N_{s1}}{N_{dr1}}\lambda_{dr} \quad (2\text{-}30)$$

$$\lambda'_{qr} = \frac{N_{s1}}{N_{qr1}}\lambda_{qr} \quad (2\text{-}31)$$

$$v'_{fr} = \frac{N_{s1}}{N_{fr1}}v_{fr} \quad (2\text{-}32)$$

$$v'_{dr} = \frac{N_{s1}}{N_{dr1}}v_{dr} \quad (2\text{-}33)$$

$$v'_{qr} = \frac{N_{s1}}{N_{qr1}}v_{qr} \quad (2\text{-}34)$$

Where N_{s1} is the number of stator turns of the fundamental component of the three winding function

N_{f1} is the effective number of turns for the field winding corresponding to the fundamental component.

N_{dr1} is the effective number of turns of the d-axis damper bar corresponding to the fundamental component of d-axis winding function N_{qr1} is the effective number of turns of the q-axis damper bar corresponding to the fundamental component of q-axis winding function

Rotor equation (equation (2-2)) can be rewritten referred to the stator side as follows:

$$v'_{dr} = r'_{dr}i'_{dr} + \rho\lambda'_{dr} = 0 \quad (2\text{-}35)$$

$$v'_{qr} = r'_{qr} i'_{qr} + \rho \lambda'_{qr} = 0 \tag{2-36}$$

$$v'_{fr} = r'_{fr} i'_{fr} + \rho \lambda'_{fr} \tag{2-37}$$

The magnetising inductances L_{md} and L_{mq} as a function of machine inductances can be written as

$$\begin{aligned} L_{md} &= \frac{3}{2} \frac{N_{s1}}{N_{fr1}} L_{sfr} \\ &= \frac{3}{2} \frac{N_{s1}}{N_{dr1}} L_{sdr} \end{aligned} \tag{2-38}$$

$$L_{mq} = \frac{3}{2} \frac{N_{s1}}{N_{qr1}} L_{sqr} \tag{2-39}$$

After referring the rotor quantities to the stator, the equivalent circuit of a synchronous machine is shown in Figure 2-4.

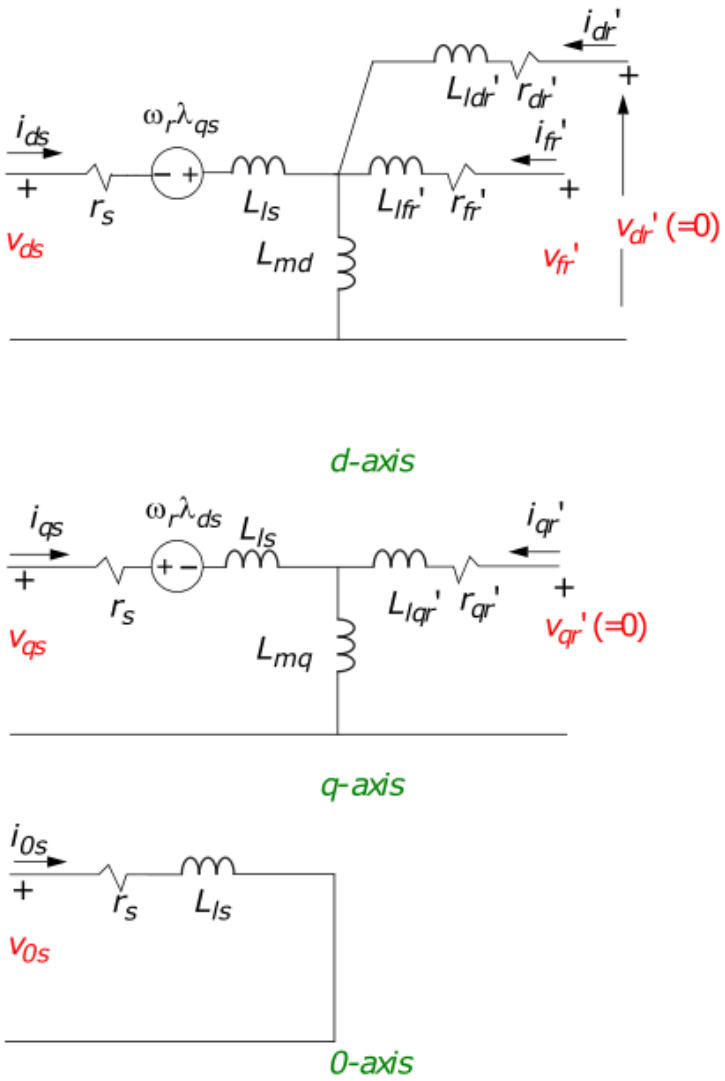


Figure 2-4 Equivalent circuit of synchronous machine after referring the rotor quantities to the stator

From Figure 2-4, the flux linkage equation can be written as a function in the mutual flux linkages λ_{md} and λ_{mq} as follows:

$$\lambda_{ds} = L_{ls} i_{ds} + \lambda_{md} \tag{2-40}$$

$$\lambda_{qs} = L_{ls} i_{qs} + \lambda_{mq} \tag{2-41}$$

$$\lambda_{0s} = L_{ls} i_{0s} \tag{2-42}$$

$$\lambda'_{fr} = L'_{lfr} i'_{fr} + \lambda_{md} \tag{2-43}$$

$$\lambda'_{dr} = L'_{ldr} i'_{dr} + \lambda_{md} \tag{2-44}$$

$$\lambda'_{qr} = L'_{lqr} i'_{qr} + \lambda_{mq} \tag{2-45}$$

Where the mutual flux linkage λ_{md} and λ_{mq} are given by:

$$\lambda_{md} = L_{md}\left(i_{ds} + i'_{dr} + i'_{fr}\right) \tag{2-46}$$

$$\lambda_{mq} = L_{mq}\left(i_{qs} + i'_{qr}\right) \tag{2-47}$$

To calculate the mutual flux linkage from the other machine flux linkages, the currents in equations (2-46) and (2-47) are replaced by their values from equation (2-40) to equation (2-45), after substituting and simplifying the equations the last yields:

$$\lambda_{md} = L_{MD}\left(\frac{\lambda_{ds}}{L_{ls}} + \frac{\lambda'_{dr}}{L'_{ldr}} + \frac{\lambda'_{fr}}{L'_{lfr}}\right) \quad \text{where } \frac{1}{L_{MD}} = \frac{1}{L_{ls}} + \frac{1}{L'_{ldr}} + \frac{1}{L'_{lfr}} + \frac{1}{L_{md}} \tag{2-48}$$

And

$$\lambda_{mq} = L_{MQ}\left(\frac{\lambda_{qs}}{L_{ls}} + \frac{\lambda'_{qr}}{L'_{lqr}}\right) \quad \text{where } \frac{1}{L_{MQ}} = \frac{1}{L_{ls}} + \frac{1}{L'_{lqr}} + \frac{1}{L_{mq}} \tag{2-49}$$

By substituting equations (2-40) and (2-41) in equations (2-16) and (2-17) yields:

$$v_{ds} = r_s i_{ds} + \rho(L_{ls} i_{ds} + \lambda_{md}) - \omega\left(L_{ls} i_{qs} + \lambda_{mq}\right)$$

$$v_{ds} = r_s i_{ds} + L_{ls}\rho i_{ds} - \omega L_{ls} i_{qs} + \left(\rho\lambda_{md} - \omega\lambda_{mq}\right) \tag{2-50}$$

$$v_{qs} = r_s i_{qs} + \rho\left(L_{ls} i_{qs} + \lambda_{mq}\right) + \omega(L_{ls} i_{ds} + \lambda_{md}) \tag{2-51}$$

$$v_{qs} = r_s i_{qs} + L_{ls}\rho i_{qs} + \omega L_{ls} i_{ds} + \left(\rho\lambda_{mq} + \omega\lambda_{md}\right)$$

$$v_{0s} = r_s i_{0s} + L_{ls}\rho i_{0s} \quad (2\text{-}52)$$

Where ω is the rotor speed in rad/sec.

Referring to equations (2-50), (2-51) and (2-52) a new variables can be defined as follows:

$$v_{ds} = r_s i_{ds} + L_{ls}\rho i_{ds} - \omega L_{ls} i_{qs} + E_{bds} \quad (2\text{-}53)$$

$$v_{qs} = r_s i_{qs} + L_{ls}\rho i_{qs} + \omega L_{ls} i_{ds} + E_{bqs} \quad (2\text{-}54)$$

$$v_{0s} = r_s i_{0s} + L_{ls}\rho i_{0s} + E_{0s} \quad (2\text{-}55)$$

Where E_{bds} , E_{bqs} and E_{0s} are the induced backs EMF in $dq0$ axices and are equal to:

$$E_{bds} = \rho\lambda_{md} - \omega\lambda_{mq} \quad (2\text{-}56)$$

$$E_{bqs} = \rho\lambda_{mq} + \omega\lambda_{md} \quad (2\text{-}57)$$

$$E_{0s} = 0 \quad (2\text{-}58)$$

Now equations (2-53) to (2-55) are transformed back to abc component by using the invers Park's transformation $[T_{dq0}]^{-1}$, and the results are given in the equations (2-59) to (2-61):

$$v_a = r_s i_a + L_{ls}\rho i_a + E_a \quad (2\text{-}59)$$

$$v_b = r_s i_b + L_{ls}\rho i_b + E_b \quad (2\text{-}60)$$

$$v_c = r_s i_c + L_{ls}\rho i_c + E_c \quad (2\text{-}61)$$

Where E_a , E_b and E_c are the induced back-emf voltages of phases a,b and c respectively

2.2.3.2 Torque Equation

The input power in the machine can be calculated from the following equation:

$$P_{in} = v_a i_a + v_b i_b + v_c i_d + v_{fr} i_{fr} \tag{2-62}$$

When equation (2-62) is transformed to the dq-reference frame, the input power can be given as in equation (2-63):

$$P_{in} = \frac{3}{2}\left(v_{ds} i_{ds} + v_{qs} i_{qs}\right) + 3 v_{0s} i_{0s} + v_{fr} i_{fr} \tag{2-63}$$

By substituting the values of machine voltage v_{ds}, v_{qs}, v_{0s} and v_{fr} from equations (2-16), (2-17), (2-18) and (2-2) respectively yields:

$$\begin{aligned} P_{in} = \frac{3}{2}\Big(r_s\left(i_{ds}^2 + i_{qs}^2\right) + i_{ds}\rho\lambda_{ds} + i_{qs}\rho\lambda_{qs} \\ + \omega_r\left(i_{qs}\lambda_{ds} - i_{ds}\lambda_{qs}\right)\Big) + 3 r_{0s} i_{0s}^2 \\ + 3 i_{0s}\rho\lambda_{0s} + r_{fr} i_{fr}^2 + i_{fr}\rho\lambda_{fr} \end{aligned} \tag{2-64}$$

By eliminating the terms related to ohmic losses and the rate of change in flux, the air gap power is given as:

$$P_{ag} = \frac{3}{2}\omega_r\left(i_{qs}\lambda_{ds} - i_{ds}\lambda_{qs}\right) \tag{2-65}$$

The relation between the rotor mechanical speed ω_{rm} and the rotor electrical speed ω_r as follows:

$$\omega_r = p\omega_{rm} \tag{2-66}$$

Where p is the number of pole pairs.

Then the air gap power can be written as

$$P_{ag} = \frac{3}{2} p\omega_{rm}\left(i_{qs}\lambda_{ds} - i_{ds}\lambda_{qs}\right) \quad (2\text{-}67)$$

The electromagnetic torque is calculated from dividing the air gap power by the rotor mechanical speed (because, $P_{ag} = T_{em} * \omega_{rm}$) and it is given as in equation (2-68) and mechanical speed is given as in equation (2-69)

$$T_{em} = \frac{3}{2}\, p\, \left(\lambda_{ds}\, i_{qs} - \lambda_{qs}\, i_{ds}\right) \quad (2\text{-}68)$$

$$T_{em} - T_{mech} - T_{damp} = J\frac{d\omega_{rm}(t)}{dt} \quad (2\text{-}69)$$

2.2.4 Matlab Simulink Model:

Since the currents in a synchronous generator change quickly, limited by short-circuit time constant while the flux linkages change slowly, limited to open-circuit time constant [38]. So the machine equations are expressed with a new variable which is a hybrid flux linkage (Ψ) by multiplying all flux linkages by a base angular speed (ω_b) that is let:

$$\Psi_{ds} = \omega_b \lambda_{ds} \quad (2\text{-}70)$$

$$\Psi_{qs} = \omega_b \lambda_{qs} \quad (2\text{-}71)$$

$$\Psi_{0s} = \omega_b \lambda_{os} \quad (2\text{-}72)$$

The unit of hybrid flux linkage is volt (V).

The equations from equation (2-16) to equation (2-18) can be written as:

$$v_{ds} = r_s i_{ds} + \frac{\rho}{\omega_b}\Psi_{ds} - \frac{\omega_r}{\omega_b}\Psi_{qs} \tag{2-73}$$

$$v_{qs} = r_s i_{qs} + \frac{\rho}{\omega_b}\Psi_{qs} + \frac{\omega_r}{\omega_b}\Psi_{ds} \tag{2-74}$$

$$v_{0s} = r_s i_{0s} + \frac{\rho}{\omega_b}\Psi_{0s} \tag{2-75}$$

And for the rotor equations become as:

$$v'_{dr} = 0 = r'_{dr} i'_{dr} + \frac{\rho}{\omega_b}\Psi'_{dr} \tag{2-76}$$

$$v'_{qr} = 0 = r'_{qr} i'_{qr} + \frac{\rho}{\omega_b}\Psi'_{qr} \tag{2-77}$$

$$e_x = x_{md} i'_{fr} + \frac{x_{md}}{r'_{fr}}\frac{\rho}{\omega_b}\Psi'_{fr} \tag{2-78}$$

And the electromagnetic equation is given as:

$$T_e = \frac{3}{2}\frac{P}{2}\frac{1}{\omega_b}\left(\Psi_{ds} i_{qs} - \Psi_{qs} i_{ds}\right) \tag{2-79}$$

Solving the flux linkage equations, equation (2-40) to equation (2-45), for the currents yields:

$$i_{ds} = \frac{\Psi_{ds} - \Psi_{md}}{x_{ls}} \tag{2-80}$$

$$i_{qs} = \frac{\Psi_{qs} - \Psi_{mq}}{x_{ls}} \tag{2-81}$$

$$i_{0s} = \frac{\Psi_{0s}}{x_{ls}} \tag{2-82}$$

$$i'_{fr} = \frac{\Psi'_{fr} - \Psi_{md}}{x'_{lfr}} \tag{2-83}$$

$$i'_{dr} = \frac{\Psi'_{dr} - \Psi_{md}}{x'_{ldr}} \tag{2-84}$$

$$i'_{qr} = \frac{\Psi'_{qr} - \Psi_{mq}}{x'_{lqr}} \tag{2-85}$$

Where the mutual flux linkage λ_{md} and λ_{mq} are given by:

$$\Psi_{md} = x_{md}\left(i_{ds} + i'_{fr} + i'_{dr}\right) \tag{2-86}$$

$$\Psi_{mq} = x_{mq}\left(i_{qs} + i'_{qr}\right) \tag{2-87}$$

Substituting equations (2-80), (2-83) and (2-84) in equation (2-86) yields:

$$\Psi_{md} = x_{md}\left(\frac{\Psi_{ds} - \Psi_{md}}{x_{ls}} + \frac{\Psi'_{fr} - \Psi_{md}}{x'_{lfr}} + \frac{\Psi'_{dr} - \Psi_{md}}{x'_{ldr}}\right) \tag{2-88}$$

By rearranging equation (2-88) gives:

$$\Psi_{md}\left(\frac{1}{x_{md}} + \frac{1}{x_{ls}} + \frac{1}{x'_{lfr}} + \frac{1}{x'_{ldr}}\right) = \frac{\Psi_{ds}}{x_{ls}} + \frac{\Psi'_{fr}}{x'_{lfr}} + \frac{\Psi'_{dr}}{x'_{ldr}} \tag{2-89}$$

A new variable x^*_{md} is defined as:

$$\frac{1}{x^*_{md}} = \left(\frac{1}{x_{md}} + \frac{1}{x_{ls}} + \frac{1}{x'_{lfr}} + \frac{1}{x'_{ldr}}\right) \tag{2-90}$$

So equation (2-89) can be rewritten as:

$$\Psi_{md} = \frac{x^*_{md}}{x_{ls}}\Psi_{ds} + \frac{x^*_{md}}{x'_{lfr}}\Psi'_{fr} + \frac{x^*_{md}}{x'_{ldr}}\Psi'_{dr} \tag{2-91}$$

In similar manner for Ψ_{mq}, substituting equations (2-81) and (2-83) in equations (2-87) yields:

$$\Psi_{mq} = x_{mq}\left(\frac{\Psi_{qs} - \Psi_{mq}}{x_{ls}} + \frac{\Psi'_{qr} - \Psi_{mq}}{x'_{lqr}}\right) \tag{2-92}$$

By rearranging equation (2-92) gives:

$$\Psi_{mq}\left(\frac{1}{x_{mq}} + \frac{1}{x_{ls}} + \frac{1}{x'_{lqr}}\right) = \frac{\Psi_{qs}}{x_{ls}} + \frac{\Psi'_{qr}}{x'_{lqr}} \tag{2-93}$$

Or in other form

$$\Psi_{mq} = \frac{x^*_{mq}}{x_{ls}}\Psi_{qs} + \frac{x^*_{mq}}{x'_{lqr}}\Psi'_{qr} \tag{2-94}$$

Where x^*_{mq} is equal to:

$$\frac{1}{x^*_{mq}} = \left(\frac{1}{x_{mq}} + \frac{1}{x_{ls}} + \frac{1}{x'_{lqr}}\right) \tag{2-95}$$

Now the current variables can be eliminated from the machine equations and substituted by machine flux linkage variables as in the following equations:

$$v_{ds} = \frac{r_s}{x_{ls}}(\Psi_{ds} - \Psi_{md}) + \frac{\rho}{\omega_b}\Psi_{ds} - \frac{\omega_r}{\omega_b}\Psi_{qs} \tag{2-96}$$

$$v_{qs} = \frac{r_s}{x_{ls}}\left(\Psi_{qs} - \Psi_{mq}\right) + \frac{\rho}{\omega_b}\Psi_{qs} + \frac{\omega_r}{\omega_b}\Psi_{ds} \tag{2-97}$$

$$v_{0s} = \frac{r_s}{x_{ls}}\Psi_{0s} + \frac{\rho}{\omega_b}\Psi_{0s} \tag{2-98}$$

And for the rotor equations become as:

$$v'_{dr} = 0 = \frac{r'_{dr}}{x'_{ldr}}(\Psi'_{dr} - \Psi_{md}) + \frac{\rho}{\omega_b}\Psi'_{dr} \tag{2-99}$$

$$v'_{qr} = 0 = \frac{r'_{qr}}{x'_{lqr}}\left(\Psi'_{qr} - \Psi_{mq}\right) + \frac{\rho}{\omega_b}\Psi'_{qr} \tag{2-100}$$

$$e_x = x_{md}\left(\frac{\Psi'_{fr} - \Psi_{md}}{x'_{lfr}}\right) + \frac{x_{md}}{r'_{fr}}\frac{\rho}{\omega_b}\Psi'_{fr} \tag{2-101}$$

2.2.4.1 Matlab Simulink Model Steps:

The following steps summarise how to build a Matlab Simulink model for a synchronous machine in the stationary reference frame dq

1- The machine flux linkages are calculated from equations (2-96) to (2-101) as shown in the following equations:

$$\Psi_{ds} = \int \left[v_{ds} - \frac{\omega_r}{\omega_b}\Psi_{qs} + \frac{r_s}{x_{ls}}(\Psi_{md} - \Psi_{ds}) \right] \omega_b \, dt \quad (2\text{-}102)$$

$$\Psi_{qs} = \int \left[v_{qs} - \frac{\omega_r}{\omega_b}\Psi_{ds} + \frac{r_s}{x_{ls}}(\Psi_{mq} - \Psi_{qs}) \right] \omega_b \, dt \quad (2\text{-}103)$$

$$\Psi_{0s} = \int \left[v_{0s} - \frac{r_s}{x_{ls}}\Psi_{0s} \right] \omega_b \, dt \quad (2\text{-}104)$$

$$\Psi'_{qr} = \int \left[\frac{r'_{dr}}{x'_{ldr}}(\Psi_{md} - \Psi'_{dr}) \right] \omega_b \, dt \quad (2\text{-}105)$$

$$\Psi'_{qr} = \int \left[\frac{r'_{dr}}{x'_{ldr}}(\Psi_{md} - \Psi'_{dr}) \right] \omega_b \, dt \quad (2\text{-}106)$$

$$\Psi'_{fr} = \int \left[e_x \frac{r'_{fr}}{x_{md}} + \frac{r'_{fr}}{x'_{lfr}}(\Psi_{md} - \Psi'_{fr}) \right] \omega_b \, dt \quad (2\text{-}107)$$

2- Calculating the mutual flux linkages Ψ_{md} and Ψ_{mq} from equations (2-91) and (2-94) respectively

3- Calculating machine currents from equations (2-80) to (2-85).

Figure 2-5 shows Matlab Simulink block diagram of dq-synchronous generator model

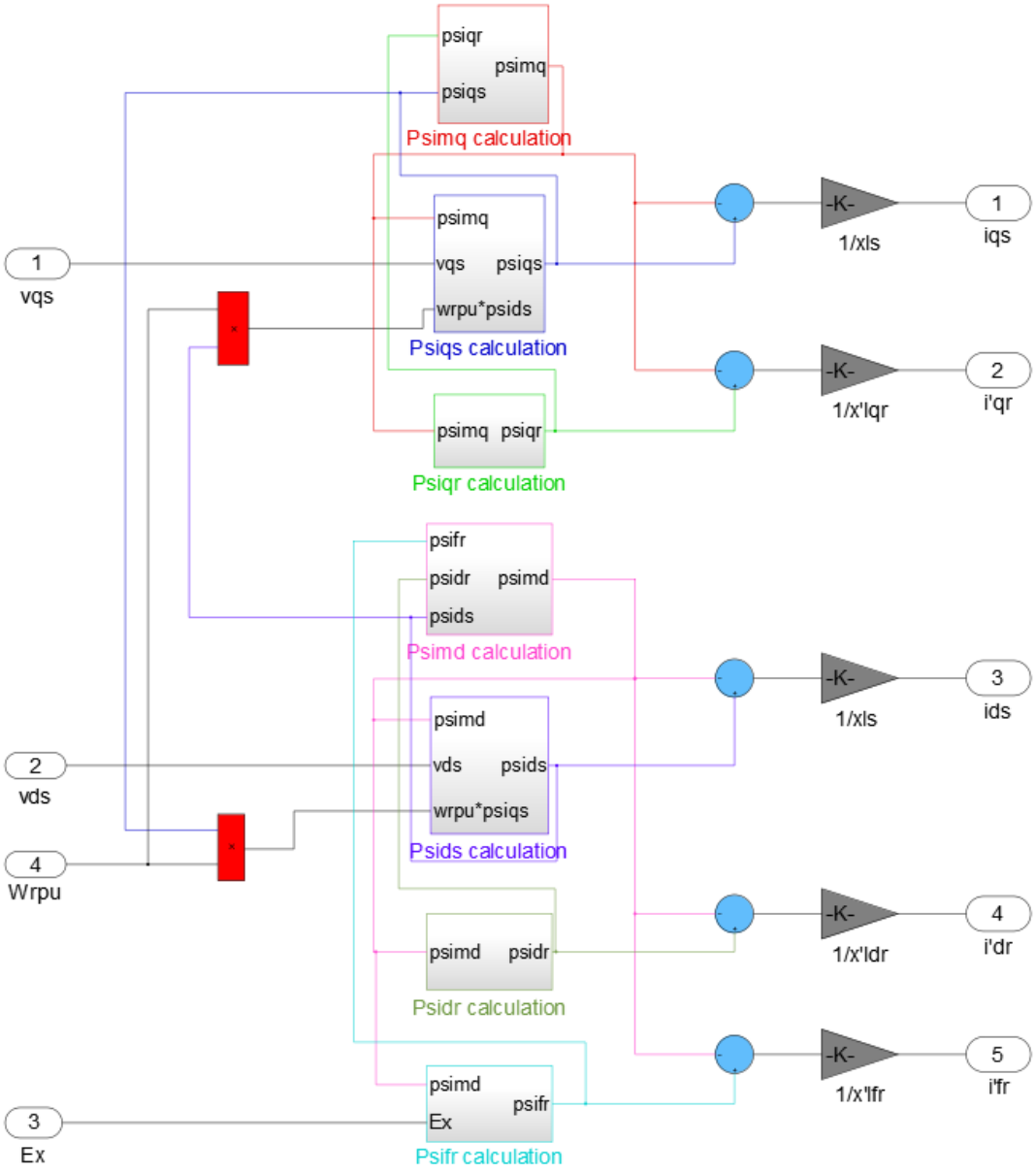


Figure 2-5 Matlab Simulink SG Model

2.2.5 Simulation Result:

This model is tested by using commercial generator data (from a Cummins UC224F generator). The generator power is 72.5 KVA and has 4-poles. The generator parameters are given in Appendix-B, two tests were done to compare the dq-model with the commercial generator data from the data sheet. The first test was open-circuit test (OCT) and the second test was short-circuit test (SCT). The open circuit test is shown in Figure 2-6, as can be seen

from the figure, the vertical axis represents the peak value of the fundamental phase voltage and the horizontal axis represents the generator field current. The dq-model matches the commercial generator data in the linear region (air-gap line) (because the saturation is not considered in the dq-mode) while in the saturation region this does not match.

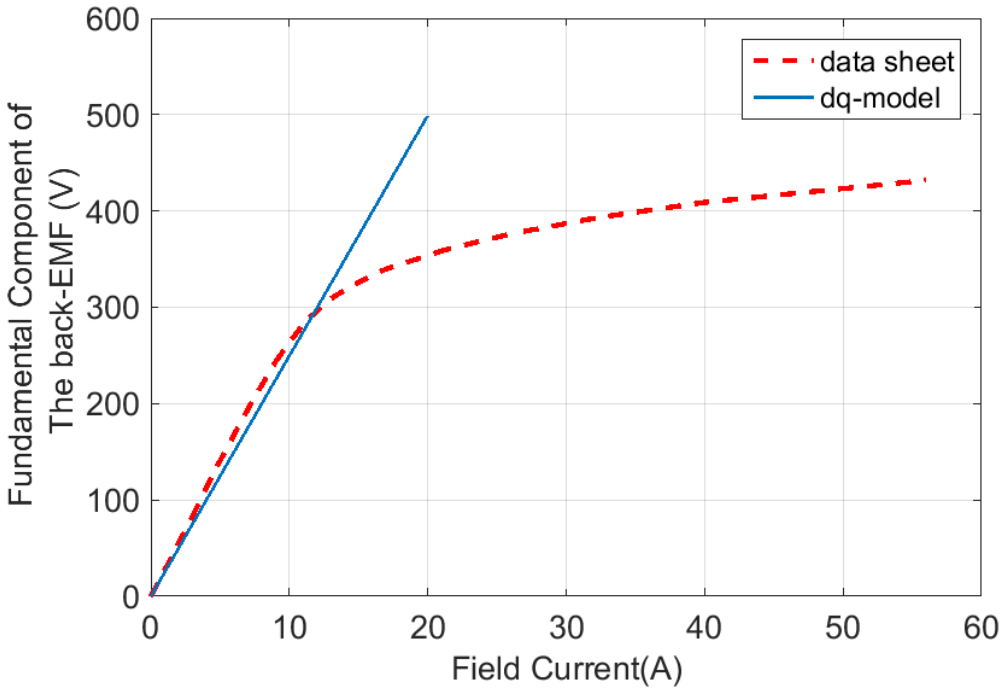


Figure 2-6 comparison between dq-model and the commercial generator OCT

In the short circuit test as shown in Figure 2-7, there is a good agreement between the dq-model and commercial generator because saturation effects are reduced in the short-circuit test.

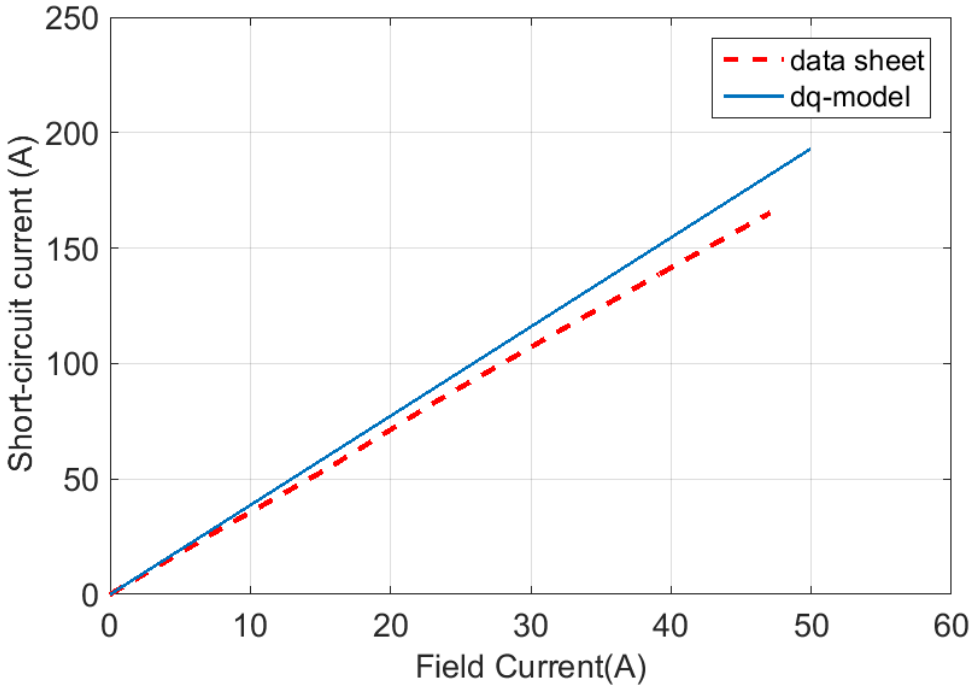


Figure 2-7 comparison between dq-model and the commercial generator SCT

The dq model gives good results when the machine has no harmonics, because when the machine variables transformed to the dq-reference frame and become DC values. However, if the machine has harmonics, the transformation to the dq-reference frame does not give DC values.

2.3 Finite Element Modelling of the Synchronous Generator

Finite element analysis (FEA) has gained a significant attention due to their superior ability to simulate the machine with high accuracy. So, a two-dimensional finite element analysis (2DFEA) model was built for the proposed generator to see how these changes in the design effect the performance of the generator and calculate the generator parameters.

2.3.1 The Original Generator:

The original generator is a standard commercial 72.5 kVA, 4-poles wound field synchronous generator. The commercial generator has a 2/3 pitch winding skewed by one slot pitch, which has 48 slots and double layer winding, and each phase consists of four coils each two connected in parallel and these two are then connected in series. The generator data sheet is given in Appendix A

2.3.2 The Proposed Generator

The proposed generator is based on the original generator with modifications made to the stator in order to simplify the manufacturing process and increase the generator capacity. It has a skewless stator with a fully pitched winding, while the rotor, it is the same rotor of the commercial generator, and is shown in Figure 2-8. The winding layout is shown in Figure 2-9.

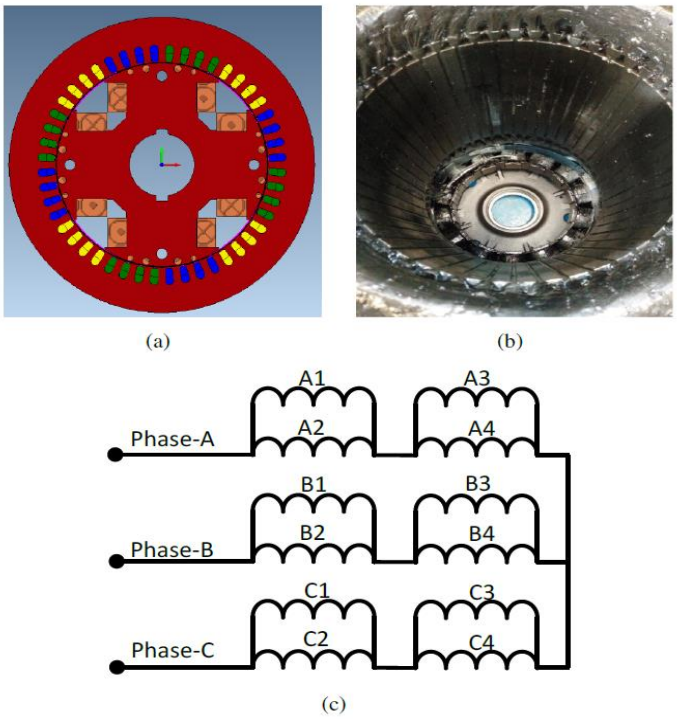


Figure 2-8 Full pitch skewless generator (a)2D finite element analysis (FEA) model (b) Experimental prototype (the proposed generator) (c) Stator coils connection diagram

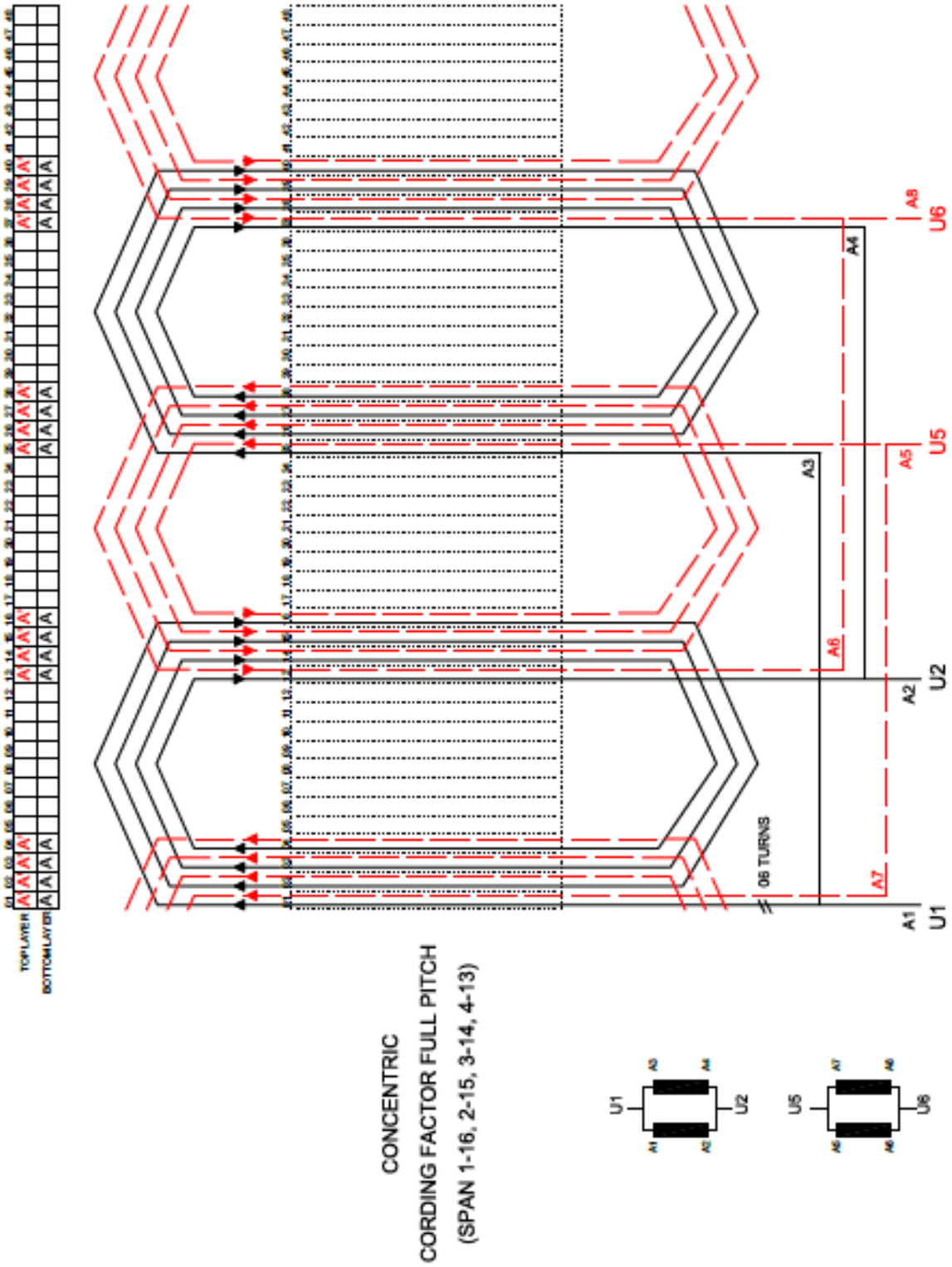


Figure 2-9 The proposed generator phase-A winding layout

In the proposed generator, the neutral wire is removed to prevent triplen current harmonics following in the generator. A load side neutral for single-phase loads will be supplied from the active power filter (APF), (more details about APF will be discussed in the next chapter).

According to [39], the fundamental back-EMF of the SG can be written as:

$$E_{rms} = 4.44\, f k_d k_p N \Phi_{pole} \tag{2-108}$$

where f is the induced voltage frequency, k_d is the distribution factor, k_p is the pitch factor, N is the number of turns per phase and Φ_{pole} is the flux per pole. Figure 2-10 shows the resultant EMF in short-pitched and full pitched coils, where E_{is} is the induced EMF in one side of the coil. Since the pitch angle in the standard commercial generator is 120° electrical degree (to cancel the third harmonic), and according to equation (2-109) it has k_p = 0.866. Due to the increased pitch factor to 1.0, the back-EMF voltage of the proposed generator will be higher by about 15% than the standard generator at the same flux density.

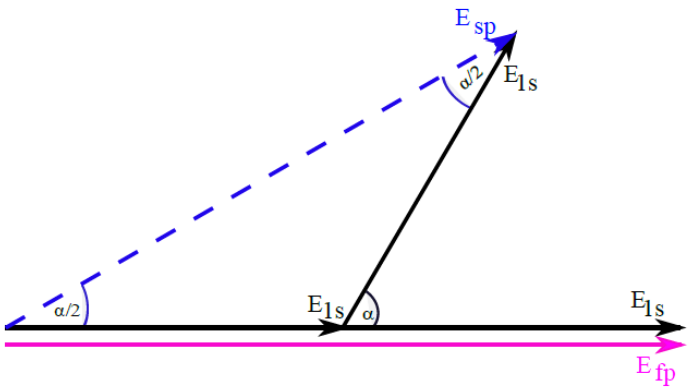


Figure 2-10 Phasor diagram of the resultant EMF of short and full pitched coil

$$k_p = \frac{EMF\ of\ short\ pitched\ coil}{EMF\ of\ full\ pitched\ coil} = \frac{E_{sp}}{E_{fp}} \qquad (2\text{-}109)$$

$$k_p = \frac{2E_{s1}\cos(\alpha/2)}{2E_{s1}} = \cos(\alpha/2)$$

2.3.3 2DFEA Model for the Proposed Generator

A 2D finite element model is built in MagNet software based on the geometry of the proposed generator with a fully pitched winding. Figure 2-11 shows the 2DFEA model for the proposed generator. A Transient 2D with Motion simulation was performed for the model for one cycle, and during this simulation the field current was kept constant. The damper bars have been removed to simplify the model.

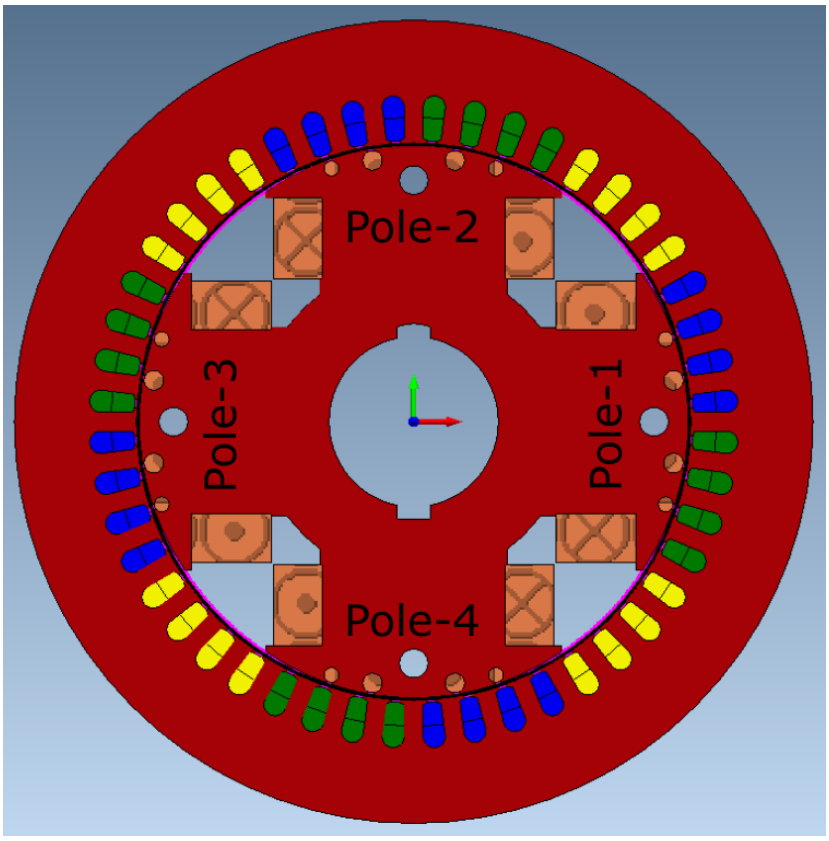
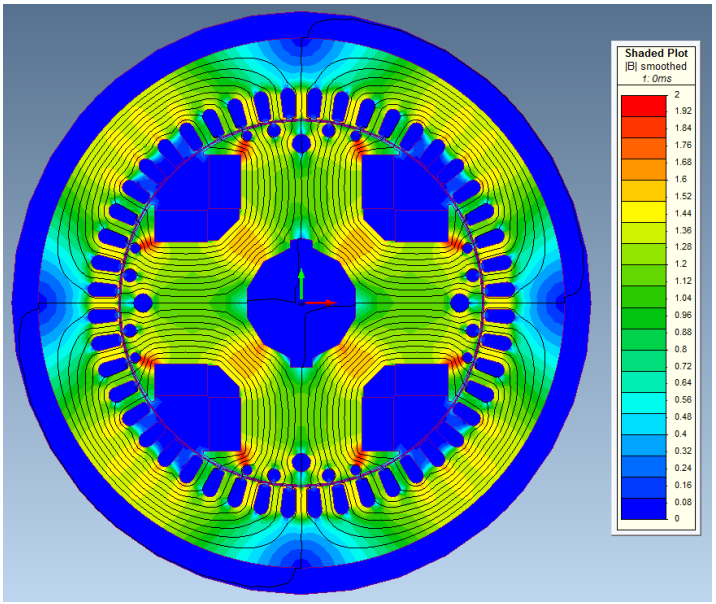
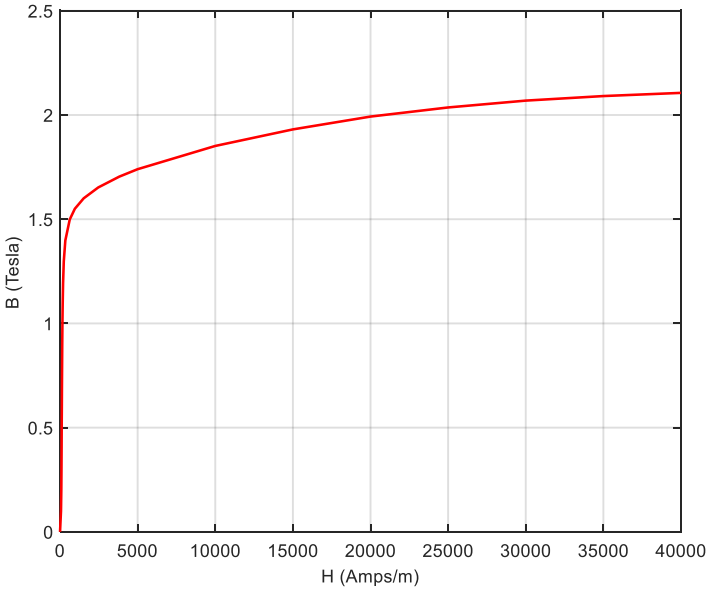


Figure 2-11 2DFEA model for the proposed generator

The flux distribution in the proposed generator is shown in Figure 2-12, as can be seen from the figure the machine is still in the linear region and doesn't saturate at the rated voltage.



(a)



(b)

Figure 2-12 (a) Flux distribution inside the proposed generator (If=11.2A), (b) B-H curve of the core material

The no load voltage of the proposed generator is shown in Figure 2-13 at a field current of 11.2A; it is clear from the figure that the

slot harmonics have a significant effect on the no load voltage due to the unskewed stator.

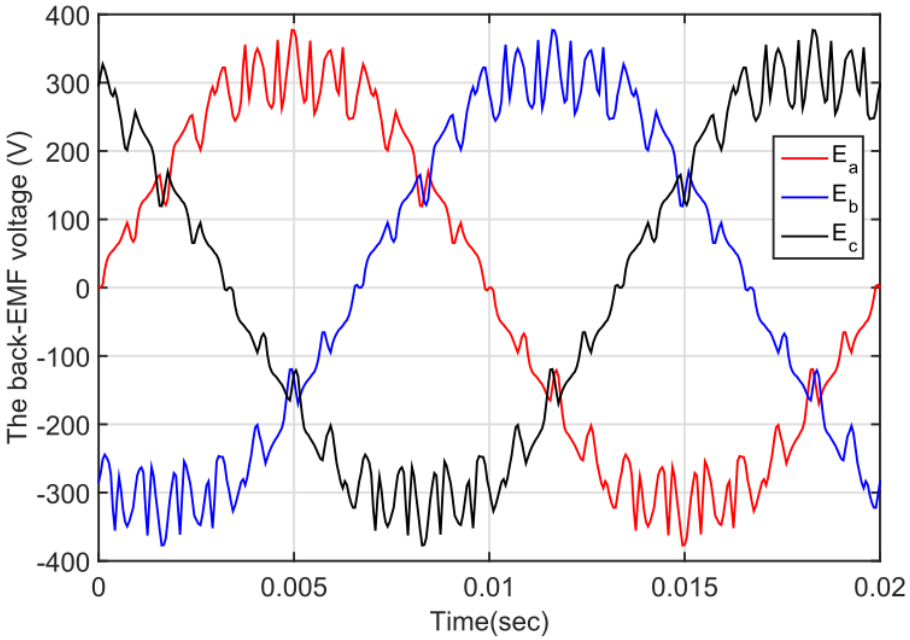


Figure 2-13 The no load voltage of the proposed generator (If=11.2A)

The FFT analysis for the no load voltage is shown in Figure 2-14 THD 11.8% and the RMS voltage is 231V.

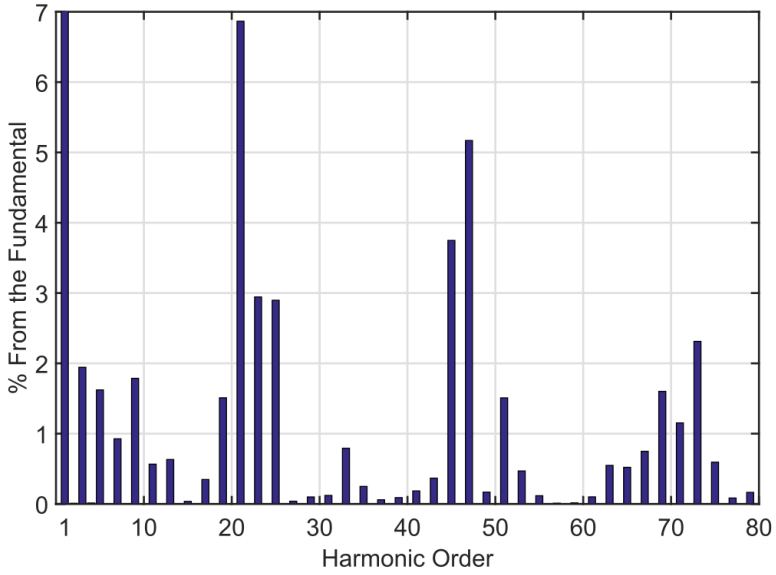


Figure 2-14 FFT analysis for the back-EMF voltage of the proposed generator

The line-to-line voltage is shown in Figure 2-15. It has less THD because the triplen harmonics cancel each other and do not appear in the line voltage. The FTT analysis of the line voltage is shown in Figure 2-16, the THD in the line voltage was 7.92% and rms voltage of 400V.

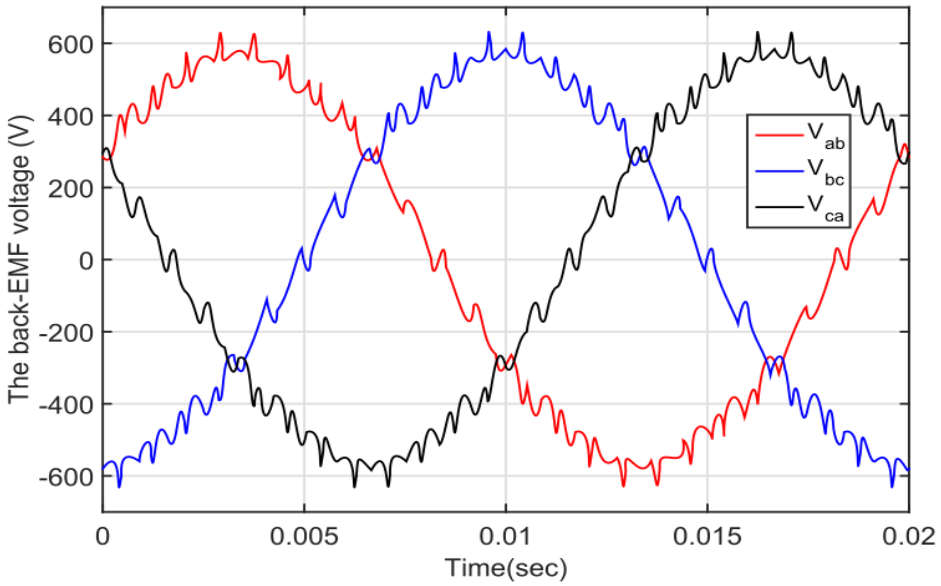


Figure 2-15 Line-to-line voltage of the proposed generator

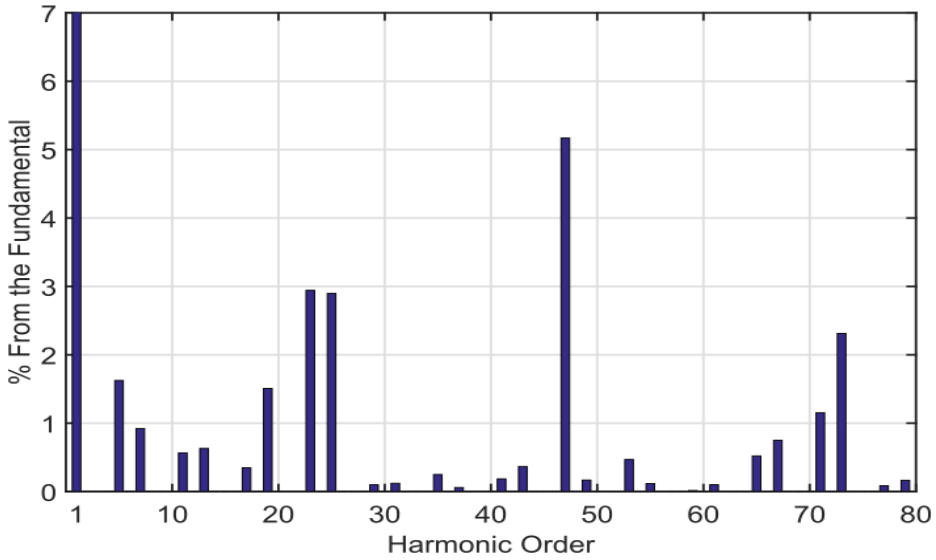


Figure 2-16 FFT analysis for the line voltage of the proposed generator

2.3.4 Inductance Matrix of the Proposed Generator:

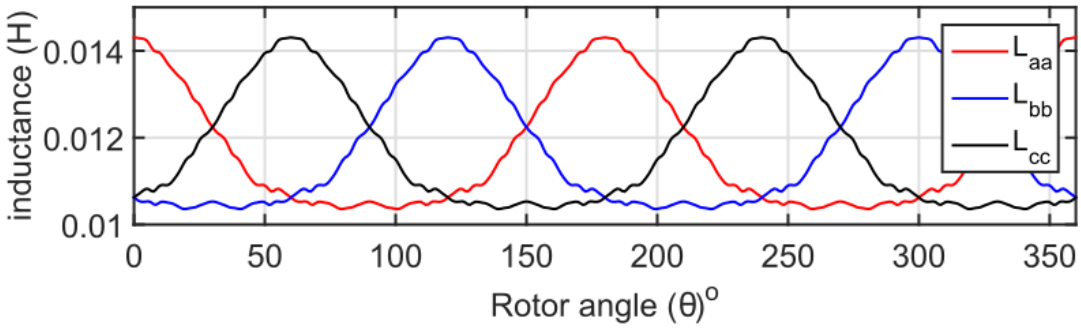
To simplify the model, the damper bars were removed from the model. Several simulations were done in MagNet software to build the inductance matrix of the proposed generator. In each simulation, one Ampere DC current was injected in one coil of the generator's coils and Transient 2D with Motion simulation was run. The simulation was done for one electrical cycle i.e. 180 mechanical degrees, and each slot divided into 16 samples to get a good accuracy in the result. The total samples in one cycle was 384. After each simulation the self and mutual inductance for that coil are calculated.

The flux linkage of the coil was extracted from the Results window in Flux Linkage tab in MagNet software and from equation (2-110) the coil inductance was calculated.

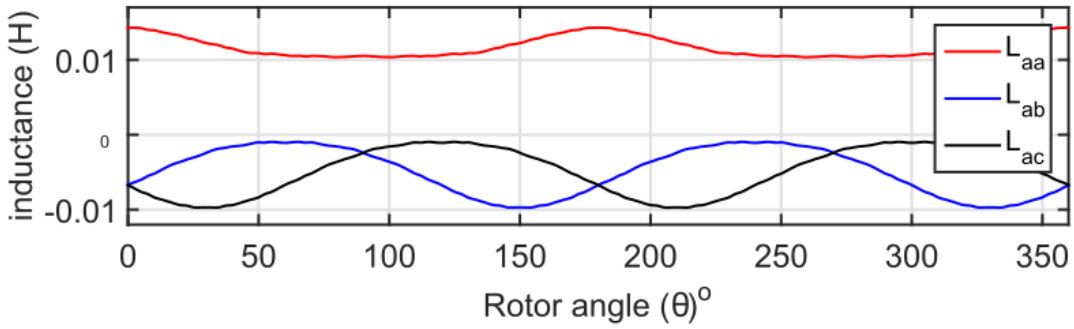
$$Machine\ Flux\ = L \times I \tag{2-110}$$

Where L is coil inductance and I the current injected in the coil. Since the current is set to 1A in the simulation, then in this case, the flux linkage will be equal to the inductance. Because the machine has 4 coils (one for the field, three for stator windings) four simulations will be run to build the full the inductance matrix of the proposed generator.

Figure 2-17 (a) shows the self-inductances of stator windings and Figure 2-17 (b) shows the self-inductance of phase-A, the mutual inductance between phase-A and phase-B and the mutual inductance between phase-A and phase-C, as can be seen from the figure (Figure 2-17), the inductances are not sinusoidal waveforms and they include harmonics.



(a) The self-inductances of stator windings



(b) Red: the self-inductace of phaseA
Blue: the mutual inductance between phase A and phase B
Black: the mutual inductance between phase A and phase C

Figure 2-17 Phase-A inductance waveforms

The mutual-inductance between the field winding and the stator winding and self-inductance of the field winding are shown in Figure 2-18, as can be seen from the figure, the self-inductance of the field winding is affected by the slot harmonics. .

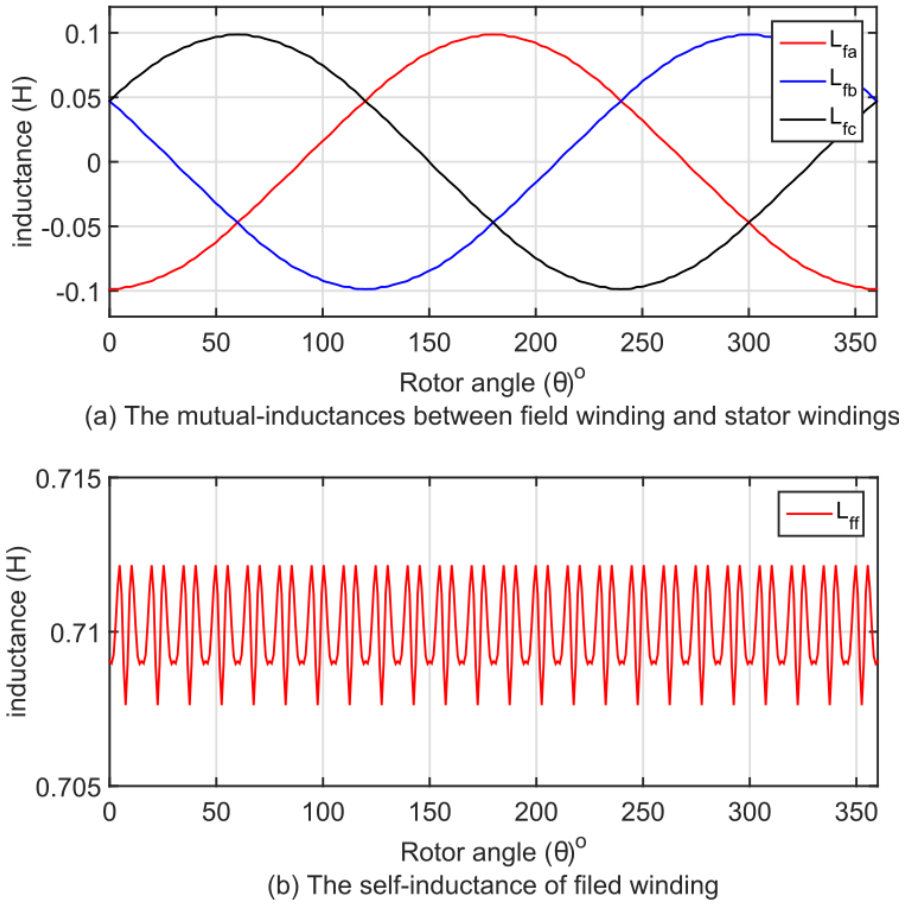


Figure 2-18 the mutual and self-inductance of the field winding

The inductance matrix was constructed, where it is a 3D matrix with size 384X4X4. Each layer contains the self-inductance and mutual inductance between machine windings at one rotor position, and the number of layers equal the number of rotor positions in the simulation (the number of samples in one cycle). This inductance matrix is stored in an Mat-file in Matlab and it used to build the Matlab Simulink model for the proposed generator.

2.4 **Accurate Modelling of Synchronous Generator in Matlab Simulink**

A Matlab Simulink based model was developed for the proposed generator as shown in Figure 2-19. This model is based on the inductance matrix of the proposed generator at different rotor

positions taken from the 2DFEA model, which was developed in the previous section. The inductance matrix is a three dimensional matrix where each layer contains the self and the mutual inductances between the windings of the generator coils (i.e. stator, and field windings) at one rotor position.

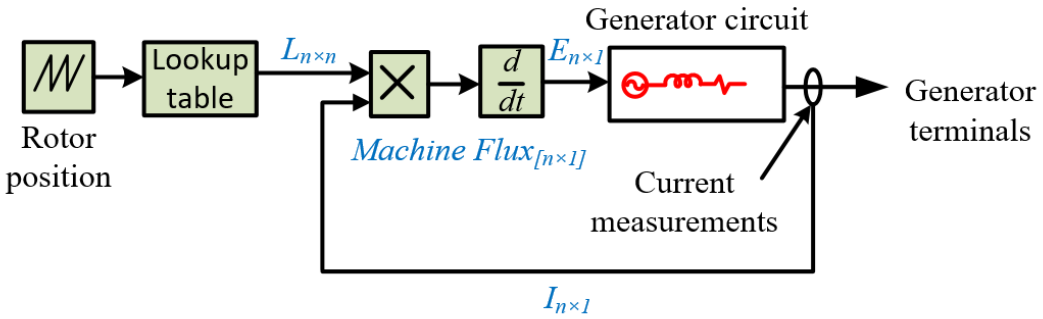


Figure 2-19 Block diagram of the generator Simulink Matlab model

This model is a linear model, where the effects of saturation were neglected, and the generator is running at constant speed (synchronous speed). The AVR circuit was replaced by a constant DC voltage source, and the value of the DC source was adjusted to give the rated voltage of the generator during the simulation time.

2.4.1 Model Description and Operation Principle:

The operation method of the model can be described as follows:

1. The model starts with repeated sequence source which determines rotor position (generator speed), the repeated sequence is a saw tooth waveform various from 0 to 2π in 20 *ms,* these values represent a constant speed of 1500 rpm.
2. The rotor position is fed to one dimensional lookup tables, where the tables data are vectors contain the generator inductances and the Breakpoint is the rotor position

vector. Figure 2-20 shows the Simulink block diagram for implementing phase-A in Matlab Simulink.

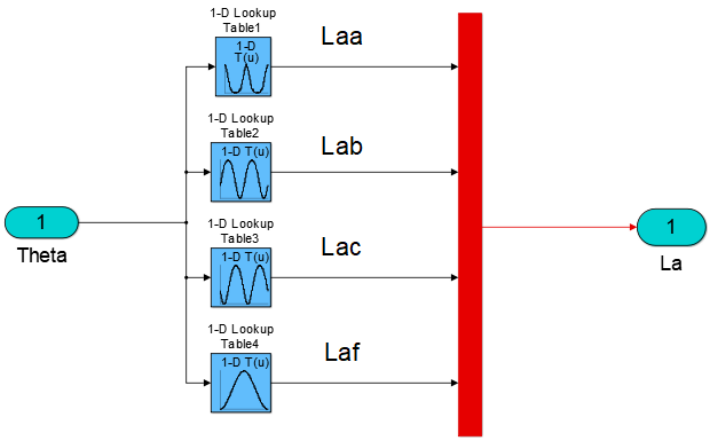


Figure 2-20 Matlab Simulink Block diagram for implementing Phase-A

3. The previous point is repeated for the other generator coils (3 coils). In this model the inductance calculation is divided to four subsystems and in each subsystem 1-coil, where the first three subsystems for the stator and the fourth subsystem for the field, in each subsystem the implemented inductance matrix is a 384X4 matrix by using the Horizontal Matrix Concatenate block as shown in Figure 2-21.

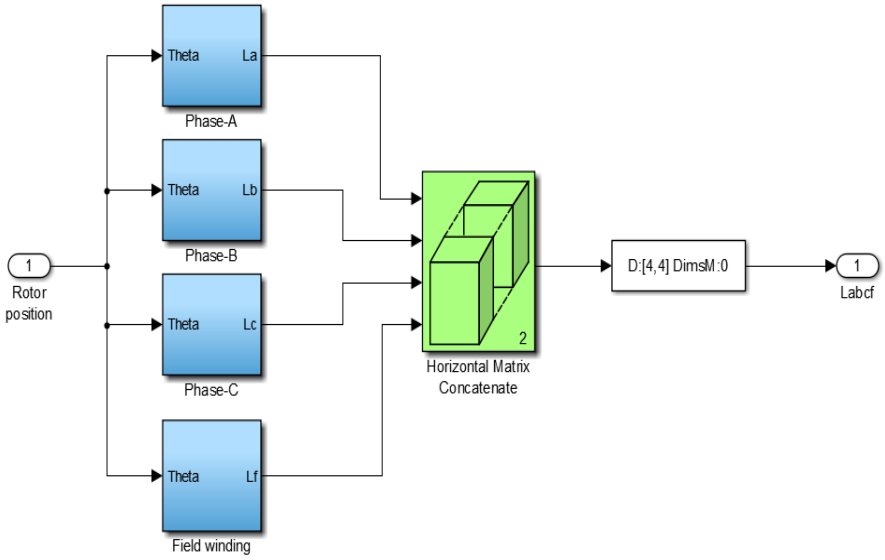


Figure 2-21 Matlab Simulink Block diagram for stator and field winding inductances

4. After generating the inductance matrix, the machine flux linkage $Machine\ Flux_{[n\times1]}$ and the induced back-EMF $\mathrm{E}_{bac-EMF[n\times1]}$ are calculated by equation (2-111) and equation (2-112) respectively.

$$Machine\ Flux_{[n\times1]} = L_{[n\times n]} \times I_{[n\times1]} \qquad (2\text{-}111)$$

$$Electromagentic\ voltage_{[n\times1]} = \frac{dMachine\ Flux_{[n\times1]}}{dt} \qquad (2\text{-}112)$$

5. Where $L_{[n\times n]}$ is the inductance matrix for the generator coils at one rotor position , $I_{[n\times1]}$ is the current at the generator coils and *n* is the number of machine coils..
6. The back-EMFs of the stator windings are fed to a controlled voltage source connected to a resistance and inductance as shown in Figure 2-22, and this resistance represent the stator winding resistance and the inductance represent the leakage inductance of the coil.

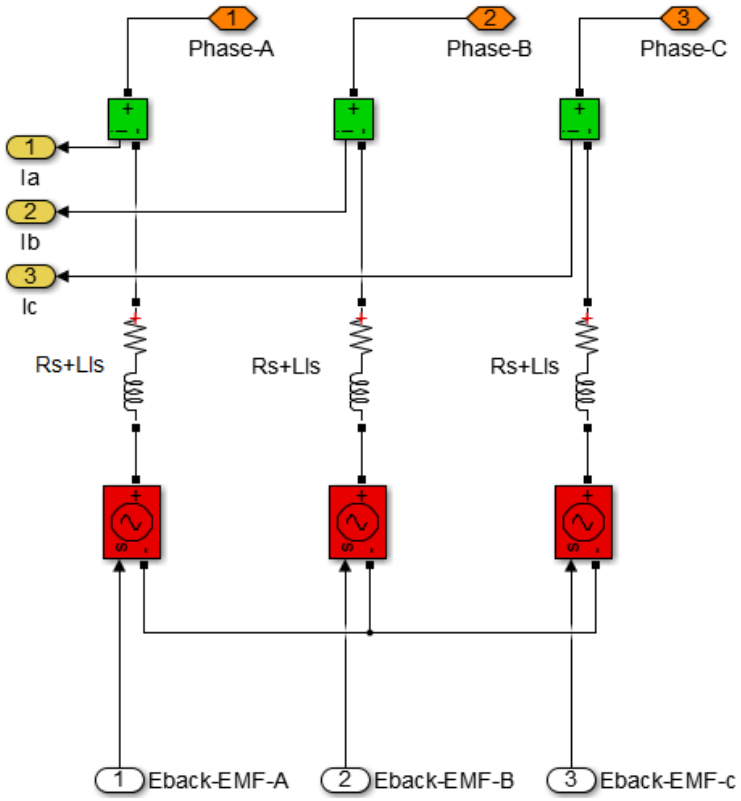


Figure 2-22 Matlab Simulink Block diagram for the back-EMF of the stator winding

The full Matlab Simulink model of the proposed generator is shown in Figure 25.

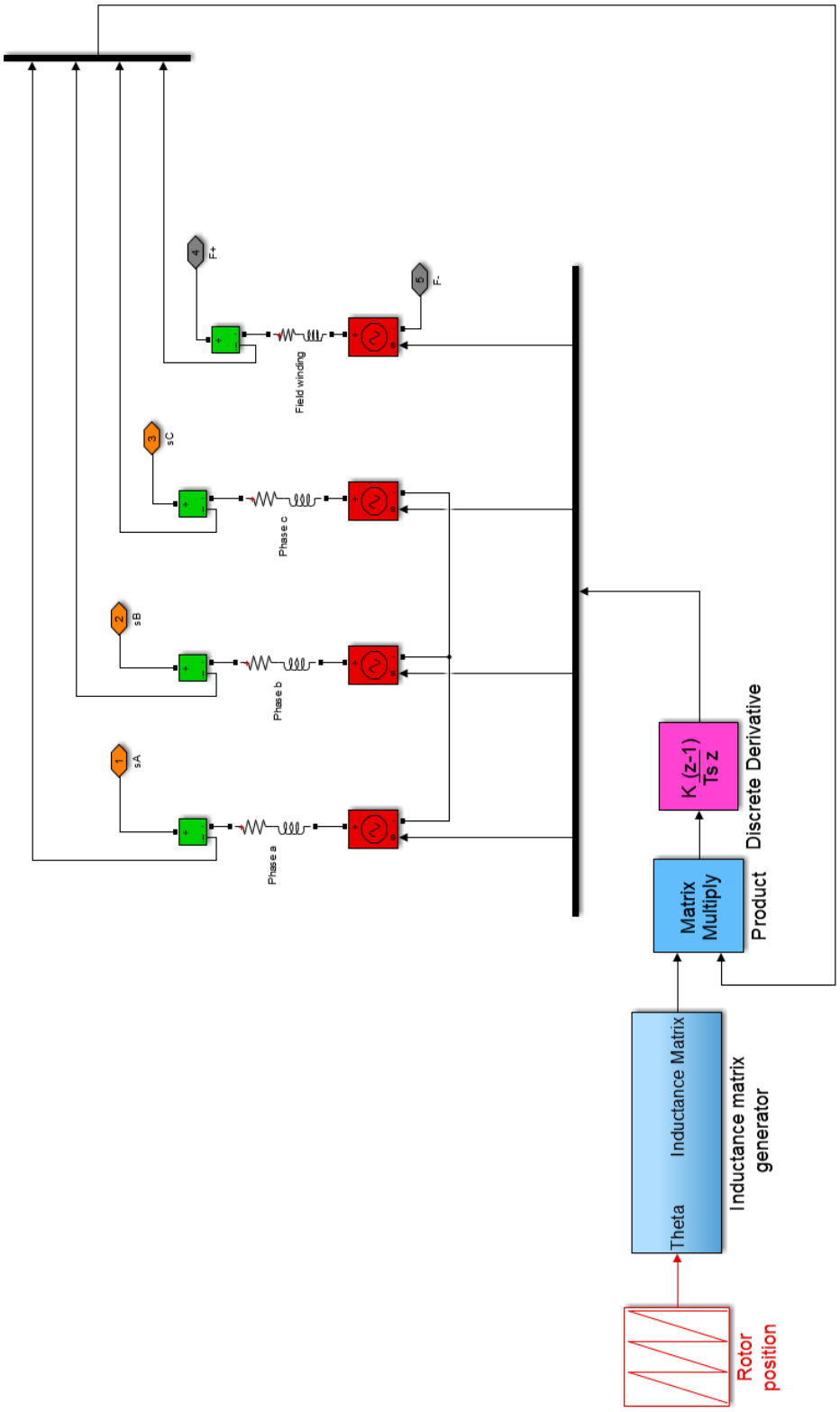


Figure 2-23 Matlab Simulink Block diagram for the proposed generator

2.5 Comparison between FEA and Matlab Simulink Models

Several test were done on the Matlab Simulink model developed in section 2.4 to compare the results from the Matlab Simulink model with 2DFEA model developed in section 02.3 The motivation of this comparison is to check the performance of the developed model in Matlab Simulink model, as it will be used to validate the harmonic compensation method in the developed generator.

The comparisons were done for the back-EMF voltage at different field current. The following subsections will discuss these comparisons in detail.

2.5.1 The back-EMF Voltage and Open Circuit Test:

In this comparison, the back-EMF voltage that was developed in the 2DFEA model is compared with the back-EMF voltage that developed in Matlab Simulink model. Both simulations were done under the circumstances (i.e. same speed and same excitation). In this simulation, the generator was run at constant speed with no load with field current of 11.2A, and the output voltage of the generator was recorded. Figure 2-24 shows the back-EMF of both models, and it is a clear from the figure that there is a good match between back-EMFs from both models. As can be noticed from the figure the back-EMF voltage from the Matlab Simulink model slightly higher than the back-EMF voltage from 2DFEA model due to the saturation effect in the 2DFEA model, while the Matlab Simulink model is a linear model. In addition, the THD in the back-EMF voltage in the 2DFEA model was 13.9% at the rated voltage and it was 15.7% in the Matlab Simulink (MS) .

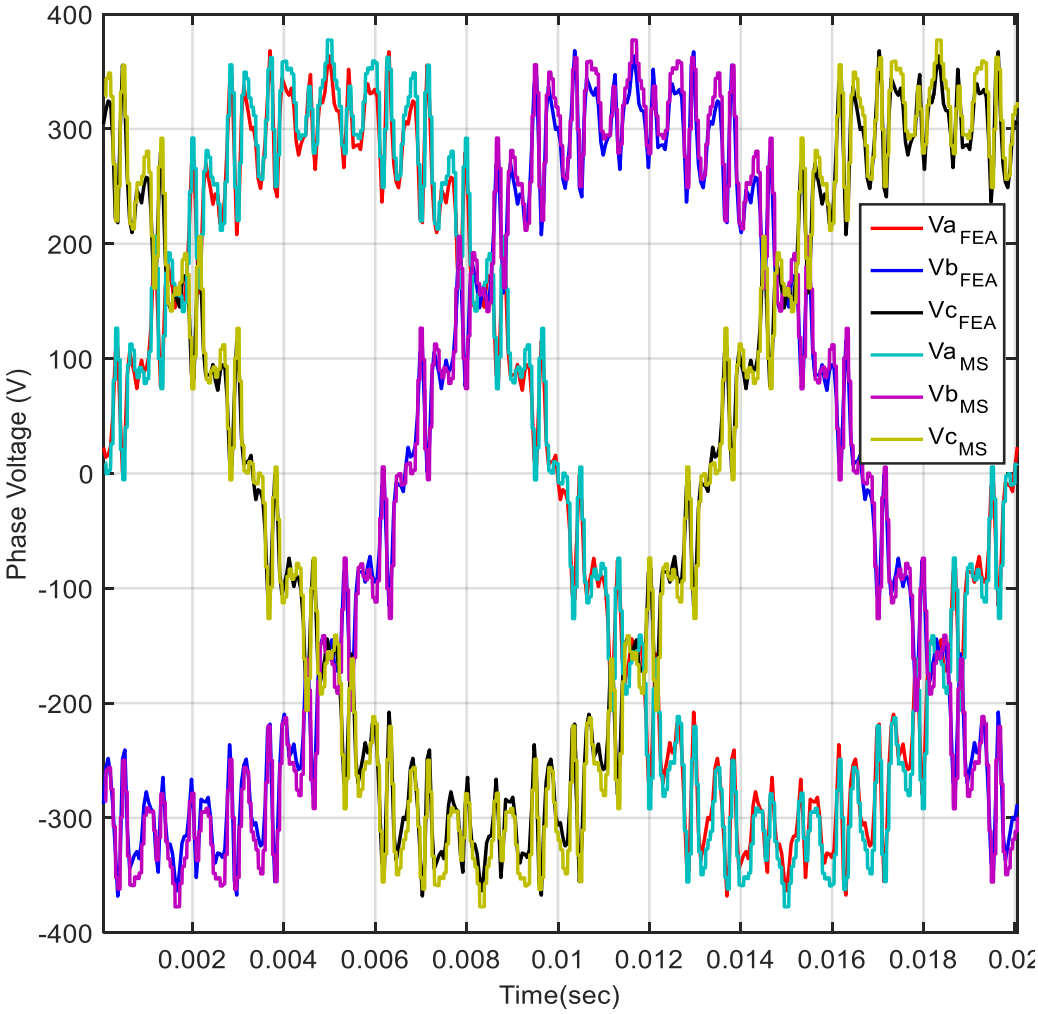


Figure 2-24 Comparison between 2DFEA (FEA) and Matlab Simulink (MS) models of the proposed generator

In addition, the open-circuit (OC) test was performed for both models, where in this simulation; the simulation was run for different values of the field current starting from 0 to 50A with unloaded generator. In each simulation, the output voltage is recorded and the RMS value of the output voltage is calculated. Figure 2-25 shows the open circuit test from the 2DFEA model and the Matlab Simulink (MS) model. As it can be seen from the figure, there is a match between the models in the linear region (airgap line), however, for

higher values of the field current ($I_f > 11A$) the saturation effect appears on the 2DFEA model while the Matlab Simulink model continued in a straight line.

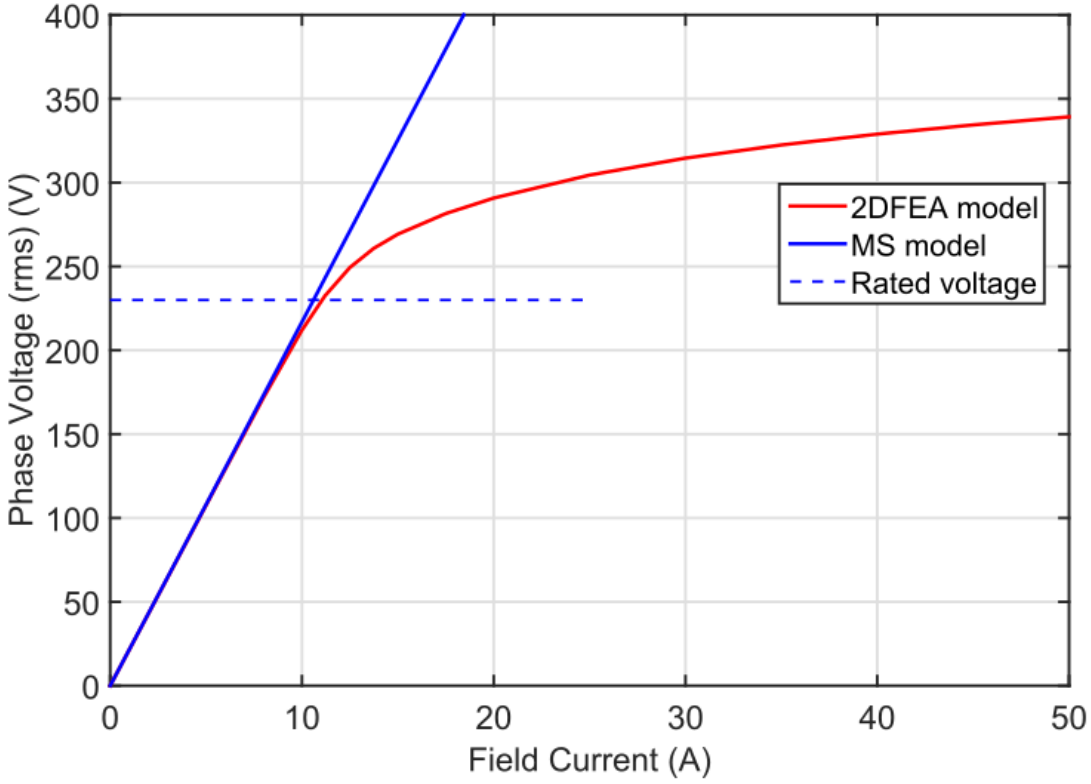
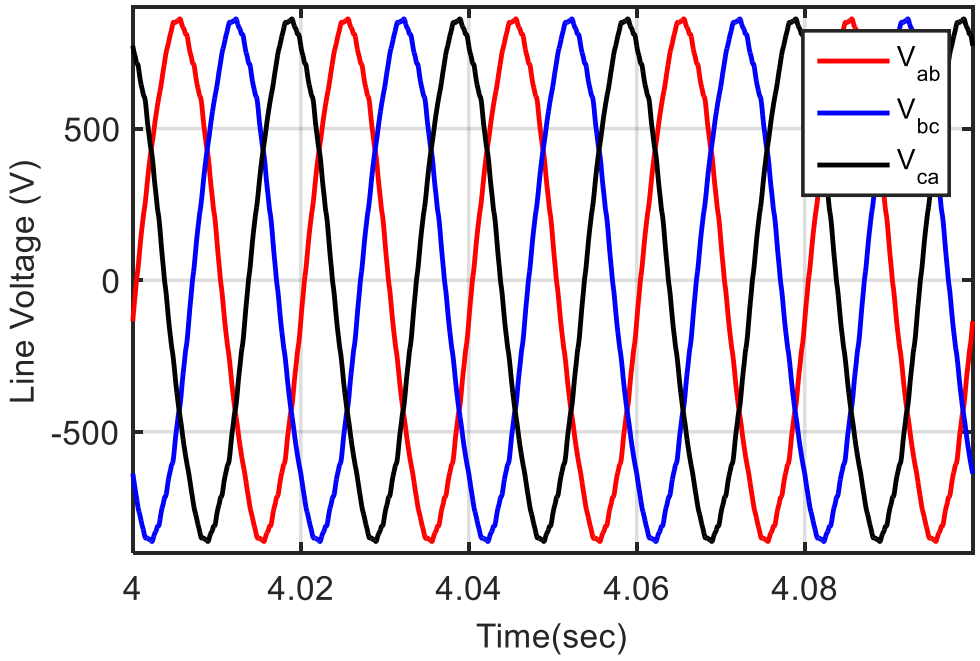


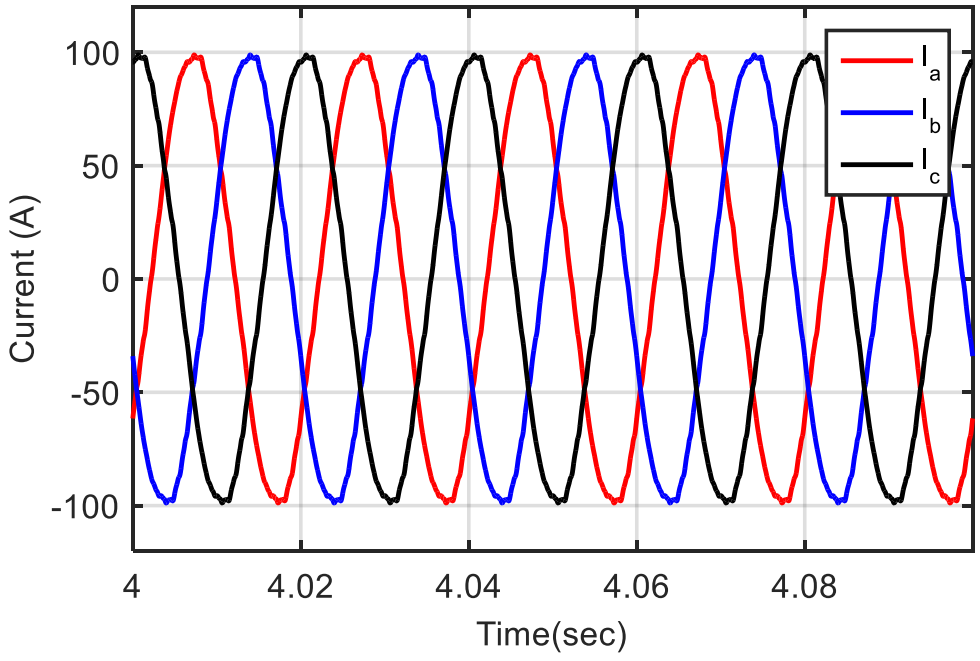
Figure 2-25 Open-circuit test form 2DFEA model and the Matlab Simulink (MS) model

2.5.2 Loaded Generator

A loaded generator test was done to compare the results from the Matlab Simulink model with the 2DFEA model of the proposed generator, the test was done for a three-phase resistive load (R = 4.92 Ω). The field current was kept constant in both simulations and was equal to 22.85A. Figure 2-26 and Figure 2-27 show the Simulink Matlab and 2DFEA models simulation results for the balanced linear load respectively, the THD (both voltage and current) in the 2DFEA model was 2.4% while in the Simulink model was 3 %. The difference in the THD and the peak value of the waveforms between the two models due to the linearity in the Malab Simulink model.

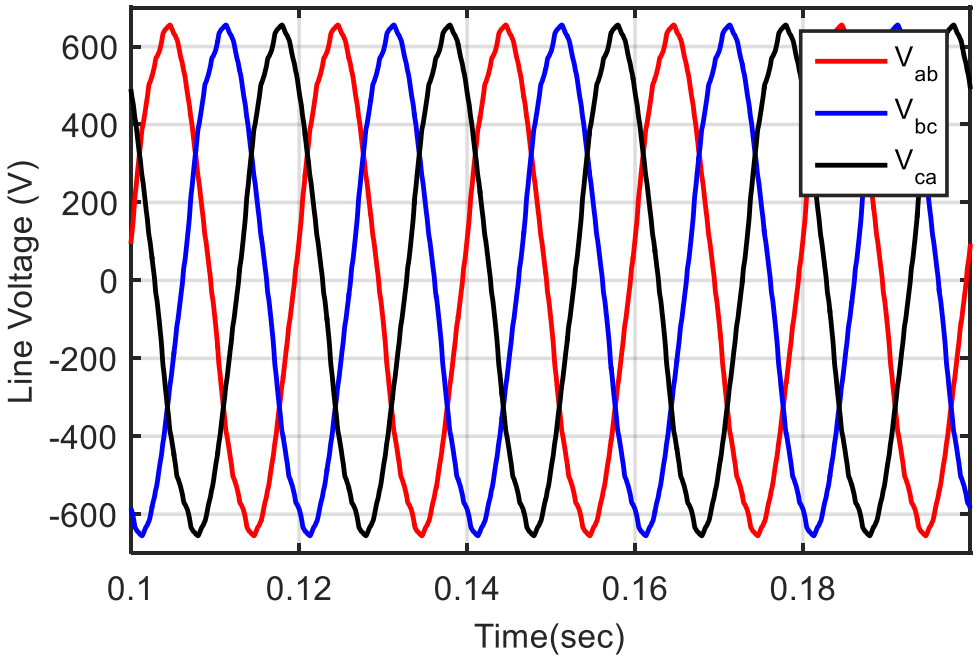


(a)Generator Line voltage for Linear Load from Matlab model

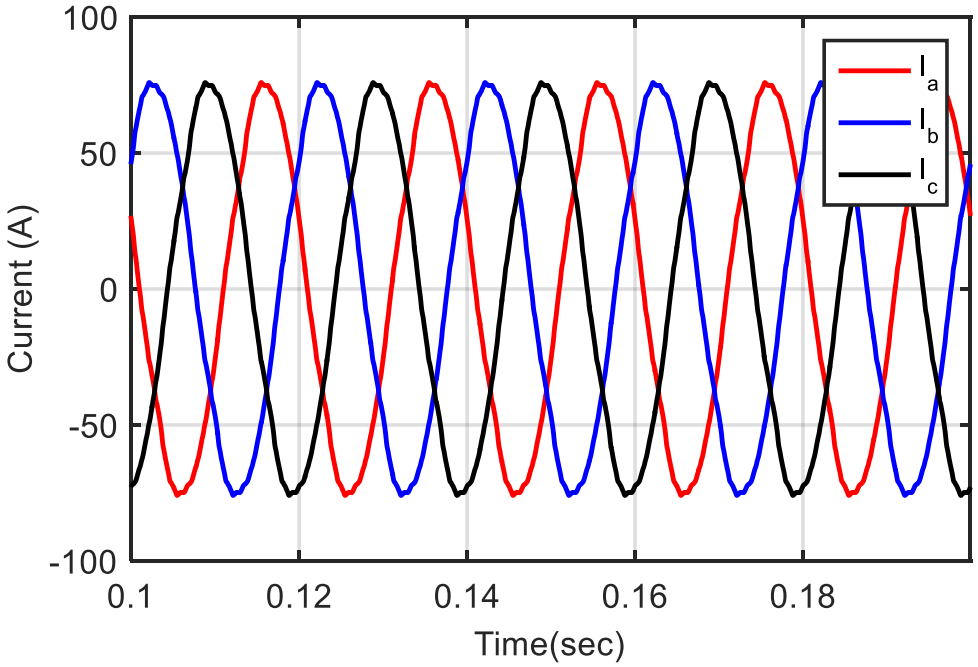


(b)Generator Current for Linear Load from Matlab model

Figure 2-26 The simulation results for a balanced linear load from Simulink Matlab model, (a) Generator output voltage (b) Generator output current



(a)Generator Line Voltage for Linear Load from FEA model



(b)Generator Current for Linear Load from from FEA Model

Figure 2-27 The simulation results for a balanced linear load from 2DFEA model, (a) Generator output voltage (b) Generator output current

2.6 **Experimental Validation**

A prototype model of the proposed generator was built, as described in section 2.3.2, where the stator is unskewed and the stator winding is fully pitched. Figure 2-28 shows the stator of the prototype generator and as can be seen in the figure the stator slots are unskewed. The proposed generator was installed on a test rig as shown in Figure 2-29. The rotor is the same as the commercial generator (4-poles).



Figure 2-28 The stator of the prototype generator

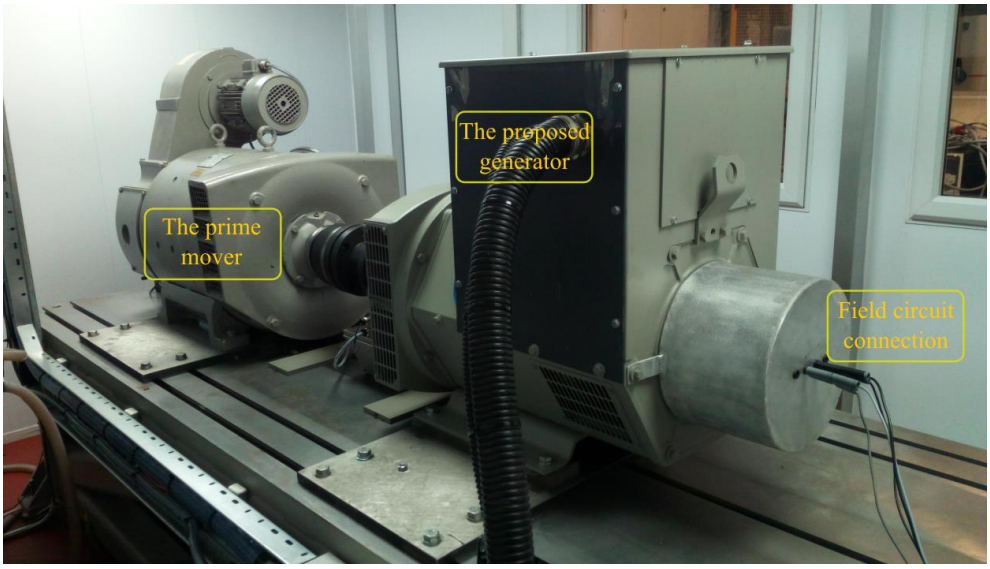


Figure 2-29 The proposed generator test rig

2.6.1 Open-Circuit Test:

The open-circuit test was done for the proposed generator, in this test the generator terminals are kept open and the field winding was fed by a DC voltage source through the field circuit connection using slip rings, as shown in Figure 2-29. The generator was run at constant speed by a prime mover (DC motor) driven by a Eurotherm Drive, a 590 Digital series with closed loop speed Control. The output voltage was measured for different values of the field current. Figure 2-30 shows the experimental values for the open-circuit test compared to the open-circuit test from the 2dFEA model for the proposed generator and the standard commercial generator (UCI224F).

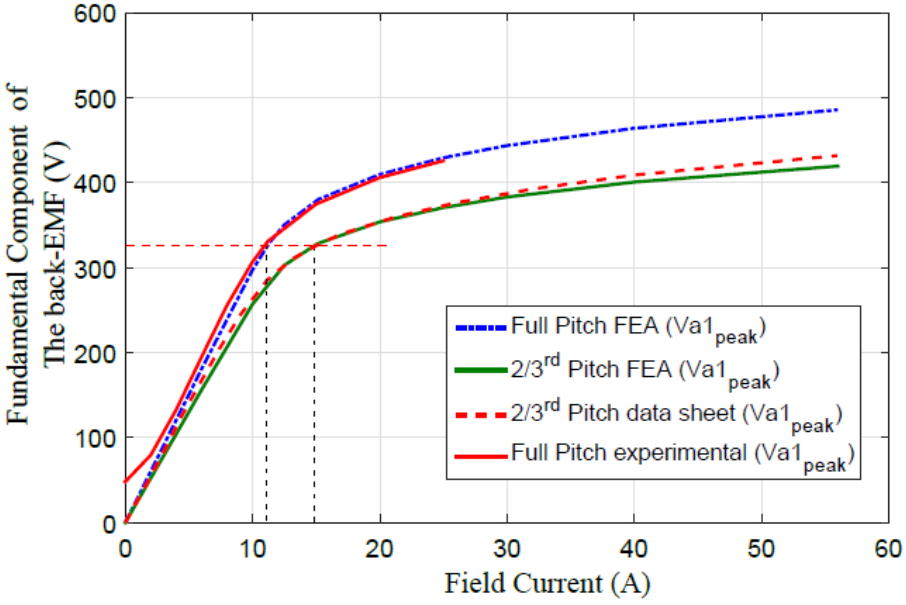


Figure 2-30 Open circuit test for the proposed generator and the standard commercial generator

As the Figure 2-30 shows, there is good match between the open-circuit test for the 2DFEA model and the experimental values for both generators. In addition, for the same fundamental output voltage the field current can be reduced from 15 A in the standard generator to 11.2 A in the proposed generator, if the power quality can be maintained.

2.6.2 Loaded Generator:

A loaded generator test was done to compare the results from the Matlab Simulink model with the experimental results of the proposed generator, the test was done for a linear *35kW* resistive load and nonlinear load i.e. three-phase diode bridge with RL load (R = 9.2 Ω and L = 5.5mH).

Figure 2-31 shows the simulation and experimental results for the balanced linear load, the THD in the Simulink model was 3 %, while in experimental test was 4.1%, a small variation due to the linearity of the Simulink model and the difference in the peak value due to the linearity in the Matlab Simulink model.

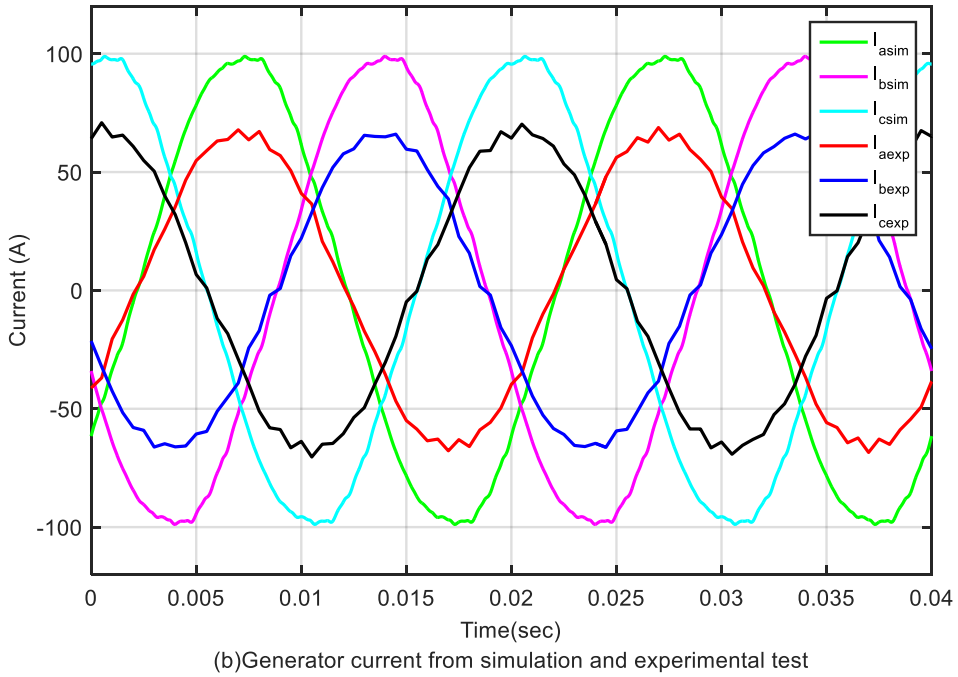


Figure 2-31 The simulation and experimental results for balanced linear load

Furthermore, the nonlinear load test was done and the results are shown in Figure 2-32, this figure shows the simulation and experimental results for balanced nonlinear load, as can be seen from the figure, the THD in the Simulink model was 15% while in the experimental test this was 25%, and the Matlab model gives a higher peak values more than the experimental values due to the linearity in the Matlab Simulink model. As can be seen from Figure 2-31 and Figure 2-32 the synchronous generator Simulink model showed a good agreement with the experimental result.

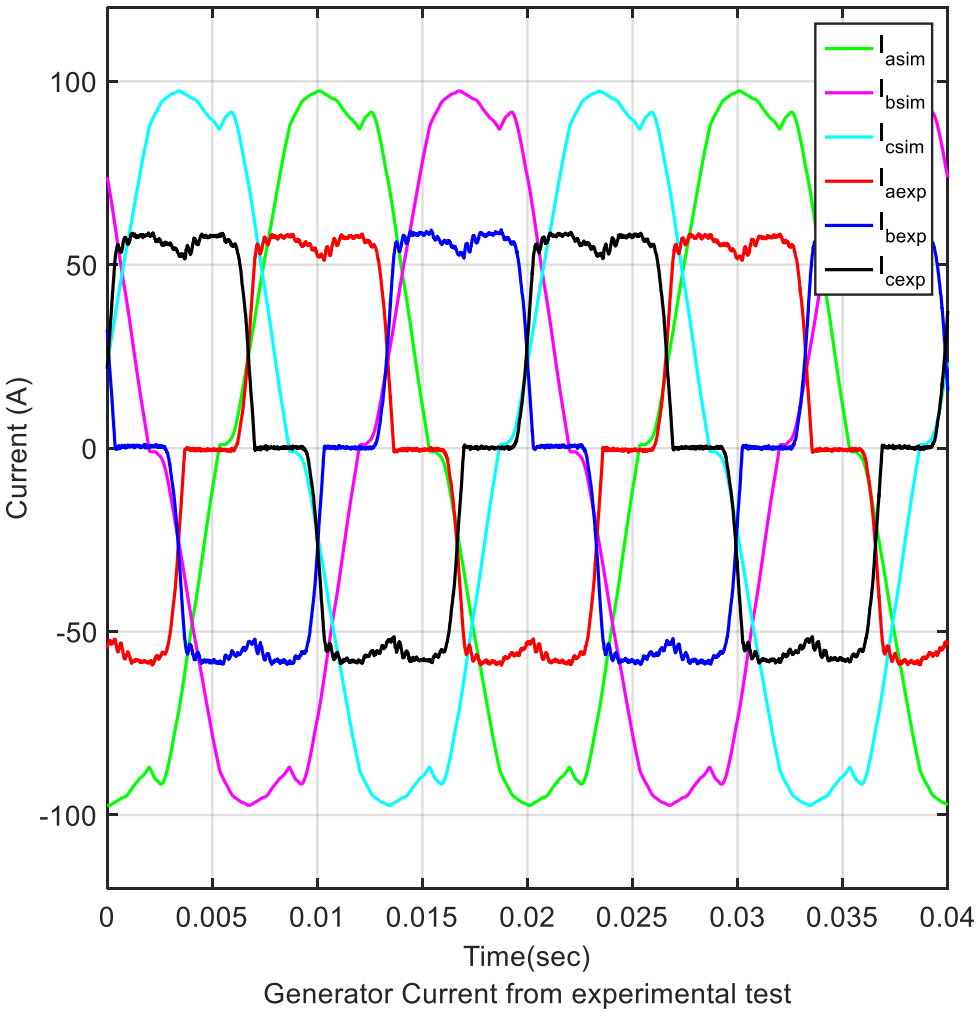


Figure 2-32 The simulation and experimental results for balanced nonlinear load

2.7 **Conclusion**

This chapter presented the proposed synchronous generator models, starting with an introduction about synchronous generators. In section 2.2 the dq model was presented, since this model is suitable for machines without harmonics, and the proposed generator does has harmonics, a different modelling approach (2DFEA) was presented in section 02.3. To build an accurate model for the proposed generator able to simulate all the proposed system (i.e. the proposed generator, the active power filter, active series filter and the load) a Matlab Simulink model based on the proposed

generator inductance matrix was presented in section 2.4. Then a comparison between the 2DFEA model and the Matlab Simulink model was presented in section 2.5 and the Matlab Simulink model showed a good agreement with the 2DFEA model. Finally, an experimental validation for the Matlab Simulink model was presented in section 0 for open-circuit test and loaded generator with linear and nonlinear loads, again the Matlab Simulink model was validated by the experimental results.

Chapter-3 Active Power Filters

Chapter-3 **Active power Filters**

This chapter introduces an introduction about the active power filters (APFs) topologies and control. Where in the first section presents a general introduction about shunt APFs, in section 3.2 APF topologies in three-phase four-wire system is presented followed by shunt and series active filters configuration in sections 3.33.4 and 3.4 respectively. Section 3.5 discusses grid synchronisation method. Current and voltage harmonic extraction techniques are presented in section 3.6 and current control methods are presented in section 3.7. The DC-link voltage control and passive element design are presented in sections 3.8 and 3.10 respectively. Finally a conclusion is presented in section 3.12.

3.1 **Introduction**

In the past, passive filters were used at the point of common coupling (PCC) to improve power quality. The passive filters have some advantages such as simple design and low cost. However, have some disadvantage for example is that each harmonic need a separate filter i.e. the single filter cannot be tuned for wide range of harmonics and hence will have limited filtering characteristic. In addition, the most serious disadvantage is causing resonance between the grid and the filter [42].

Shunt Active power filters (SAPF), which compensate harmonics and reactive current component for the power supplies, can be connected in parallel at the PCC and improve the power qualities and enhance the reliability and stability of power system. In 1982, an active power filter of 800 kVA, which consisted of current source PWM inverter using GTO thyristors, was put into practical use for harmonic compensation for the first time, [43].

The basic task of the proposed APFs (parallel and series) in this work is to compensate the current harmonics that exist in the proposed low cost generator and the current harmonics produced by the nonlinear loads, and to improve the quality of the voltage waveform at the PCC and to balance generator loading . Figure 3-1 shows the block diagram of the proposed system (the proposed generator and the proposed two filters).

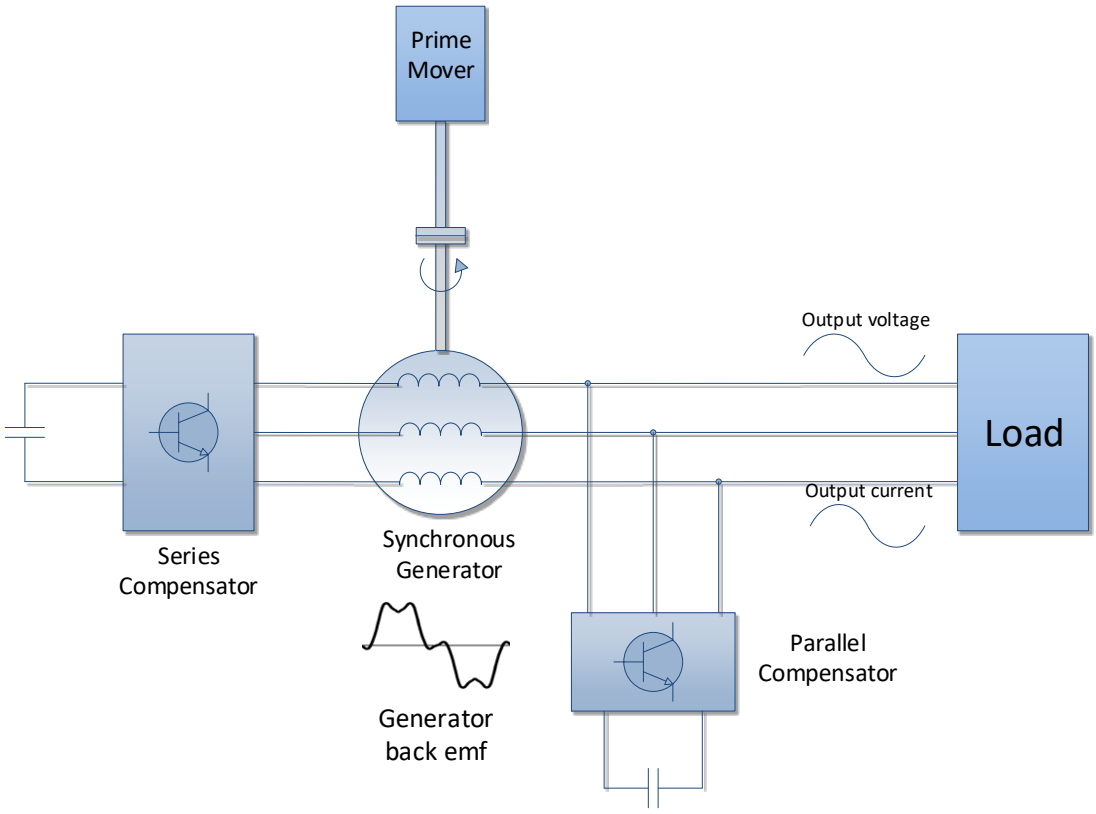


Figure 3-1 Block diagram of the propose system

The APF can be classified in different ways according to power rating, power circuit configuration, compensated variable, etc. , The classification according to the power circuit configuration is presented in Figure 3-2, [25].

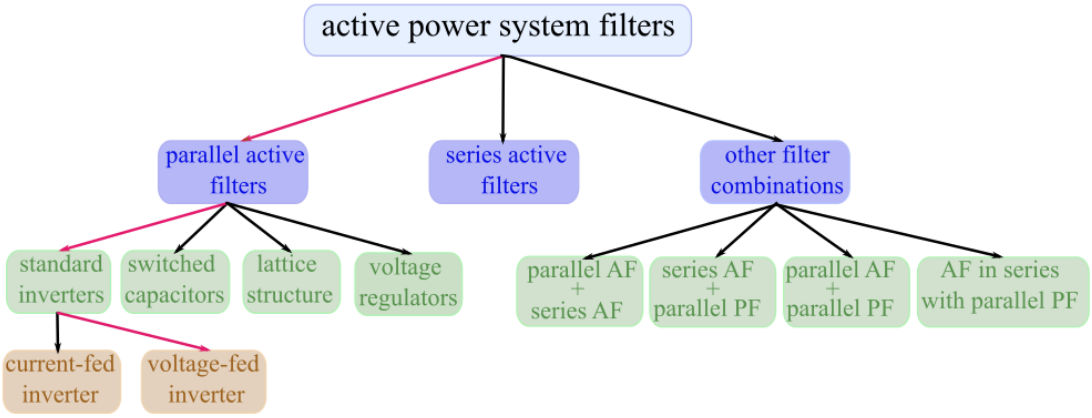


Figure 3-2 Subdivision of power system filters according to power circuit configuration and connection (AF: Active Filter, PF: Passive Filter)

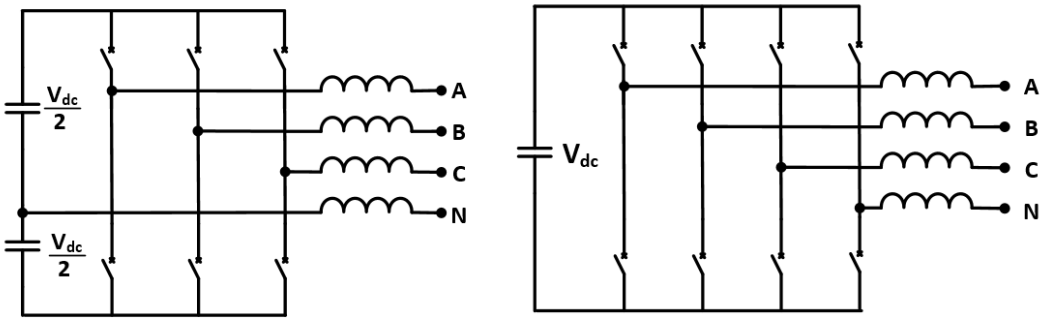
This chapter, will start with a review of converter topologies suitable for three-phase four-wire system. Then shunt active power filter and series active filter will be presented, a detailed discussion on grid synchronisation and harmonic extraction methods and current controllers design will be provided. Next, the APF passive component design will be given. Finally, conclusion will be drawn and presented.

3.2 **Active Power Filter Topologies**

Most of the research on active power filter has been focused on voltage source active power filters (VSAPF), while current source active power filters (CSAPF) have gained some attention. According to [44] the voltage source converter is more desirable than the current source converter in terms of efficiency, size and cost.

In three-phase four-wire system the converter topology can be either a conventional three-phase inverter with DC-link split capacitor with midpoint connection for neutral wire, or four-leg inverter where the neutral wire in connected to the fourth leg, see Figure 3-3. In this thesis the second configuration is chosen to reduce the DC-link capacitor size by reducing the current rating of

the DC-link capacitor [45]. In addition, since there is only one capacitor in the four-leg topology, there is only on voltage to be controlled. However, in split capacitor with midpoint topology there are two voltages to be regulated that makes the control algorithm more complex [46]. Figure 3-3 shows the three-phase four-wire APF topologies.



(a) Capacitor Midpoint topology **(b) Four-leg topology**

Figure 3-3 Three-Phase four-wire APF topologies

3.3 **Shunt Active Power Filter:**

The shunt active filter is connected in parallel between the generator and the point of common coupling (PCC), it can be used for load harmonic compensation as well as generator harmonics. It also used to supply neutral connection for single phase loads.

Figure 3-4 shows the connection and the control loops (the voltage and the current control loops) for shunt active power filters.

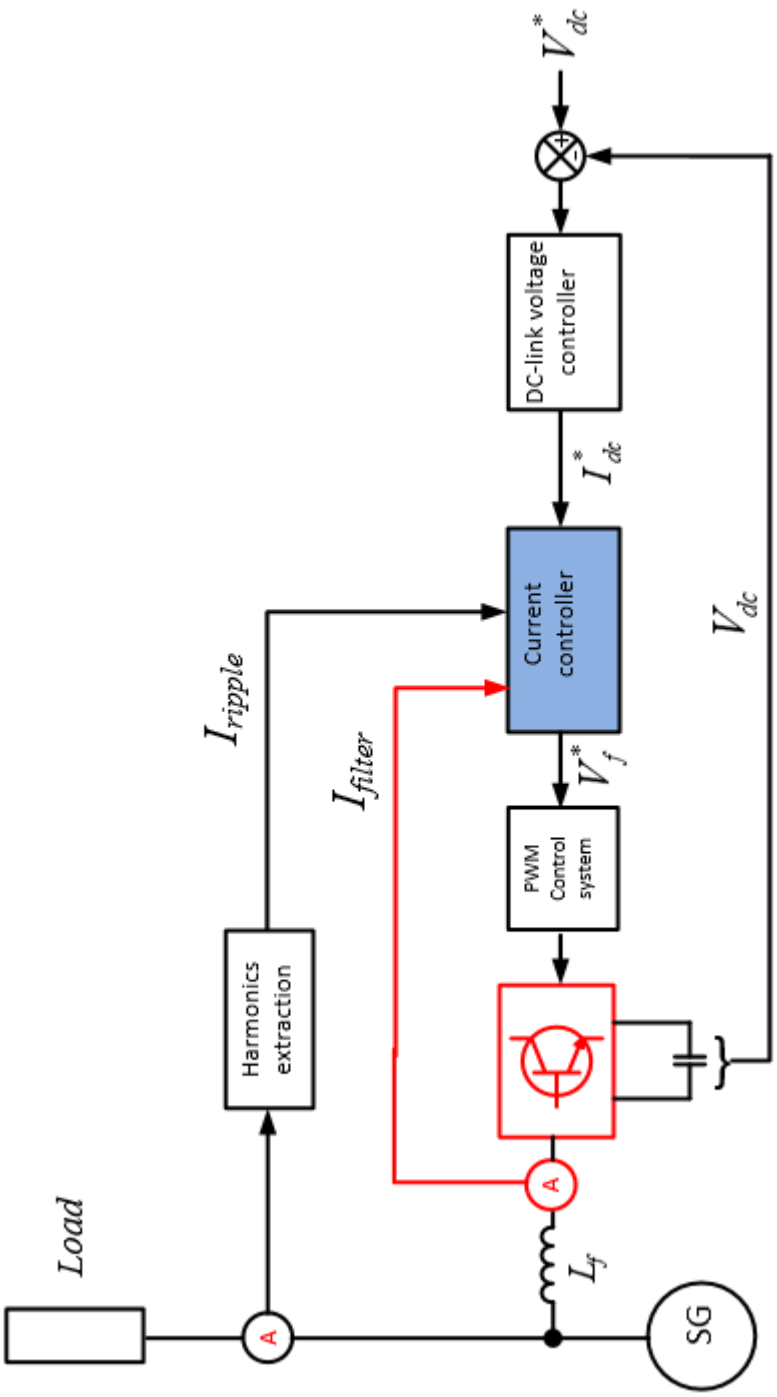


Figure 3-4 circuit configuration of Shunt APF controller

3.4 **Series Active Power Filter:**

The series active filter is connected in series with the generator windings where the neutral point was opened and the winding terminal are connected to the three legs of the voltage source inverter as shown in Figure 3-1.

The operation principle of this filter is sensing the generator windings voltages and then extract the harmonic from these voltage. Then the voltage ripples that were extracted from the voltage waveform is used as references voltage with negative sign for the series compensator to cancel the ripples at the generator connection point. The control circuit of the series active filter is shown in Figure 3-4.

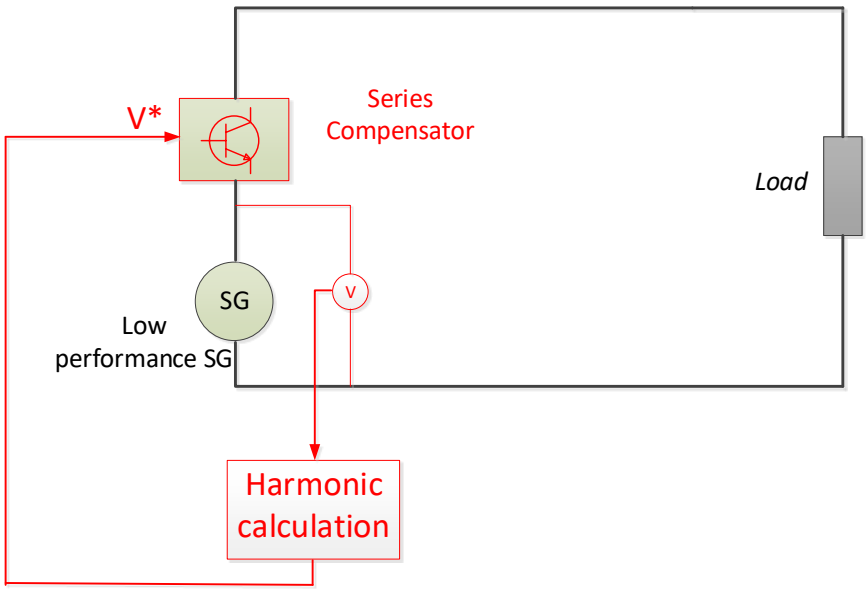


Figure 3-4 Active series filter control circuit

3.5 **Grid Synchronization Methods**

Grid phase angel detection is an important requirement for the APF operation and control. Good compensation performance of APF is highly dependent on accurate tracking of the phase angle. There are many methods in literature for synchronization with three phase grids, [47]. Phase Locked Loop based on Synchronous Reference Frame (SRF-PLL) is the common method used to synchronise the APF with the three-phase grid voltages at and point. In this section, a detailed discussion of three types of SRF-PLL will be presented, a conventional synchronous frame PLL (SFR-PLL) and other two methods, which are, decoupled double synchronous reference frame PLL (DDSRF-PLL) and dual second order generalised integrator PLL (DSOGI-PLL).

3.5.1 Conventional SRF-PLL

This synchronisation method is simple and assuming a high quality voltage source. The general block diagram of SRF-PLL is shown in Figure 3-5. The operation of SRF-PLL can be divided into two stages, which are the phase angle detector and the loop filter (i.e. controller). The phase detection is based on transforming the measured PCC voltages into a synchronous reference frame by using Park's transformation [T_{dq0}]. The angle $\grave{\theta}$ (the output of SRF-PLL) is used in this transformation as shown in equations (3-1) to (3-3). The loop filter is used to derive the input signal (v_q) to the command value ($v_q^* = 0$). By deriving $v_q$to zero, the d-axis will be aligned to the grid voltage vector. Where W_{ref} is the rated system frequency ($2\pi f=2\pi*50$).

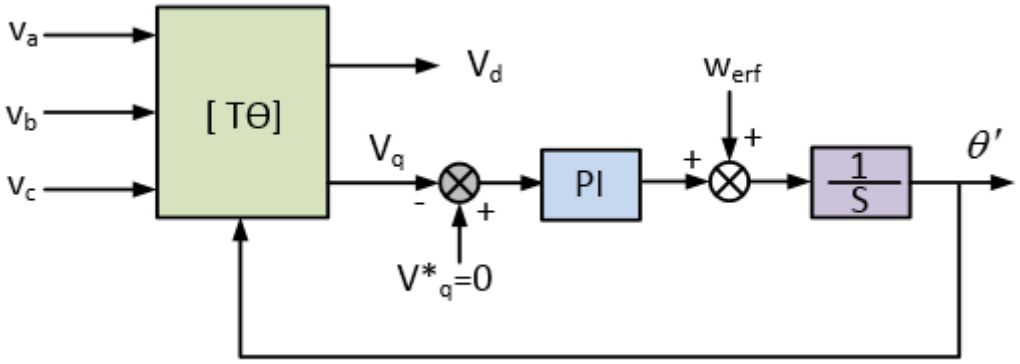


Figure 3-5 SRF-PLL block diagram

The grid voltage is assumed balanced and undistorted as given in equation (3-1).

$$\begin{bmatrix} v_a \\ v_b \\ v_c \end{bmatrix} = \begin{bmatrix} V\cos\theta \\ V\cos\left(\theta - \frac{2\pi}{3}\right) \\ V\cos\left(\theta + \frac{2\pi}{3}\right) \end{bmatrix} \tag{3-1}$$

Where V is the peak value of the voltage source.

By using Park's transformation, the three-phase voltages are transformed to the synchronous reference frame (dq0) and become DC components as shown in (3-2) and (3-3).

$$\begin{bmatrix} v_\alpha \\ v_\beta \\ v_0 \end{bmatrix} = \frac{2}{3}\begin{bmatrix} 1 & -\frac{1}{2} & -\frac{1}{2} \\ 0 & \frac{\sqrt{3}}{2} & -\frac{\sqrt{3}}{2} \\ \frac{1}{2} & \frac{1}{2} & \frac{1}{2} \end{bmatrix}\begin{bmatrix} V\cos\theta \\ V\cos\left(\theta - \frac{2\pi}{3}\right) \\ V\cos\left(\theta + \frac{2\pi}{3}\right) \end{bmatrix} \tag{3-2}$$

$$\begin{bmatrix} v_d \\ v_q \end{bmatrix} = \begin{bmatrix} \cos\hat{\theta} & \sin\hat{\theta} \\ -\sin\hat{\theta} & \cos\hat{\theta} \end{bmatrix}\begin{bmatrix} v_\alpha \\ v_\beta \end{bmatrix} = V\begin{bmatrix} \cos(\theta - \hat{\theta}) \\ \sin(\theta - \hat{\theta}) \end{bmatrix} \tag{3-3}$$

Where $\hat{\theta}$ is the angle that is calculated by the PLL, when this angle is equal to the voltage source phase angle θ, the v_d becomes equal to the peak value of the phase voltage V and v_q is equal to zero.

From equation (3-3) a new variable $\Delta\theta$ is used, which is the difference between the source phase angle and the calculated angle by the SRF-PLL as given in equation (3-4).

$$\theta - \hat{\theta} = \Delta\theta \tag{3-4}$$

Then the q-axis component of the voltage source v_q is given by:

$$v_q = V \sin\Delta\theta \tag{3-5}$$

To simplify the PLL control model, the small signal value of $\sin\Delta\theta \cong \Delta\theta$, and equation (3-5) can be simplified to:

$$v_q = V\Delta\theta$$

$$G_q(s) = \frac{v_q}{\Delta\theta} = V \tag{3-6}$$

The PLL can be assumed a linear control system with a forward gain equal to the amplitude of the source voltage [48]. Figure 3-6 shows the block diagram of PI controller based SRF-PLL.

By considering the sampling time T_s delay into account, the Figure 3-6 can be redrawn as in Figure 3-7

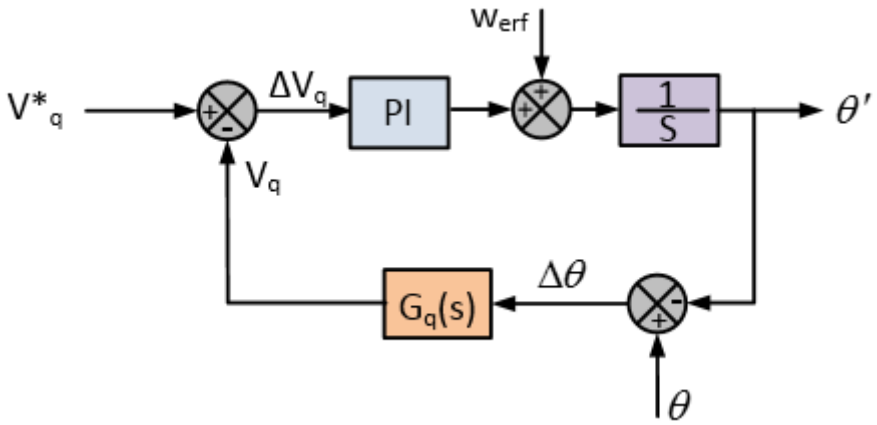


Figure 3-6 PLL control circuit diagram

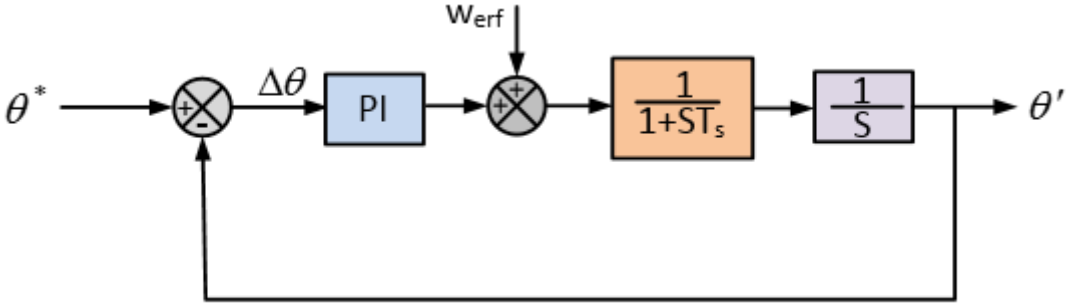


Figure 3-7 Control block diagram of the SRF-PLL

The transfer function of the PI controller is Figure 3-7 given as in (3-7).

$$PI(s) = K_P + \frac{K_I}{s} \tag{3-7}$$

Where K_P is the proportional gain and K_I is the integral gain.

The open loop transfer function of the SRF-PLL is defined as follows

$$H_{OL}(s) = \left(K_P + \frac{K_I}{s}\right)\left(\frac{V}{s}\right)\left(\frac{1}{1+sT_s}\right) = \frac{V(sK_P + K_I)}{s^2(1+sT_s)} \quad (3\text{-}8)$$

Hence, the closed loop transfer function is given as

$$\frac{\dot{\theta}(s)}{\theta\,(s)} = \frac{(VK_P)s + VK_I}{s^3T_s + s^2 + (VK_P)s + VK_I} \quad (3\text{-}9)$$

By knowing the system response requirements, damping ratio(ξ) and natural frequency (ω_n) , the K_P and K_I can be calculated by using a simple control design method. In this thesis, the SISO tool of Matlab has been used to calculate the controller parameters.

Choosing the bandwidth of the PI-controller is a trade-off between fast response and robustness to system noise. High bandwidth design guarantee fast response and give high tracking error if the source voltage is distorted. On the other hand lower bandwidth decreases the tracking error but slows the system response [49, 50].

To test the performance of the conventional SRF-PLL, a Matlab Simulink model was built based on Figure 3-5. In the first simulation, the source voltage was ideal and the values of the source peak value is equal to $340\,V$ and the controller design parameters are $K_P = 2.22$ and $K_I = 61.69$. The simulation is carried out for different values of K_P and keeping K_I constant and setting the initial angle of the SRF-PLL different from the initial source angle to investigate the tracking performance of the PLL. The results are shown in Figure 3-8 by increasing the controller gain gives faster response and the SRF-PLL is decreasing the error between the calculated phase angle $\dot{\theta}$ and the source angle θ faster.

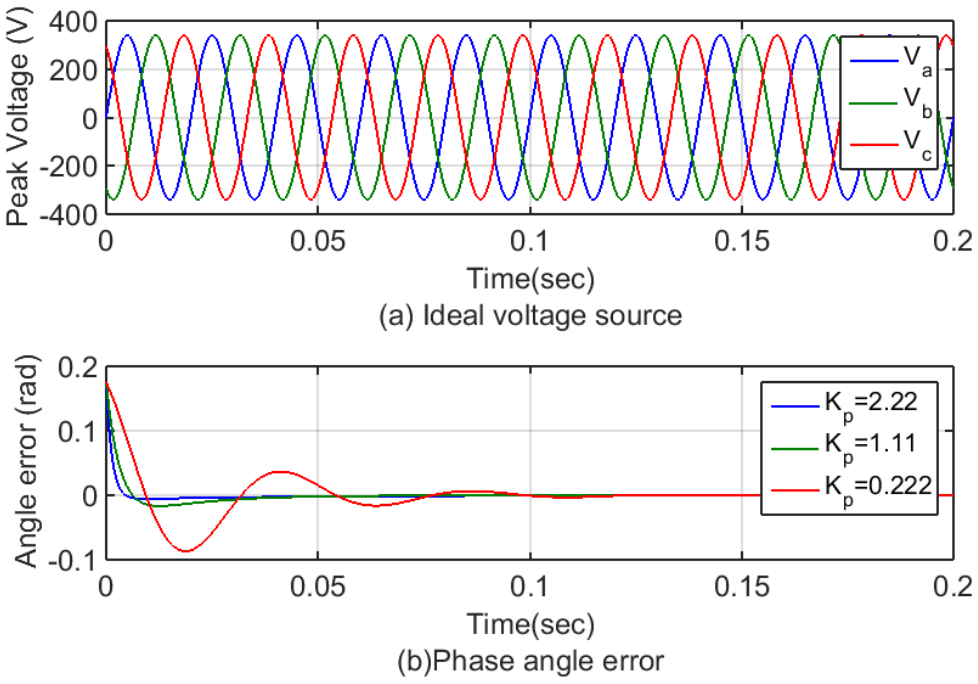


Figure 3-8 SRF-PLL performance under ideal voltage source and different values for K_P

However, for unbalanced voltage source, the values of this source are ($v_a = 272\cos\theta, v_b = 408\cos cos(\theta - 2\pi/3)$ and $v_c = 340\cos(\theta + 2\pi/3))$, by increasing the proportional gain of the PI controller, the SRF-PLL gives faster response but with increased error in the calculated angle $\hat{\theta}$. In the other hand lower value of K_P makes the SRF-PLL response slower but with decreased error in the calculated angle $\hat{\theta}$ as shown in Figure 3-9

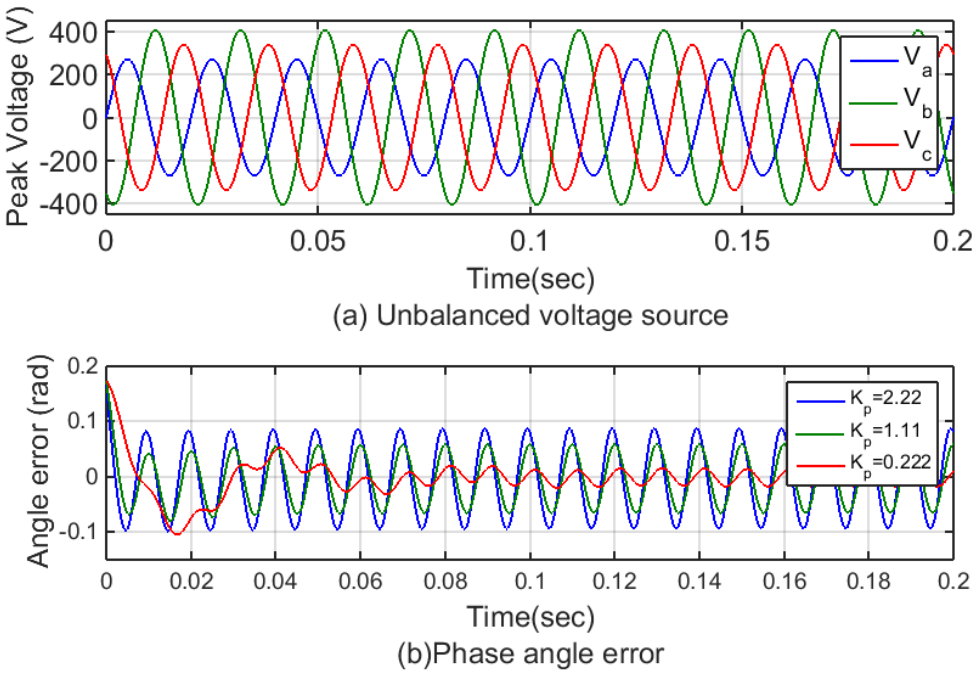


Figure 3-9 SRF-PLL performance under Unbalanced voltage source and different values for K_P

In conclusion, the SRF-PLL under unideal grid voltages will have poor dynamic response and this will be reflected in a negative effect on APF operation. In order to improve the PLL response, advanced PLLs are needed. The next section gives an improved synchronization technique based on decoupling the effects of the positive- and negative-sequence components of the input voltage vector.

3.5.2 Decoupled Double Synchronous Reference Frame PLL (DDSRF-PLL)

This section presents the design of an enhanced SRF-PLL depending on two synchronous reference frames, positive and negative rotating reference frames , [51-54]. By using the two reference frames, the effect of negative-sequence voltage component on positive sequence voltage component phase angle detection and vice versa can be reduced.

Three-phase voltage vector, can be expressed in terms of positive, negative and zero sequence components as:

$$v_{abc} = \begin{bmatrix} v_a \\ v_b \\ v_c \end{bmatrix} = \sum_{n=1}^{\infty} (v_{abc}^{+n} + v_{abc}^{-n} + v_{abc}^{0n}), \tag{3-10}$$

Where V^{+n} is the positive sequence of the voltage vector and rotates in same direction of the voltage vector, V^{-n} is the negative sequence of the voltage vector and rotates in the opposite direction of the voltage vector and V^{0n} is the zero sequence of the voltage vector.

$$v_{abc}^{+n} = V^{+n} \begin{bmatrix} \cos(n\omega t + \emptyset^{+n}) \\ \cos\left(n\omega t - \frac{2\pi}{3} + \emptyset^{+n}\right) \\ \cos\left(n\omega t + \frac{2\pi}{3} + \emptyset^{+n}\right) \end{bmatrix} \tag{3-11}$$

$$v_{abc}^{-n} = V^{-n} \begin{bmatrix} \cos(-n\omega t + \emptyset^{-n}) \\ \cos\left(-n\omega t - \frac{2\pi}{3} + \emptyset^{-n}\right) \\ \cos\left(-n\omega t + \frac{2\pi}{3} + \emptyset^{-n}\right) \end{bmatrix} \tag{3-12}$$

$$v_{abc}^{0n} = V^{0n} \begin{bmatrix} \cos(n\omega t + \emptyset^{+0n}) \\ \cos(n\omega t + \emptyset^{+0n}) \\ \cos(n\omega t + \emptyset^{+0n}) \end{bmatrix} \tag{3-13}$$

Where *+n*, *-n* and *0n* represents the positive, negative and zero-sequence components of the n^{th} harmonic of the voltage vector respectively.

The fundamental positive-sequence and negative-sequence voltage vector magnitude are V^{+1} and V^{-1}, while $\emptyset^{+}$ and $\emptyset^{-}$ represent the positive- and negative-sequence phase angles respectively.

By applying Clarke transformation, the fundamental component of v_{abc} is transformed to the $\alpha-\beta$ reference frame as (neglecting the zero sequence component):

$$\begin{bmatrix} v_\alpha \\ v_\beta \end{bmatrix} = [T_{\alpha\beta}] \begin{bmatrix} v_a \\ v_b \\ v_c \end{bmatrix}, \quad [T_{\alpha\beta}] = \frac{2}{3} \begin{bmatrix} 1 & -\frac{1}{2} & -\frac{1}{2} \\ 0 & \frac{\sqrt{3}}{2} & -\frac{\sqrt{3}}{2} \end{bmatrix} \tag{3-14}$$

$$\begin{bmatrix} v_\alpha \\ v_\beta \end{bmatrix} = V^{+1} \begin{bmatrix} \cos(\omega t + \emptyset^+) \\ \sin(\omega t + \emptyset^+) \end{bmatrix} + V^{-1} \begin{bmatrix} \cos(-\omega t + \emptyset^-) \\ \sin(-\omega t + \emptyset^-) \end{bmatrix} \tag{3-15}$$

Now, the positive sequence dq-component (dq+) of the voltage vector is calculated by applying Park's transformation to (3-15), the result is given by equation (3-16) to equation (3-18):

$$\begin{bmatrix} v_d^+ \\ v_q^+ \end{bmatrix} = [T_{dq}^+] \begin{bmatrix} v_\alpha \\ v_\beta \end{bmatrix}, [T_{dq}^+] = \begin{bmatrix} \cos\acute{\theta} & \sin\acute{\theta} \\ -\sin\acute{\theta} & \cos\acute{\theta} \end{bmatrix} \tag{3-16}$$

$$\begin{bmatrix} v_d^+ \\ v_q^+ \end{bmatrix} = \begin{bmatrix} \cos\acute{\theta} & \sin\acute{\theta} \\ -\sin\acute{\theta} & \cos\acute{\theta} \end{bmatrix} \left(V^{+1} \begin{bmatrix} \cos(\omega t + \emptyset^+) \\ \sin(\omega t + \emptyset^+) \end{bmatrix} + V^{-1} \begin{bmatrix} \cos(-\omega t + \emptyset^-) \\ \sin(-\omega t + \emptyset^-) \end{bmatrix} \right) \tag{3-17}$$

$$\begin{bmatrix} v_d^+ \\ v_q^+ \end{bmatrix} = V^{+1} \begin{bmatrix} \cos\left(\omega t + \emptyset^+ - \acute{\theta}\right) \\ \sin\left(\omega t + \emptyset^+ - \acute{\theta}\right) \end{bmatrix} + V^{-1} \begin{bmatrix} \cos\left(-\omega t + \emptyset^- - \acute{\theta}\right) \\ \sin\left(-\omega t + \emptyset^- - \acute{\theta}\right) \end{bmatrix} \tag{3-18}$$

To extract the negative sequence dq-components (dq-) of the voltage vector, the Park's transformation with negative angle is applied to (3-15), the result is given by (3-19):

$$\begin{bmatrix} v_d^- \\ v_q^- \end{bmatrix} = V^{+1} \begin{bmatrix} \cos\left(\omega t + \emptyset^+ + \acute{\theta}\right) \\ \sin\left(\omega t + \emptyset^+ + \acute{\theta}\right) \end{bmatrix} + V^{-1} \begin{bmatrix} \cos\left(-\omega t + \emptyset^- + \acute{\theta}\right) \\ \sin\left(-\omega t + \emptyset^- + \acute{\theta}\right) \end{bmatrix} \tag{3-19}$$

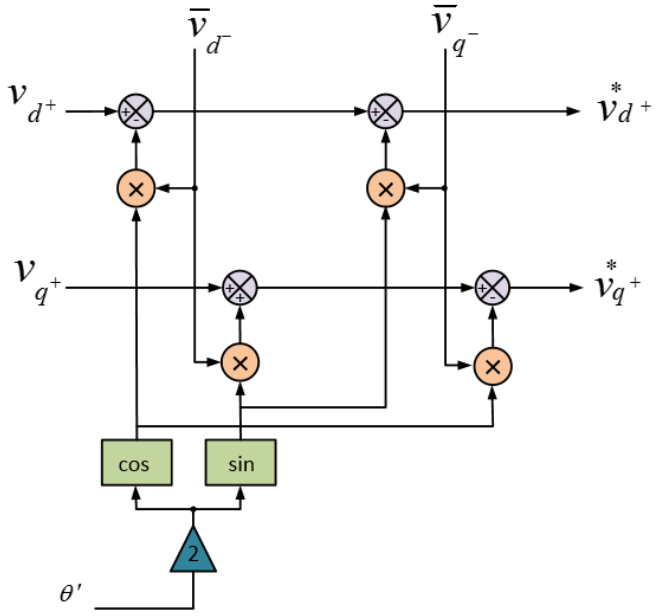
Using the SRF-PLL to calculate the phase angle $\acute{\theta} \approx \omega t$. Then, equations (3-18) and (3-19) can be simplified as in (3-20) and (3-21).

$$\begin{bmatrix} v_d^+ \\ v_q^+ \end{bmatrix} = V^{+1} \begin{bmatrix} \cos(\emptyset^+) \\ \sin(\emptyset^+) \end{bmatrix} + V^{-1} \cos(\emptyset^-) \begin{bmatrix} \cos(2\omega t) \\ -\sin(2\omega t) \end{bmatrix} + V^{-1} \sin(\emptyset^-) \begin{bmatrix} \sin(2\omega t) \\ \cos(2\omega t) \end{bmatrix} \quad (3\text{-}20)$$

$$\begin{bmatrix} v_d^- \\ v_q^- \end{bmatrix} = V^{-1} \begin{bmatrix} \cos(\emptyset^-) \\ \sin(\emptyset^-) \end{bmatrix} + V^{+1} \cos(\emptyset^+) \begin{bmatrix} \cos(2\omega t) \\ \sin(2\omega t) \end{bmatrix} + V^{+1} \sin(\emptyset^+) \begin{bmatrix} -\sin(2\omega t) \\ \cos(2\omega t) \end{bmatrix} \quad (3\text{-}21)$$

It can be concluded from equation (3-20) that the DC values of (dq+) voltage components are superimposed by oscillating voltage components of frequency equal two times the fundamental frequency (2ω) as a results of the existence of the negative sequence voltage components and vice versa occurred for the (dq-) voltage components as shown in (3-21). This coupling between the two reference frames can be cancelled by using decoupling terms as shown in Figure 3-10 to compensate for the second order frequency voltage components of (4.26) and (4.47).

(a



(b

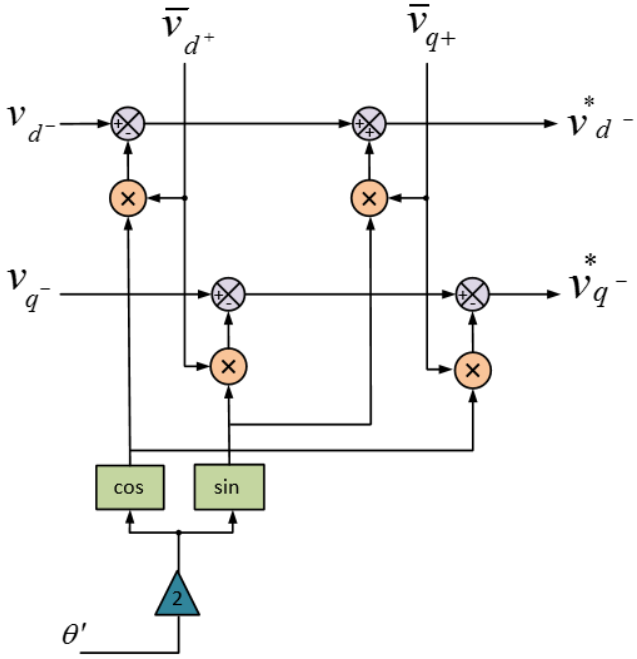


Figure 3-10 Block diagram of decoupling terms, (a) for (dq+) reference frame (b) for (dq-) reference

The positive and negative reference frames voltage components ($\overline{v_d^+}, \overline{v_q^+}, \overline{v_d^-}$ and $\overline{v_q^-}$) are fed to low pass filters (LPF), (as a simple filter and no need to use a complex filter) to extract the DC values. The transfer function of the LPF is given as:

$$LPF(s) = \frac{\omega_f}{s + \omega_f} \tag{3-22}$$

Where ω_f is the cut-off frequency. The optimal value of the cut-off frequency of low pass filter that gives fast dynamic response with no oscillation in the amplitude of the filtered signal is $\omega_f = \frac{\omega}{\sqrt{2}}$, [51], where ω is the fundamental frequency. Figure-3-11 shows the decoupling network block diagram of the Decouple Double Synchronous Reference Frame (DDSRF)

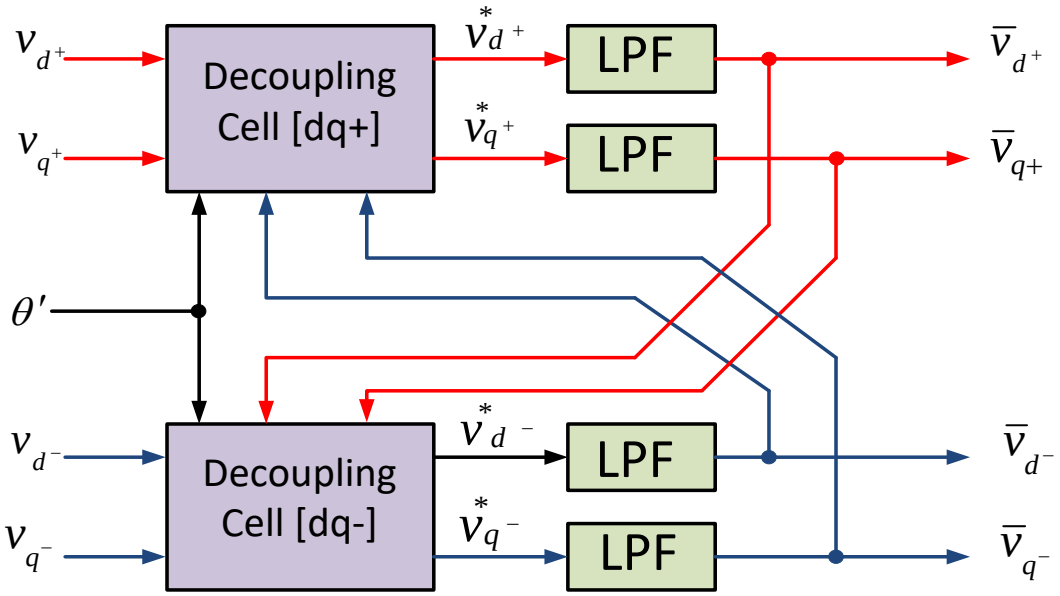


Figure-3-11 Block diagram of decoupling network of DDSRF-PLL

Now after eliminating the effect of the negative sequence component, a classical SRF-PLL is applied to v^*_{q+} to determine the voltage phase angle $\acute{\theta}$ of the positive sequence voltage component. The full diagram of DDSRF is shown in Figure-3-12

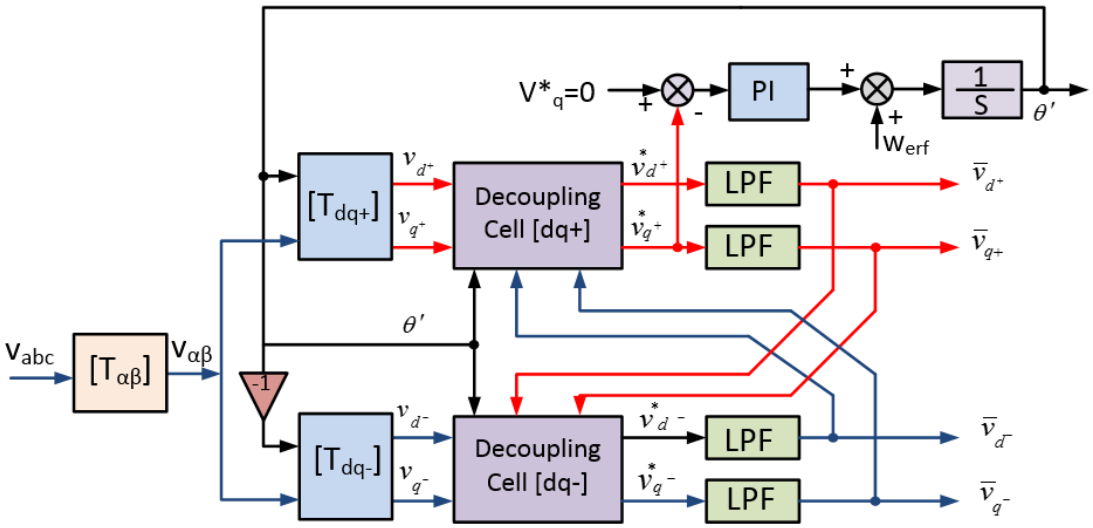


Figure-3-12 The block diagram of the decoupling double synchronous reference frame (DDSRF_PLL)

To study the performance of the DDSRF-PLL a Matlab Simulink model was built based on Figure-3-12 with the same values of the controller gains as in section 3.5.1 and the unbalanced voltages as given in the previous section are applied. The simulation result is shown in Figure-3-13. As can be seen from the Figure-3-13(b), the DDSRF-PLL extracted the positive sequence from the unbalanced voltages and calculated the voltage phase angle. By comparing the performance of the DDSFR-PLL with the SRF-PLL, the DDSRF-PLL is accurately estimating the phase angle of the unbalanced voltage source while the SRF-PLL suffered a significant phase angle error, see Figure-3-13(c).

The second simulation was carried out to test the DDSRF-PLL under unbalanced and distorted voltage source, the values of the source voltages are given in Table 3-1, and the same values for the PI controller are used.

Table 3-1 the numerical values of unideal voltage source

Phase	Value of the fundamental	% of 5th harmonic	% of 7th harmonics
Phase-A	$272 \times \cos\theta$	15 %	10 %
Phase-B	$408 \times \cos\left(\theta - \frac{2\pi}{3}\right)$	15 %	10 %
Phase-C	$340 \times \cos\left(\theta + \frac{2\pi}{3}\right)$	15 %	10 %

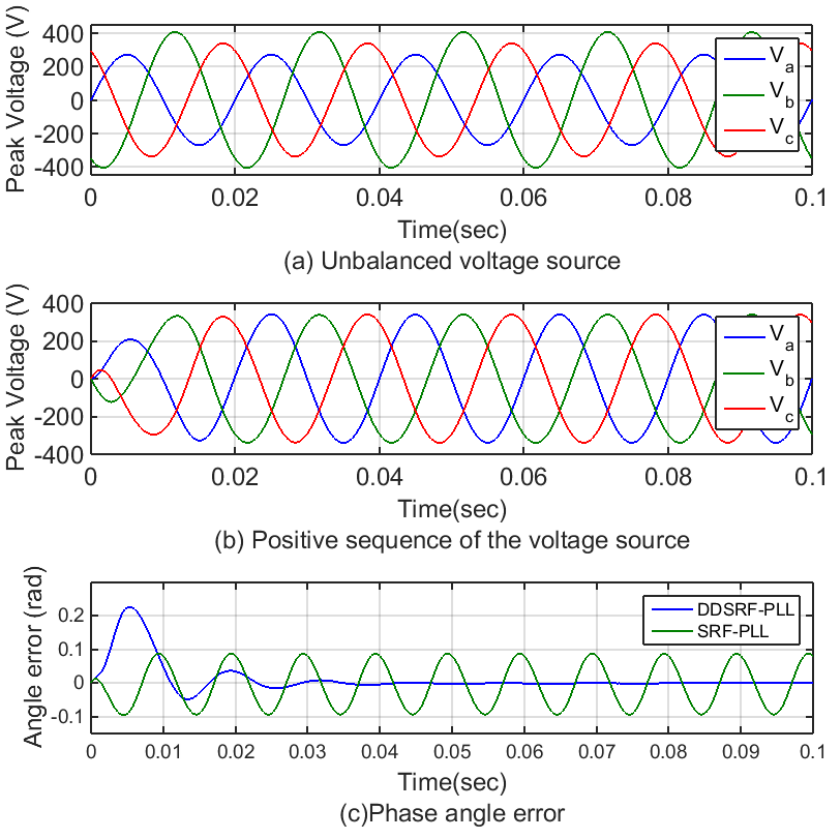


Figure-3-13 DDSRF-PLL performance under Unbalanced voltage source

As can be seen from the Figure-3-14 when the voltage source is unbalanced and distorted, the DDSRF-PLL cannot track the phase angle of the source, and the tracked angle has oscillation of six times the source frequency due to the fifth and seventh harmonics.

Then, the DDSRF-PLL is not the optimal choice for distorted voltage source as the case of the proposed generator in this thesis, where the proposed generator as discussed in Chapter-2 has distorted back-EMF. Therefore, the synchronisation method should have the capability to extract the phase angle of the fundamental voltage component from the distorted generator output voltage with high precision and accuracy to ensure high performance of the used APF.

The next section, the Dual Second Order Generalised Integrator PLL (DSOGI-PLL) will be presented and used for high performance tracking of the voltage phase angle under distorted and unbalanced voltage sources.

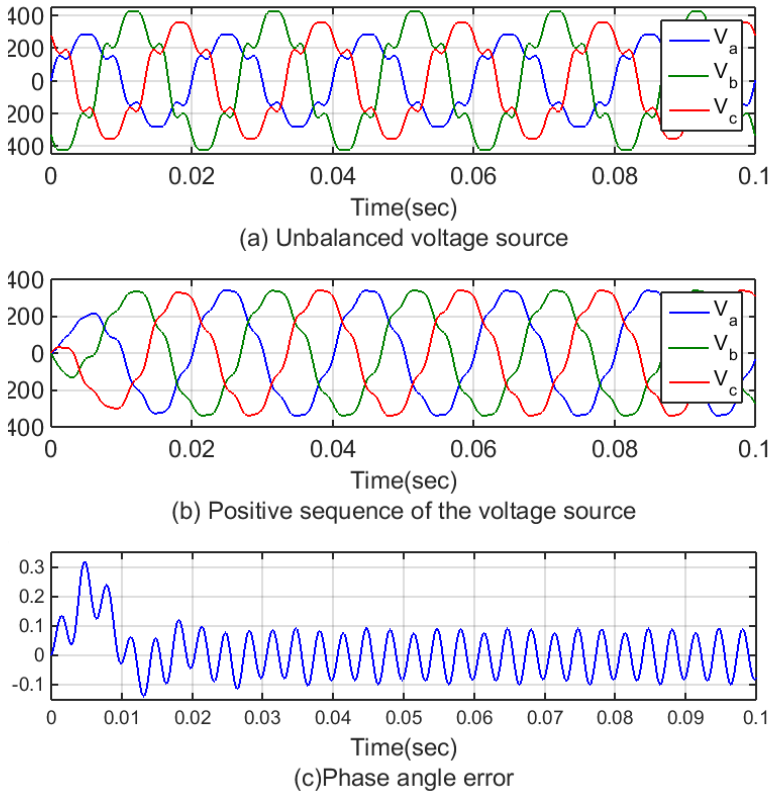


Figure-3-14 DDSRF-PLL performance under Unbalanced and distorted voltage source

3.5.3 Dual Second Order Generalised integrator (DSOGI-PLL)

This synchronisation method is presented to calculate the grid phase angle and to synchronise the power converters with distorted and unbalanced grid voltages, [55-58]. The principle operation of the DSOGI-PLL can be divided into three steps: the quadrature-signal generator (QSG), the positive-sequence calculator (PSC) and the phase locked loop (PLL).

a) Quadrature-Signal Generator (QSG)

This is the first step in DSODI-PLL operation, where the quadrature signal (lagged 90°) of the input signal is generated and provides the input signals to the PSC on the αβ reference frame. The proposed system is using dual second order generalized integrator (DSOGI) to perform the QSG [33, 59]. Figure-3-14 show the block diagram of SOGI where k and ω' are the damping factor and the resonant frequency of SOGI-QSG.

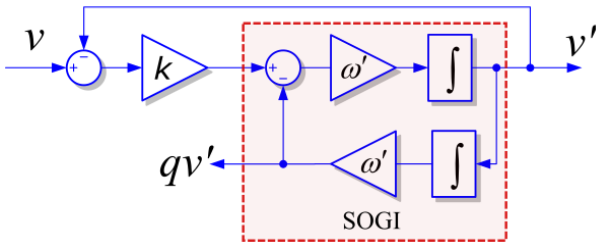


Figure-3-15 SOGI-QSG block diagram

The characteristic transfer functions of SOGI can be calculate from Figure-3-15, and given in (3-23) and (3-24). The first output signal from SOGI (v') is a filtered version of the input signal and the second output signal (qv') is shifted 90° from the input signal.

$$D(s) = \frac{v'(s)}{v(s)} = \frac{k\omega' s}{s^2 + k\omega' s + \omega'^2} \qquad (3\text{-}23)$$

$$Q(s) = \frac{qv'(s)}{v(s)} = \frac{k\omega'^2}{s^2 + k\omega' s + \omega'^2} \quad (3\text{-}24)$$

A detailed analysis were performed in [55] about the optimum value of k, the value $k = \sqrt{2}$ gives the best response in terms of stabilization time and overshot limitation.

b) Positive-Sequence Calculator (PSC)

It based on instantaneous symmetrical components (ISC) and the instantaneous positive- and negative-sequence components for the voltage vector are [60]:

$$V_{abc}^{+} = [v_a^{+} \quad v_b^{+} \quad v_c^{+}]^T = [T_+]V_{abc} \quad (3\text{-}25)$$

$$V_{abc}^{-} = [v_a^{-} \quad v_b^{-} \quad v_c^{-}]^T = [T_-]V_{abc} \quad (3\text{-}26)$$

Where $[T_+]$ and $[T_-]$ is the transformation matrices and given as:

$$[T_+] = \begin{bmatrix} 1 & a & a^2 \\ a^2 & 1 & a \\ a & a^2 & 1 \end{bmatrix} \text{ and } [T_-] = \begin{bmatrix} 1 & a^2 & a \\ a & 1 & a^2 \\ a^2 & a & 1 \end{bmatrix} \quad (3\text{-}27)$$

Where $a = e^{j\frac{2\pi}{3}}$

Using Clarke transformation to calculate the instantaneous components of the positive- and negative-sequence voltage in the αβ reference frame:

$$V_{\alpha\beta}^{+} = \left[T_{\alpha\beta}\right]V_{abc}^{+} = \left[T_{\alpha\beta}\right][T_+]V_{abc} \quad (3\text{-}28)$$

$$V_{\alpha\beta}^{-} = \left[T_{\alpha\beta}\right]V_{abc}^{-} = \left[T_{\alpha\beta}\right][T_-]V_{abc} \quad (3\text{-}29)$$

Where

$$[T_{\alpha\beta}] = \sqrt{\frac{2}{3}}\begin{bmatrix} 1 & -\frac{1}{2} & -\frac{1}{2} \\ 0 & \frac{\sqrt{3}}{2} & -\frac{\sqrt{3}}{2} \end{bmatrix} \quad (3\text{-}30)$$

The positive- and negative component ($V_{\alpha\beta}^{+}$ and $V_{\alpha\beta}^{-}$) can be calculated directly from αβ values of the voltage vector by using the invers Clarke transformation as follows

$$V_{abc} = [T_{\alpha\beta}]^{T} V_{\alpha\beta} \quad (3\text{-}31)$$

The equation (3-28) and equation (3-29) can be rewrites as:

$$V_{\alpha\beta}^{+} = [T_{\alpha\beta}]V_{abc}^{+} = [T_{\alpha\beta}][T_{+}][T_{\alpha\beta}]^{T} V_{\alpha\beta} \quad (3\text{-}32)$$

$$V_{\alpha\beta}^{-} = [T_{\alpha\beta}]V_{abc}^{-} = [T_{\alpha\beta}][T_{-}][T_{\alpha\beta}]^{T} V_{\alpha\beta} \quad (3\text{-}33)$$

By calculating the values of $[T_{\alpha\beta}][T_{+}][T_{\alpha\beta}]^{T}$ and $[T_{\alpha\beta}][T_{-}][T_{\alpha\beta}]^{T}$ the equation (3-32) and equation (3-33) can be simplified as:

$$V_{\alpha\beta}^{+} = \frac{1}{2}\begin{bmatrix} 1 & -q \\ q & 1 \end{bmatrix} V_{\alpha\beta} \quad (3\text{-}34)$$

$$V_{\alpha\beta}^{-} = \frac{1}{2}\begin{bmatrix} 1 & q \\ -q & 1 \end{bmatrix} V_{\alpha\beta} \quad (3\text{-}35)$$

Where $q = e^{-j\frac{\pi}{2}}$ is a phase-shift time domain operator used to generate the quadrature (90° phase shift) waveform of the input signal and this signal is obtained in the first step.

The positive sequence calculator is implemented as follows

$$\begin{bmatrix} V_\alpha^+ \\ V_\beta^+ \end{bmatrix} = \frac{1}{2}\begin{bmatrix} V_\alpha - qV_\beta \\ qV_\alpha + V_\beta \end{bmatrix} \quad (3\text{-}36)$$

$$\begin{bmatrix} V_\alpha^- \\ V_\beta^- \end{bmatrix} = \frac{1}{2}\begin{bmatrix} V_\alpha + qV_\beta \\ -qV_\alpha + V_\beta \end{bmatrix} \quad (3\text{-}37)$$

Figure-3-16 shows the DSOGI block diagram with a positive sequence calculator (PSC). As can be seen from the figure that the positive sequence voltage can be calculated by applying the invers of Clarke transformation to the output of PSC which is considered as the second advantages of DSOGI-PLL.

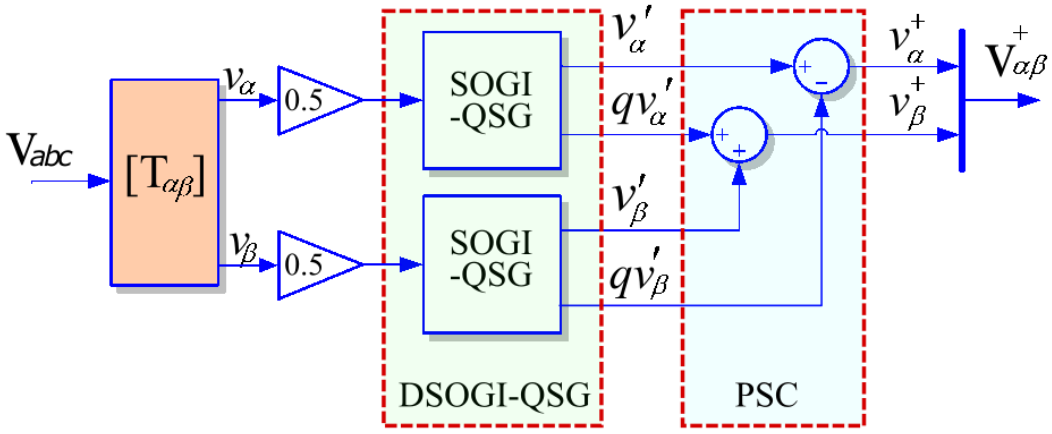


Figure-3-16 block diagram SOGI-QSG and PSC

c) Phase Locked Loop (PLL)

This the final step in DOSGI-PLL, the positive sequence voltage component is calculated and fed to the conventional SRF-PLL to calculate the phase angle of the input signal (V_{abc}). Figure-3-16 Shows the full block diagram of SOGI-PLL

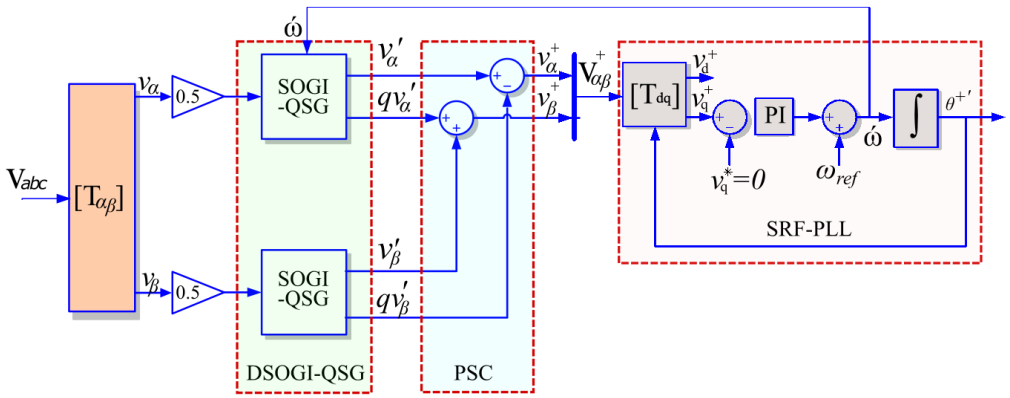


Figure-3-17 block diagram DSOGI-PLL

A Matlab Simulink model was built based on Figure-3-17 to investigate the performance of the DSODI-PLL under unbalanced and distorted voltage supply. The supply voltages are as given in Table 3-1 and the controller values were the same as in the previous two sections. The simulation results are shown in Figure-3-18, as can be seen from the figure the proposed synchroniser (DSOGI-PLL) provides good tracking performance for the voltage source phase angle under these conditions compared to the DDSRF-PLL which has high tracking error as shown in Figure-3-18 (c).

In this section a three type of synchronisation method for grid connected converter have been presented, under ideal voltage source, the conventional SRF-PLL with high proportional control gain able to track the phase angle with fast dynamic and high accuracy. However, for distorted and unbalanced voltage sources, two advanced synchronisation methods based on conventional SRF-PLL have been presented. The DDSRF-PLL has provided good performance under unbalanced grid voltage, but when the gird voltage was distorted (has harmonic content), it gave error in the detected angle with oscillation depending on the harmonic content of the grid voltage. The last synchroniser presented in this section

was the DSOGI-PLL, which was able to track the phase angle under unbalanced and distorted grid voltage with a good performance.

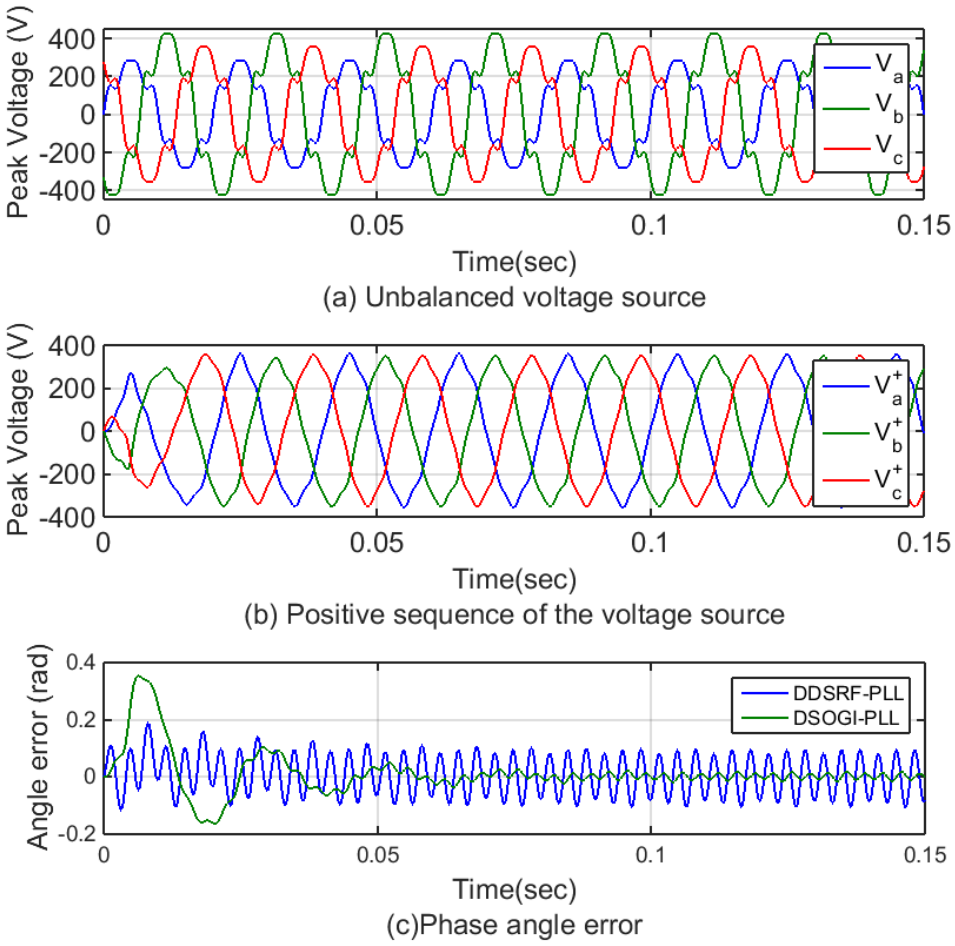


Figure-3-18 DSOGI-PLL performance under Unbalanced and distorted voltage source

3.6 Current/Voltage Harmonics Extraction Techniques

Extracted current/voltage harmonics component is calculating the reference current/voltage that APF should inject to compensate

these harmonics and to improve the quality of the generator's power.

The current reference extraction techniques can be classified into two main categories, time domain and frequency domain [61-63]. The frequency domain method is based on Fourier analysis, while the time domain method is based on the filtration of the instantaneous value of the current signals, so it can be used in transient and steady state.

Since the time domain methods are faster in terms of calculating time and simpler for online implementation, it gained more interest and are widely used.

Current reference calculation for APF is widely discussed in the literatures [27, 43, 61, 62, 64]. In this section, two method in time domain will be presented, P-Q method and synchronous reference frame d-q model.

3.6.1 Current Reference Extraction: P-Q Method

This p-q method is based on the instantaneous reactive power theory [65], which has been published in 1984. Since the theory was first developed for three-phase there-wire system, the zero sequence component was neglected. The calculation block diagram of this method is shown in Figure-3-19.

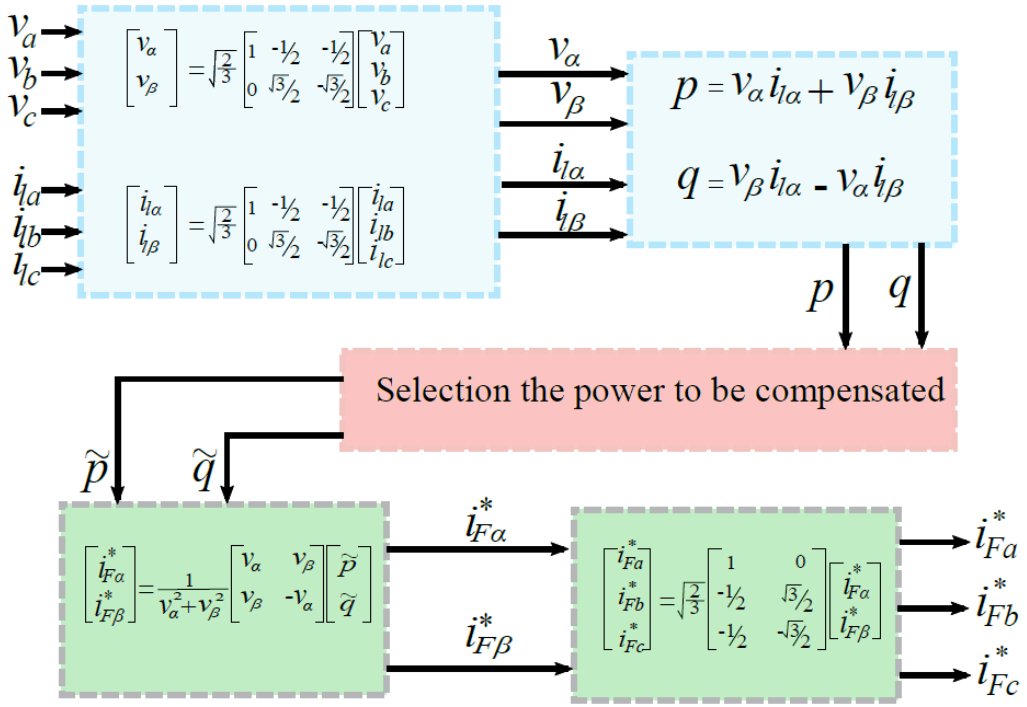


Figure-3-19 Calculation block diagram of P-Q method

At first, the three-phase voltage and the three-phase load currents are sensed and transformed into $(\alpha-\beta)$ coordinates as given in equation (3-38) and equation (3-39).

$$\begin{bmatrix} v_\alpha \\ v_\beta \end{bmatrix} = \sqrt{\frac{2}{3}} \cdot \begin{bmatrix} 1 & -1/2 & -1/2 \\ 0 & \sqrt{3}/2 & -\sqrt{3}/2 \end{bmatrix} \begin{bmatrix} v_a \\ v_b \\ v_c \end{bmatrix} \tag{3-38}$$

$$\begin{bmatrix} i_{l\alpha} \\ i_{l\beta} \end{bmatrix} = \sqrt{\frac{2}{3}} \cdot \begin{bmatrix} 1 & -1/2 & -1/2 \\ 0 & \sqrt{3}/2 & -\sqrt{3}/2 \end{bmatrix} \begin{bmatrix} i_{la} \\ i_{lb} \\ i_{lc} \end{bmatrix} \tag{3-39}$$

Then, the instantaneous complex power is calculated as [66],

$$\begin{aligned} s &= V * I^* = (v_\alpha + jv_\beta)(i_\alpha - ji_\beta) \\ &= (v_\alpha i_\alpha + v_\beta i_\beta) + j(v_\beta i_\alpha - v_\alpha i_\beta) \end{aligned} \quad (3\text{-}40)$$

Where the term $v_\alpha i_\alpha + v_\beta i_\beta$ is the instantaneous real power p and the term $v_\beta i_\alpha - v_\alpha i_\beta$ is the instantaneous reactive power q.

According to the instantaneous reactive power theory, p and q, are decomposed into,

$$p = \bar{p} + \tilde{p} \quad , \qquad q = \bar{q} + \tilde{q} \quad (3\text{-}41)$$

Where $\bar{p_l}$ and $\bar{q_l}$ are the DC component corresponding to the fundamental current, and $\tilde{p_l}$ and $\tilde{q_l}$ are the ac components corresponding to the harmonics current. A low pass filter can be used to extract the DC components and the DC power is then subtracted from the full power to get the AC power component.

So the current reference for the APF in α-β frame ($i^*_{F\alpha}$ and $i^*_{F\beta}$) can be obtained as in (3-42) :

$$\begin{bmatrix} i^*_{F\alpha} \\ i^*_{F\beta} \end{bmatrix} = \frac{1}{v_\alpha^2 + v_\beta^2} \begin{bmatrix} v_\alpha & v_\beta \\ v_\beta & -v_\alpha \end{bmatrix} \begin{bmatrix} \tilde{p} \\ \tilde{q} \end{bmatrix} \quad (3\text{-}42)$$

Then, the current in the α-β coordinates are transformed back to the abc frame by using the invers Clarke transformation.

Later this theory is extended to be suitable for three-phase four-wire-system [67], where the zero component is add to the equations.

In three-phase four-wire system, the instantaneous power in abc frame is given by:

$$P_{3\emptyset} = v_a i_a + v_b i_b + v_c i_c \tag{3-43}$$

$$P_{3\emptyset} = v_\alpha i_\alpha + v_\beta i_\beta + v_0 i_0 = p + p_0 \tag{3-44}$$

The instantaneous real p, imaginary q and zero-sequence power p_0 as function of α-β-0 coordinates currents are given in (3-45).

$$\begin{bmatrix} p_0 \\ p \\ q \end{bmatrix} = \begin{bmatrix} v_0 & 0 & 0 \\ 0 & v_\alpha & v_\beta \\ 0 & v_\beta & -v_\alpha \end{bmatrix} \begin{bmatrix} i_0 \\ i_\alpha \\ i_\beta \end{bmatrix} \tag{3-45}$$

As in equation (3-41), the zero sequence power p_0 can be expressed as

$$p_0 = \overline{p_0} + \widetilde{p_0} \tag{3-46}$$

Where, the $\overline{p_0}$ is the zero-sequence average power delivered to the load through the neutral wire. Since the component of zero sequence power $\overline{p_0}$ and $\widetilde{p_0}$ can not be produced separately [67], and the active power filter doesn't have DC source, so additional real power Δp ($\Delta p = \overline{p_0}$) will be added to the reference signal $\tilde{p}$.

The reference current for the APF in three-phase four-wire system can be calculated as shown in equation (3-47)

$$\begin{bmatrix} i_{F\alpha}^* \\ i_{F\beta}^* \\ i_{F0}^* \end{bmatrix} = \frac{1}{v_\alpha^2 + v_\beta^2} \begin{bmatrix} v_\alpha & v_\beta & 0 \\ v_\beta & -v_\alpha & 0 \\ 0 & 0 & 1 \end{bmatrix} \begin{bmatrix} \tilde{p} + \overline{p_0} \\ \tilde{q} \\ i_0 \end{bmatrix} \tag{3-47}$$

Then these currents are transformed back to the abc frame $[i_{Fa}^* \quad i_{Fb}^* \quad i_{Fc}^*]^T$ by using the invers Clarke transformation. The reference current for the neutral leg i_{Fn}^* is given as:

$$i_{Fn}^{*} = -(i_{Fa}^{*} + i_{Fb}^{*} + i_{Fc}^{*}) \quad (3\text{-}48)$$

3.6.2 Current/voltage Reference Extraction: Synchronous Reference (d-q) Method

This method is based on normalised Park transformation and only depend on the sensed current or voltage. Where the sensed three-phase waveforms abc are transformed to the synchronous reference $dq0$ rotating frame [64, 68].

The harmonics reference waveform calculation in this scheme can be described as follows:

1- Extracting the zero-sequence component from the sensed waveform by subtracting the zero-sequence from the three phase waveform as

$$x_{abc_dq} = (x_{abc} - x_0) \quad (3\text{-}49)$$

Where x_{abc_dq}, are the sensed waveform without zero-sequence component i.e. they contains just d and q component. i_0 is the zero-sequence component and is given by:

$$i_0 = \frac{1}{3}(x_a + x_b + x_c) \quad (3\text{-}50)$$

2- Transforming the calculated waveform in step-1 to synchronous reference frame x and x_q by using Park transformation. The x_d and x_q will contain DC and AC components as.

$$x_d = \overline{x_d} + \widetilde{x_d} \quad , \quad x_q = \overline{x_q} + \widetilde{x_q} \quad (3\text{-}51)$$

Where $\bar{x}$ and $\overline{x_q}$ are the DC values and $\widetilde{x_d}$ and $\widetilde{x_q}$ are the ripple component of x_d and x_q respectively.

3- A low-pass filter or moving average filter is used to extract the DC values $\overline{x_d}$ and $\overline{x_q}$ from x_d and x_q.

4- Calculating the *abc* fundamental component by applying the invers Park transformation on the DC values $\overline{x_d}$ and $\overline{x_q}$ as follows:

$$\begin{bmatrix} x_a^1 \\ x_b^1 \\ x_c^1 \end{bmatrix} = \sqrt{\frac{2}{3}}.\begin{bmatrix} \cos(\theta) & -\sin(\theta) \\ \cos\left(\theta - \frac{2\pi}{3}\right) & -\sin\left(\theta - \frac{2\pi}{3}\right) \\ \cos\left(\theta + \frac{2\pi}{3}\right) & -\sin\left(\theta + \frac{2\pi}{3}\right) \end{bmatrix}\begin{bmatrix} \overline{x_d} \\ \overline{x_q} \end{bmatrix} \quad (3\text{-}52)$$

Now the calculated fundamental waveform is balanced and harmonic free.

5- To calculate the reference waveform for the APFs, the fundamental waveform is subtracted from the sensed *abc* waveform (current or voltage).

$$\begin{bmatrix} x_{Fa}^* \\ x_{Fb}^* \\ x_{Fc}^* \end{bmatrix} = \begin{bmatrix} x_a \\ x_b \\ x_c \end{bmatrix} - \begin{bmatrix} x_a^1 \\ x_b^1 \\ x_c^1 \end{bmatrix} \quad (3\text{-}53)$$

Figure-3-20 shows the simulation block diagram for calculation of the reference waveforms by synchronous reference (d-q) method.

One of the most important characteristics of this method is that the reference currents are derived directly from the instantaneous value of the current without considering the source voltage as in p-q theory. The generation of the reference signals is not affected by voltage unbalance or voltage distortion, therefore increasing the compensation robustness and performance.

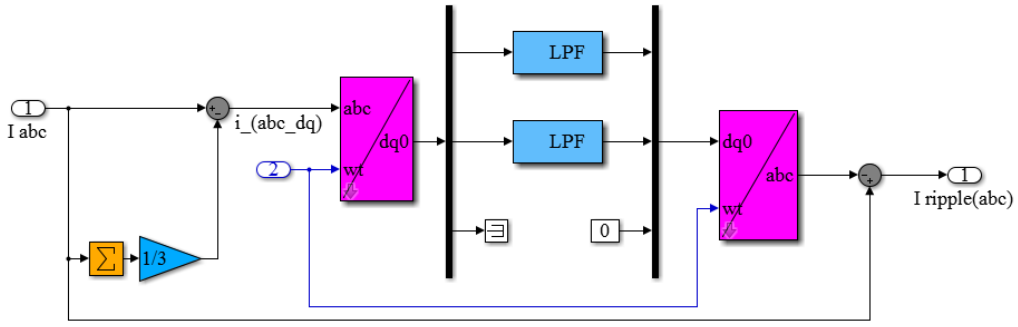


Figure-3-20 The block diagram for SRF reference current calculation

In this section a description of the two most popular methods of reference current calculation has been presented, the p-q theory and the synchronous reference d-q methods for both current and voltage references. In the p-q method, both the voltage and the current at the PCC are needed to calculate the reference current, while in synchronous d-q only the current is needed in addition to the phase angle from the synchronisation algorithm. As the p-q method is sensitive to voltage waveform and requires more computation than the synchronous reference d-q method, thus the synchronous reference method is adopted for both filters in this thesis.

3.7 **Shunt APF Current Control Techniques**

The duty of the current controller is to generate the voltage reference for the AFT to supply the reference current. The performance of the active power filter is affected significantly by the selection of current control technique. The APF and its current controller must have the capability to effectively track the reference current.

Many control techniques are discussed in the literature [69-72]. The control techniques can be generally classified to linear and nonlinear control techniques. This section will present one controller

from nonlinear controller and two controllers from linear controllers. Finally, pulse width modulation (PWM) technique will be discussed.

3.7.1 Hysteresis Current Control

The basic principle of current hysteresis control is that the switching signals are derived directly from the comparison of the current error signal with a fixed width hysteresis band as shown in Figure 3-21 . These signals (pulses) are used to control the switching devices in the APF.

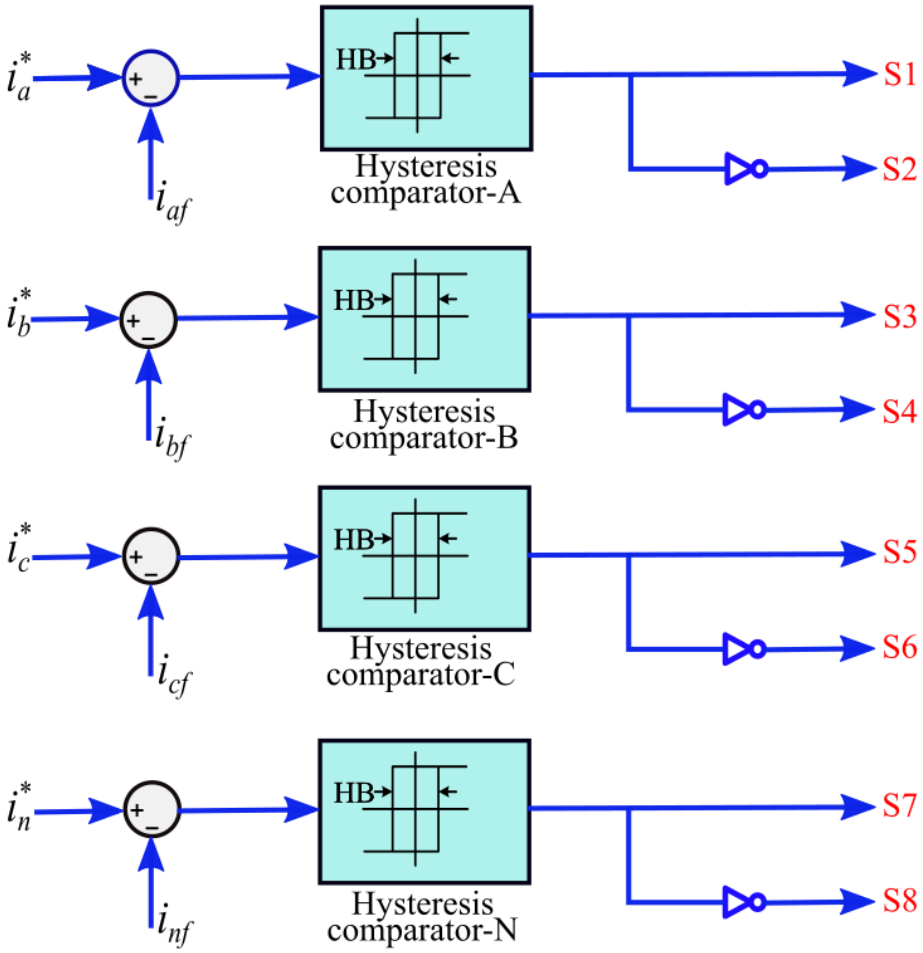


Figure 3-21 The block diagram of the hysteresis current controller

The operation concept of the hysteresis current controller is shown in Figure 3-22. As shown in the figure, the measured current

is compared with the reference current in a two level hysteresis comparator, if the error within the controller hysteresis bandwidth HB, the output status of the controller will not change. When the measured current value exceeded the reference current by half of the bandwidth $HB/2$ (upper limit), the output of the controller will be 0 ($S1 = 0\,, S2 = 1$). On the other hand, when the measured current value is less than the reference current by half of the bandwidth $HB/2$ (lower limit), the output of the controller will be equal to 1 ($S0 = 0\,, S2 = 0$). Therefor the filter current will follow the reference current within the controller bandwidth, i.e. more smaller bandwidth the filter current will be more closely to the reference current, but this will increase the switching frequency of the converter.

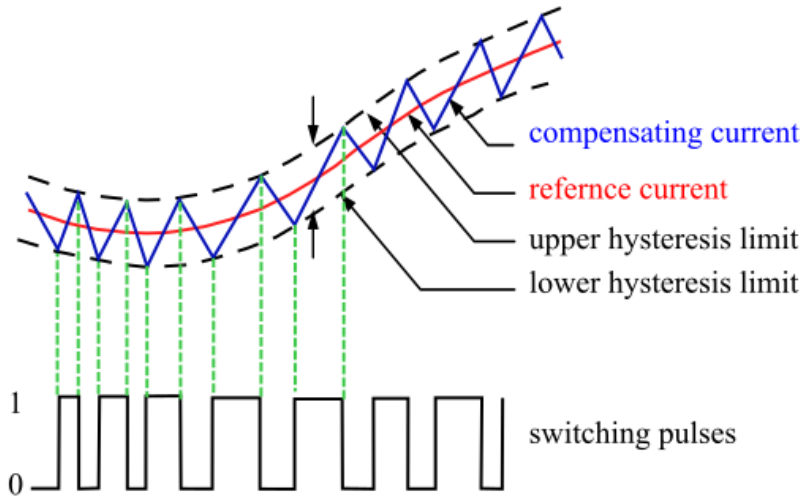


Figure 3-22 The basic concept of the hysteresis current controller

The main advantages of this controller, are being simple, robust and having fast dynamic response. However, the main drawback of this controller is it has a variable switching frequency and might exceed the limit of the inverter switches [73].

3.7.2 Synchronous Reference PI Controller (SRF-PI)

This method is based on Park transformation, where, both the reference signals and the measured signals are converted into synchronous reference frame by using normalised Park transformation. The difference is passed through a PI controller then to a decoupling stage to remove the mutual effect between the axes to produce the reference voltage in dq reference frame, and then transformed back to natural frame (abc frame).

The AFP plant model can be derived from Figure 3-23, as the output voltage of the inverter is given by :

$$v_{af} = R_f\, i_{fa} + L_f \frac{di_{fa}}{dt} + v_{ga}$$

$$v_{bf} = R_f\, i_{fb} + L_f \frac{di_{fb}}{dt} + v_{gb} \qquad (3\text{-}54)$$

$$v_{cf} = R_f\, i_{fc} + L_f \frac{di_{fc}}{dt} + v_{gc}$$

Where L_f is the filter inductance, R_f is filter resistance, i_{fa}, i_{fb}, and i_{fc} are the APF output currents, v_{af}, v_{bf} and v_{cf} are is the output voltage and v_{ga}, v_{gb} and v_{gc} are the grid voltages at the PCC.

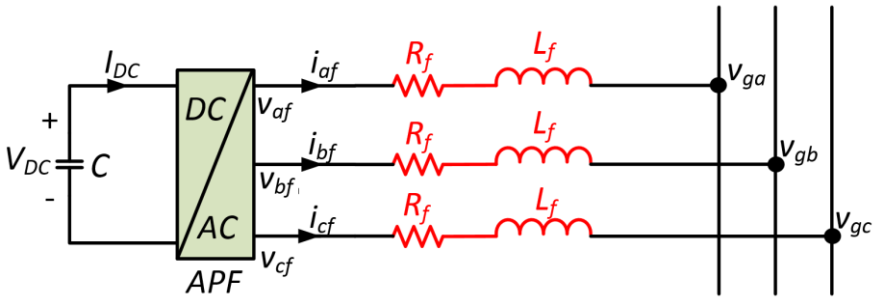


Figure 3-23 APF connection to the grid through interface L-filter

Equation (3-54) can be rewritten in matrix form as follows:

$$\begin{bmatrix} v_{af} \\ v_{bf} \\ v_{cf} \end{bmatrix} = \begin{bmatrix} R_f & 0 & 0 \\ 0 & R_f & 0 \\ 0 & 0 & R_f \end{bmatrix} \begin{bmatrix} i_{af} \\ i_{bf} \\ i_{cf} \end{bmatrix} + L_f \frac{d}{dt} \begin{bmatrix} i_{af} \\ i_{bf} \\ i_{cf} \end{bmatrix} + \begin{bmatrix} v_{ga} \\ v_{gb} \\ v_{gc} \end{bmatrix} \quad (3\text{-}55)$$

The abc model is transformed to dq reference frame as given in equation (3-56)

$$\begin{bmatrix} v_{df} \\ v_{qf} \\ v_0 \end{bmatrix} = \begin{bmatrix} R_f & 0 & 0 \\ 0 & R_f & 0 \\ 0 & 0 & R_f \end{bmatrix} \begin{bmatrix} i_{df} \\ i_{qf} \\ i_{0f} \end{bmatrix} + L_f \frac{d}{dt} \begin{bmatrix} i_{df} \\ i_{qf} \\ i_{0f} \end{bmatrix} - L_f \begin{bmatrix} 0 & \omega & 0 \\ -\omega & 0 & 0 \\ 0 & 0 & 0 \end{bmatrix} \begin{bmatrix} i_{df} \\ i_{qf} \\ i_{0f} \end{bmatrix} + \begin{bmatrix} v_{gd} \\ v_{gq} \\ v_{g0} \end{bmatrix} \quad (3\text{-}56)$$

The equation (3-56) can be given in a simple form as follows:

$$v_{df} = R_f i_{df} + L_f \frac{di_{df}}{dt} - \omega L_f i_{qf} + v_{gd}$$

$$v_{qf} = R_f i_{qf} + L_f \frac{di_{qf}}{dt} + \omega L_f i_{df} + v_{gq} \quad (3\text{-}57)$$

Where ω is the angular frequency of the grid voltage vector.

As seen from equation (3-57) there are coupling between the two voltages (v_{df} and v_{qf}) equations due to the transformation. To cancel this coupling, a new reference voltage are defined as given in equation (3-58)

$$v_{df}{}^{*} = \acute{v}_{df} - \omega L_f i_{qf} + v_{gd}$$

$$v_{qf}{}^{*} = \acute{v}_{qf} + \omega L_f i_{df} + v_{gq} \quad (3\text{-}58)$$

Which yields to completely decoupled model,

$$\acute{v}_{df} = R_f i_{df} + L_f \frac{di_{df}}{dt}$$
$$\acute{v}_{qf} = R_f i_{qf} + L_f \frac{di_{qf}}{dt} \quad (3\text{-}59)$$

Taking the Laplace transform of equation (3-59) the control plant transfer function is given in equation (3-60)

$$\frac{I_{df}(s)}{\acute{V}_{df}(s)} = \frac{1}{R_f + SL_f}$$
$$\frac{I_{qf}(s)}{\acute{V}_{qf}(s)} = \frac{1}{R_f + SL_f} \quad (3\text{-}60)$$

The decoupling can be implemented from equation (3-58) as shown in Figure 3-24

The final step in SRF-PI controller is to calculate the reference voltage in abc frame by applying the inverse of Park transformation to the reference voltage signals ${v_{df}}^*$ and ${v_{qf}}^*$. Figure 3-24 shows the full block diagram of SRF-PI controller.

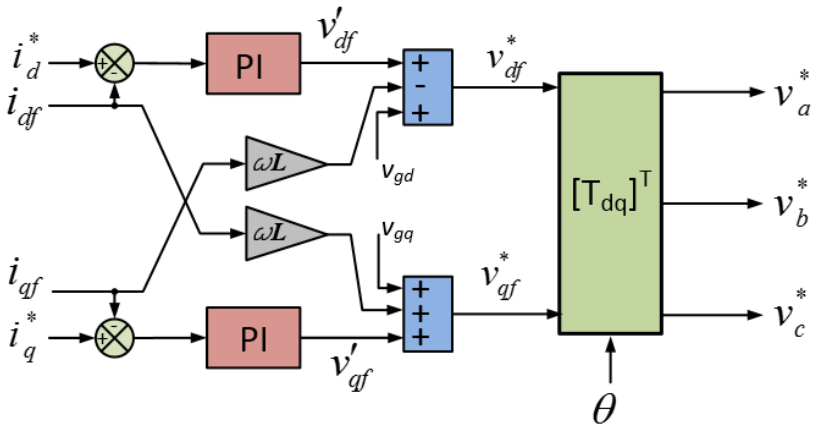


Figure 3-24 Block diagram of SRF PI controller with decoupling between the axes

The control block diagram of the SRF-PI scheme is then represented as shown in Figure 3-25.

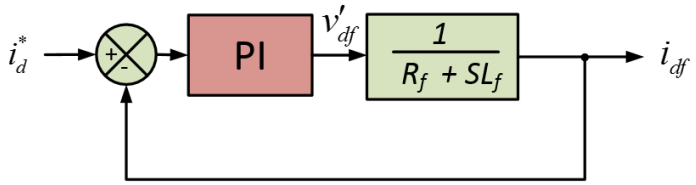


Figure 3-25 Block diagram of the SRF-PI controller for PI parameter calculation

The open loop transfer function of the current control loop is

$$G_{ol}(s) = C(s)\,G(s) \tag{3-61}$$

Where $G(s)$ is the plant transfer function and is given by:

$$G(s) = \frac{1}{sL_f + R_f} = \frac{b}{s + a} \tag{3-62}$$

Where $a = {}^{R_f}\!/_{L_f}$ and $b = {}^{1}\!/_{L_f}$

And $C(s)$ is he PI controller transfer function is:

$$G_{c_PI}(s) = K_p + \frac{K_i}{s} = \frac{sK_p + K_i}{s} \quad (3\text{-}63)$$

Where K_P is the proportional gain and K_I is the integral gain of the PI controller

Then, the open loop transfer function can be expressed as:

$$G_{ol}(s) = \frac{b(sK_p + K_i)}{s^2 + as} \quad (3\text{-}64)$$

The closed loop transfer function is also given as:

$$T(s) = \frac{b(sK_p + K_i)}{s^2 + s(a + bK_p) + bK_i} \quad (3\text{-}65)$$

The PI controller gains are designed by comparing the denominator of (4.76) and the denominator of the second order system which is given in equation (3-66):

$$\frac{\omega_n^2}{s^2 + (2\zeta\omega_n)s + \omega_n^2} \quad (3\text{-}66)$$

For a specified damping coefficient (ξ)and natural system frequency (ω_n), the gains are calculated as:

$$K_p = \frac{2\zeta\omega_n - a}{b} \quad (3\text{-}67)$$

and

$$K_i = \frac{\omega_n^2}{b} \quad (3\text{-}68)$$

Due to the zero that exist in the nominator of equation (3-65), so the response of equation (3-65) will not be as the response of equation (3-66). Thus the PI gains calculated from equation (3-67)

and equation (3-68) will not give the desired dynamic response. However, it will give close values to the optimal solution, which can be tuned using iterative methods, taking the values calculated from (3-67) and (3-68) as initial values.

To validate the performance of the designed SRF-PI controller, a simulation study was carried out using Matlab/Simulink. In this simulation, a controlled voltage source was used instead of voltage source inverter and a reference current was applied to the current controller. Different current reference waveforms were used in the simulation to check the controller capability to track the fundamental and harmonics current components. Figure 3-26 shows the simulation results for SRF-PI controller for four cases, only the fundamental current, only the fifth harmonic, only seventh harmonic and distorted waveform combining fundamental and fifth and seventh harmonics (10% amplitude from the fundamental) for design values of $K_p = 15$ and $K_I = 2400$.

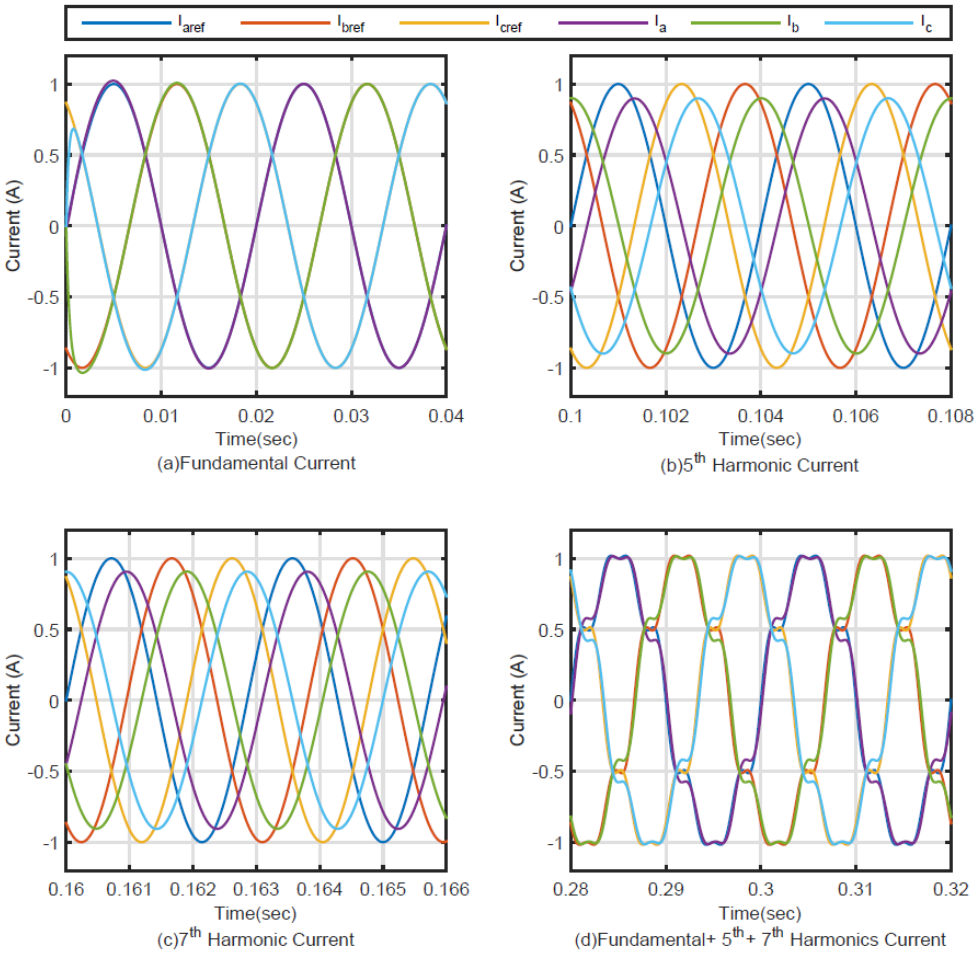


Figure 3-26 the simulation results for SRF-PI controller for different current references

As can be seen from Figure 3-26 (a) the generated current by the AFP follows the reference current waveform with high accuracy, but in the other subfigures (b), (c) and (d) the generated current didn't match the reference current due to the existence of harmonics.

SRF-PI controller gives a good dynamic response for the fundamental but with reduced tracking performance for higher harmonics components. Advanced controllers have been proposed to overcome these drawbacks, such as dual current control scheme in case of unbalanced voltage [74], where two synchronous reference frame are used, the first for the positive sequence and

second for the negative sequence. In distorted voltage source a multiple synchronous reference frames are proposed in [75], where the author propose synchronous reference frame for each harmonic. However, this will increase the computation burden of the controller. As a consequence a proportional resonant current controller (PR) has gained more interest in regulating AC reference currents due to high tracking accuracy.

3.7.3 Proportional Resonant Current Controller (PR)

Proportional resonant controllers (PR) are implemented in stationary reference frame and has superior response to sinusoidal reference waveforms. PR is an interesting alternative to the conventional SRF-PI controller [76, 77]. The PR controller has an infinite gain at the resonant frequency thereby the steady state error can be eliminated at this particular frequency.

The PR controller transfer function in the stationary reference frame is equivalent to the transformed PI current controller transfer function from synchronous reference frame to the stationary reference (using the formula in equation (3-69)). Therefore, the PR in the stationary frame transfer will provide the same frequency response of the SRF-PI, [78, 79].

$$G_{c_PR} = \frac{1}{2}\{G_{c_PI}(s - jw) + G_{c_PI}(s + jw)\} \tag{3-69}$$

From equation (3-63) and equation (3-69), the transfer function of the ideal PR current controller is given in equation (3-70).

$$G_{c_PR} = K_p + K_r \frac{s}{s^2 + \omega^2} \tag{3-70}$$

Where k_p is the proportional gain and k_r the resonant gain and they are the same PI controller parameters K_p and K_i respectively. ω is the resonant frequency where the PR gain becomes infinity. The Bode blot of ideal PR current controller for $K_p = 1$ and $K_r = 40$ is shown in Figure 3-27, as can be seen from the figure it has infinite gain at the resonant frequency (2π×50) and this infinite gain might leads to instability.

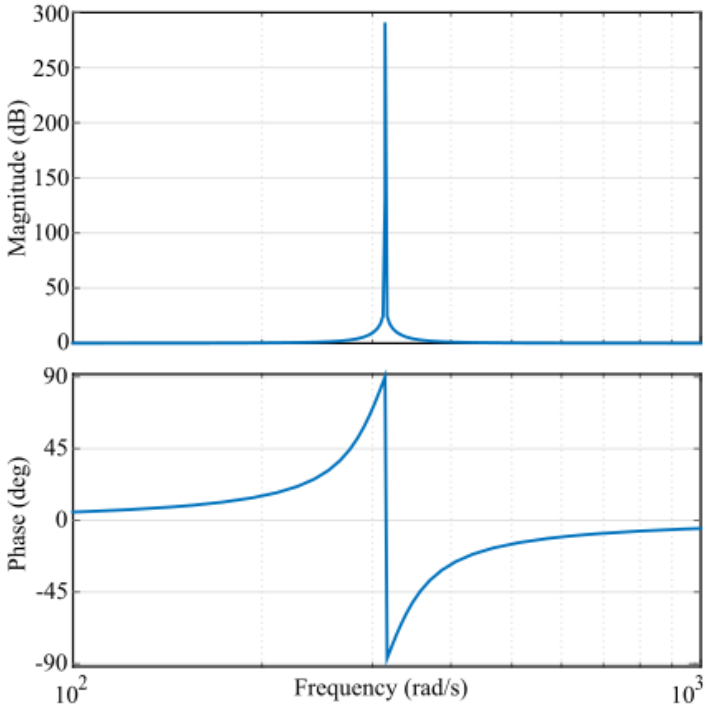


Figure 3-27 Bode blot of ideal PR current controller

To overcome the stability problems related to infinite gain, non-ideal PR current controller can be used [80]. The non-ideal PR controller has finite gain and its transfer function can be deduced by applying equation (3-69) on a low pass filter which has a transfer function as given in equation (3-71), [81].

$$G_{c_PR} = \frac{1}{1 + \frac{s}{\omega_c}} \tag{3-71}$$

Where ω_c is the cut-off frequency. The equation that result from the transformation is given in the following equation, where the controller parameters K_p and K_r added to the equation.

$$G_{c_PR} = K_p + \frac{2K_r\omega_c s}{s^2 + 2\omega_c s + \omega^2} \quad (3\text{-}72)$$

$\omega_c$helps reducing the controller sensitivity, higher values for ω_c giver a wider resonant peak. In [81], authors claimed that the value of ω_c that gives a good performance should be between 5 to 15 rad/sec. Figure 3-28 shows the Bode plot for a non-ideal PR current controller for $K_p = 1$ and $K_r = 1$ and different values for ω_c.

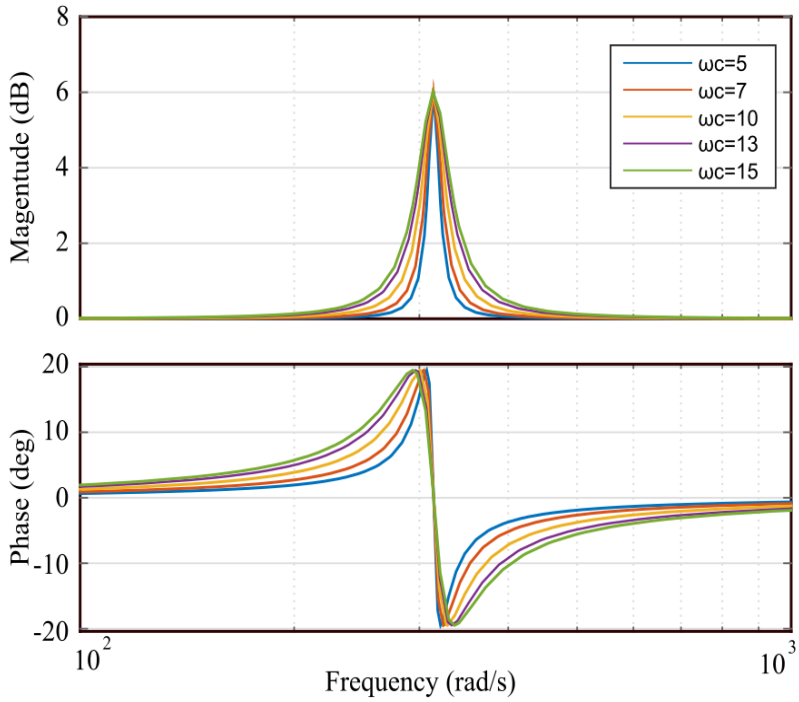


Figure 3-28 Bode blot of non-ideal PR current controller with different ω_c

As can be seen from Figure 3-28, by reducing the value of ω_c, the resonant beak become wider and decrease the sensitivity of the controller.

In addition, for multiple frequency compensation, a several selective harmonic compensation (HC) can be done. Each harmonic compensator is tuned for a single harmonic component. For example the transfer function of a non-ideal HC designed to compensate the 5th, 7th, 11th, 13th, 17th, 19th, 23rd and 25th are given as:

$$G_{c_HC} = \sum_{h=5,7,11,13,17,19,23,25} \frac{2K_{rh}\omega_c s}{s^2 + 2\omega_c s + (h\omega)^2} \qquad (3\text{-}73)$$

The total transfer function of the non-ideal PR+HC is given in equation (3-74). The block diagram of the controller is shown in Figure 3-29.

$$G_{c_PR+HC} = K_p + \sum_{h=1,5,7,11,13,17,19,23,25} \frac{2K_{rh}\omega_c s}{s^2 + 2\omega_c s + (h\omega)^2} \qquad (3\text{-}74)$$

The neutral leg reference voltage is calculated from equation (3-75)

$$v_n^* = -3 * (v_a^* + v_b^* + v_c^*) \qquad (3\text{-}75)$$

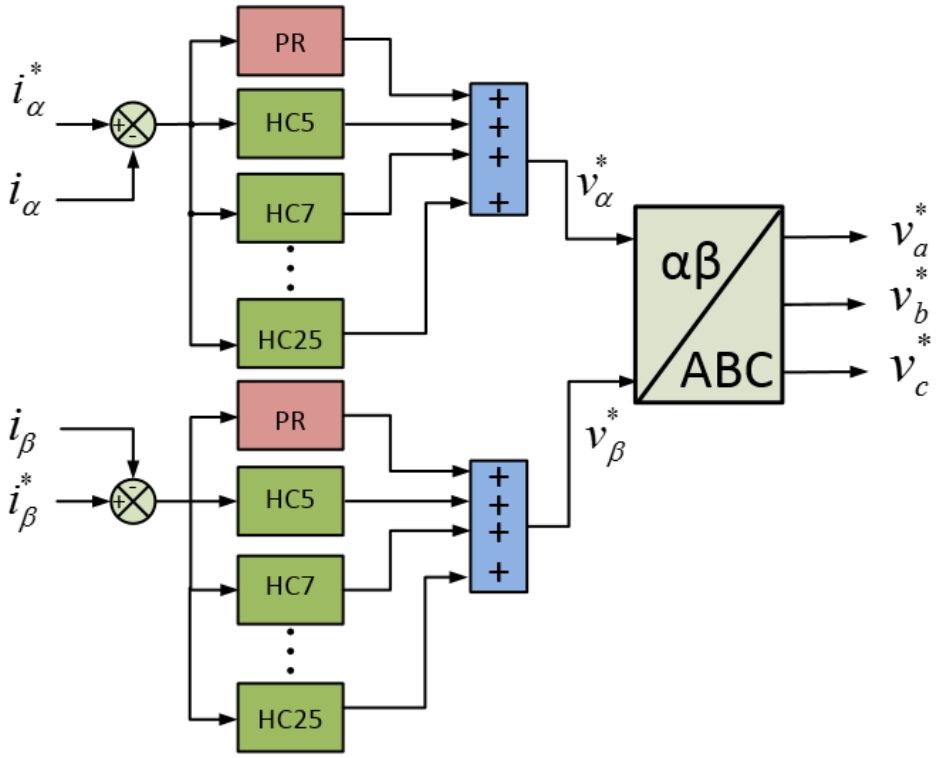


Figure 3-29 Block diagram of PR+HC controller

The Bode plot of non-ideal PR+HC for $K_p = 1$, $K_{rh} = 1$ and $\omega_c = 7$ rad/sec is shown in Figure 3-30. As can be seen from the figure, each harmonic has a resonant peak with zero degree phase shift making the gain higher.

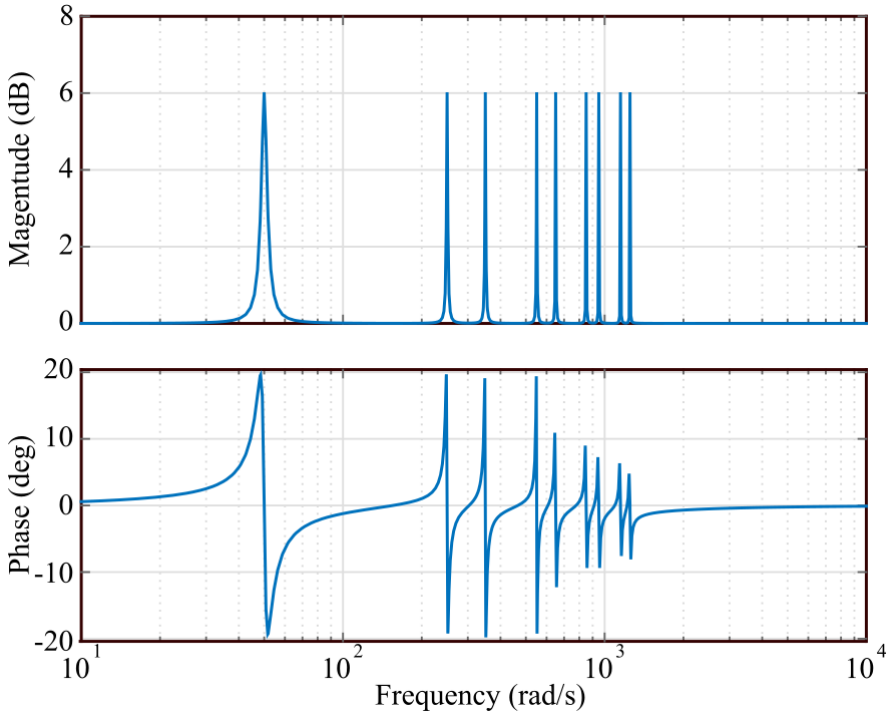


Figure 3-30 Bode blot of non-ideal PR+HC current controller

To investigate the performance of the PR+HC current controller, a Matlab/Simulink simulation was carried out. The current controller consists of a non-ideal PR controller with a cut-off frequency $\omega_c = 7$ rad/sec and a HC for the 5th, 7th, 11th, 13th, 17th, 19th, 23rd and 25th harmonics. Figure 3-31 shows the simulation results for PR+HC controller for four cases, the fundamental current, only fifth harmonic, only seventh harmonic and a combination from the fundamental, and all the harmonics with 10% in amplitude from the fundamental. The controller gains used are $K_p = 15$, and $K_r = 2400$ and $K_{rh} = 2500$. As can be seen from the figure, the PR+HC current controller tracked all the harmonics with good match to the reference current and better performance in comparison to the SRF-PI current controller.

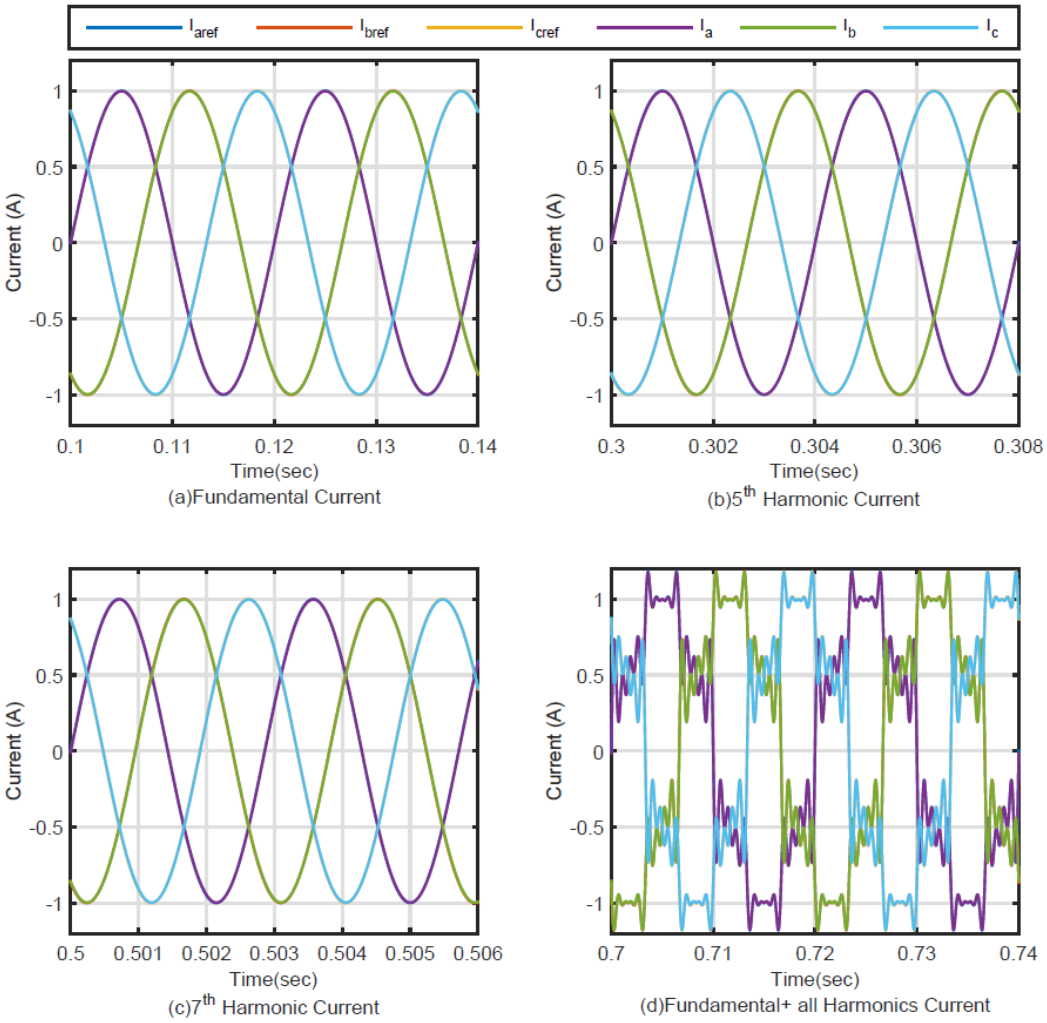


Figure 3-31 the simulation results for PR+HC controller for different current references

A significant advantage of the PR+HC controller, the dynamics of fundamental PR controller are not affected by the added HC controllers, where each harmonic compensator (HC) only compensate close to the tuned resonant frequency [80].

This section presented a three type of current controller, one nonlinear current controller and two linear current controllers. The nonlinear current controller is simple in construction but it has variable switching frequency. The PI current controller has superior performance in DC- signals, but in sinusoidal signal it gives high steady state error and unable to track the signal. The non-ideal

PR+HC current controller has a high performance in tracking sinusoidal current reference and able to compensate low order harmonics.

There are many other control methods in the literatures used to control the AFP current such as, Dead Beat controller, wavelet control, sliding mode control, delta-sigma modulation vector control, SFX control, repetitive control etc. [82].

3.8 Modulation technique

After reference voltages have been calculated, these voltages can be generated at APF terminal by using PWM technique. Figure-3-32 shows the block diagram of this technique. In this scheme, the reference voltages are compared with the triangular carrier signals by using the limit comparators to generate the switching pulses for APF switches.

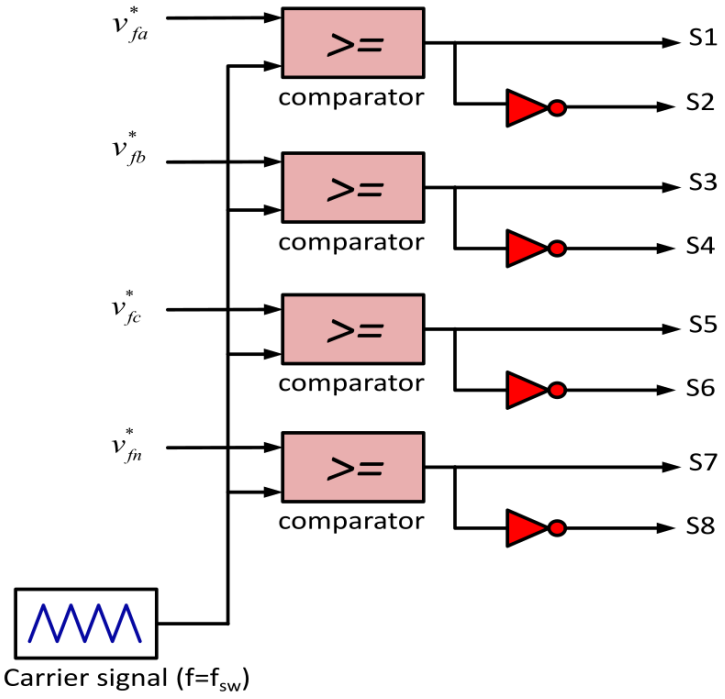


Figure-3-32: The block diagram of carrier-based PWM current control

The principle of the carrier-based PWM current control is illustrated in Figure-3-33. For example in phase a, if the reference voltage (v_{fa}^{*}) is greater than the triangular carrier voltage (v_{tr}) then the comparator output is 1 (S1=1, S2=0). In the other hand, If (v_{fa}^{*}) is less than (v_{tr}) then the comparator output is 0 (S1=0, S2=1).

The switching frequency of this technique is constant and it is equal to the frequency of triangular carrier (f_{tr}) signal.

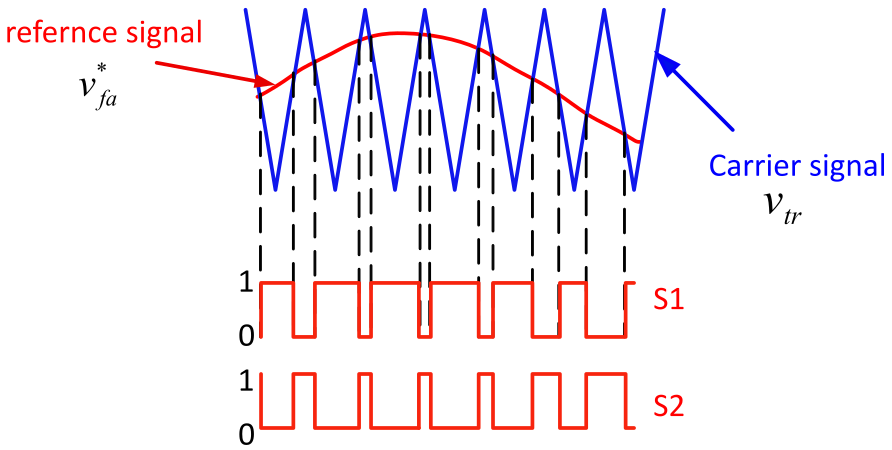


Figure-3-33: The basic concept of carrier-based PWM current control

3.9 **DC-link Voltage Control**

The DC-link voltage controller function is to regulate the voltage of the capacitor of the APF DC-link at a specific value. The voltage of the DC-link capacitor is measured and compared to a reference value, and then the error is passed through a PI controller to produce the current reference of the DC-link regulator. The output current of the PI controller is the direct axis reference current ($I_{d_{DC-link}}$). This current converted to $\alpha\beta$ domain then added to the APF reference current. Figure-3-34 shows the block diagram of the DC-link voltage controller.

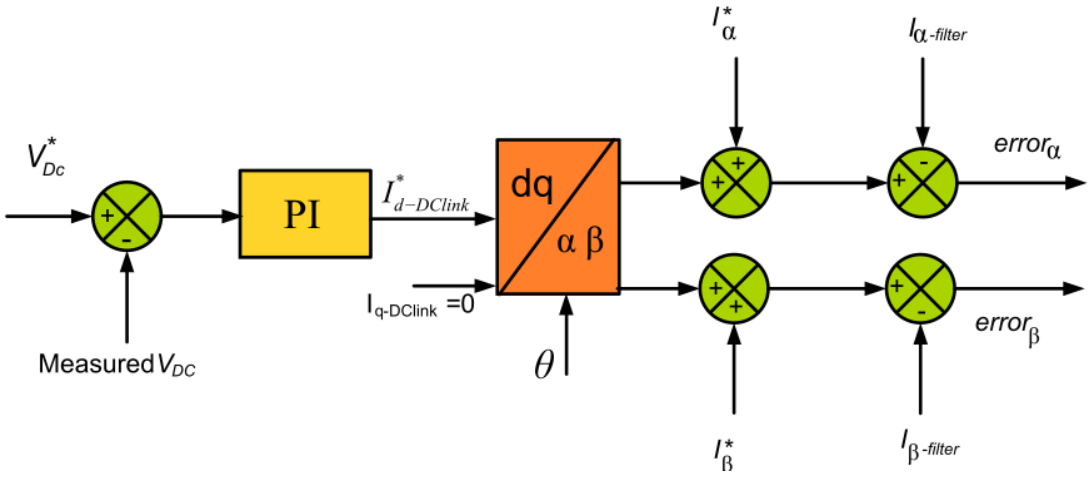


Figure-3-34: The block diagram of the DC-link voltage controller

To design the PI of the DC-link voltage regulator, the system control plant transfer function should be derived first. By assuming converter losses equal to zero, the DC link current I_{DC} can be derived from the power balance of the APF converter. Hence,

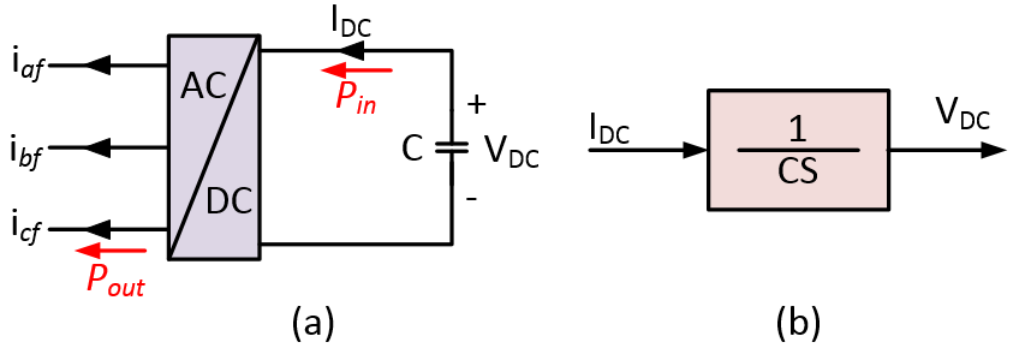


Figure 3-35 DC-link regulator and the transfer function derivation

$$V_{DC}I_{DC} = \frac{3}{2}\left(V_{df}I_{df} + V_{qf}I_{qf}\right) \qquad (3\text{-}76)$$

Where V_{df} and V_{qf} are the output voltages of the converter in SRF, I_{df} and I_{qf} are the output currents of the converter in SRF.

From equation (3-76) the DC-link current I_{DC} is given by:

$$I_{DC} = \frac{\frac{3}{2}\left(V_{df}I_{df} + V_{qf}I_{qf}\right)}{V_{DC}} \tag{3-77}$$

Because the synchroniser aligns V_d with the grid voltage vector and makes V_q equal to zero, the equation (3-77) can be simplified as:

$$I_{DC} = \frac{3V_{df}I_{df}}{2V_{DC}} \tag{3-78}$$

The relationship between V_{DC} and I_{DC} and the plan transfer function for DC-link voltage control are given in (3-79)

$$I_{DC} = C\frac{dV_{DC}}{dt}$$

$$I_{DC}(S) = CSV_{DC}(S) \tag{3-79}$$

$$\frac{V_{DC}(S)}{I_{DC}(S)} = \frac{1}{CS}$$

Figure 3-36 shows the control block diagram of the DC-link voltage controller

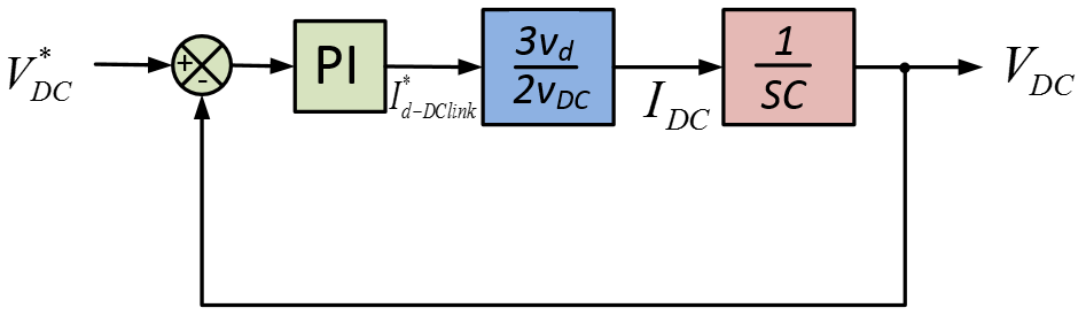


Figure 3-36 Block diagram for DC-link voltage control circuit

The parameters of PI controller of voltage control loop can be calculated by taking into consideration that voltage control loop

dynamic response (outer loop) should be slower than the inner current control loop.

3.10 **Passive Elements Design:**

The passive elements in the APF circuit are interface filter, which couples the APF with the grid at the PCC, to minimize the injected switching harmonics to the system, and the DC link capacitor. The interface filter of the converter could be L-filter [83], LC-filter [84-86] or LCL-filter [87, 88]. LCL-filter has better performance and gives smoother output current. However, the parameter design of LCL filter is more complex and might cause a resonant frequency with the gird. So for simplicity in construction and control [89] , L-filter is adopted in this thesis for interfacing the APF converter to the PCC. This section calculates the size of the main passive elements of the APF, which are the filter inductance and the DC-link capacitor.

3.10.1 Filter Inductance

Calculation of the interface L-filter inductance depends on many factors such as, converter topology, modulation strategy and maximum allowed current ripples. The current ripples is defined as the maximum difference between the output filter current and its reference current in a switching period [90], the minimum value of the interface inductance that gives maximum current ripple I_{ripple} given as:

$$L_{min} = \frac{V_{DC}}{8\ f_s\ I_{ripple}} \tag{3-80}$$

Where f_s is the frequency of the carrier signal and equal to($f_s = 1/T_s$). (see Appendix- for more details)

There are other methods to calculate the inductance of L-filter as reported in [91]. The author of [90] compared the performance of an APF with L-filter designed with using equation (3-80) and other three method given in equation (3-81) [83], equation (3-82) [92] and equation (3-83) [93], and they claimed that the performance of the APF with L-filter designed using equation (3-80) has a better accuracy and in general more applicable in designing the interface L-filter.

$$L \geq \frac{3}{16} \frac{V_{DC}}{f_s \Delta I_r} \tag{3-81}$$

$$L > \frac{V_{DC}}{6 f_s \Delta I_r} \tag{3-82}$$

$$\frac{\Delta V}{\omega_1 I_{c_max}} \leq L \leq \frac{\Delta V_{max}}{4 f_s \Delta I_r} \tag{3-83}$$

Where ΔV is the difference between the source voltage and the inverter voltage $\Delta V = \left| V_{filter} - V_{source} \right|$, $\Delta V_{max} = (V_s + 0.5 V_{DC})$, ω_1 is source frequency and I_{c_max} is the maximum filter current.

In practice, for current ripple 15% to 20% of the rated current is acceptable [86] to meet the harmonics standard [18]. For switching frequency of 10kHz, the maximum filter current 33.6A and the DC-link voltage is 730 V, according to equation (3-80) the minimum inductance tom meet 15% current ripple is 3.6 mH.

3.10.2 DC-link Capacitor

The design of energy-storage capacitor can be based on either the required energy stored in the capacitor using energy balance concept or reducing the oscillation in DC-link voltage due to the low order harmonic or unbalance lodging [91]. The DC-link capacitor

sizing was based on the work of the authors in [91] and can be calculated using equation (3-84).

$$C_{DC} = \frac{\pi I_{f1rated}}{\sqrt{3}\ \omega\ V_{DCp-p(\max)}} \tag{3-84}$$

Where $\pi I_{f1rated}$ is the APF rated current (30% of the proposed generator current), ω is the rated frequency in rad/sec, and $V_{DCp-p(\max)}$ is the maximum allowed DC-link voltage.

For $V_{DCp-p(\max)}$ 5% of the DC-link voltage, the capacitance of the DC-link capacitor is 5 mF**.**

3.11 **APF Design Validation**

A Matlab Simlink simulation was done to test all the shunt APF system. The simulation was harmonic compensation of a nonlinear load connected to a generator. The nonlinear load was three-leg diode rectifier connected to RL-load (R=9 Ω and L=5.5 mH). The shunt APF switched on at t=1 sec. The simulation results are shown in Figure 3-37, as can be seen from the figure when the shunt APF switched on compensate the nonlinear load harmonic and significantly reduce the THD in generator current from 25.4% to just about 4%.

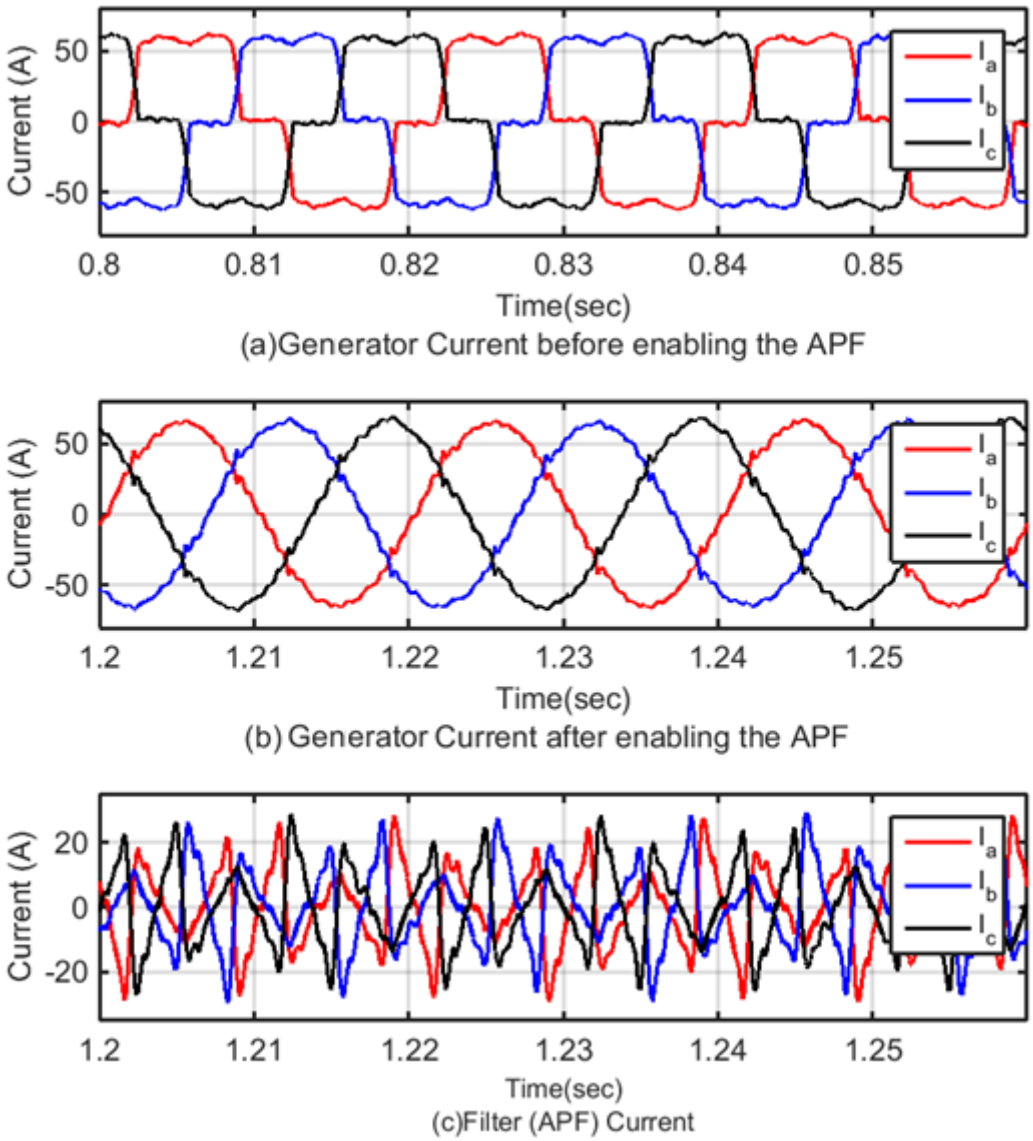


Figure 3-37 APF system test with nonlinear load

Figure 3-38 shows the fast Fourier analysis (FFT) for the generator current, as can be seen from the figure all the harmonics are significantly reduced.

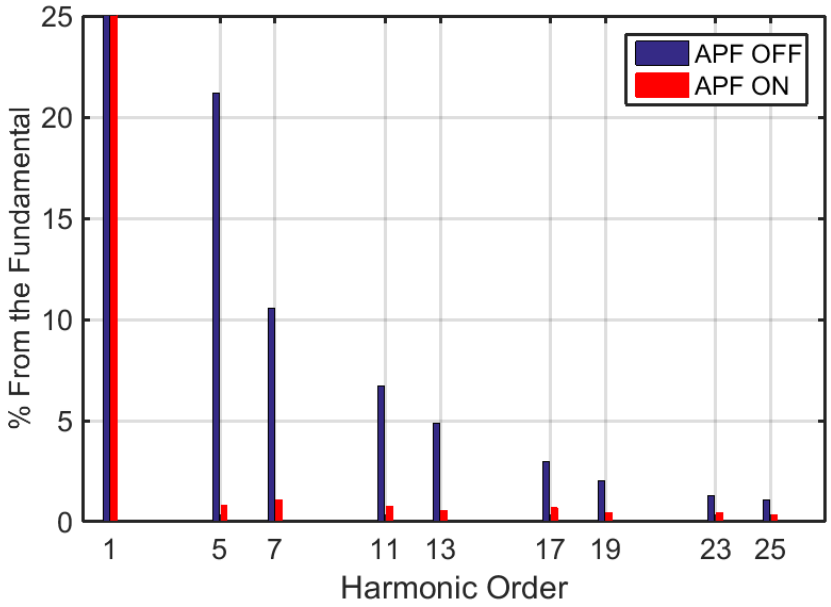


Figure 3-38 FFT Analysis for generator current

3.12 **Conclusion**

This chapter presented the active power filters (APFs) configuration and control, started with an introduction about APFs followed by the filter topologies in three-phase four-wire systems and shunt active power filter and series active power filter configurations. In section 3.43.5 three synchronisation methods were presented and the DSOGI-PLL was proven to be most suitable choice for unbalanced and distorted voltage, so this method is adopted in APF synchronisation in this thesis. Section 3.6 presented the most two widely used APF waveform reference generation techniques, where synchronous reference d-q method was chosen in this research because the simplicity and robustness to source voltage distortion. Current control techniques were reviewed in section 3.7, the PR+HC has shown better performance in sinusoidal reference current tracking, so it has been used in this research. The APF DC-link voltage controller were presented and designed in section 3.8 respectively. section 3.10 presented the APF passive element design where the interface L-filter inductance and the DC-

link capacitor capacitance values were calculated for the APF circuit configuration used in this thesis. Finally, a validation of the shunt APF design was presented in section 3.11.

To conclude the specification of the shunt APF filter developed and discussed in this chapter is shown in Table 3-2:

Table 3-2 The specification of the shunt APF filter

No.	**Description**	**Type/Value**
1	Topology	four-leg inverter
2	Synchronisation method	DSOGI-PLL
3	Reference current generation	synchronous reference d-q method
4	Interface filter	4.2mH
5	DC-link capacitance	5 mF
6	DC-link voltage	730
7	Switching frequency	10kHz

In addition the specification of the series APF filter developed and discussed in this chapter is Table 3-3:

Table 3-3 The specification of the series APF filter

No.	**Description**	**Type/Value**
1	Topology	Three-leg inverter
2	Synchronisation method	DSOGI-PLL
3	Reference current generation	synchronous reference d-q method
4	Interface filter	4.2mH
5	DC-link voltage	730
6	Switching frequency	10kHz

Chapter-4 Synchronous Generator Power Quality Improvements

Chapter-4 **Synchronous Generator Power Quality Improvements**

In this chapter, the application of (APFs) with the proposed synchronous generator are presented. Where in the first section a general description of the proposed system is presented. Then the operation of each individual filter is investigated. For shunt filter (section 4.2), linear load power quality improvement is presented in section 4.2.1 and current harmonics compensation on nonlinear load is discussed in section 4.2.2. Generator load balancing and nonlinear load harmonic compensation are discussed in section 4.2.3. For series active filter for a linear load is presented in section 4.3. The operation of all proposed system is investigated in section 4.3.34.4. Finally, the conclusion of the chapter is presented in section 4.5

4.1 **System Configuration**

The proposed system is a three-phase four wire system consisting of a simplified synchronous generator (SSG), four leg shunt active power filter (APF), three leg series active filter, interface L-filter and a different kind of load, which may be linear or nonlinear, and balanced or unbalanced as shown in Figure 4-1. The proposed generator model is as presented in section 2.4 and the APF configuration and control is as discussed in Chapter-3.

Three different kind of load will be presented in the following sections. In the two first simulations the APF is used to compensate the system harmonics, and in the last simulation the APF is used to compensate system harmonics and balance the proposed generator currents.

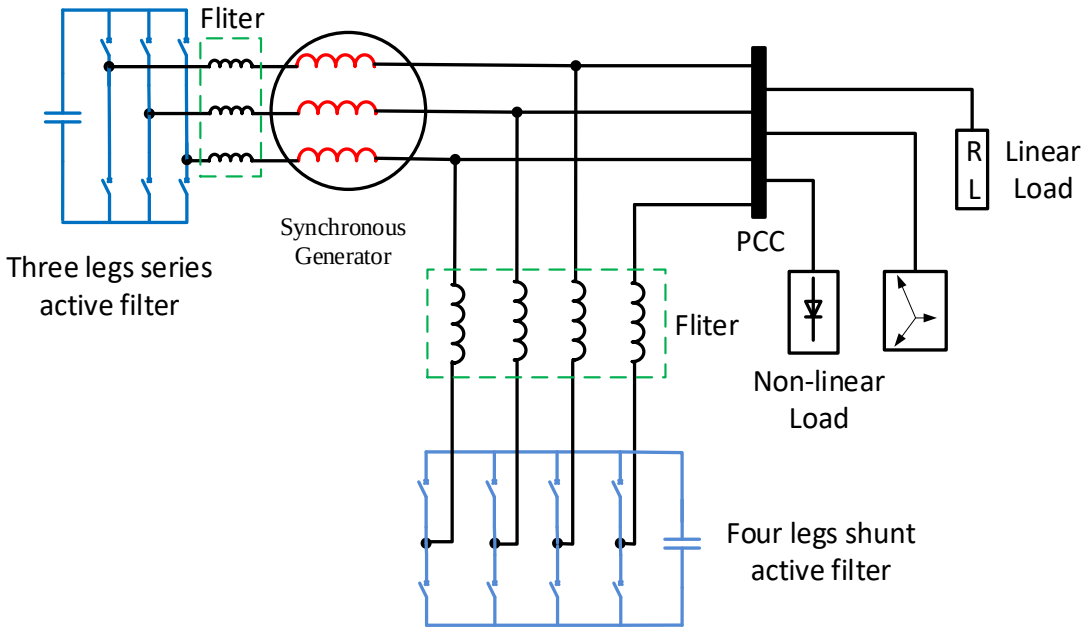


Figure 4-1 Block diagram of the proposed system

4.2 **Shunt Active Filter:**

4.2.1 Output Power Quality Improvements of Synchronous Generator with Linear Load

The output current of the SSG contains harmonics, and when a linear load is connected, the load should be supplied with good power quality, thus the first application of the APF with the simplified synchronous generator, which is presented in this section, is suppling a linear load with good power quality. In this simulation, a three-phase resistive load (35 kW, about 50% of the generator loading) is connected to the generator at the point of the common coupling (PCC) where the APF was connected as shown the Figure 4-2. In this kind of load the APF should absorb the harmonics that exist in the generator current leaving just the fundamental waveform current supplied to the load.

4.2.1.1 Compensation Procedure:

The operation principle of the compensation method can be described as follows:

1- Sensing the generation voltage at the PCC and calculating the phase angle of the voltage vector by using DSOGI as discussed in section 3.5.3.
2- Sensing the generator current and calculating the reference current by using synchronous reference (d-q) method as explained in section3.6.2.
3- Generating the reference voltage which required to absorb the reference current from the PCC point. A proportional resonant controller was used to generate the reverence voltage as discussed in section 3.7.3.
4- A PI controller was used to maintain the DC-link voltage at constant value (730 V) as explained in section 3.8.

All the compensation steps that were discussed in chapter-3 were coded in Matlab script code in Matlab function in the Simulink simulation which shown in Figure 4-2, the Matlab code is given in Appendix .

The simulation was started with the APF was turned off leaving the generator current reaching a steady state. At t=2.0 sec the APF was turned on and worked as expected.

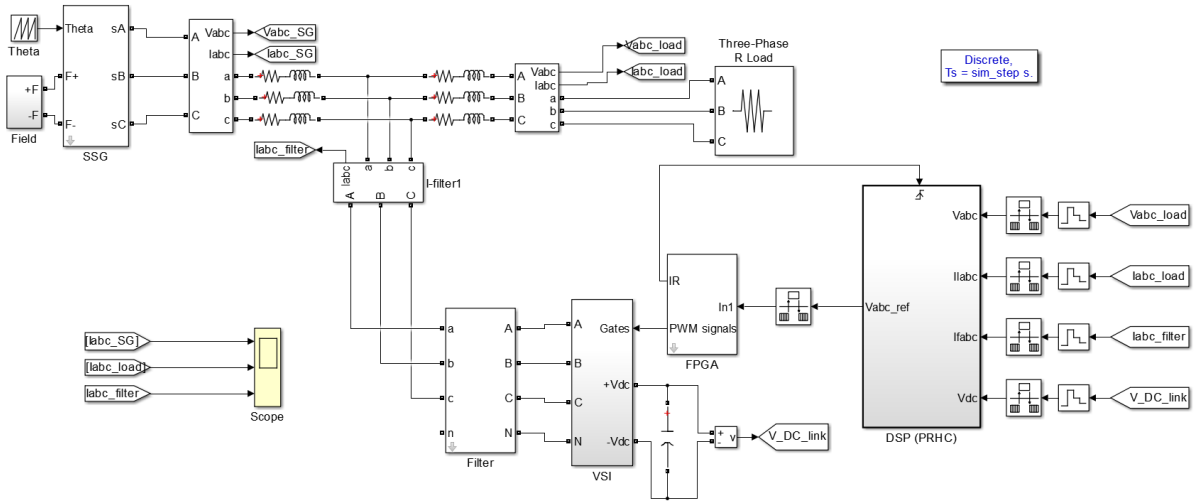


Figure 4-2 Simulation circuit for balanced linear load

4.2.1.2 Simulation Results:

The simulation results are shown in Figure 4-3, after enabling the APF, the APF absorbed the harmonics from generator current and let just the fundamental current to reach to the load, in this case the APF works as high pass filter. The total harmonic distortion in the load current (THD) is reduced from 4.5% to around 2.1% and this is within IEEE Std 519 limits which given in Table 1-1.

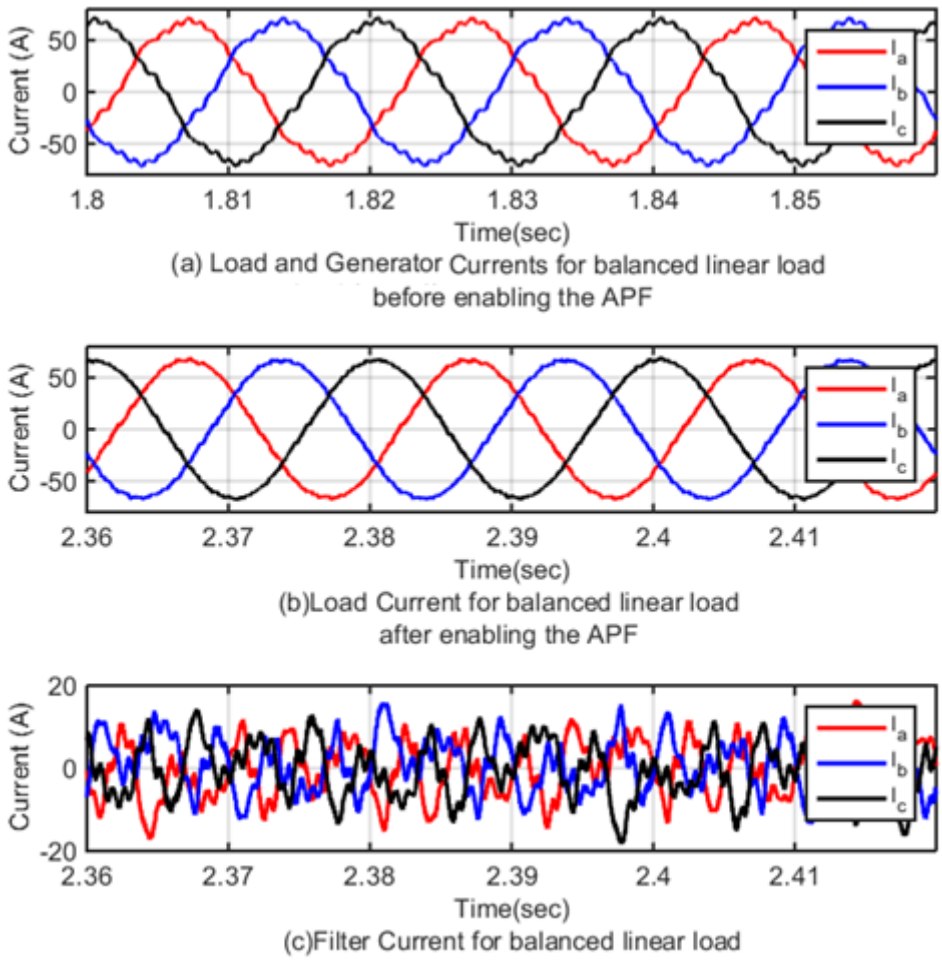


Figure 4-3 simulation results for harmonic compensation for balanced linear load (a) generator and load currents before enabling the APF (b) load currents after enabling the APF (c) the APF currents

4.2.2 Current Harmonics Compensation of Nonlinear Loads

In this case the load is nonlinear, so the focus will be on the generator currents, thus the second application of the APF with the simplified synchronous generator which is presented in this section, is mitigating the harmonics in the proposed generator currents. In this simulation, a three-phase diode bridge and RL load (R=9.2 Ω and L=5.5 mH) (about 35 KW) was connected to the SSG to represent the nonlinear load as can be seen in Figure 4-4.

In this kind of load the APF should supply the nonlinear load harmonics that exist in the load current leaving just the fundamental waveform current supplied by the proposed generator.

4.2.2.1 Compensation Procedure:

The operating principle of the compensation method is this simulation can be described as follows:

1- Sensing the generation voltage at the PCC and calculating the phase angle of the voltage vector by using DSOGI as discussed in section 3.5.3.
2- Sensing the nonlinear load current and calculating the reference current by using synchronous reference (d-q) method as explained in section3.6.2.
3- Generating the reference voltage which required to inject the reference current, the nonlinear load harmonics, into the PCC point. A proportional resonant controller was used to generate the reverence voltage as discussed in section 3.7.3.
4- A PI controller was used to maintain the DC-link voltage at constant value (730 V) as explained in section 3.8

The simulation was started with the APF was turned off leaving the generator current reaching a steady state. At t=2.0 sec the APF was turned on and did its job as expected and compensated the nonlinear load harmonics.

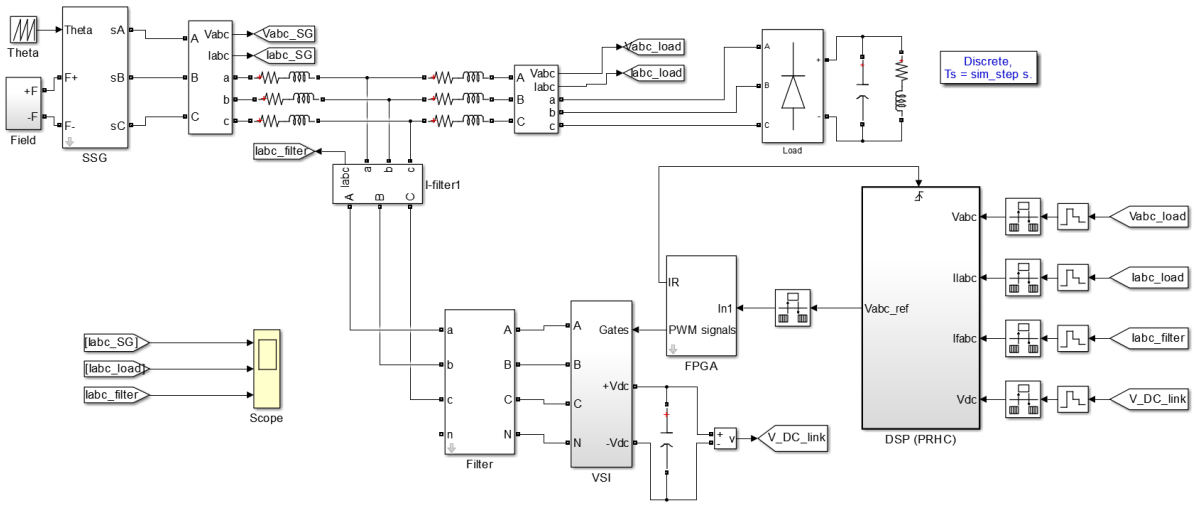


Figure 4-4 Simulation circuit for balanced nonlinear load

4.2.2.2 Simulation Results:

The simulation results are shown in Figure 4-5. When the APF was switched on, the APF supplied the nonlinear load harmonics leaving the proposed generator supplying the fundamental current. The THD in the generator current decreased from 22.3% before enabling the APF and to 3.43% after enabling it. Again the APF worked as expected and calculated the nonlinear load harmonics and injected them at the PCC point. Figure 4-5 shows the generator, the load and the filter before and after the compensation.

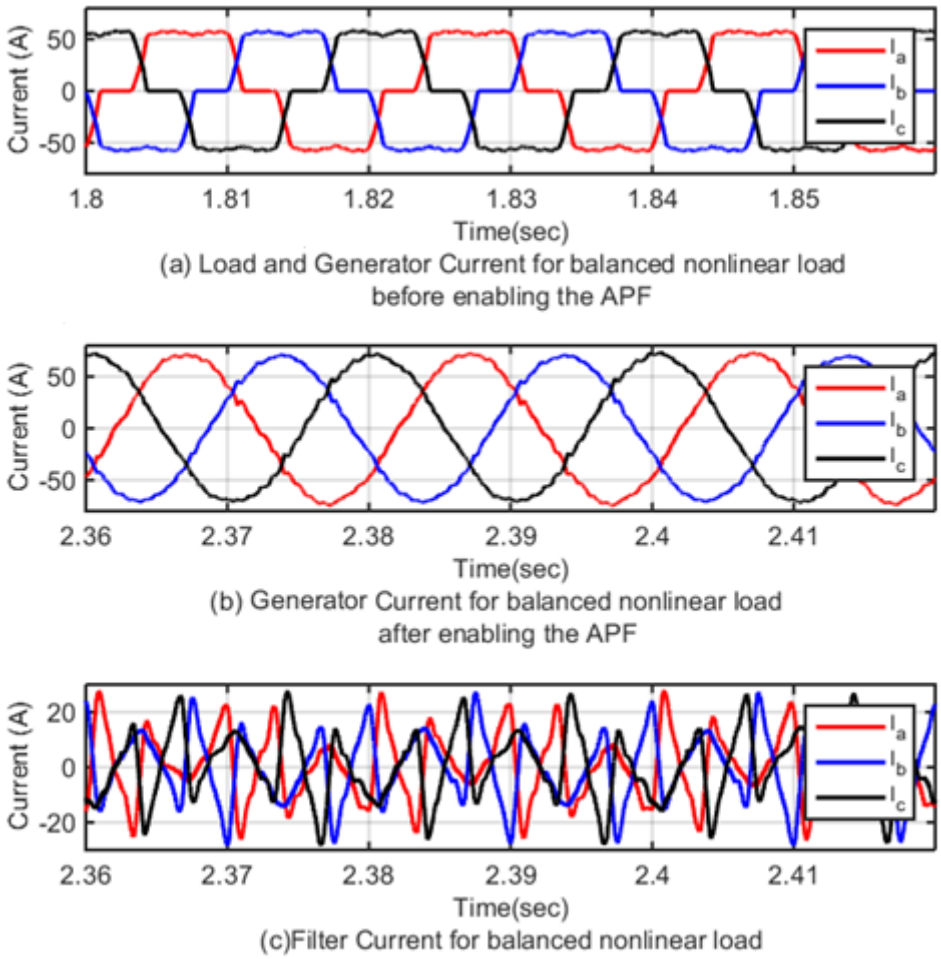


Figure 4-5 Simulation results for balanced nonlinear load (a) generator and load currents before enabling the APF (b) generator currents after enabling the APF (c) the APF currents

4.2.3 Synchronous Generator Load Balancing

Due to the unbalance caused by single-phase loads in the generator current, the APF in this section is used to balance the generator currents and to compensate for the harmonics in these currents.

There are two types of unbalance considered in this section, the first one is where the sum of the three phase currents is zero (Just negative sequence components) i.e. the neutral point is not connected. In the second type, the sum of the three phase current

is not zero i.e. there is a current in the neutral wire (negative and zero sequence components).

4.2.3.1 Compensation Procedure:

The operation principle of the compensation method is this section can be described as the same as in subsection 4.2.2.1.

4.2.3.2 Simulation Results

The simulations were done for both types of unbalanced loading. In both cases the simulation was started with the APF turned off. At t=2.0 sec the APF was turned on to compensate the nonlinear load harmonics and balance the generator currents.

4.2.3.2.1 Unbalanced Non-Linear Load with Only Negative Sequence Components (Type-1):

To simulate the first type of unbalance, (only negative sequence), a nonlinear load (full bridge diode rectifier) is added to the circuit which shown in Figure 4-4 and connected between phase-A and phase-B feeding a RL load . The RL load was L = 5.5 mH and R = 27 Ω as shown in Figure 4-6.

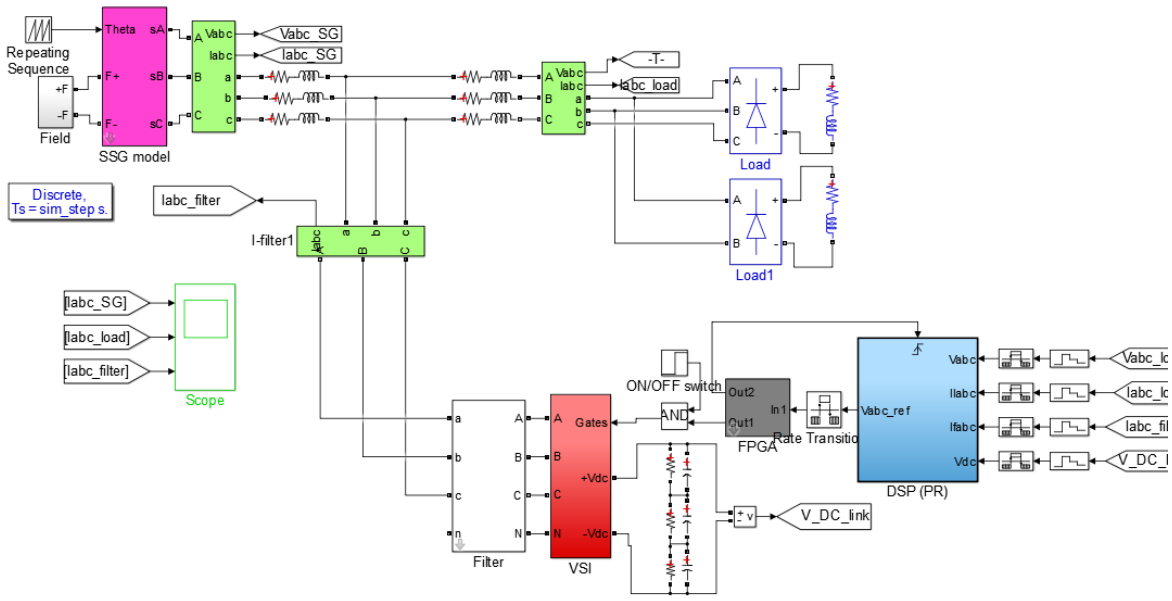


Figure 4-6 Simulation circuit for type-1 of unbalanced nonlinear load

The simulation results are shown in Figure 4-7, as can be seen from the figure, when the APF is enabled, the APF is supplied the nonlinear load harmonics currents and balanced the proposed generator currents. The THD significantly improved. For example, the THD in phase-C drops from 20.1% to 3.8%. Table 4-1 summarises the THD and the current values of the system before and after enabling the APF.

Table 4-1 The simulation results for the THD and currents values before and after enabling the APF for unbalanced nonlinear load with just negative sequence

	Before enabling the APF		**After enabling the APF**			
	load/generator		**Load**		**Generator**	
	THD %	Amp	THD %	Amp	THD %	Amp
Phase-A	14.6	57.6	20.3	60.0	3.7	54.6
Phase-B	15.4	56.5	19.7	58.9	3.3	52.9
Phase-C	20.1	45.4	25.5	47.1	3.8	53.7

As can be summarised from the Table 4-1 the APF mitigated the harmonics in the generator current and balanced them. At the load side the highest difference between the three phase currents is the difference between the phase-A current (highest current) and the phase-C current (lowest current), where the phase-A current is bigger than phase-C by 27.39%, while in the generator side the APF maintained the difference between the phase current to maximum 3.21 %

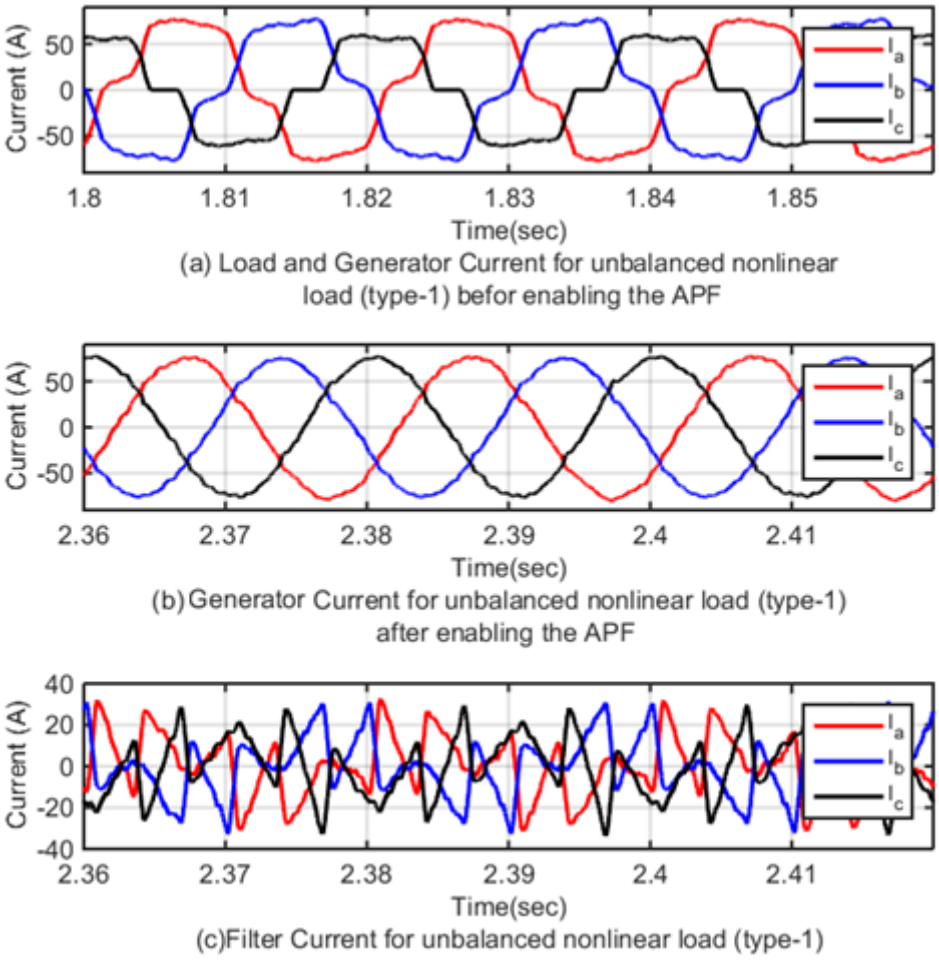


Figure 4-7 System currents after enabling the APF with nonlinear and unbalanced load type-1

4.2.3.2.2 Unbalanced Non-Linear Load with Negative and Zero Sequence Components (type-2):

To simulate this type of unbalance a full bridge diode rectifier was connected between phase A and the fourth leg of the converter (APF neutral leg) instead of phase-B in Figure 4-6, As shown in Figure 4-8.

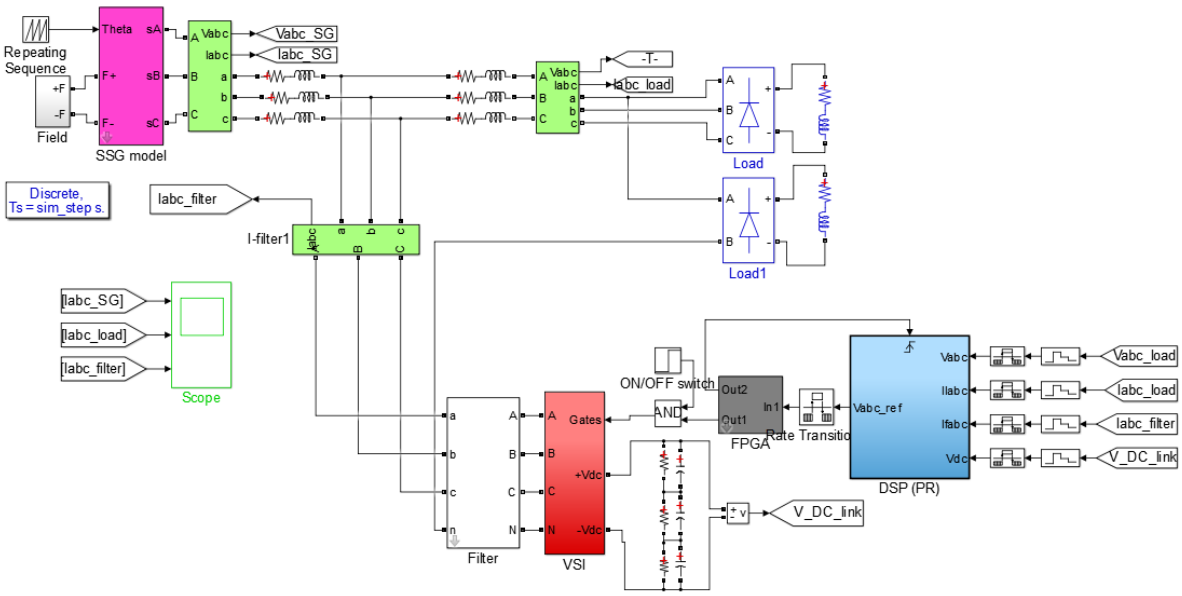


Figure 4-8 Simulation circuit for type-2 of unbalanced nonlinear load

The simulation results are shown in Figure 4-9. As can be seen from the figure, when the APF is enabled it supplied the nonlinear load harmonic currents and the single-phase load. In addition, it maintained the proposed generator current balanced. The THD was significantly improved, as can be seen from Figure 4-9 the APF decreased THD in the generator current from 22.3% to 3.65% and supplied the single phase load (connected between the phase-A and the neutral leg of the APF) when it was enabled.

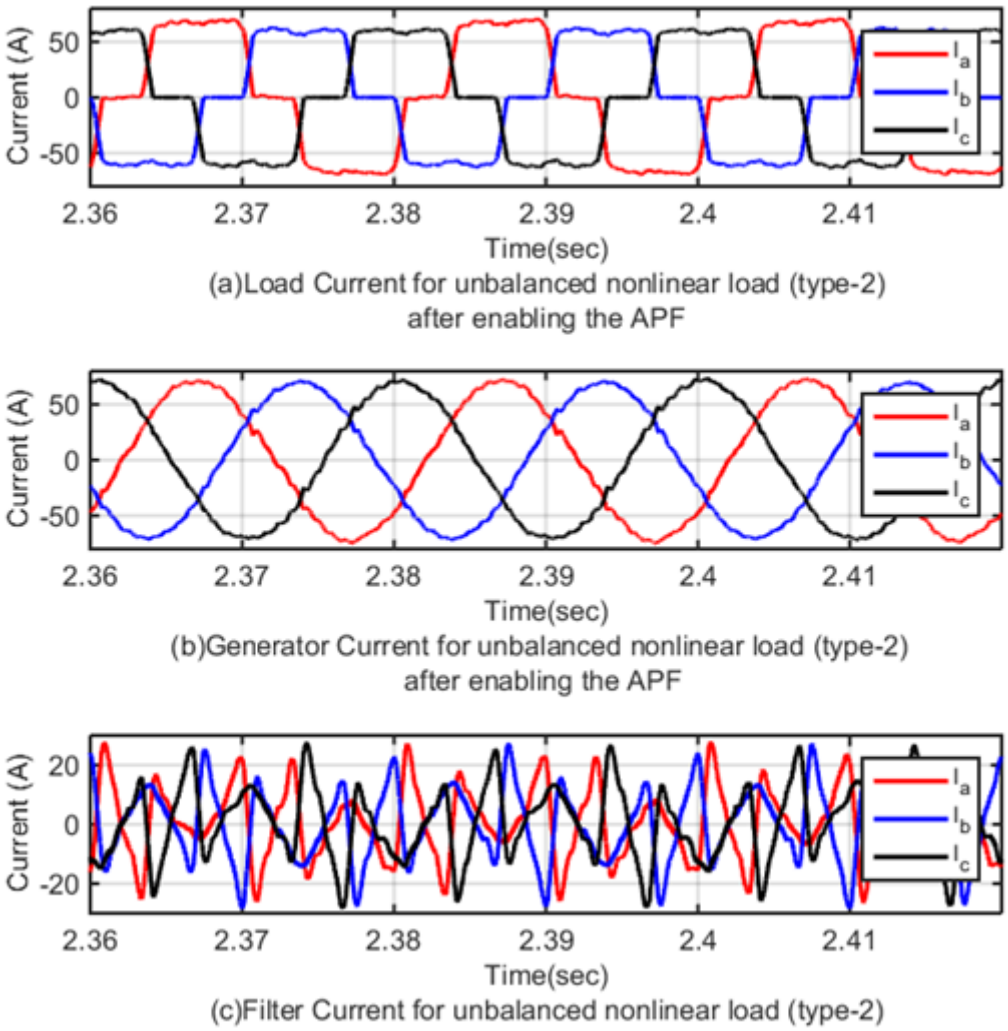


Figure 4-9 System currents after enabling the APF with nonlinear and unbalanced load type-2

Table 4-2 summarises the THD and the current values of the system (nonlinear unbalanced load type-2) before and after enabling the APF.

Table 4-2 The simulation results for the THD and currents values before and after enabling the APF for unbalanced nonlinear load type-2

	Before enabling the APF		**After enabling the APF**			
	load/generator		**Load**		**Generator**	
	THD %	Amp	THD %	Amp	THD %	Amp
Phase-A	22.3	44.92	23.4	53.29	3.96	50.55
Phase-B	22.3	44.86	25.3	47.74	2.71	49.58
Phase-C	22.3	44.82	25.3	47.88	3.56	50.54

As can be concluded from the Table 4-2 the APF supplied the single-phase load and kept the generator current balanced where in load side the phase-A current (highest current) is higher than phase-B current (lowest current) by 11.63%, while in the generator side the APF maintained this difference to just 1.96 %

4.3 **Series Active Filter:**

This filter is connected in series with the generating windings. To compare the operation of the active series filter with the proposed generator and the proposed generator alone in one simulation, a switch installed between the series filter and the generating windings. In the beginning of the simulation the switch is ON and the filter is OFF, at the desired time the situation is reversed (i.e. switch OFF and filter ON). In simulation the DC-link of voltage of the active filter was fed by a DC voltage source as shown in Figure 4-10.

Figure 4-10 shows the different component of active series filter such as the inverter power module, the controller module and voltage sensors which send the feedback signals to the control module. It also shows how the active series filter connected to the proposed generator.

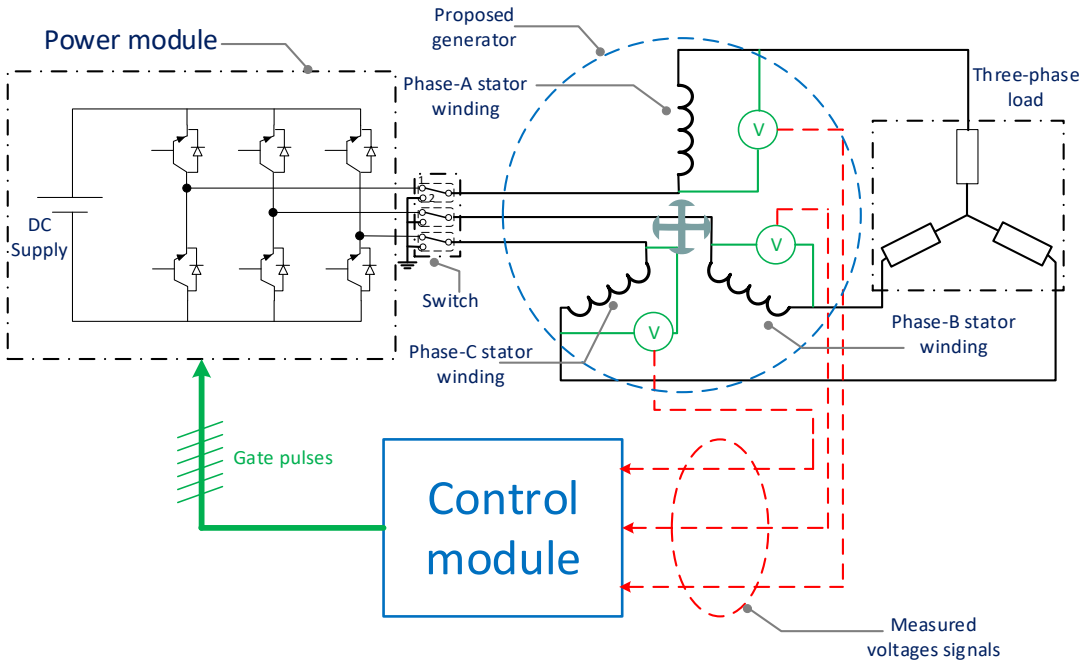


Figure 4-10 Series active filter simulation circuit

4.3.1 Control Method of Series Active Filter

The control method of the Series Active Filter (SAF) is shown in the schematic diagram Figure 4-11, and explained as follows:

1. Sensing the generator winding voltages as a feedback signal to the control module helps to calculate the phase angle of the voltage space vector (by using DSOGI as discussed in section 3.5.3).
2. Starting from the measured voltage signals in the abc reference frame and the computed angle derived in point 1, the Park's transformation can be applied and the representation of the measured voltages in the d-q rotating reference frame can be achieved, as shown in the schematic diagram.
3. The d-q signals represent both, fundamental and undesired harmonics components of the measured winding voltages. The main idea behind the series active filter is to generate these

undesired harmonic signals in the opposite phase to the original waveforms to cancel them.

Therefore, in the control module, a Low Pass Filter (LPF) has been used to separate the fundamental from the undesired harmonics of the d-q voltage signals.

$$V_{abc-filter} = V_{abc_ratedf} - V_{abc_measured} \quad (4\text{-}1)$$

4. Then, the inverted undesired harmonics signals are used as reference signals to the Pulse-Width Modulation (PWM) algorithm. The control module then computes the switching pattern that used to drive the power module switches (IGBTs) of the ASF inverter.

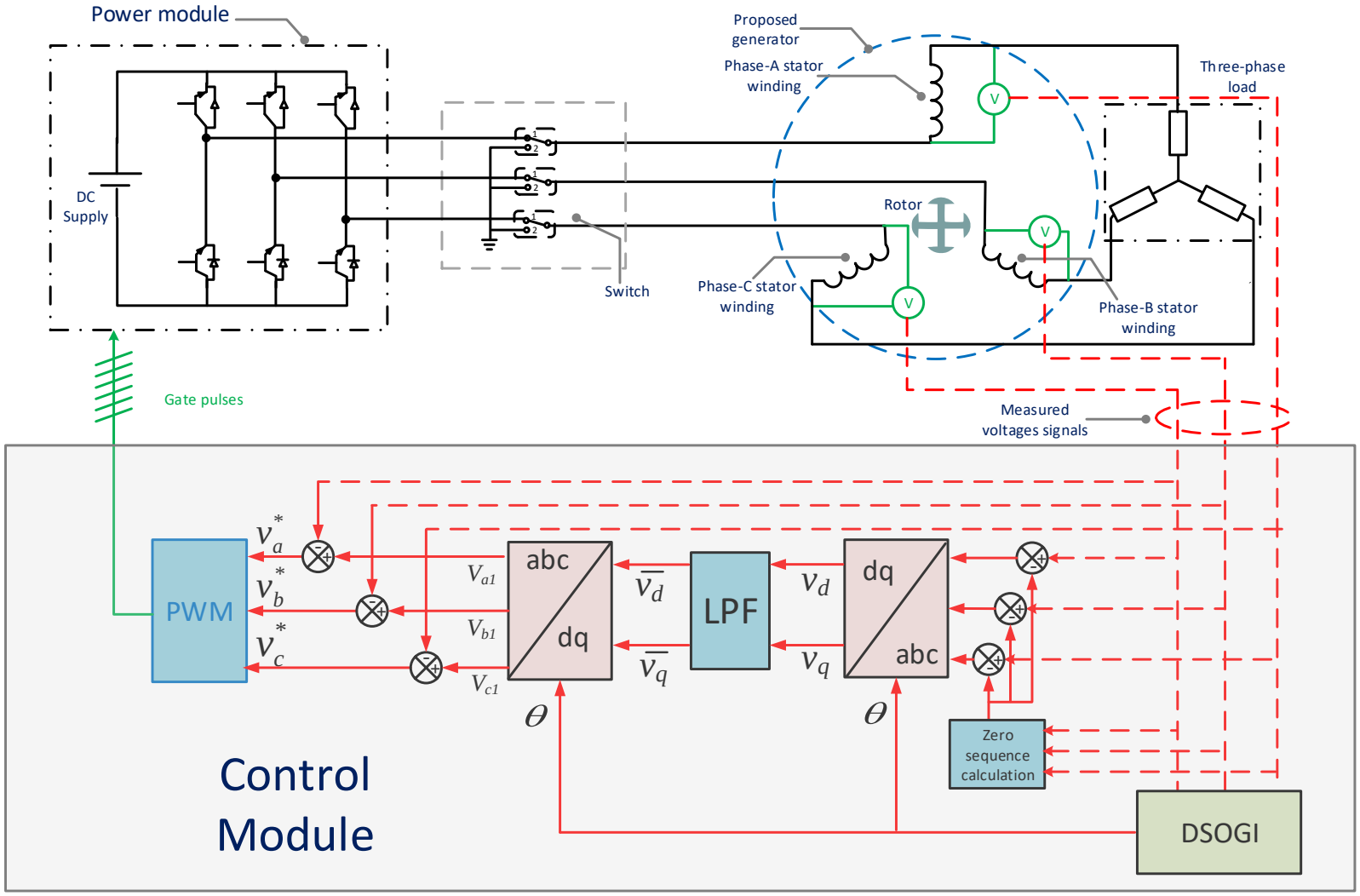


Figure 4-11 Block diagram showing control method of the series ASF

The simulation were done for two different types of loads, linear load and nonlinear load during the simulation generator output voltage an current were saved and analysed. The following two section a detailed discussion about the simulation for both kind of loads.

4.3.2 Output Power Quality Improvements of Synchronous Generator with Linear Load

A linear resistive load connected to the proposed generator, the load was (35 kW and nominal phase to phase voltage 415 V). To simplify the simulation, the active series filter was implemented by three controlled voltage sources fed by the reference voltage in all active series filter simulations.

4.3.2.1 Compensation Procedure:

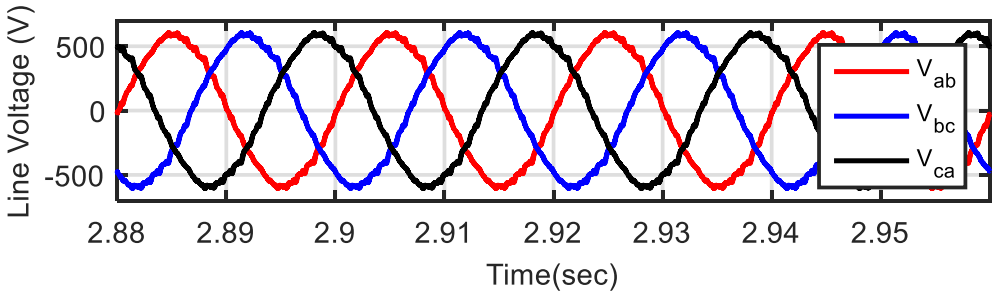
The simulation was started with no series active filter, at t=3.0 sec, the series active filter switched ON and connected in series with the generator windings. The simulation results are shown in Figure 4-12.

As can be seen from the figure the series active filter switched ON improved the output voltage (regulated the output voltage and compensate its harmonics) of the proposed generator and because the connected load is linear the output current of the generator also improved. The THD in the proposed generator voltages dropped from 2% to 0.3%.

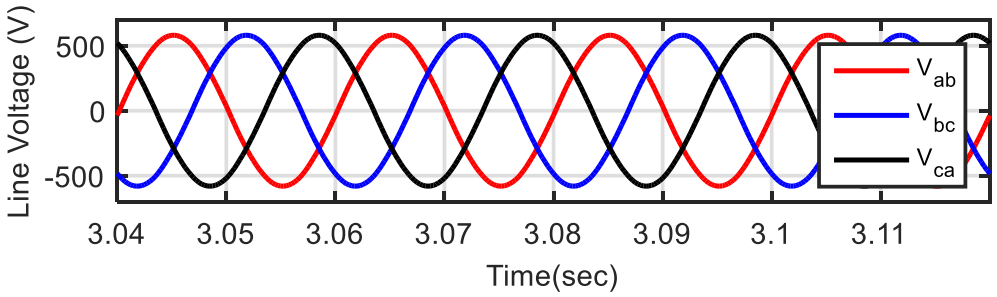
As a linear load is connect to the generator, the THD has a low value (2%), Although, this small value of the THD sees a further reduction by about 1.7% after connecting the ASF, as can be noted in Table 4-3.

Table 4-3 The Total Harmonic Distortion (THD) in the output voltage of the proposed generator feeding linear load

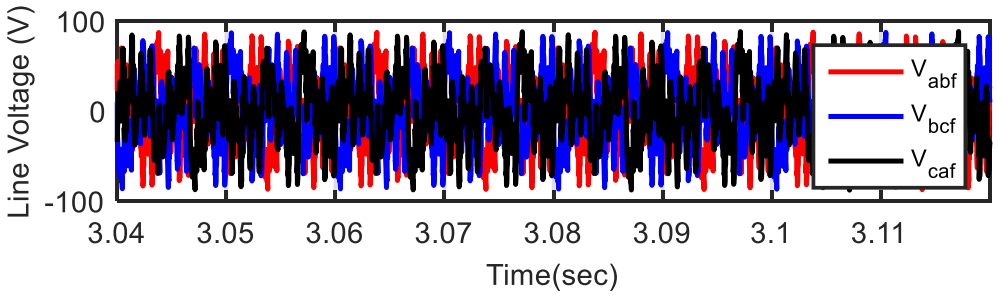
	Without ASF	With ASF
THD%	2%	0.3%



(a) Generator Line voltage Feeding Linear Load without the ASF



(b) Generator Line Voltage Feeding Linear Load with the ASF



(c) The Injected/Compensating Voltage Produsedby the ASF

Figure 4-12 The Proposed Generator Output Voltage with and without Active Series Filter feeding Linear Load

4.3.3 Output Power Quality Improvements of Synchronous Generator with Nonlinear Load

In this simulation a nonlinear load (three phase diode bridge rectifier with RL load, R=6 Ω , L=15 mH). The simulation started with unloaded generator scenario to capture the back EMF harmonic distortion. Then, at t=3 the nonlinear has been connected to the generator. At time t=6 sec the active series filter was connected to in series with the generator windings to compensate both back EMF harmonics and nonlinear load harmonics.

4.3.3.1 Compensation Procedure:

The operating principle of the compensation method is the as presented in the subsection 4.3.2.1

The simulation result is shown in Figure 4-13. As can be seen from the figure, connecting the nonlinear load to the generator, the harmonic content of the voltage waveforms is higher than those of the unloaded generator as shown in Figure 4-13 (a) and (b). The series active filter has improved the output voltage of the proposed synchronous generator, as shown in Figure 4-13 (c). The THD in the output voltage of the proposed generator dramatically decreased from 30.2% to 4.8%.

From the simulation results, the series active filter has improved the output power quality (current and voltage waveforms in the same time) of the proposed generator in case of linear load was connected to the generator. However in case on nonlinear load the series active filter just compensate the harmonic in the generator voltages.

The THD in the generator running without connecting the load has a low value (5.3%), as reported in Table 4-4. This is due to the

generator design (space/spatial harmonics). Connecting the non-linear load adds more harmonics (time harmonics) due to the high harmonic content of the current, and this increases the THD to 30.2%. The ASF significantly reduced the THD from 30.2% to 4.8% after connected it to the generator.

Table 4-4 The Total Harmonic Distortion (THD) in the output voltage in the proposed generator feeding non-linear load for different operation condition

	Without ASF		**With ASF**
	Unloaded generator	Loaded generator	Loaded generator
THD	5.3%	30.2%	4.8 %

From table 4-3 and table 4-4, it can be noted that the THD of unloaded generator (5.3%) is higher than that of the loaded generator (2%). This is because the THD has inverse relationship with the generator loading.

Furthermore, several simulations have been done in my model for different values of the resistive load, and these values was percentage from the original value for the loaded generator (R=4.92Ω) and THD has been calculated in each simulation and reported in the following table

Table 4-5 The THD of the output voltage of the proposed generator for different values of loading

Load value (Ω)	THD%	Notes
4.92*0.1	**1.25%**	
4.92	**2%**	The case study for loaded generator
4.92*50	**4.7%**	
4.92*100	**5%**	
4.92*1000	**5.3%**	Very high load represent (open circuit). The case study for unloaded generator

As can be seen from the table the THD in the loaded generator (R=4.92Ω) output voltage was 2% and this value increase to 5.3% in the unloaded generator.

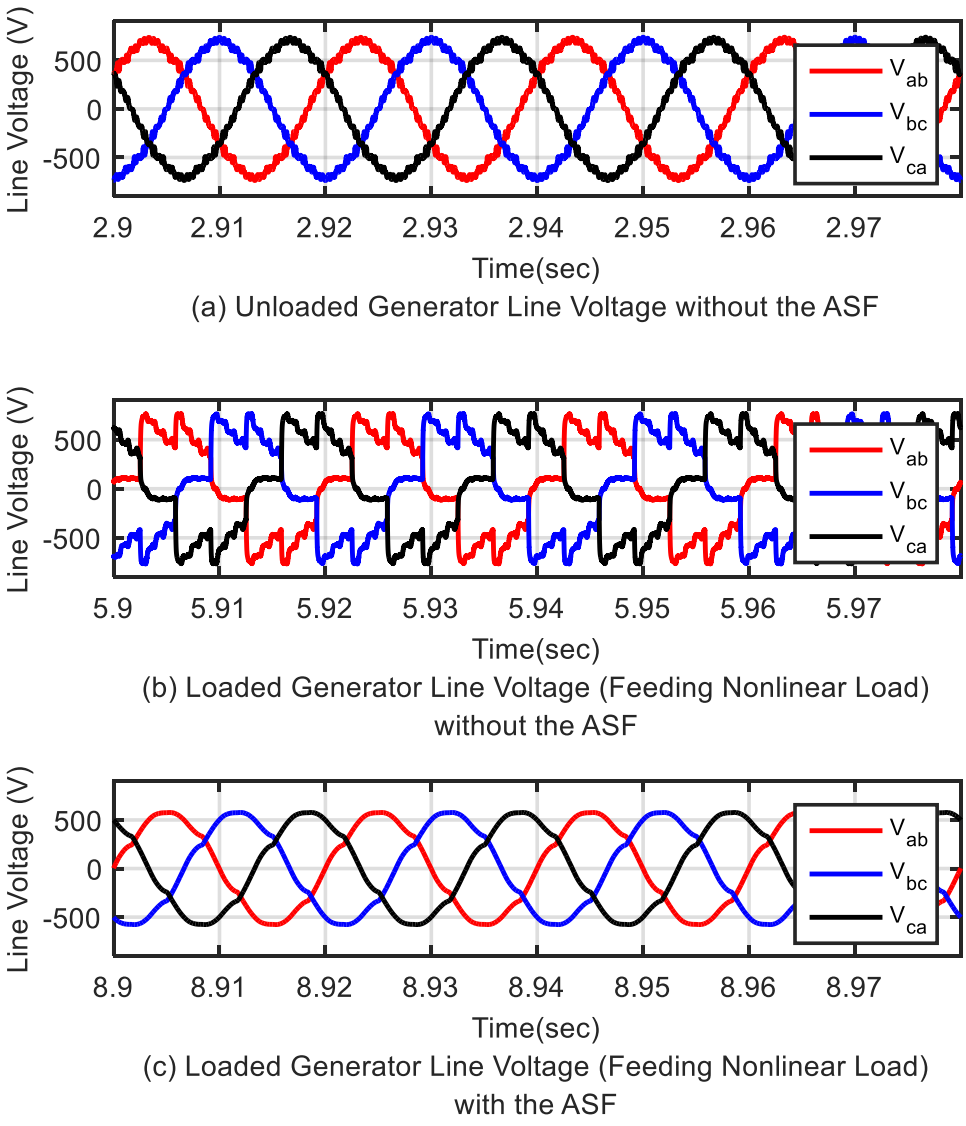


Figure 4-13 The Proposed Generator Output Voltage with Active Series Filter feeding Nonlinear Load

Therefore, to improve the output power quality of the proposed generator, the two proposed filters (shunt and series) must be connected with the proposed generator at the same time and work together to improve the output power quality of the proposed generator.

4.4 The Proposed Generator with Shunt and Series Active Filters Simulation:

The effect of adding active power filters to the proposed generator has been presented in the previous two section. Where in section 4.2, the shunt active power filter was discussed, and the simulation results showed that the shunt filter improved the output current more than the output voltages especially in nonlinear load. While in section 4.3 the active series filter was introduced, and the simulation results showed that the active series filter improved the output voltage and of the proposed generator, however in nonlinear load did not improved the generator current. So the both filters should be operated at the same time with proposed generator to improve the output power quality of this generator.

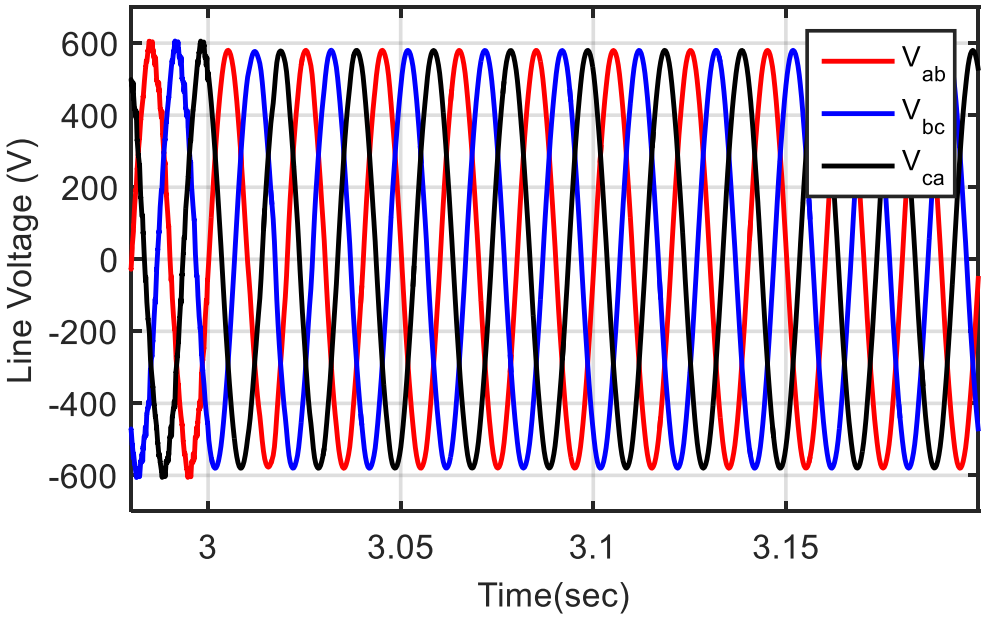
This section will present the effect of both filters connected to the proposed generator at same time as shown in Figure 4-1.

4.4.1 Output Power Quality Improvements of the proposed Generator with Linear Load

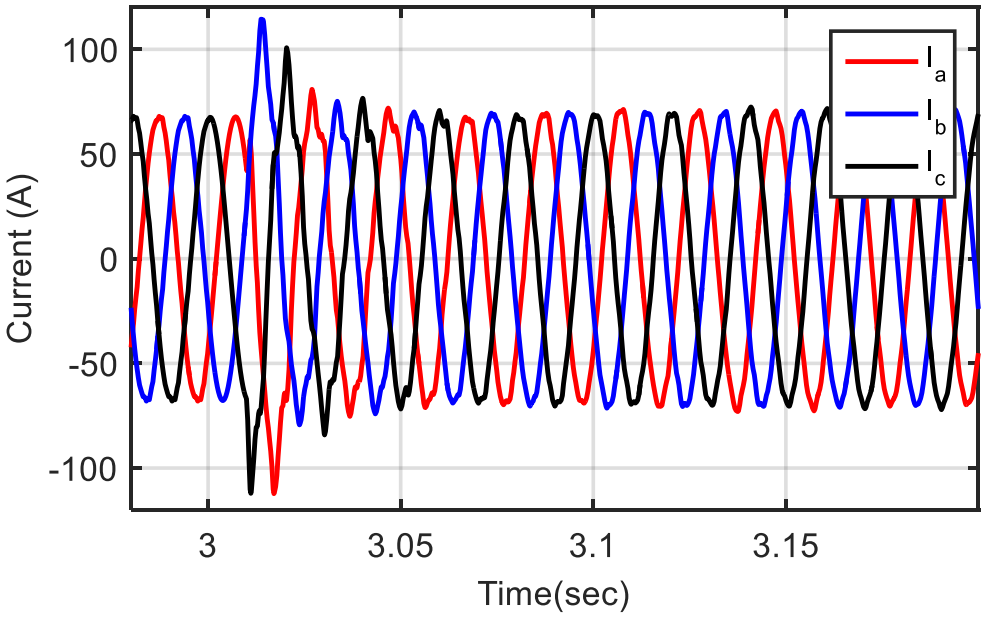
In addition to the simulation in section 0 a shunt active filter was connected to the system between the generator and the load, at simulation time t=3sec the both filter switched ON. And the result was saved and analysed.

4.4.1.1 Compensation Procedure:

For the series active filter the procedure was as described in section 4.3.2.1, for the shunt active filter the procedure was as described in section 4.2.2.1. The simulation results shown in Figure 4-14



(a)Generator Line voltage for Linear Load before and after Switching ON both Filters



(b)Generator Current for Linear Load before and after Switching ON both Filters

Figure 4-14 The Proposed Generator Output Voltage and Output current with both Filters for Linear Load

As showed in the figure the harmonic distortion in the output voltage of the proposed generator was decreased and the output current slightly improved. The THD in the generator voltage was decreased from 3% to 0.6% while the THD in the output current of the proposed generator dropped from 2% to 1.7%.

As can noticed the in case of linear load, just series active filter has improved the output power quality of the proposed generator better than when there are the filter connected because the effect of the shunt filter.

4.4.2 Output Power Quality Improvements of the proposed Generator with Nonlinear Load

In addition to the simulation in section 4.3.3 a shunt active filter was connected to the system between the generator and the load, at simulation time t=3sec the both filter switched ON. And the result was saved and analysed

4.4.2.1 Compensation Procedure:

The operating principle of the compensation method is the as presented in the subsection 4.4.1.1

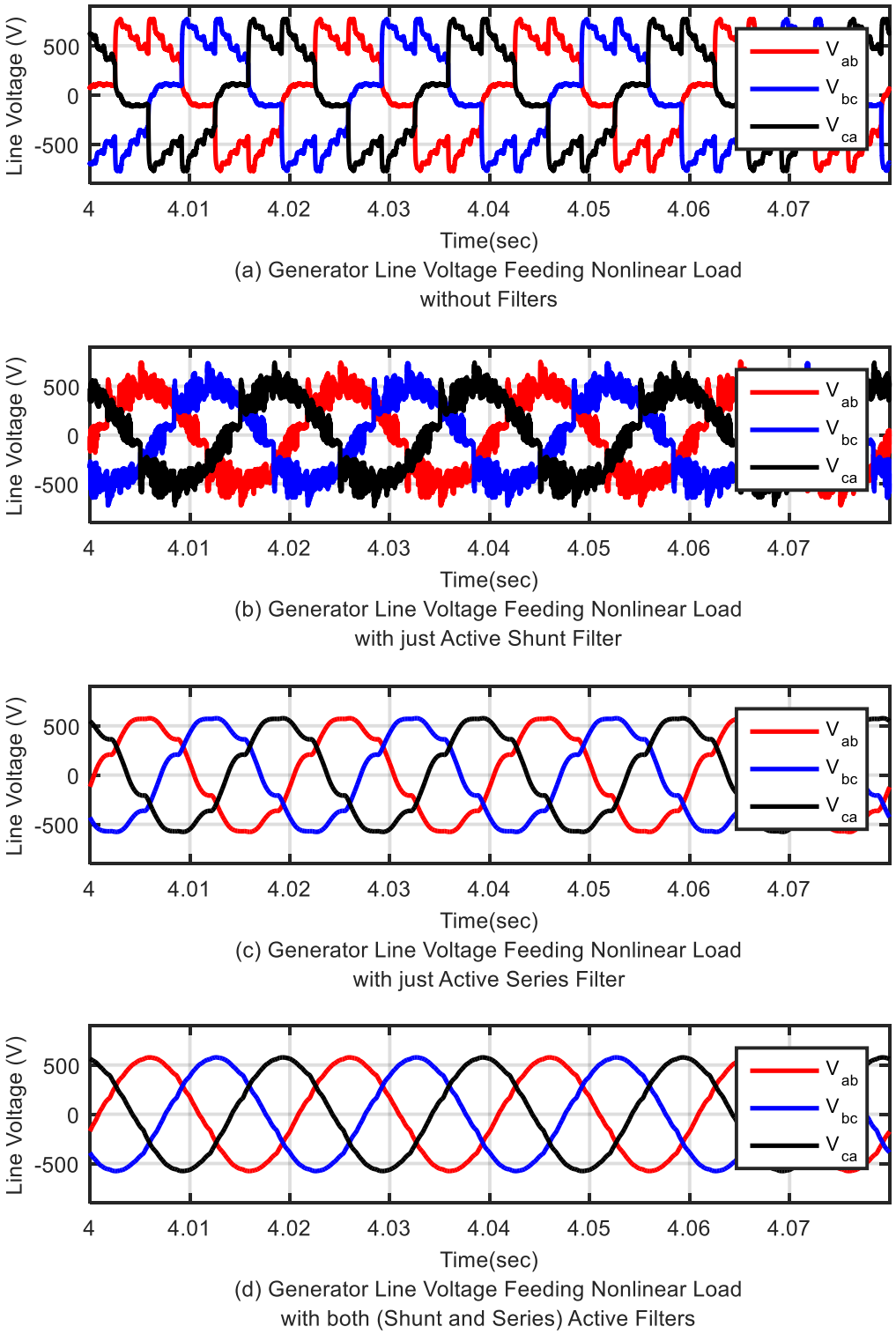
The simulation result is shown in Figure 4-15. As can be seen from the figure the both filters have improved the output voltage and the output current of the proposed synchronous generator. The THD in the output voltage of the proposed generator dramatically decreased from 30.2% to just about 2%.

Compared to section 4.3.3 where was just series active filter was used, when the shunt active filter was added the system, the output power quality of the proposed generator has dramatically improved.

It can be noted that the THD of the proposed generator voltage without connecting any active filter has a significant value (30.2%). From Table 4-6, it can be noted that the active series filter is more effective than the shunt active filter in reducing the THD of the generator winding voltage. Combining both active series and shunt filters together yields a further reduction in the THD of the generator winding voltage which reaches 2%, as reported in Table 4-6.

Table 4-6 The Total Harmonic Distortion (THD) in the output voltage in the proposed generator feeding non-linear load for different Connected filters

	Without Active Filter	**With Active Filter**		
		Shunt	Series	Both (Shunt + Series)
THD	30.2%	21.7%	4.8%	2 %



(a) Generator Line Voltage Feeding Nonlinear Load without Filters

(b) Generator Line Voltage Feeding Nonlinear Load with just Active Shunt Filter

(c) Generator Line Voltage Feeding Nonlinear Load with just Active Series Filter

(d) Generator Line Voltage Feeding Nonlinear Load with both (Shunt and Series) Active Filters

Figure 4-15 The Proposed Generator Output Voltage with both Filters feeding Nonlinear Load

4.5 **Conclusion**

The effect of using an active power filters to compensate for the poor harmonic output of a simplified synchronous generator has been investigated. The simulation results show that the APFs can be integrated with a simplified synchronous generator to provide an acceptable level of power quality (voltage and current) from a simple generator with a poor quality output waveform at the point of common coupling (PCC) for any kind of loads.

This chapter presented the simulation for both active filters. For the shunt active power filter alone, balanced linear load, the THD in the load after enabling the shunt APF was 2.1% while without the shunt APF it was 4.5% as show in Figure 4-3 . In the second case, balanced nonlinear load, the shunt APF supplied the nonlinear load harmonics and reduced the THD in the generator current from 22.3% before enabling the shunt APF and to 3.43% after enabling it as shown in Figure 4-5. Finally in the third case, unbalanced nonlinear load and this is done for the two types of unbalance loading, type-1 and type-2, in type-1 the shunt APF decreased the THD in the generator current from 20.1% to 3.8% (in phase-c) by supplying the nonlinear load harmonics, and balanced the generator currents as shown in Figure 4-7 and Table 4-1. In type-2 The THD was significantly improved, as can be seen from Figure 4-9 and Table 4-2, the shunt APF decreased THD in the generator current from 22.3% to 3.65% and supplied the single-phase load, in addition, it maintained the proposed generator currents balanced. For series active filter, in balanced linear load, the THD

In addition, when the just series active filter was connected, in case of linear load, the THD in the proposed generator voltage and current decreased to 0.6% and 1.7% respectively. In the second

case, nonlinear load, the THD in the proposed generator voltage and current decreased to 2% and 3.5% respectively.

Finally, the simulation results were presented in this chapter showed that the active power filter can be used with simplified synchronous generator to improve the output power quality of the generator and balance the generator current for different kind of loads.

Chapter-5 Dynamics performance Improvements of Synchronous Generator without Damper bars

Chapter-5 Dynamics Performance Improvements of Synchronous Generator without Damper Bars

This chapter studies the dynamic effect of the APF on synchronous generator without damper. The APF is used to improve the dynamic response of a synchronous generator without damper bars when there is a sudden change in the generator loading. The chapter started with an introduction about the damper bars and their function in section 5.1. Section 5.2 studies the dynamic performance of synchronous generators with and without damper bars. Section 5.3 discusses the proposed control approach of APF for Dynamic performance Improvements of Synchronous Generator and section 5.4 presents simulation procedure and results. Finally, the conclusion of this chapter is given in section 5.5.

5.1 Introduction

In the transient condition the current induced in the damper bars helps the generator to reach a steady state faster. When there is a sudden change in SG load, the SG speed will drift from the synchronous speed. This change in synchronous speed induces currents in the damper bar circuit and these currents produce torque, which acts to drive the rotor towards synchronous speed. When the SG does not have damper bars, sudden changes in load will cause more fluctuation in SG speed and load angle and can potentially lead to SG desynchronization with the grid and pullout of the system. To maintain a generator without damper bars stability, an active power filter is proposed to improve the dynamic stability of this generator and decrease speed fluctuation during a sudden change in the generator loading.

5.2 Study of Dynamic Performance of Synchronous Generator with and without Damper Bars

When there is a step change in generator loading, the rotor of the generator will accelerate or deaccelerate with respect to the synchronous rotating magnetic field, and relative motion will appear between them. This relative motion can be described by the swing equation. The following two subsections presented this equation in the two cases, with and without damper bars.

5.2.1 Swing Equation without Damper Torque:

When the damping and frictional torque are neglected, the electromechanical system equation in the synchronous machine during the disturbance is given by equation (5-1) [38, 94].

$$T_m - T_e = J \times \frac{d^2\theta_m}{dt^2} \tag{5-1}$$

Where T_m is the mechanical torque in N.m, T_e is the electrical torque in N.m, J is the total moment of inertia of the generator and the prime mover in kgm^2 and θ_m is the angular displacement of the rotor to stationary reference axis on the stator in rad/sec.

It is more convenient to use the torque angle (δ_m), which is the angle between the rotor position and the synchronous rotating reference frame rotating with angular constant velocity ω_{ms} , and it is given by equation (5-2)

$$\theta_m = \delta_m + \omega_{sm}t \tag{5-2}$$

$$\omega_m = \frac{d\theta_m}{dt} = \frac{d\delta_m}{dt} + \omega_{ms} \tag{5-3}$$

$$\frac{d^2\theta_m}{dt^2} = \frac{d^2\delta_m}{dt^2} \quad (5\text{-}4)$$

Equation (5-1) can be written as function of $\delta_m$as presented in equation (5-4)

$$T_m - T_e = J \times \frac{d^2\delta_m}{dt^2} \quad (5\text{-}5)$$

By multiplying equation (5-5) by rotor mechanical speed ω_m (rad/sec) the following equations are extracted

$$\omega_m T_m - \omega_m T_e = J\omega_m \times \frac{d^2\delta_m}{dt^2} \quad (5\text{-}6)$$

$$P_m - P_e = J\omega_m \times \frac{d^2\delta_m}{dt^2} \quad (5\text{-}7)$$

$$P_m - P_e = M \times \frac{d^2\delta_m}{dt^2} \quad (5\text{-}8)$$

Where M is called the inertia constant. The kinetic energy of the synchronous generator rotor and the prime mover W_k is given by:

$$W_k = \frac{1}{2}J\omega_m^2 = \frac{1}{2}M\omega_m \quad (5\text{-}9)$$

$$M = \frac{2W_k}{\omega_m} \quad (5\text{-}10)$$

Despite M being called the inertia constant, in fact, when the rotor speed diverges from the synchronous speed it is not constant. However, because the change in ω_m is small before the generator became unstable,

M is calculated at synchronous speed and assumed to be constant and equation (5-10) become

$$M = \frac{2W_k}{\omega_{sm}} \tag{5-11}$$

To express the swing equation in in terms of electrical power angle (δ), equation (5-12) is used.

$$\delta = \frac{P}{2}\delta_m \tag{5-12}$$

$$\omega_e = \frac{P}{2}\omega_m \tag{5-13}$$

Where P is the number of poles of a synchronous generator.

The swing equation in equation (5-8) becomes

$$P_m - P_e = \frac{2}{P}M \times \frac{d^2\delta}{dt^2} \tag{5-14}$$

To convert equation (5-14) to per unit system, it is divided by the base power in MVA (S_B).

$$\frac{P_m}{S_B} - \frac{P_e}{S_B} = \frac{2}{P}\frac{2W_k}{\omega_{sm}S_B} \times \frac{d^2\delta}{dt^2} \tag{5-15}$$

The H constant (per unit inertia constant) is given be equation (5-16) and it is unit in second.

$$H = \frac{Kinetic\ energy\ in\ MJ\ at\ rated\ speed}{machine\ rating\ in\ MVA} = \frac{W_k}{S_B} \tag{5-16}$$

By using the value of H in equation (5-16) and substituting it equation (5-15) yields,

$$P_M - P_E = \frac{2}{P}\frac{2H}{\omega_{sm}} \times \frac{d^2\delta}{dt^2} \quad (5\text{-}17)$$

Where P_M is the mechanical power in per unit and P_E is the electrical power in per unit. The electrical angular velocity (ω_s) and the relation between it and the mechanical velocity (ω_{sm}) depends on generator pole numbers, and it is given be equation (5-18)

$$\omega_{sm} = \frac{2}{P}\omega_s \quad (5\text{-}18)$$

The equation (5-17) can be written as function of the electric angular velocity (ω_s) by using the relation in equation (5-18) as follows:

$$P_M - P_E = \frac{2H}{\omega_s} \times \frac{d^2\delta}{dt^2} \quad (5\text{-}19)$$

The swing equation is often expressed in terms of fundamental frequency (f_0) where ($\omega_s = 2\pi f_0$). The swing equation, when the electrical power angle (δ) in electrical radian, is given by:

$$P_M - P_E = \frac{H}{\pi f_0} \times \frac{d^2\delta}{dt^2} \quad (5\text{-}20)$$

And the swing equation when the electrical power angle (δ) in electrical degree is given by:

$$P_M - P_E = \frac{H}{180 f_0} \times \frac{d^2\delta}{dt^2} \quad (5\text{-}21)$$

5.2.2 Swing Equation with Damper Torque:

Now let us assume the damping torque in not neglected but the frictional torque is neglected. The damper torque which produced by the

damper bars is proportional to the speed difference between the rotor and the rotating magnetic field and is given by [5].

$$T_d = k_d \Delta\omega \tag{5-22}$$

Where k_d is the constant of proportionality in Nm/rad/s, and $\Delta\omega$ is the rotor speed deviation from synchronous speed and given by:

$$\Delta\omega = \omega_m - \omega_{sm} \tag{5-23}$$

$$T_d = k_d(\omega_m - \omega_{sm}) \tag{5-24}$$

$$T_d = k_d\left(\frac{d\theta_m}{dt} - \omega_{sm}\right) \tag{5-25}$$

By substituting equation (5-2) in equation (5-25) yields:

$$T_d = k_d\left(\frac{d(\delta_m + \omega_{sm}t)}{dt} - \omega_{sm}\right) \tag{5-26}$$

$$T_d = k_d\frac{d\delta_m}{dt} \tag{5-27}$$

The damping torque in terms of electrical torque angle (δ) is given using equation (5-12)

$$T_d = \frac{2k_d}{P}\frac{d\delta}{dt} \tag{5-28}$$

By multiplying equation (5-28) with (ω_m) and dividing by the base power in MVA (S_B) yields:

$$P_D = D\frac{d\delta}{dt} \tag{5-29}$$

Where P_D is the damping power in per unit and D is the damping coefficient and equal:

$$D = \frac{2\omega_m k_d}{PS_B} \tag{5-30}$$

Then the swing equation with damper bar included in electrical radian is given by:

$$P_M - P_E = \frac{H}{\pi f_0} \times \frac{d^2\delta}{dt^2} + D\frac{d\delta}{dt} \tag{5-31}$$

And when the electrical power angle (δ) in electrical degree the swing equation can be expressed as in equation (5-32)

$$P_M - P_E = \frac{H}{180 f_0} \times \frac{d^2\delta}{dt^2} + D\frac{d\delta}{dt} \tag{5-32}$$

5.3 Proposed Control Approach of APF for Dynamic Performance Improvements of Synchronous Generator

The proposed scheme, which is similar to VSG and *synchronverters,* based on sharing the power between the synchronous generator and the APF for short time interval during step load changing. To decrease the effect of sudden load changes on a SG without damper bars, the active power filter (APF) is used with the SG to compensate for the load step by introducing a compensatory filter step current that increase/decays gradually to allow the generator smoothly to go to the new operating point, as shown in Figure 5-1.

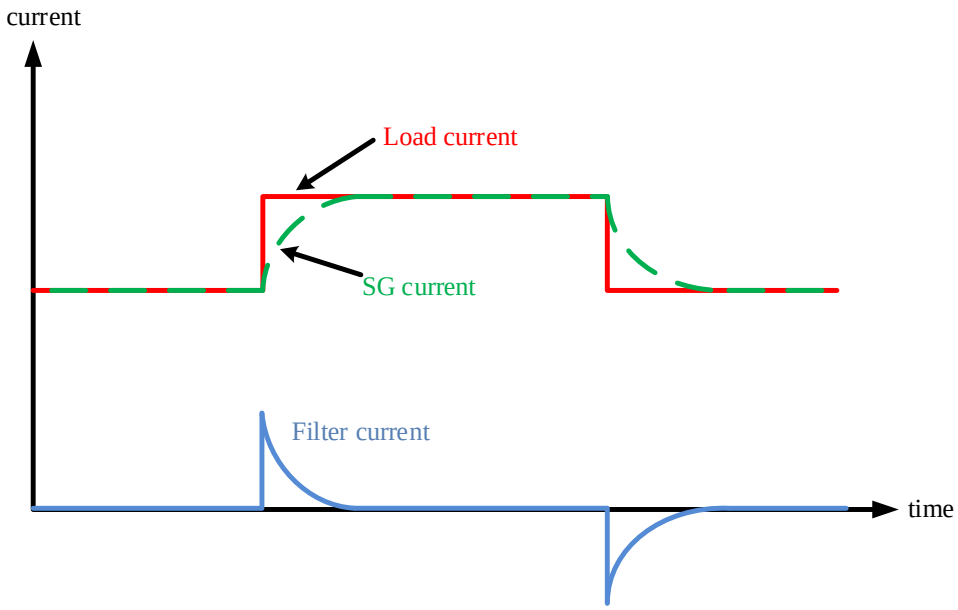


Figure 5-1 Proposed filter, load, and generator currents during a step load change for the generator without damper bars and APF

As can be seen from Figure 5-1, when the load is connected to the generator, the APF will supply the transient current component leaving the SG current and the electromagnetic torque to increase gradually, and when the generator load becomes equal to load current, the APF current drops to zero. On the other hand, when the load is disconnected, the APF will absorb the transient generator current component allowing the generator current and the electromagnetic torque to decrease gradually until it equals the load current.

5.4 **Simulation Procedure and Results**

To study the dynamic performance of the synchronous generator during load step change, a Matlab/Simulink model was built. The consists of the synchronous generator model, that was developed in Chapter-2, APF model, that was discussed in Chapter-3, and two three-phase resistive

loads, the second load can be connected or disconnected by a circuit breaker during the simulation. Figure 5-2 shows the block diagram of the simulated model.

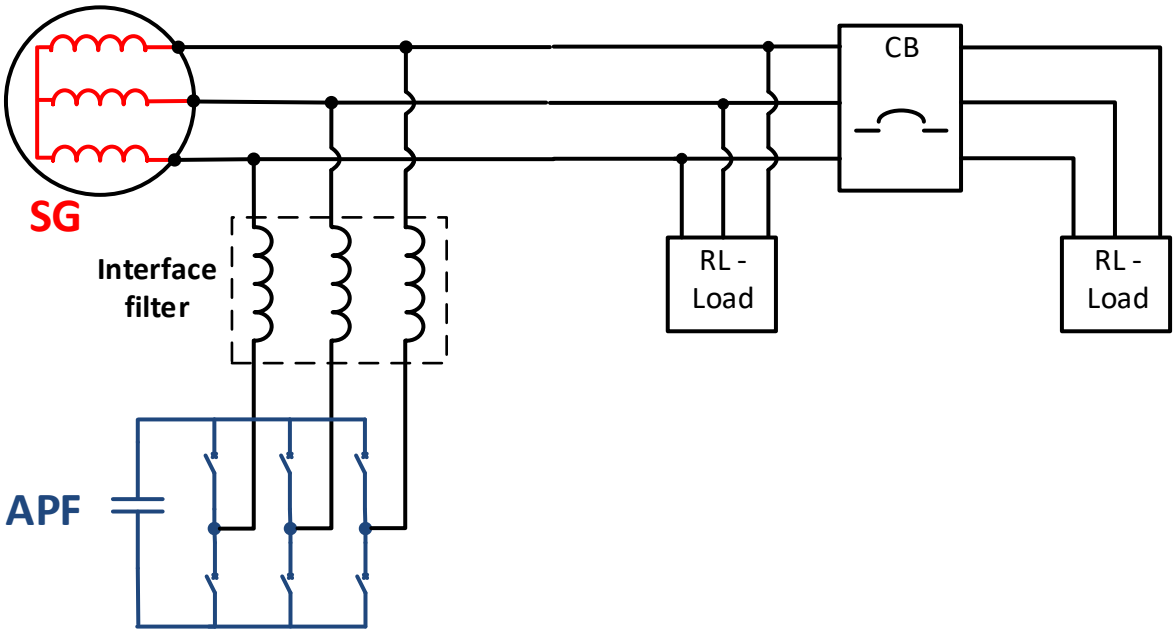


Figure 5-2 Block diagram of the proposed system

Due to load change and to see the effect of adding an APF on the generator speed a speed controller model and exciter model was added in the simulation circuit to keep the generator speed and generator voltage constant after the load changing. A description for speed controller and exciter is presented in the following subsections.

5.4.1 Speed Controller and Diesel Engine Dynamic model

When considering transient behaviour and damping, a model of the mechanical system driving the generator is required. The speed loop controller consists of a regulator, diesel engine transfer function (throttle actuator and engine delay)

Figure 5-3 shows the block diagram of the speed controller. A throttle actuator and engine delay represent the dynamic model of the diesel engine [95].

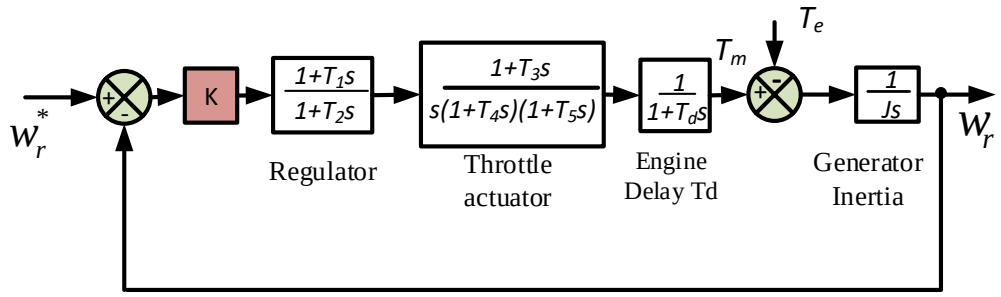


Figure 5-3 Block Diagram of Speed Controller

The time constant and their values scaled values that taken from Matlab demo library and their values were given in Table 5-1

Table 5-1 Speed controller time constants and their values

Parameters	Description	Value in simulation
T_1 and T_2	regulator time constants	0.15 and 0.3 (ms)
T_3, , T_4 and T_5	throttle actuator time constants	3.75, 0.135 and 0.576 (ms)
T_d	Engine delay time constant	0.36 (ms)
J	Generator inertia	0.45 kg.m^2

5.4.2 Exciter Model

To maintain the output voltage of the generator constant after generator load changing, an exciter model (IEEE type-1) which is defined

by IEEE [96, 97], was used to maintain the output voltage constant during load changes. Figure 5-4 shows the IEEE excitation system.

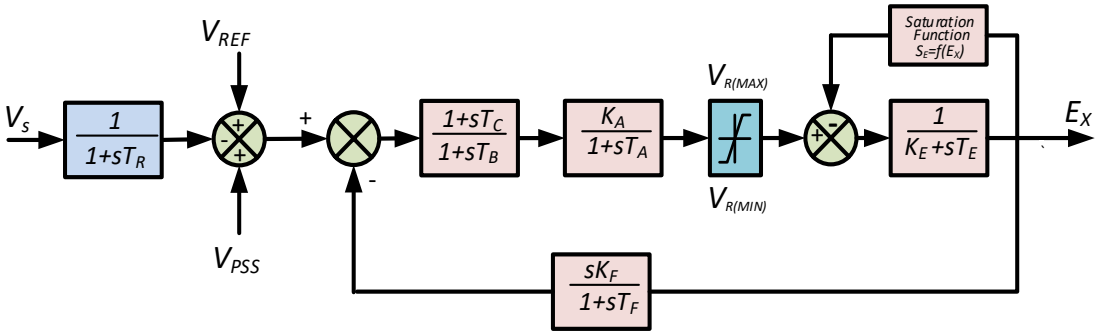


Figure 5-4 IEEE Type 1 (Type DC1A) excitation system

The typical values of IEEE Type 1 exciter is given in Table 5-2[38]

Table 5-2 Typical per unit data for an IEEE Type 1 DC exciter

$\boldsymbol{K_A = 187}$	$\boldsymbol{T_A = 0.89}$	$\boldsymbol{K_E = 1.0}$	$\boldsymbol{T_E = 1.15\ s}$
$\boldsymbol{K_F = 0.058}$	$T_F = 0.62$	$T_B = 0.06$	$T_C = 0.173$
$\boldsymbol{V_{R(\max)} = 1.7}$	$V_{R(\min)} = -1.7$	$T_R = 0.015$	

5.4.3 Simulation Results

To study the effect of the APF a Malab Simulink file was built, with the simulated circuit as shown in Figure 5-2. The simulation circuit consists of a synchronous generator models, the models as developed in section 2.4, active power filter as presented in Chapter-3, and linear RL load (R = 5 , L = 2.5 mH). All the parameter of the speed controller and the excitation system in Figure 5-3 and Figure 5-4 were taken from Matlab demo library as given in Table 5-1.

The simulation period was 6 sec, the generator is started with a RL load (R = 5 Ω , L = 2.5 mH). At time t = 1.5 sec the load was doubled and at time t = 3 sec the load was returned back to the initial value. All the currents and developed electromagnetic torque were recorded and analysed.

When the load was suddenly changed, the APF worked as virtual synchronous generator and shared the load with the synchronous generator, then the share of APF gradually decreased until the load is completely supplied by the generator. This gradually generator loading makes the developed electromagnetic torque in the generator gradually increased and then the speed fluctuation will be small. On the other hand, when the load was suddenly decreased, the APF worked as a load and instantaneously consumed the current deference between the two loads. This loading (the APF) gradually decreased until zero loading, so the generator doesn't see this sudden change, and the developed electromagnetic torque gradually decreased and this gradually change in the developed electromagnetic torque makes the generator speed fluctuation as small as possible.

As can be seen from Figure 5-5, which shows the change in the generator current during a sudden load change, when the APF was disconnected, the full load suddenly connected and disconnected to/from the generators as shown in Figure 5-5 (a). This makes the speed fluctuation as big as possible, however, when the APF was connected, and when the load was changed the generator load gradually increased to the new operating point, and when the load was disconnected, the generator load gradually decreased to the previous operating point as shown in Figure 5-5 (b). This slow change in generator load makes the speed fluctuation as small as possible.

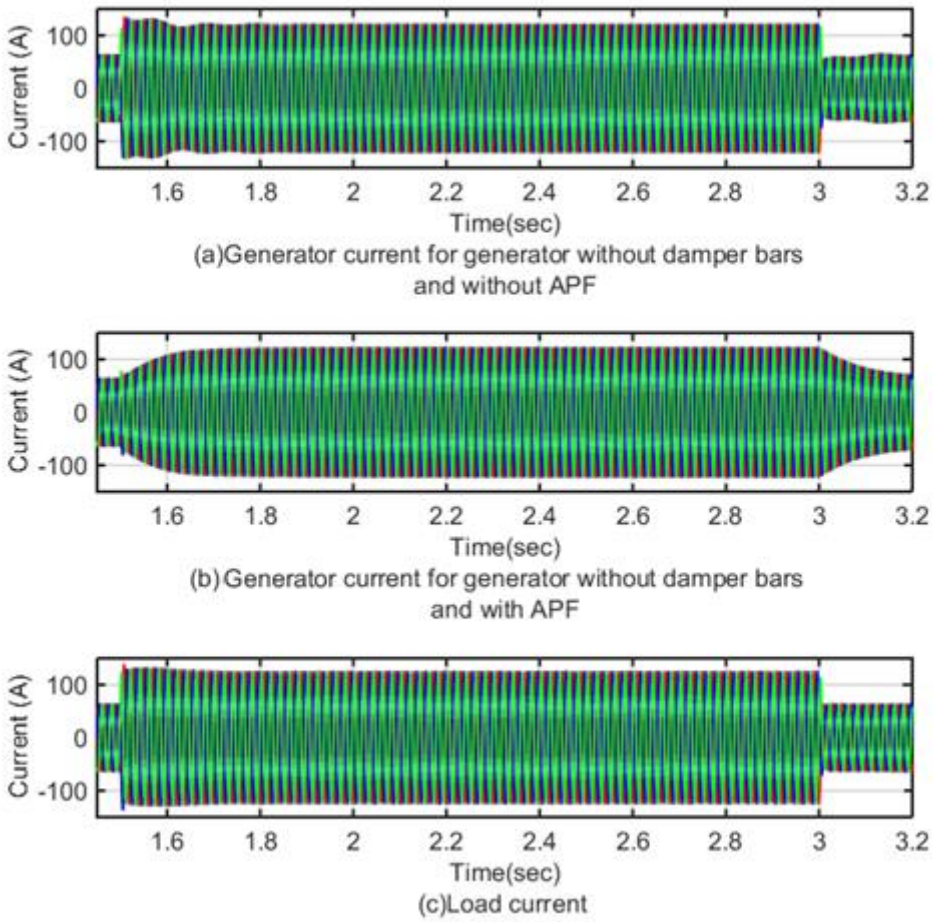


Figure 5-5 Generator current with and without APF during sudden load change

The APF current and power are shown in Figure 5-6, as can be seen from the figure the APF worked as power supply and supply the transient component to the load when the load was connected and worked as a load and absorbed the transient component when the load was disconnected.

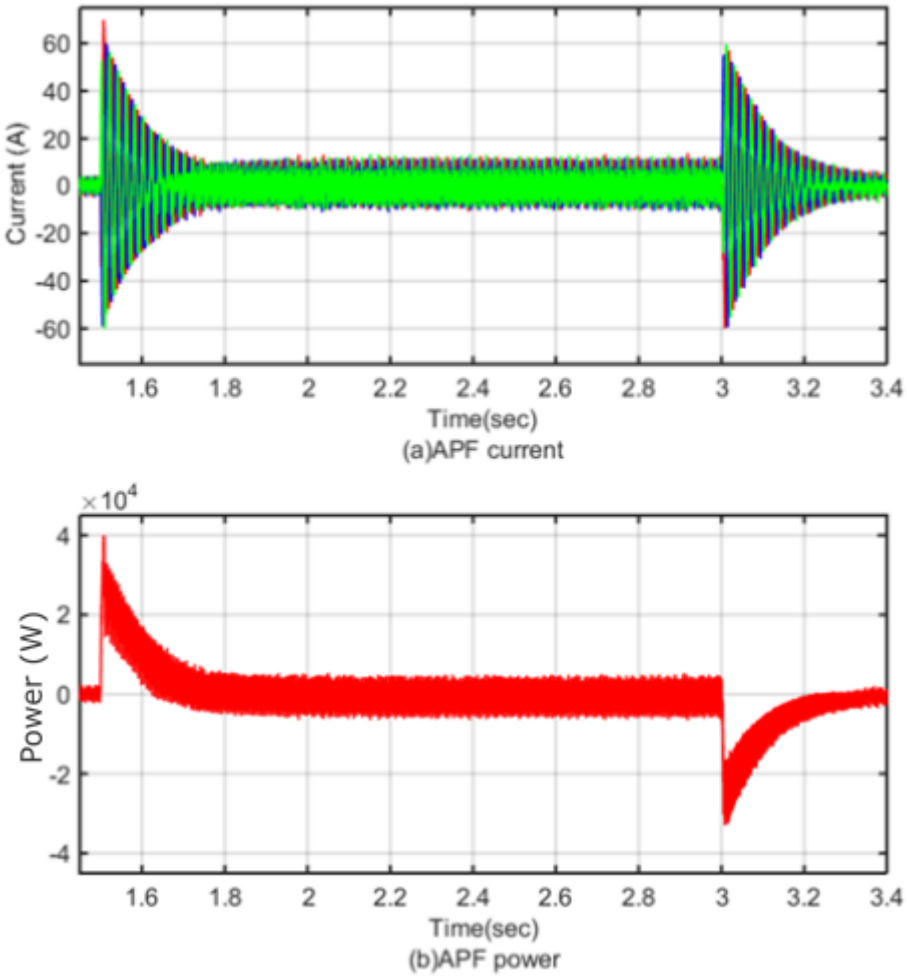


Figure 5-6 APF current and power

Figure 5-7 shows a comparison between the proposed SSG with and without damper bars for speed fluctuation during a sudden change in load as described. As Figure 5-7 shows the disturbance in the generator speed was increased when damper bars were not present (as expected), but when the APF was connected the speed disturbance became much smaller even than that of the SSG with damper bars.

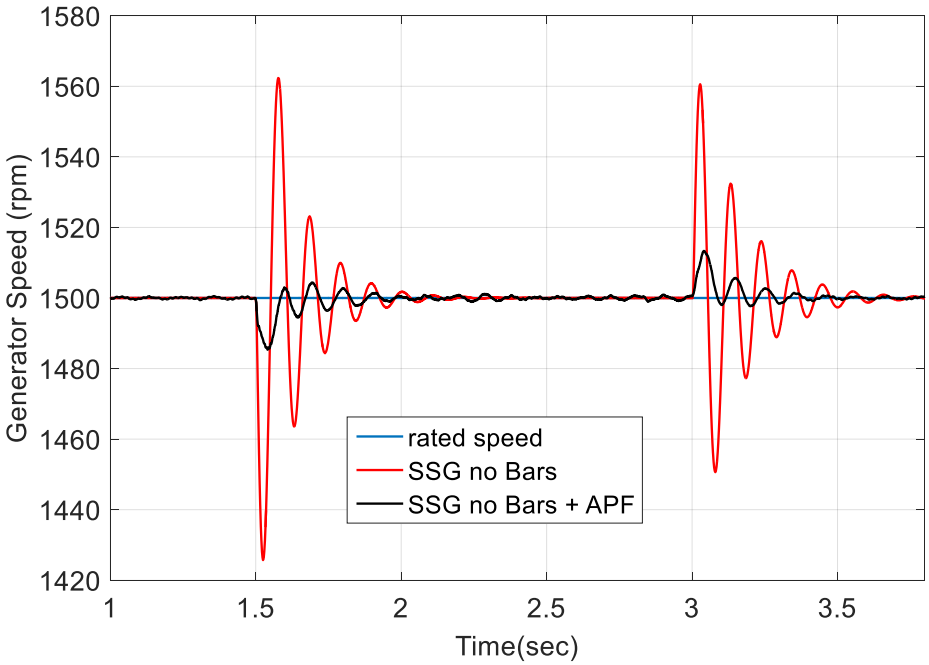


Figure 5-7 Speed response to sudden change in the generator loading with and without APF

In addition, the transient electromagnetic torque was reduced when the APF was connected because the APF supplied the transient component when the load was connected and absorbed the transient component when the load was disconnected, as can be seen from Figure 5-8, giving less generator speed fluctuation with the APF when load steps were applied.

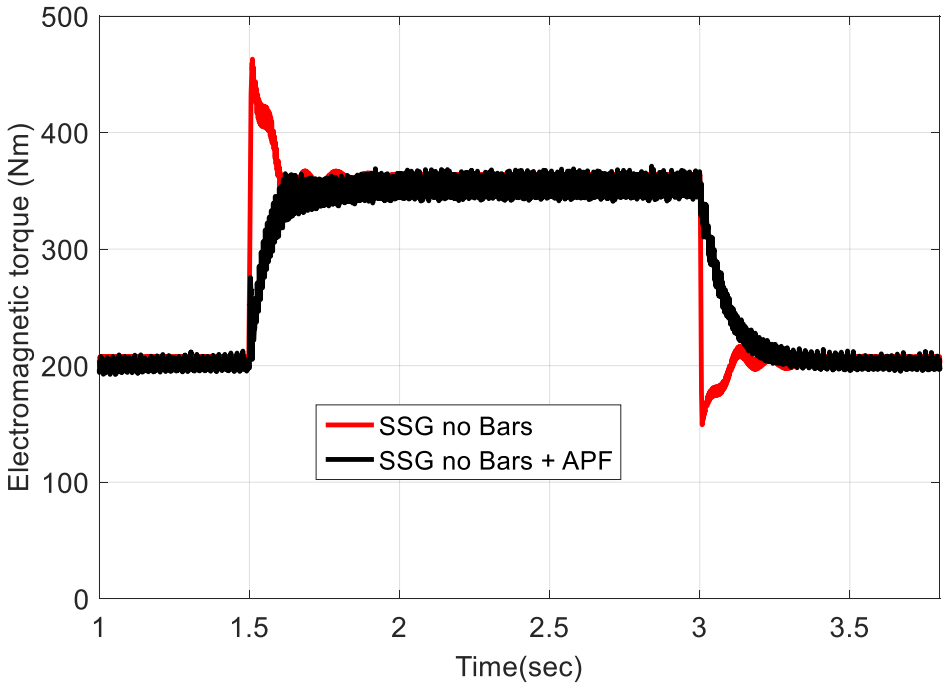


Figure 5-8 Developed electromagnetic torque at sudden change in the generator loading with and without APF

5.5 **Conclusion**

In this chapter, a dynamic study on synchronous generators with and without damper bars is presented. A proposed scheme based APF to improve the dynamic performance of a synchronous generator without damper bars was discussed and the simulation results were presented. The simulation results showed that the APF can be used to improve the transient stability of a synchronous generator without damper bars, giving improved stability compared to systems using damper bars while also allowing for a significant simplification of the rotor design and construction and improving the rotor magnetic circuit.

Chapter-6 Experimental Results

Chapter-6 **Experimental Setup and Experimental Results**

This chapter presents the test rig setup and the experimental validation of using the APF to improve the power quality of simplified synchronous generator. In section 6.1 presents the test rig setup and section 6.2 explains the implantation of the APF in the lab. The interference inductance and DC-link capacitor back is presented in section 6.3. The FPGA/DSP control platform and measurement boards are presented in sections 6.4 and 6.5 respectively and testing the APF is presented in section 6.6. Section 6.7 presents the experimental validation for harmonic compensation for balanced linear. Section 6.8 presents the experimental validation for compensation of balanced nonlinear load harmonic and section 6.9 presents experimental validation for compensation of unbalanced nonlinear load harmonic and balancing the generator current. A comparison between the experimental results and simulation results which presented in Chapter-4 is given in section 6.10. Finally, the conclusion of this chapter is summarised in section 6.11.

6.1 **Test Rig Setup:**

A test rig was built in the lab to approve the simulation results, this test rig consists from a DC motor (as a prime mover), two SKAI module type converters, an interface inductance, a DC-link capacitor bank, an FPGA/DSP control platform and measurement boards as shown in Figure 6-1 and Figure 6-2. A brief description for each part is presented in this section.

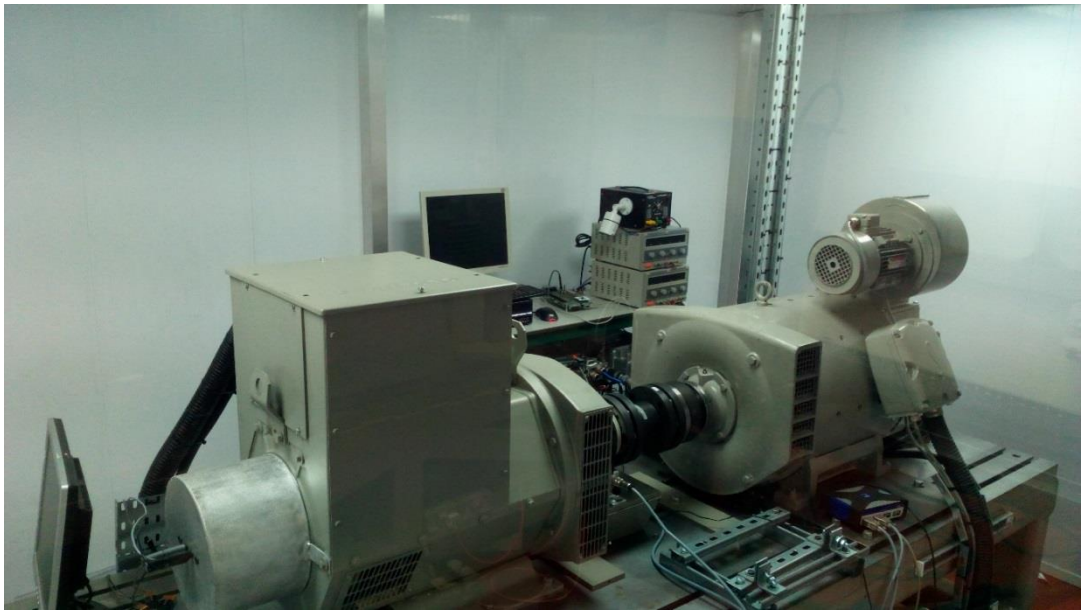


Figure 6-1 The test rig

6.2 **Experimental Active Power Filter Implementation**

To implement the active power filter in the lab, two commercial SKAI modules (three-leg IGBT 2 level converter) designed by Semikron for HEV and EV are used in the test rig to get four-leg inverter as shown in Figure 6-3. The SKAI models that were used in the test are SKAI45A2GD12-W24DI [98] which have a maximum current rating of 300 A each. These two converters are connected in parallel with one DC-link capacitor, where only one leg was used from the second SKAI module

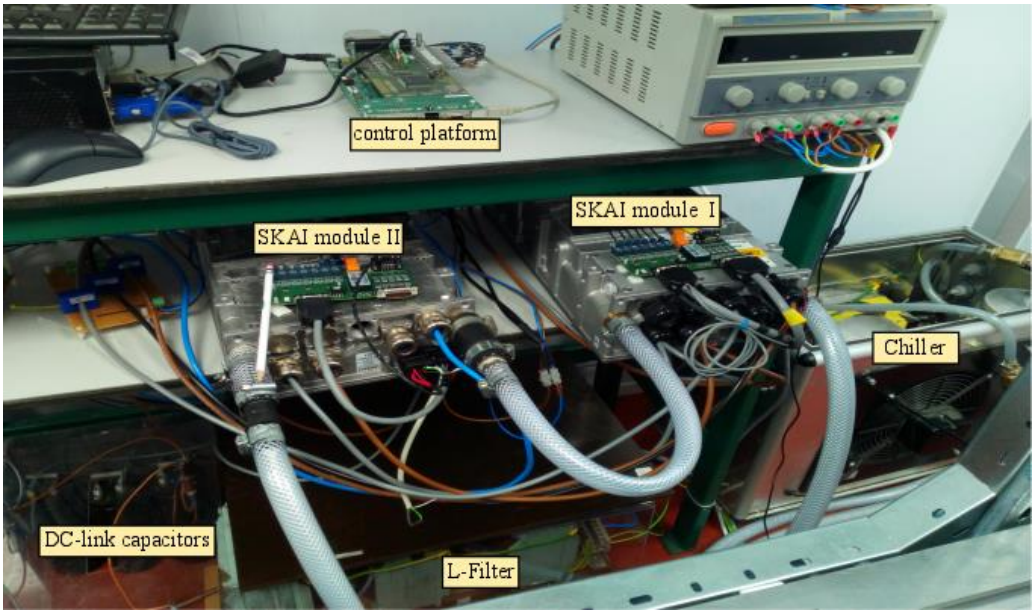


Figure 6-2 The active power filter

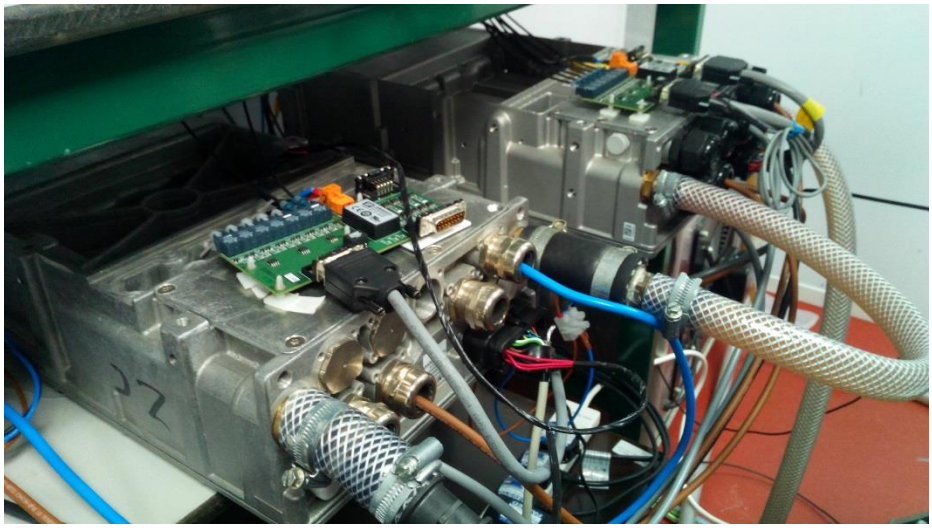


Figure 6-3 SKAI Modules

6.3 **Interface Inductance and DC-link Capacitor Bank.**

Three capacitors are connected in series to make the DC-link, each capacitor was 15132μF, 450VDC. An L-filter of 4.2 mH was used as an

interface between the APF and the PCC point. Figure 6-4 shows a photo for the DC-link capacitor bank and the L-filter.



Figure 6-4 the Capacitor bank and the interface filter

6.4 **FPGA/DSP Control Platform**

The control platform that was used to experimentally implement the active power filer control is FPGA (Field Programmable Gate Array), DSP (Digital Signal Processor) and HPI daughter card (TMS320C6713 DSK HPI Daughter card) as can be seen in Figure 6-5.

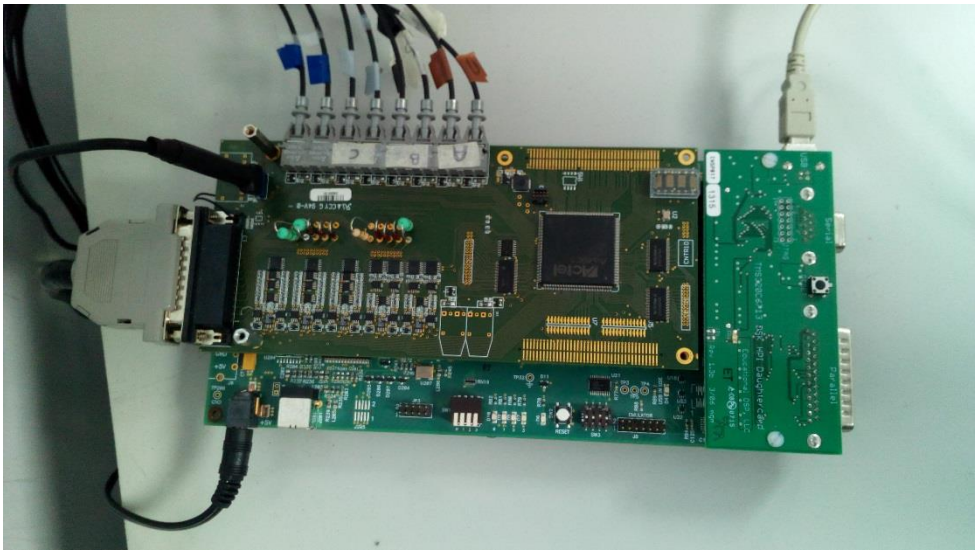
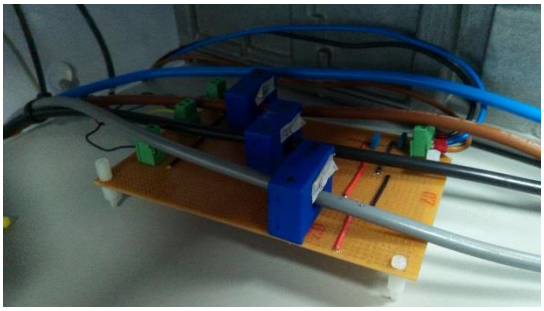


Figure 6-5 FPGA and DSP platform controller

The control algorithm is programmed in the DSP using Code Composer Studio, which calculated the reference signals for the APF. Then the FPGA takes these reference signals and generate the gate pulses for the APF switches. The switching frequency was 10kHz. The gate pulses are transferred to the SKAI modules interface board by using fiber-optic cables.

6.5 **Measurement Boards**

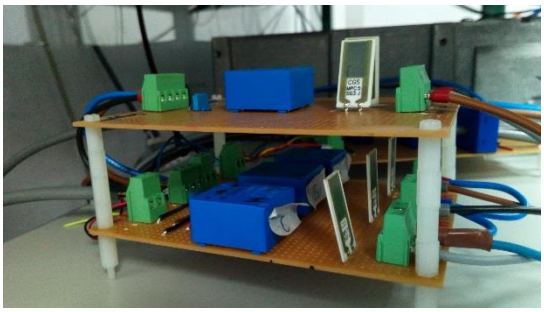
To implement a closed loop control, a measurement device must be used in the system to compare the generated signal with the reference signal. In the test rig, there are ten measurement devices, four for voltage measurement (one for the DC-link voltage and three for the generator phase voltages) and six for current measurement. The voltage transducer are hall-effect transducer LEM LV25-P [99]. The current transducers were used in this test also which were a hall-effect transducer, three for output filter current, which are LEM LA55-P[100] and three for the load current, which are LEM LA125-P[101].



(A)



(B)



(C)

Figure 6-6 Measurement Boards, (A) and (B) current transducers, and (C) voltage transducers

The outputs of these transducers are read by the FPGA through digital to analogue converters, and then transferred to the DSP to calculate the corresponding real values of these signals.

6.6 **APF Test**

Before applying the control algorithm on the proposed generator, several tests were done to check the measurement board accuracy and the controller performance. In addition, some harmonic tests were conducted by using a programmable AC source (Chroma 61511) to validate the controller and APF operation. When the APF test was done, the work moved to the proposed generator with different loads and the results are presented in the following subsections.

6.7 **Balanced Linear Load**

The first test was done in the lab was linear load test to validate the simulation was done in section 4.2, a three-phase resistive load (35 kW) was connected to the generator. The generator is run by using a DC motor as a prime mover, and the DC motor is driven by an Industrial DC drive

constructed by Eurotherm Drives (590C/ 0350/6/4/0/1/0/00/000). A Littlefuse T4500 synchroniser was used to maintain the generator frequency matching the grid frequency (50 Hz).

The generator/ load current waveform at 35 kW loading is shown in Figure 6-7, and the frequency spectrum is shown in Figure 6-8.

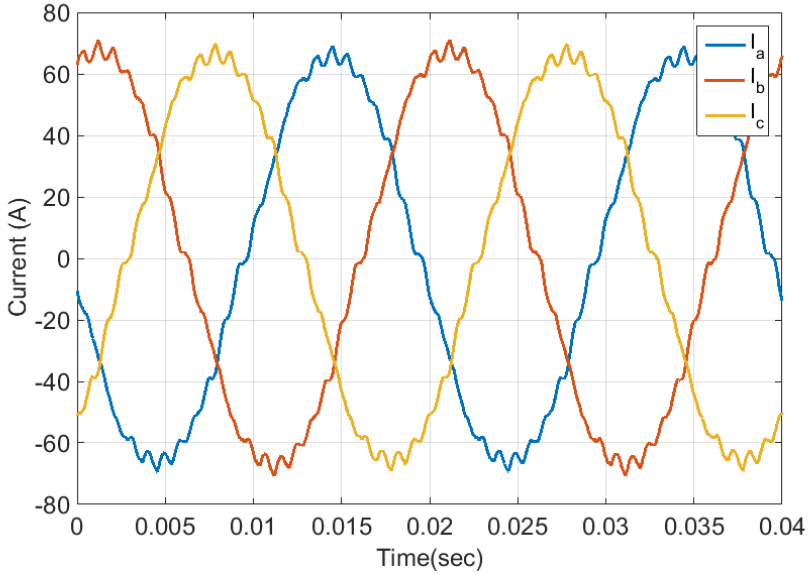


Figure 6-7 Generator/ load current at 35 kW loading

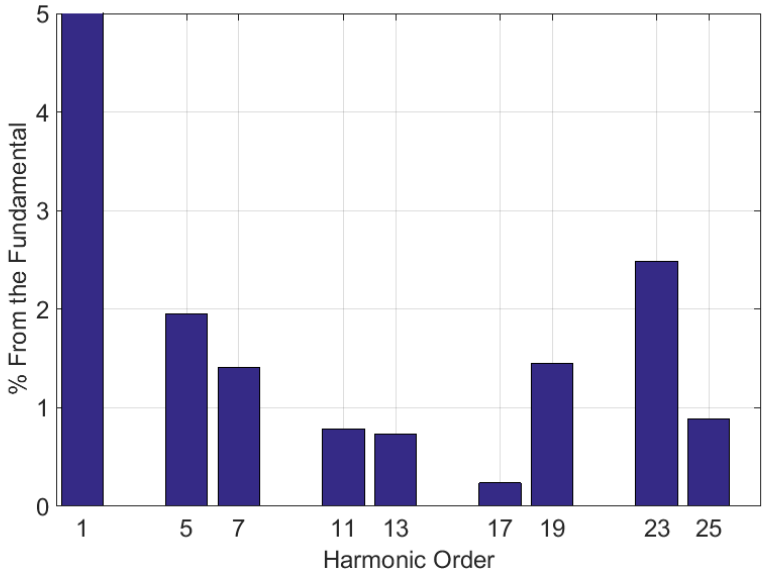


Figure 6-8 Frequency spectrum for the phase-A current

As can be seen from the Figure 6-7 and Figure 6-8 the total harmonic distortion (THD) in the load current is 4.1%

To reduce the THD in the load current, the APF is activated, and the current controller was proportional-resonant with harmonic compensator (PRHC) as described in Chapter-3. Figure 6-9 shows the load current with APF and as can be seen from the figure the THD in the load current reduced to just 1.9% and this within the limit in IEEE Std 519 [18]. and it shown in Table 1-1.

It is clear from the Figure 6-10 that the APF significantly reduces all the targeted harmonics, and improves the THD in the load current.

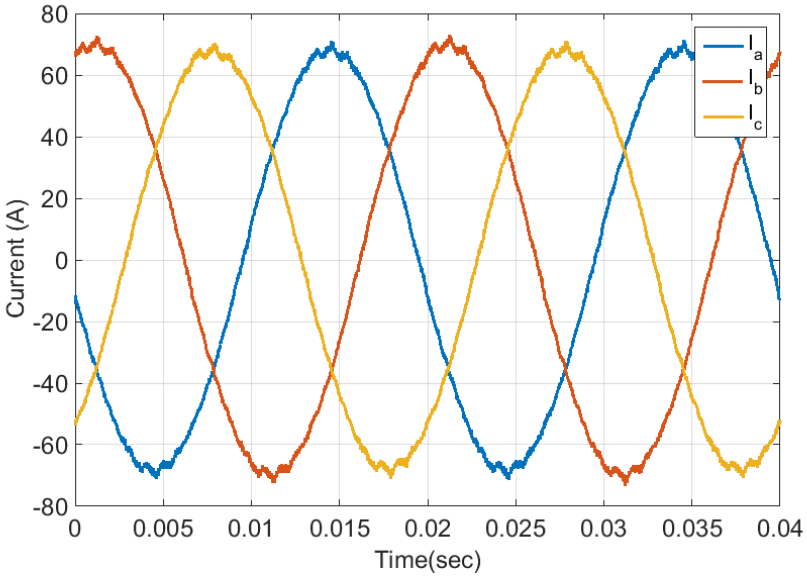


Figure 6-9 Load current with enabled APF

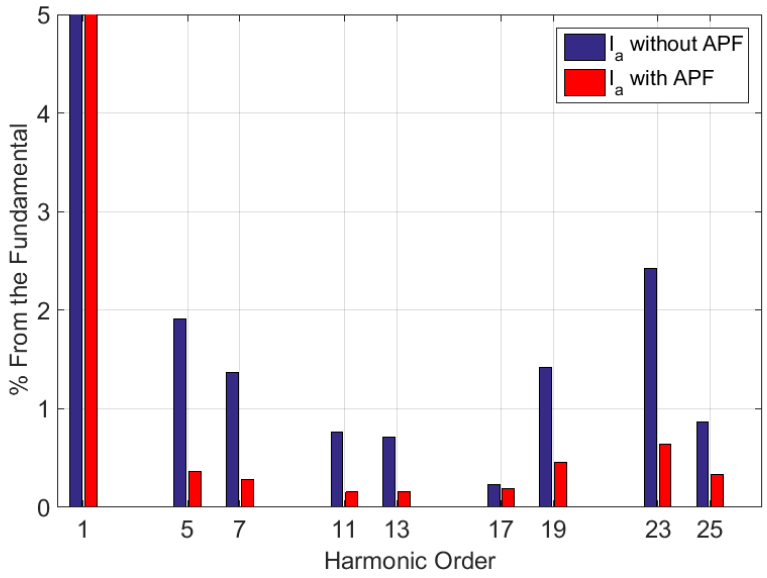


Figure 6-10 Spectrum analysis of the phase-A load current with and without APF

6.8 **Balanced Nonlinear Load**

The second test that was done in the lab on the proposed generator was a nonlinear load test to validate the simulation was done in section 4.2.2. A three-phase diode bridge rectifier with R-L load (R=9.2 Ω and

L=5.5 mH) was used as nonlinear load for the proposed generator. Figure 6-11 shows the generator/load current without APF and Figure 6-12 shows the frequency spectrum of this current. The THD in the load/generator current was 25%.

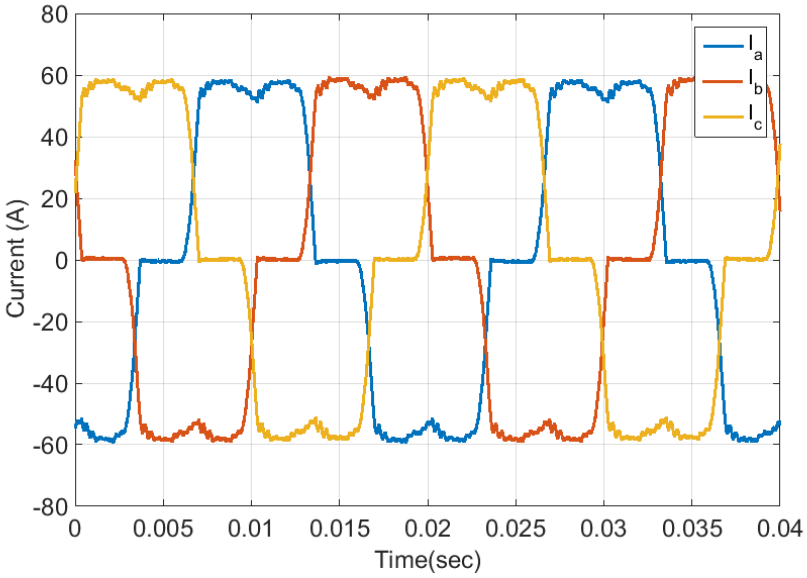


Figure 6-11 Generator/ load current with nonlinear load

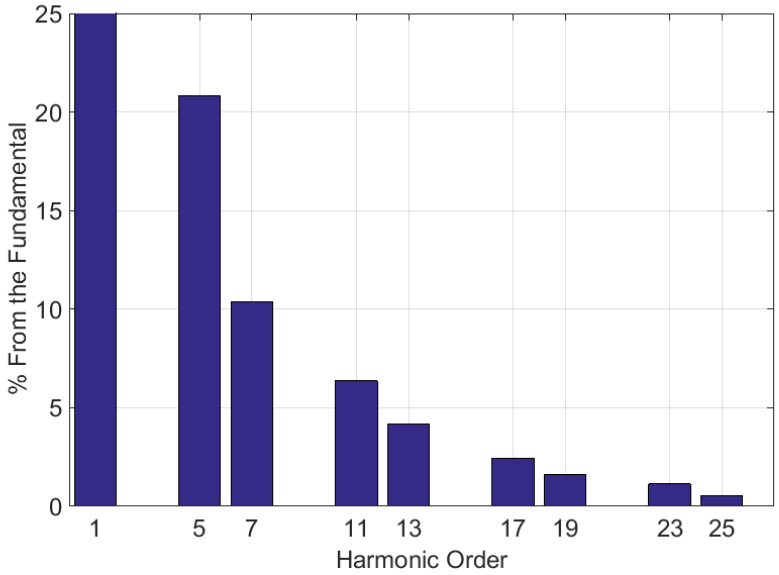


Figure 6-12 Frequency spectrum for the generator/load phase-A current with nonlinear load

When the APF was enabled, the APF dramatically reduced the THD in the generator current and THD decreased from 25% before enabling the APF to just about 5% after enabling the APF as show in Figure 6-13.

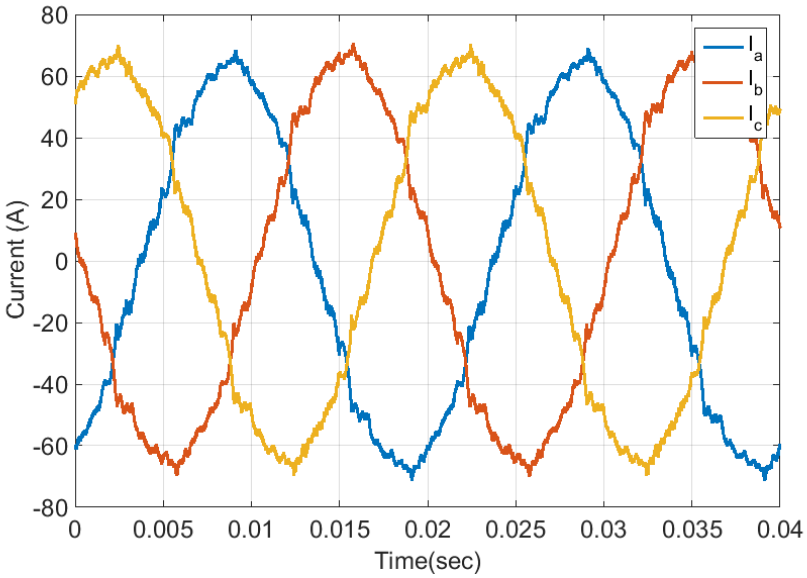


Figure 6-13 Generator current with balanced nonlinear load with enabled APF

Figure 6-14 shows the frequency spectrum analysis of the phase-A current for the generator with nonlinear load and with and without APF, as can be seen from the figure most of the harmonics in the controller range had been decreased.

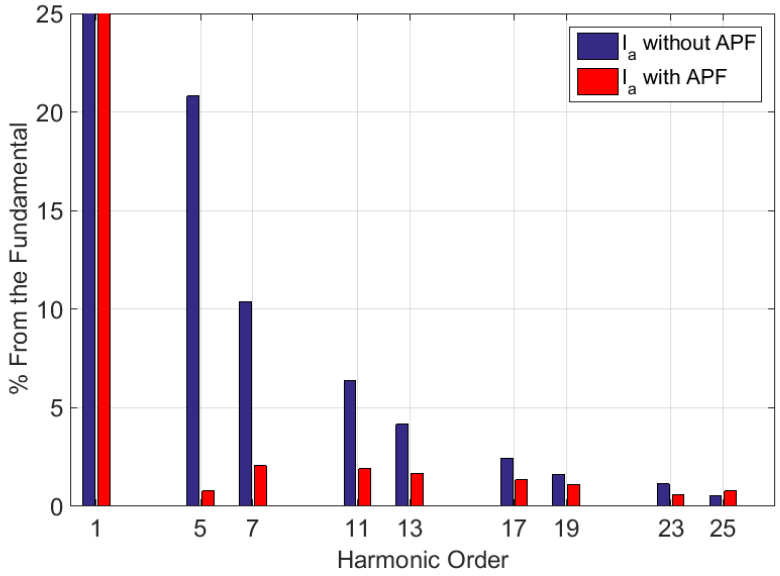


Figure 6-14 Frequency Spectrum analysis of the phase-A generator current with nonlinear load, with and without APF

6.9 **Unbalanced Nonlinear Load (type-2)**

The final test in harmonic compensation tests was unbalanced nonlinear load. To construct a nonlinear load in the lab, a single-phase resistive load of (30 Ω), was connected between the phase-A and the APF neutral leg in the circuit described in section 6.8. The total power was about 34.5 Kw.

The generator was started with a connected load (the three-phase diode bridge and the single-phase load) and the APF was disabled. So the single phase-load is not supplied without the APF, because the single-phase circuit is still open (the neutral wire was supplied through the APF). The current waveforms for both the generator and the load were the same as the waveform shown in Figure 6-11 and has a THD of 25%.

When the APF was enabled, the single-phase load that connected between the generator phase-A and forth-leg of the APF was supplied and this makes the phase-A current in the load side have a higher current than the other two phases (phase-B and phase-C) as shown in Figure 6-15.

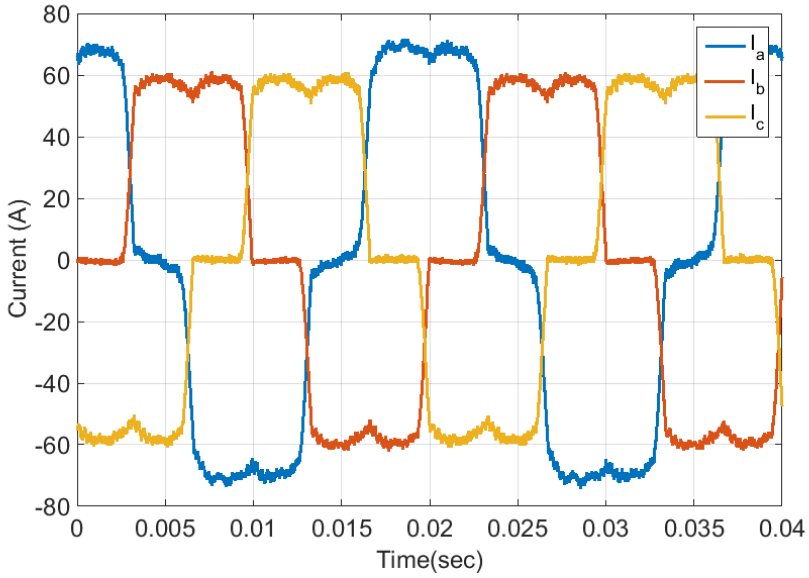


Figure 6-15 Generator/ load current with unbalanced nonlinear load before enabling the APF

The RMS value and the total harmonic distortion of each phase of the load current is given in Table 6-1.

Table 6-1 The RMS value and the THD of the unbalanced nonlinear load

Phase	**RMS value (A)**	**THD %**
Phase-A	57.4	22.8
Phase-B	49.3	27
Phase-C	47.5	26.8

The frequency spectrum of the three phase currents of the unbalanced nonlinear load is shown in Figure 6-16 and as the figure shows phase-A has a higher current with 75.36 V fundamental peak value and phase-B and phase-C 63.32 V and 62.62 V fundamental peak values respectively.

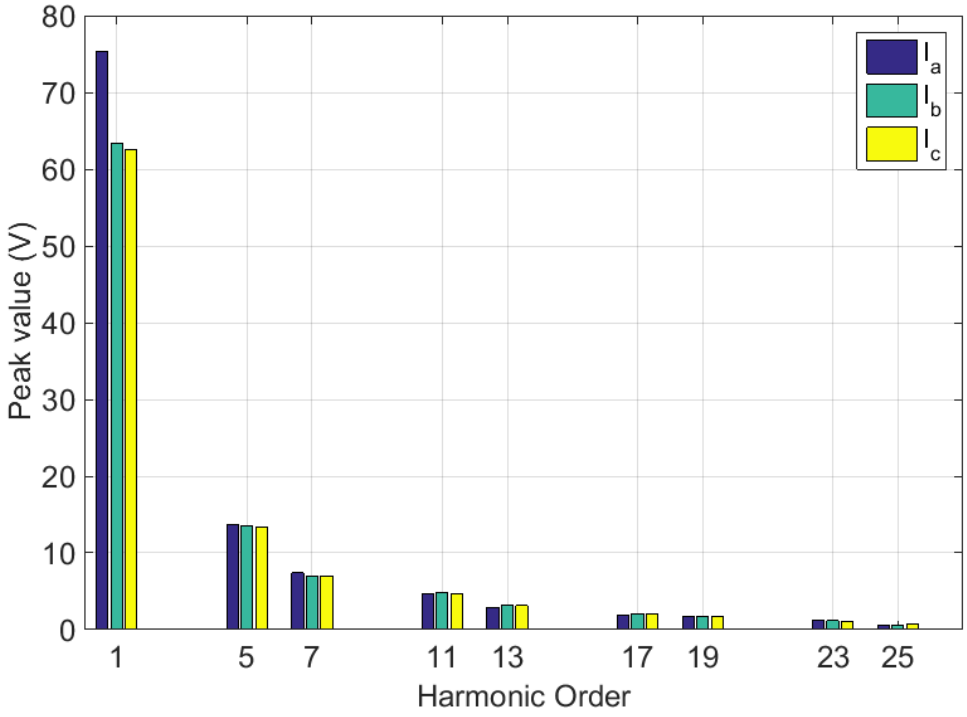


Figure 6-16 Frequency spectrum for Generator/ load current with unbalanced nonlinear load before enabling the APF

However, in the generator side the APF compensated the harmonics and decreased the THD in the generator current to about 5.6% retained the generator current balanced as shown in Figure 6-17.

Table 6-2 summarise the RMS values and the THD in the generator and the nonlinear unbalanced load with and without APF. As can be seen from the table the maximum difference between the highest phase current and the lowest phase current in the load side is 9.9 A and in the generator side is 2.6 A.

Table 6-2 the RMS value and the THD value of the generator and the load current before and after enabling the APF

Quantity	Before enabling the APF		After enabling the APF			
	Load/generator		Load		Generator	
	Current (A)	THD %	Current (A)	THD %	Current (A)	THD %
Phase-A	47.4	25.1	57.4	22.8	51.6	5.7
Phase-B	48.4	24.8	49.3	27	52.8	5.3
Phase-C	46.7	25	47.5	26.8	50.2	5.9

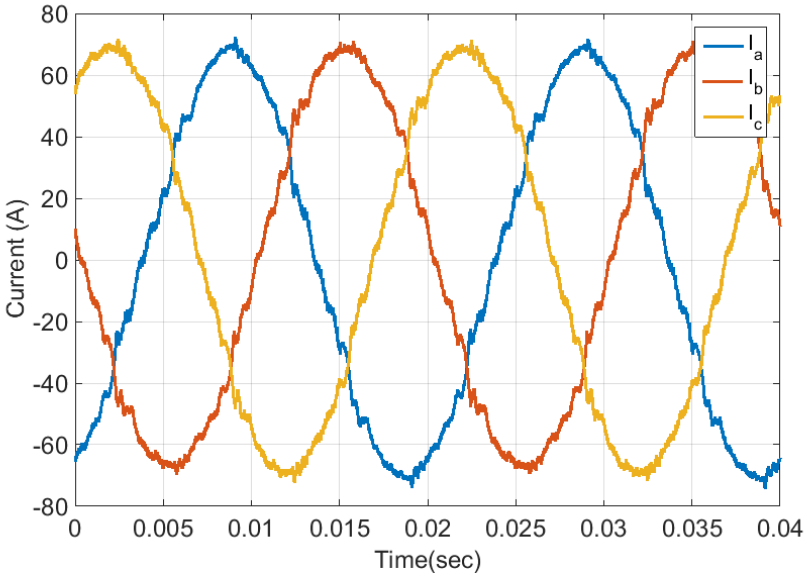


Figure 6-17 Generator current with unbalanced nonlinear load and with enabled APF

The frequency spectrum of the generator and the load current for the unbalanced nonlinear load with APF is shown in Figure 6-18, the figure shows that the APF compensates the harmonics in the generator currents and reduces the THD from 22.8% to 5.7 (for phase-A) and retains generator current balance.

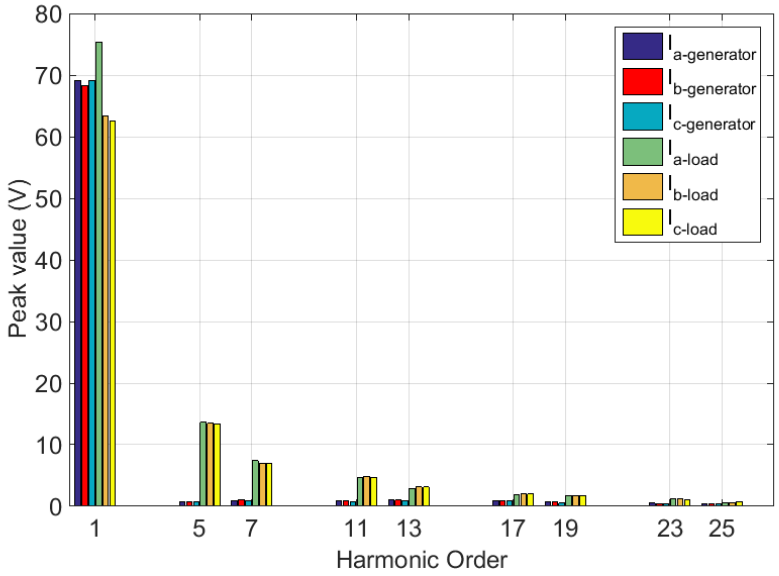


Figure 6-18 Frequency Spectrum analysis of the generator current and the load current with nonlinear unbalanced load with APF

6.10 Comparison Between the Simulation and the Experimental Results:

In Chapter-5 and this Chapter the simulation and experimental results were presented, and the experimental results have supported the simulation results in the three cases. For the first case, balanced linear load, the THD in the load current after enabling the controller in the simulation was (2.1%) and it is close to the experimental result which was (1.9%) as shown in Figure 4-3 and Figure 6-9 respectively. In the second case, balanced nonlinear load, also the simulation results and experimental results had good agreement, where in the simulation the THD in the generator current was (3.4%), while in the experimental result was (5%), as can be seen from Figure 4-5 and Figure 6-13. Finally in the third case, unbalanced nonlinear load (type-2), also the THD in the simulation result was (3.65%) and in the experimental result was (5.8%) as shown in Figure 4-9 and Figure 6-17 respectively, and the APF supplied the single-phase load while maintaining the generator current balance as shown in Table 6-2. Table 6-3 summarises the comparison between the simulation results and experimental results in the three different cases. As can be seen from

the table the THD in the experimental results for the nonlinear loads were slightly higher than the simulation results due to the nonlinearity and saturation effect.

Table 6-3 Comparison between the simulation results and the experimental results for the THD in the load/generator current

	Before enabling the APF		**After enabling the APF**	
	Sim.	Exp.	Sim.	Exp.
Balanced Linear load (Load)	4.5%	4.1%	2.1%	1.9%
Balanced Nonlinear Load (Generator)	22.3%	25%	3.4%	5.0%
Unbalanced Nonlinear Load (Generator)	22.3%	25%	3.6%	5.8%

6.11 **Conclusion**

In this chapter, the method of adding an active power filter to a simplified synchronous generator to improve its output quality was experimentally validated. It was shown that adding APF to simplified synchronous generator could improve the output power quality of the generator. In case of linear load, the APF reduced the THD in the load current within the limit in IEEE Std 519 [18]. In addition, compensation of nonlinear load harmonic was investigated, the simulation result and experimental tests showed that adding APF to the simplified synchronous generator had improved output current of the generator and dramatically decreased the THD in generator current. Furthermore, balancing the generator current in case of unbalanced and nonlinear load was discussed, and the results showed that the APF balanced and compensate the generator current.

Chapter-7 Conclusions and Future work

Chapter-7 **Conclusion and Future Work**

7.1 **Conclusion**

The application of power electronics in electrical power systems and electrical machine is in increasing trend, such as, motor drives, coupling renewable energy sources with the grid, and harmonic and reactive power compensation in micro grids. The synchronous generator is considered the workhorse of power generation, and synchronous generator designers use different approaches to make the output voltage of these generator sinusoidal (less harmonics), i.e. efficient but complex. However, these approaches complicate the design and/or decrease the output power. This research investigated another usage of power electronics, which is improving power quality of a simple design synchronous generator (efficient and simple).

Chapter-2 presented the proposed synchronous generator model including the harmonic content in the generator. The active power filter topology and control were discussed in Chapter-3. The harmonic compensation for different kind of loads were presented in Chapter-4. The dynamic response improvement of synchronous generator without damper bars by using the active power filter was presented in Chapter-5. The experimental results were presented in Chapter-6, and good correlation between experimental and simulation results was achieved.

This thesis has presented the effect of using an active power filters (shunt and series) to compensate for the poor harmonic output of a simplified synchronous generator by both simulation and experiment. The proposed generator has full-pitch winding and unskewed stator to increase the generator output power and make the manufacturing process easier and less expensive. The shunt active power filter is controlled using a

proportional resonant controller cascaded with harmonic compensator tuned at the targeted harmonics.

The experimental results have validated the simulation results, and shown that the active power filters (shunt and series) can be integrated with a simplified synchronous generator to provide an acceptable level of power quality to the load from a simple design generator with a poor quality output waveform at the point of common coupling (PCC).

The novelty of this work is the use of a combination of active power filters (shunt and series) to allow the simplification of the design of the synchronous generator, allowing the generator capacity and/or efficiency to be increased, and further permitting a simplified design that is both less expensive and faster to produce while maintaining an acceptable level of power quality at the load.

With the use of the active filters and the proposed generator, a good quality power were delivered to the linear and nonlinear load and generator harmonics were compensated .In addition, the shunt active power filter maintained the proposed generator current balanced despite the load being unbalanced.

As well as the benefits defined above, the use of active power filters to compensate for poor generator output power quality was particularly apt for the use of fractional slot concentrated windings, allowing for decreased end winding length and fully automated coil winding and placement, while compensating for the windings natural high harmonic content. The active power fitters may also be used to improve transient response during sudden changes in generator loading and improve fault ride-through capability. Therefore it can be concluded that the active power filters can be integrated with a simple design synchronous generator to deliver a good quality power and improve the dynamic response.

7.2 Future Work

The work that has been presented in this thesis could be considered as a base work for the following:

- The proposed synchronous generator model which developed in Chapter-2 was a linear model and the damper cage was neglected, and the model could be developed to take in consideration the saturation effects and the damper cage.
- While this system achieved a satisfactory level of power quality in terms of THD, for the systems that require more restricted THD values such as micro grids, the proposed system THD could be improved by using an LCL-interface filter instead of L-filter, increasing the switching frequency above 10kHz or the use of other types of controllers
- Study the possibility of integrating the APFs with the synchronous generator body to decrease space and increase system efficiency
- Experimental validation for all the proposed system and using the APF with synchronous generator without damper bars to improve the dynamic response
- A coordinated control scheme should be investigated for the two active power filters, as these two systems both require fast control actions on the same plant. There is a chance that the two filter controllers may "fight" against each other during some operating conditions, including when load transients are applied and removed.

References:

1. Kocabas, D.A., *Novel Winding and Core Design for Maximum Reduction of Harmonic Magnetomotive Force in AC Motors.* Ieee Transactions on Magnetics, 2009. **45**(2): p. 735-746.
2. Asgharpour-Alamdari, H., Y. Alinejad-Beromi, and H. Yaghobi, *Reduction in distortion of the synchronous generator voltage waveform using a new winding pattern.* Iet Electric Power Applications, 2017. **11**(2): p. 233-241.
3. Walker, J.H., N. Kerruish, and B.J. Chalmers, *Ac Machine Windings with Reduced Harmonic Content.* Proceedings of the Institution of Electrical Engineers-London, 1965. **112**(6): p. 1859-1863.
4. Kimbark, E.W., *Power System Stability, Volume III, Synchronous Machines*. IEEE Press Power Systems Engineering Series, ed. P.M. Anderson. 1995, New York: Wiley-IEEE Press.
5. Abhijit Chakrabarti, S.D., *Electrical Machines*. 2015, India: McGraw Hill Education.
6. Driesen, J. and K. Visscher. *Virtual synchronous generators*. in *2008 IEEE Power and Energy Society General Meeting - Conversion and Delivery of Electrical Energy in the 21st Century*. 2008.
7. Shintai, T., Y. Miura, and T. Ise, *Oscillation damping of a distributed generator using a virtual synchronous generator.* IEEE Transactions on Power Delivery, 2014. **29**: p. 668-676.
8. Tolbert, Y.M.a.W.C.a.L.Y.a.F.W.a.L.M., *Virtual Synchronous Generator Control of Full Converter Wind Turbines With Short-Term Energy Storage.* IEEE Transactions on Industrial Electronics, 2017. **64**: p. 8821-8831.
9. Bevrani, H., T. Ise, and Y. Miura, *Virtual synchronous generators: A survey and new perspectives.* International Journal of Electrical Power and Energy Systems, 2014. **54**: p. 244-254.
10. *VSYNC Project*. 10/11/2017]; Available from: http://www.vsync.eu.
11. Zhong, Q.-C. and G. Weiss, *Synchronverters: Inverters that mimic synchronous generators.* IEEE Transactions on Industrial Electronics, 2011. **58**(4): p. 1259-1267.
12. Zhong, Q.-C., et al., *Improved Synchronverters with Bounded Frequency and Voltage for Smart Grid Integration.* IEEE Transactions on Smart Grid, 2017. **PP**: p. 1-11.
13. Wang, J.q., et al. *Analysis of Operation of Synchronous Generator under the Distortion of Harmonic Current*. in *2012 Asia-Pacific Power and Energy Engineering Conference*. 2012.
14. Fan, W. and Y. Liao. *Impacts of flickers, harmonics and faults on synchronous generator operations*. in *Proceedings of the 2012 44th Southeastern Symposium on System Theory (SSST)*. 2012.
15. Samra, A.H. and K.M. Islam. *Harmonic effects on synchronous generators voltage regulation*. in *Southeastcon '95. Visualize the Future., Proceedings., IEEE*. 1995.
16. Ma, W., et al. *Stability of a synchronous generator with diode-bridge rectifier and back-EMF load*. in *2000 IEEE Power Engineering Society Winter Meeting. Conference Proceedings (Cat. No.00CH37077)*. 2000.
17. Baggini, A., *Handbook of power quality*. 2008, West Sussex: John Wiley & Sons.
18. IEEE, *IEEE Recommended Practices and Requirements for Harmonic Control in Electrical Power Systems.* IEEE Std 519-1992, 1993: p. 1-101.
19. Portillo, R., et al., *Modeling strategy for back-to-back three-level converters applied to high-power wind turbines.* Ieee Transactions on Industrial Electronics, 2006. **53**(5): p. 1483-1491.
20. Ng, C.H., et al., *A multilevel modular converter for a large, light weight wind turbine generator.* Ieee Transactions on Power Electronics, 2008. **23**(3): p. 1062-1074.
21. Wang, Z. and H. Li, *An Integrated Three-Port Bidirectional DC-DC Converter for PV Application on a DC Distribution System.* Ieee Transactions on Power Electronics, 2013. **28**(10): p. 4612-4624.

22. Liang, Z.G., et al., *A High-Efficiency PV Module-Integrated DC/DC Converter for PV Energy Harvest in FREEDM Systems.* Ieee Transactions on Power Electronics, 2011. **26**(3): p. 897-909.
23. Pena, R., J.C. Clare, and G.M. Asher, *A doubly fed induction generator using back-to-back PWM converters supplying an isolated load from a variable speed wind turbine.* Iee Proceedings-Electric Power Applications, 1996. **143**(5): p. 380-387.
24. Muller, S., M. Deicke, and R.W.D. Doncker, *Doubly fed induction generator systems for wind turbines.* IEEE Industry Applications Magazine, 2002. **8**(3): p. 26-33.
25. El-Habrouk, M., M. Darwish, and P. Mehta, *Active power filters: A review.* IEE Proceedings-Electric Power Applications, 2000. **147**(5): p. 403-413.
26. Jou, H.L., et al., *Novel power converter topology for threephase four-wire hybrid power filter.* IET Power Electronics, 2008. **1**(1): p. 164-173.
27. Montero, M.I.M., E.R. Cadaval, and F.B. Gonzalez, *Comparison of Control Strategies for Shunt Active Power Filters in Three-Phase Four-Wire Systems.* IEEE Transactions on Power Electronics, 2007. **22**(1): p. 229-236.
28. Dey, P. and S. Mekhilef, *Current Controllers of Active Power Filter for Power Quality Improvement: A Technical Analysis.* Automatika–Journal for Control, Measurement, Electronics, Computing and Communications, 2015. **56**(1).
29. Burgos-Mellado, C., et al., *Experimental Evaluation of a CPT-Based Four-Leg Active Power Compensator for Distributed Generation.* Ieee Journal of Emerging and Selected Topics in Power Electronics, 2017. **5**(2): p. 747-759.
30. Huang, S.J. and J.C. Wu, *A control algorithm for three-phase three-wired active power filters under nonideal mains voltages.* IEEE Transactions on Power Electronics, 1999. **14**: p. 753-760.
31. Salmerón, P. and R.S. Herrera, *Distorted and unbalanced systems compensation within instantaneous reactive power framework.* IEEE Transactions on Power Delivery, 2006. **21**: p. 1655-1662.
32. Chen, C.C. and Y.Y. Hsu, *A novel approach to the design of a shunt active filter for an unbalanced three-phase four-wire system under nonsinusoidal conditions.* IEEE Transactions on Power Delivery, 2000. **15**: p. 1258-1264.
33. Yuan, X.M., et al., *Stationary-frame generalized integrators for current control of active power filters with zero steady-state error for current harmonics of concern under unbalanced and distorted operating conditions.* Ieee Transactions on Industry Applications, 2002. **38**(2): p. 523-532.
34. Surgevil, T. and E. Akpınar. *Application of shunt active power filter to isolated synchronous generator system*. in *Industrial Electronics, 2009. IECON'09. 35th Annual Conference of IEEE*. 2009. IEEE.
35. Nishida, K., T. Ahmed, and M. Nakaoka. *Advanced Active Power Filter Controlled permanent-magnet synchronous generator for Automotive Applications*. in *Power Electronics Specialists Conference, 2007. PESC 2007. IEEE*. 2007. IEEE.
36. Abu-Jalala, A., et al. *Performance improvement of simplified synchronous generators using an active power filter*. in *2017 IEEE Energy Conversion Congress and Exposition (ECCE)*. 2017.
37. *Vehicle technologies multi-year program plan 2011-2015*. 2010, U.S. Department of Energy: U.S. p. 122.
38. Lipo, T.A., *Analysis of Synchronous Machines*. 2012, New York: Taylor & Frank Group, LLC.
39. Ong, C.-M., *Dynamic Simulation of Electric Machinery Using Matlab/Simulink*. 1998, New Jersey: USA: Prentice Hall PTR.
40. Seilmeier, M. *Modelling of electrically excited synchronous machine (EESM) considering nonlinear material characteristics and multiple saliencies*. in *Power Electronics and Applications (EPE 2011), Proceedings of the 2011-14th European Conference on*. 2011. IEEE.
41. Ghassemi, M., H. Lesani, and S.M. Nabavi. *Synchronous Machine Modelling and Identification via Network Equivalent Techniques*. in *Power Engineering, 2007 Large Engineering Systems Conference on*. 2007. IEEE.

42. Demirdelen, T., et al. *Review of hybrid active power filter topologies and controllers*. in *4th International Conference on Power Engineering, Energy and Electrical Drives*. 2013.
43. Chen, D. and S. Xie. *Review of the control strategies applied to active power filters*. in *Electric Utility Deregulation, Restructuring and Power Technologies, 2004.(DRPT 2004). Proceedings of the 2004 IEEE International Conference on*. 2004. IEEE.
44. Akagi, H., *Active harmonic filters.* Proceedings of the Ieee, 2005. **93**(12): p. 2128-2141.
45. Quinn, C.A. and N. Mohan, *Active filtering of harmonic currents in three-phase, four-wire systems with three-phase and single-phase nonlinear loads.* [Proceedings] APEC '92 Seventh Annual Applied Power Electronics Conference and Exposition, 1992: p. 829-836.
46. Quinn, C.A., N. Mohan, and H. Mehta, *A four-wire, current-controlled converter provides harmonic neutralization in three-phase, four-wire systems*, in *Proceedings Eighth Annual Applied Power Electronics Conference and Exposition,*. 1993. p. 841-846.
47. Timbus, A., et al. *Synchronization methods for three phase distributed power generation systems-An overview and evaluation*. in *Power Electronics Specialists Conference, 2005. PESC'05. IEEE 36th*. 2005. IEEE.
48. Kaura, V. and V. Blasko, *Operation of a phase locked loop system under distorted utility conditions.* IEEE Transactions on Industry Applications, 1997. **33**(1): p. 58-63.
49. Se-Kyo, C., *A phase tracking system for three phase utility interface inverters.* IEEE Transactions on Power Electronics, 2000. **15**(3): p. 431-438.
50. Teodorescu, R., M. Liserre, and P. Rodriguez, *Grid converters for photovoltaic and wind power systems*. Vol. 29. 2011: John Wiley & Sons.
51. Rodriguez, P., et al., *Double synchronous reference frame PLL for power converters control.* 2005 IEEE 36th Power Electronic Specialists Conference (PESC), Vols 1-3, 2005: p. 1415-1421.
52. Rodriguez, P., et al., *Decoupled Double Synchronous Reference Frame PLL for Power Converters Control.* IEEE Transactions on Power Electronics, 2007. **22**(2): p. 584-592.
53. Rodriguez, P., et al., *Grid Synchronization of Wind Turbine Converters under Transient Grid Faults using a Double Synchronous Reference Frame PLL.* 2008 Ieee Energy 2030 Conference, 2008: p. 517-+.
54. Luna, A., et al., *Grid Voltage Synchronization for Distributed Generation Systems Under Grid Fault Conditions.* Ieee Transactions on Industry Applications, 2015. **51**(4): p. 3414-3425.
55. Rodriguez, P., et al. *New positive-sequence voltage detector for grid synchronization of power converters under faulty grid conditions*. in *Power Electronics Specialists Conference, 2006. PESC'06. 37th IEEE*. 2006. IEEE.
56. Rodriguez, P., et al., *Advanced grid synchronization system for power converters under unbalanced and distorted operating conditions.* Iecon 2006 - 32nd Annual Conference on Ieee Industrial Electronics, Vols 1-11, 2006: p. 5057-+.
57. Luna, A., et al., *Grid Synchronization for Advanced Power Processing and FACTS in Wind Power Systems.* Ieee International Symposium on Industrial Electronics (Isie 2010), 2010: p. 2915-2920.
58. Rodríguez, P., et al., *A Stationary Reference Frame Grid Synchronization System for Three-Phase Grid-Connected Power Converters Under Adverse Grid Conditions.* IEEE Transactions on Power Electronics, 2012. **27**(1): p. 99-112.
59. Teodorescu, R., et al., *A new control structure for grid-connected LCL PV inverters with zero steady-state error and selective harmonic compensation.* Apec 2004: Nineteenth Annual Ieee Applied Power Electronics Conference and Exposition, Vols 1-3, 2004: p. 580-586.
60. Lyon, W.V., *Applications of the method of symmetrical components*. Electric engineering texts. 1937, New York, London: McGraw-Hill book company, inc. vii, 579 p.

61. Asiminoaei, L., F. Blaabjerg, and S. Hansen, *Evaluation of harmonic detection methods for active power filter applications.* APEC 2005: Twentieth Annual IEEE Applied Power Electronics Conference and Exposition, Vols 1-3, 2005: p. 635-641.
62. Grady, W.M., M.J. Samotyj, and A.H. Noyola, *Survey of Active Power-Line Conditioning Methodologies.* Ieee Transactions on Power Delivery, 1990. **5**(3): p. 1536-1542.
63. Massoud, A.M., S.J. Finney, and B.W. Williams, *Review of harmonic current extraction techniques for an active power filter.* 2004 11th International Conference on Harmonics and Quality of Power, 2004: p. 154-159.
64. Marques, G. *A comparison of active power filter control methods in unbalanced and non-sinusoidal conditions*. in *Industrial electronics Society, 1998. IECON'98. Proceedings of the 24th Annual Conference of the IEEE*. 1998. IEEE.
65. Akagi, H., Y. Kanazawa, and A. Nabae, *Instantaneous Reactive Power Compensators Comprising Switching Devices without Energy Storage Components.* IEEE Transactions on Industry Applications, 1984. **IA-20**(3): p. 625-630.
66. Akagi, H., E.H. Watanabe, and M. Aredes, *Instantaneous Power Theory and Applications to Power Conditioning*. 2007, New Jersey: IEEE Press series John Wiley & Sons.
67. Aredes, M. and E.H. Watanabe, *New control algorithms for series and shunt three-phase four-wire active power filters.* IEEE Transactions on Power Delivery, 1995. **10**(3): p. 1649-1656.
68. Santiprapan, P. and K.-L. Areerak. *Performance improvement of harmonic detection using synchronous reference frame method*. in *Advances in Energy Engineering (ICAEE), 2010 International Conference on*. 2010. IEEE.
69. Buso, S., L. Malesani, and P. Mattavelli, *Comparison of current control techniques for active filter applications.* Ieee Transactions on Industrial Electronics, 1998. **45**(5): p. 722-729.
70. Kazmierkowski, M.P. and L. Malesani, *Current control techniques for three-phase voltage-source PWM converters: a survey.* Industrial Electronics, IEEE Transactions on, 1998. **45**(5): p. 691-703.
71. Parvez, M., et al., *Current control techniques for three-phase grid interconnection of renewable power generation systems: A review.* Solar Energy, 2016. **135**(Supplement C): p. 29-42.
72. Hassaine, L., et al., *Overview of power inverter topologies and control structures for grid connected photovoltaic systems.* Renewable and Sustainable Energy Reviews, 2014. **30**(Supplement C): p. 796-807.
73. Rahman, K.M., et al., *Variable-band hysteresis current controllers for PWM voltage-source inverters.* Ieee Transactions on Power Electronics, 1997. **12**(6): p. 964-970.
74. Song, H.S. and K. Nam, *Dual current control scheme for PWM converter under unbalanced input voltage conditions.* Ieee Transactions on Industrial Electronics, 1999. **46**(5): p. 953-959.
75. Mattavelli, P., *A closed-loop selective harmonic compensation for active filters.* Ieee Transactions on Industry Applications, 2001. **37**(1): p. 81-89.
76. Timbus, A.V., et al., *Adaptive resonant controller for grid-connected converters in distributed power generation systems.* Apec 2006: Twenty-First Annual Ieee Applied Power Electronics Conference and Exposition, Vols 1-3, 2006: p. 1601-1606.
77. Khalfalla, H., et al., *An Adaptive Proportional Resonant Controller for Single Phase PV Grid Connected Inverter Based on Band-Pass Filter Technique.* 2017 11th Ieee International Conference on Compatibility, Power Electronics and Power Engineering (Cpe-Powereng), 2017: p. 436-441.
78. Zmood, D.N., D.G. Holmes, and G.H. Bode, *Frequency-domain analysis of three-phase linear current regulators.* Ieee Transactions on Industry Applications, 2001. **37**(2): p. 601-610.
79. Zmood, D.N. and D.G. Holmes, *Stationary frame current regulation of PWM inverters with zero steady-state error.* Ieee Transactions on Power Electronics, 2003. **18**(3): p. 814-822.

80. Teodorescu, R., et al., *Proportional-resonant controllers and filters for grid-connected voltage-source converters.* IEE Proceedings - Electric Power Applications, 2006. **153**(5): p. 750-762.
81. Tan, P.C., P.C. Loh, and D.G. Holmes, *High-performance harmonic extraction algorithm for a 25kV traction power quality conditioner.* Iee Proceedings-Electric Power Applications, 2004. **151**(5): p. 505-512.
82. Vanjani, H. and U. Choudhury. *Performance analysis of Three-phase Four-wire Shunt Active Power filter*. in *Optimization, Reliabilty, and Information Technology (ICROIT), 2014 International Conference on*. 2014. IEEE.
83. Cavini, A., F. Ronchi, and A. Tilli, *Four-wires shunt active filters: Optimized design methodology.* Iecon'03: The 29th Annual Conference of the Ieee Industrial Electronics Society, Vols 1 - 3, Proceedings, 2003: p. 2288-2293.
84. Balcells, J., M. Lamich, and G. Capella, *LC coupled shunt active power filter (APF): New topology and control method.* Proceedings of the 9th International Conference on Electrical Power Quality and Utilisation, Vols 1 and 2, 2007: p. 854-859.
85. Lam, C.S., et al., *Design and Performance of an Adaptive Low-DC-Voltage-Controlled LC-Hybrid Active Power Filter With a Neutral Inductor in Three-Phase Four-Wire Power Systems.* Ieee Transactions on Industrial Electronics, 2014. **61**(6): p. 2635-2647.
86. Ahmed, K.H., S.J. Finney, and B.W. Williams, *Passive filter design for three-phase inverter interfacing in distributed generation.* 2007 Compatibility in Power Electronics, 2007: p. 130-138.
87. Tang, Y., et al., *Generalized Design of High Performance Shunt Active Power Filter With Output LCL Filter.* Ieee Transactions on Industrial Electronics, 2012. **59**(3): p. 1443-1452.
88. Liu, Q., et al., *A Novel Design and Optimization Method of an LCL Filter for a Shunt Active Power Filter.* Ieee Transactions on Industrial Electronics, 2014. **61**(8): p. 4000-4010.
89. Sosa, J.M., et al., *Comparative evaluation of L and LCL filters in transformerless grid tied converters for active power injection.* 2014 Ieee International Autumn Meeting on Power, Electronics and Computing (Ropec), 2014.
90. Dai, N.-Y. and M.-C. Wong. *Design considerations of coupling inductance for active power filters*. in *Industrial Electronics and Applications (ICIEA), 2011 6th IEEE Conference on*. 2011. IEEE.
91. Chaoui, A., et al., *On the Design of Shunt Active Filter for Improving Power Quality.* 2008 Ieee International Symposium on Industrial Electronics, Vols 1-5, 2008: p. 2331-+.
92. Ronchi, F. and A. Tilli, *Design methodology for shunt active filters.* Proc. 10th EPE-PEMC 2002, 2002.
93. Azevedo, H.J., et al., *Direct current control of an active power filter for harmonic elimination, power factor correction and load unbalancing compensation.* Proceedings of the EPE 2003, 2003.
94. Saadat, H., *Power system analysis*. 1999, United States of America: McGraw-Hill.
95. Rongliang, S., et al. *Research on power compensation strategy for diesel generator system based on virtual synchronous generator*. in *2016 IEEE 8th International Power Electronics and Motion Control Conference (IPEMC-ECCE Asia)*. 2016.
96. Report, I., *Computer representation of excitation systems.* IEEE Transactions on Power Apparatus and Systems, 1968(6): p. 1460-1464.
97. *Ieee recommended practice for excitation system models for power system stability studies*, in *Energy development and power generation committee of power engineering society*. IEEE Standard 421.5–1992.
98. Semikron, *Three-phase IGBT Inverter SKAI 45A2GD12-W24DI*. 2011, Semikron.
99. LEM, *Voltage Transducers LV 25-P*, LEM, Editor. 2014, LEM.
100. LEM, *Current Trancducer LA 55-P* LEM, Editor. 2015, LEM.
101. LEM, *Current Transducer LA 125-P/SP*, LEM, Editor. 2013, LEM.

A. Appendix-A

The original generator datasheet.

UCI224F STAMFORD

WINDING 311

CONTROL SYSTEM	SEPARATELY EXCITED BY P.M.G.							
A.V.R.	MX321	MX341						
VOLTAGE REGULATION	± 0.5 %	± 1.0 %	With 4% ENGINE GOVERNING					
SUSTAINED SHORT CIRCUIT	REFER TO SHORT CIRCUIT DECREMENT CURVES (page 7)							
CONTROL SYSTEM	SELF EXCITED							
A.V.R.	SX460	AS440						
VOLTAGE REGULATION	± 1.0 %	± 1.0 %	With 4% ENGINE GOVERNING					
SUSTAINED SHORT CIRCUIT	SERIES 4 CONTROL DOES NOT SUSTAIN A SHORT CIRCUIT CURRENT							
INSULATION SYSTEM	CLASS H							
PROTECTION	IP23							
RATED POWER FACTOR	0.8							
STATOR WINDING	DOUBLE LAYER CONCENTRIC							
WINDING PITCH	TWO THIRDS							
WINDING LEADS	12							
STATOR WDG. RESISTANCE	0.065 Ohms PER PHASE AT 22°C SERIES STAR CONNECTED							
ROTOR WDG. RESISTANCE	0.83 Ohms at 22°C							
EXCITER STATOR RESISTANCE	20 Ohms at 22°C							
EXCITER ROTOR RESISTANCE	0.078 Ohms PER PHASE AT 22°C							
R.F.I. SUPPRESSION	BS EN 61000-6-2 & BS EN 61000-6-4,VDE 0875G, VDE 0875N. refer to factory for others							
WAVEFORM DISTORTION	NO LOAD < 1.5% NON-DISTORTING BALANCED LINEAR LOAD < 5.0%							
MAXIMUM OVERSPEED	2250 Rev/Min							
BEARING DRIVE END	BALL. 6312-2RS (ISO)							
BEARING NON-DRIVE END	BALL. 6309-2RS (ISO)							
	1 BEARING				2 BEARING			
WEIGHT COMP. GENERATOR	337 kg				350 kg			
WEIGHT WOUND STATOR	120 kg				120 kg			
WEIGHT WOUND ROTOR	110.69 kg				102.32 kg			
WR² INERTIA	0.6071 kgm²				0.5754 kgm²			
SHIPPING WEIGHTS In a crate	360 kg				371 kg			
PACKING CRATE SIZE	105 x 57 x 96(cm)				105 x 57 x 96(cm)			
	50 Hz				60 Hz			
TELEPHONE INTERFERENCE	THF<2%				TIF<50			
COOLING AIR	0.216 m³/sec 458 cfm				0.281 m³/sec 595 cfm			
VOLTAGE SERIES STAR	380/220	400/231	415/240	440/254	416/240	440/254	460/266	480/277
VOLTAGE PARALLEL STAR	190/110	200/115	208/120	220/127	208/120	220/127	230/133	240/138
VOLTAGE SERIES DELTA	220/110	230/115	240/120	254/127	240/120	254/127	266/133	277/138
kVA BASE RATING FOR REACTANCE VALUES	72.5	72.5	72.5	55	83.8	87.5	87.5	93.8
Xd DIR. AXIS SYNCHRONOUS	2.29	2.07	1.92	1.30	2.52	2.35	2.15	2.12
X'd DIR. AXIS TRANSIENT	0.18	0.16	0.15	0.10	0.21	0.20	0.18	0.18
X"d DIR. AXIS SUBTRANSIENT	0.12	0.11	0.10	0.07	0.14	0.13	0.12	0.12
Xq QUAD. AXIS REACTANCE	1.05	0.95	0.88	0.59	1.16	1.08	0.99	0.98
X"q QUAD. AXIS SUBTRANSIENT	0.16	0.14	0.13	0.09	0.13	0.12	0.11	0.11
X_L LEAKAGE REACTANCE	0.07	0.06	0.06	0.04	0.08	0.07	0.07	0.07
X_2 NEGATIVE SEQUENCE	0.14	0.13	0.12	0.08	0.13	0.12	0.11	0.11
X_0 ZERO SEQUENCE	0.11	0.10	0.09	0.06	0.10	0.09	0.09	0.08
REACTANCES ARE SATURATED	VALUES ARE PER UNIT AT RATING AND VOLTAGE INDICATED							
T'd TRANSIENT TIME CONST.	0.03 s							
T"d SUB-TRANSTIME CONST.	0.008 s							
T'do O.C. FIELD TIME CONST.	0.75 s							
Ta ARMATURE TIME CONST.	0.0065 s							
SHORT CIRCUIT RATIO	1/Xd							

Approved Document

B.Appendix-B

The parameters of dq-model of the synchronous generator are given as:

Table B-1 dq-model parameters

Variable	Value	Unit
VA	72.5	KVA
P	4	-
ω_b	314.1592	Rad/sec
r_s	0.065	Ω
x_{ls}	0.1324	Ω
x_{md}	4.43586	Ω
x^*_{md}	0.06019	Ω
x^*_{mq}	0.0757	Ω
r'_f	0.0191	Ω
x'_{lfr}	0.2322	Ω
r'_{dr}	0.1207	Ω
x'_{ldr}	0.2207	Ω
r'_{qr}	0.1265	Ω
x'_{lqr}	0.1940	Ω

C. Appendix-C

Proof of equation (3-80)

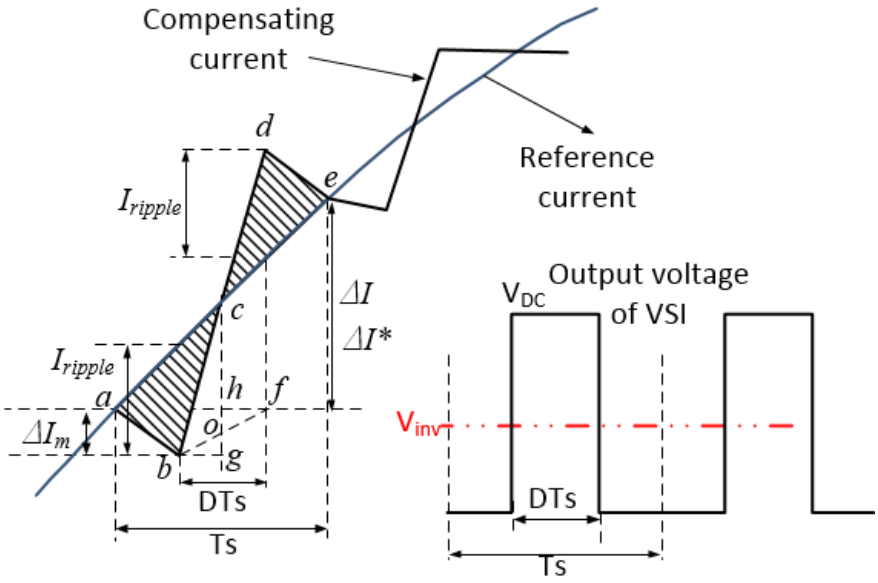


Figure C-1 current ripple and symmetrical-aligned modulation signal

The error between the reference current and the APF output current is as seen in ***Figure C-1***. When the switching frequency of PWM controller is sufficiently high, the passing current through the coupling inductor varies linearly, as given by equation (C-1).

$$\Delta I^* = \frac{v_{inv} - v_s}{L} T_s \qquad \text{(C-1)}$$

Where v_s is the voltage at the PCC, v_{inv} is the average output voltage of the APF in a switching period, L is the inductance of coupling inductor and T_s is the PWM time period.

The average output voltage of the inverter during the switching period is given by:

$$v_{inv} \,.\, T_s = V_{DC} \,.\, DT_s$$
$$v_{inv} \;= DV_{DC} \tag{C-2}$$

Where D is the duty ratio.

From ***Figure C-1***, the current ΔI can be expressed as:

$$\Delta I = \frac{-v_s}{L}\,\frac{1-D}{2}T_s + \frac{V_{DC}-v_s}{L}\,DT_s + \frac{-v_s}{L}\,\frac{1-D}{2}T_s$$
$$\Delta I = \frac{DV_{DC}-v_s}{L}\,T_s \tag{C-3}$$

According equation (C-2) , ΔI^* in equation (C-1) and ΔI in equation (C-3)are the same. However, in practice due to control system delay, dead time and inductor tolerance, these factors might cause errors in the current value $(\Delta I^* \neq \Delta I)$, but in this derivation is not considered [90].

As can be seen from ***Figure C-1***, the error between the compensating current and the reference current (the two dashed areas$(\Delta_{abc} + \Delta_{cde})$) is symmetrical around the midpoint of the switching period, so the area of the two triangles is equal. Then the total area is

$$S_{error} = 2\big[Area\ of\ \Delta_{ahc} + Area\ of\ \Delta_{abf} - Area\ of\ \Delta_{bcg}\big] \tag{C-4}$$

(Note that: $Area\ of\ \Delta_{ofh} = Area\ of\ \Delta_{obg}$)

$$S_{error} = 2\left[\frac{1}{2}\left(\frac{T_s}{2}\right)\left(\frac{\Delta I}{2}\right) + \frac{1}{2}\left(\frac{T_s + DT_s}{2}\right)(\Delta I_m) - \frac{1}{2}\left(\frac{DT_s}{2}\right)\left(\frac{\Delta I}{2} + \Delta I_m\right)\right] \tag{C-5}$$

$$S_{error} = \frac{T_s}{2}\left(\frac{1-D}{2}\,\Delta I + \Delta I_m\right)$$

Where ΔI_m is the change of APF output current from the beginning of switching period to the pulse (i.e. from a to b).

$$\Delta I_m = \frac{v_s}{L}\,\frac{1-D}{2}T_s \qquad \text{(C-6)}$$

From equations (C-3), (C-5) and (C-6):

$$S_{error} = \frac{T_s}{2}\left(\frac{1-D}{2}\left(\frac{DV_{DC}-v_s}{L}\,T_s\right) + \left(\frac{v_s}{L}\,\frac{1-D}{2}T_s\right)\right) \qquad \text{(C-7)}$$

$$S_{error} = \frac{{T_s}^2}{4L}\,(DV_{DC} - D^2V_{DC}) \qquad \text{(C-8)}$$

To find the maximum value of the error as a function of the duty ratio (*D*), and by assuming all other variables are constants, the derivative of equation (C-8) with respect to duty ratio is given as:

$$\frac{dS_{error}}{dD} = \frac{{T_s}^2}{4L}\,(V_{DC} - 2DV_{DC}) = 0 \qquad \text{(C-9)}$$

As can be seen from equation (C-9) the maximum value of the error (i.e. maximum ripple) occurs when D=0.5.

From ***Figure C-1***, the ripple current is defined as the maximum variation of the output current of the APF during the switching period and is equal:

$$I_{ripple} = \Delta I_m + \frac{1-D}{2}\,\Delta I \qquad \text{(C-10)}$$

From equations (C-5) and (C-10), the error between the reference current and the output current is given as:

$$S_{error} = \frac{T_s}{2} \left(I_{ripple}\right) \quad \text{(C-11)}$$

From equations (C-8) and equation (C-11) and for D=0.5 the ripple current is equal to:

$$I_{ripple} = \frac{T_s V_{DC}}{8 \times L} \quad \text{(C-12)}$$

Therefore, the minimum value of the interface inductance that gives the maximum current ripple I_{ripple} is given as:

$$L_{min} = \frac{V_{DC}}{8\ f_s\ I_{ripple}} \quad \text{(C-13)}$$

Where f_s is the frequency of the carrier signal and equal to($f_s = 1/T_s$).

D. Appendix D

The active power filter code:

```
function [Vabc_ref,y1] = fcn(Vabc,Ilabc,Ifabc,Vdc,SQRT2,ki,kp, M1,fb)
%#codegen

fs=10000;
Ts=1/fs;
w=2*pi*50;
A=w/SQRT2;
num=A/(A+M1);
den=(A-M1)/(A+M1);

wc=7;
M1_1=w/tan(w*Ts/2);
M1_3=(3*w)/tan(3*w*Ts/2);
M1_5=(5*w)/tan(5*w*Ts/2);
M1_7=(7*w)/tan(7*w*Ts/2);

B2 = M1_1^2+2*wc*M1_1+w^2;
B1 = 2*(w^2-M1_1^2);
B0 = M1_1^2-2*wc*M1_1+w^2;

A2= kp_pr*B2+2*ki_pr*wc*M1_1;
A1= kp_pr*B1;
A0 = kp_pr*B0-2*ki_pr*wc*M1_1;

A32=2*ki_pr*wc*M1_3;

A52=2*ki_pr*wc*M1_5;

A72=2*ki_pr*wc*M1_7;


B32 = M1_3^2+2*wc*M1_3+(3*w)^2;
B31= 2*((3*w)^2-M1_3^2);
B30 = M1_3^2-2*wc*M1_3+(3*w)^2;

B52 = M1_5^2+2*wc*M1_5+(5*w)^2;
B51= 2*((5*w)^2-M1_5^2);
B50 = M1_5^2-2*wc*M1_5+(5*w)^2;

B72 = M1_7^2+2*wc*M1_7+(7*w)^2;
B71= 2*((7*w)^2-M1_7^2);
B70 = M1_7^2-2*wc*M1_7+(7*w)^2;


VdAlpha_1=fb(1);    VdAlpha_2=fb(2);    QVdAlpha_1=fb(3);
QVdAlpha_2=fb(4);   V_Alpha_1=fb(5);    V_Alpha_2=fb(6);
VdBeta_1=fb(7);     VdBeta_2=fb(8);     QVdBeta_1=fb(9);
QVdBeta_2=fb(10);   V_Beta_1=fb(11);    V_Beta_2=fb(12);
Theta=fb(13);       error_theat_1=fb(14);   int_Vq_1=fb(15);
int_w_1 = fb(16);   w=fb(17);
ild_1=fb(18);       ilq_1=fb(19);       ild_DC_1=fb(20);
ilq_DC_1=fb(21);
```

```
Igd_1=fb(22);       Igq_1=fb(23);       Igd_DC_1=fb(24);
Igq_DC_1=fb(25);

error_DC_link_1=fb(26);                  PIDC_1=fb(27);

 Ialpha_PRHC_1=fb(28);   Ialpha_PRHC_2=fb(29);    PRalpha_1=fb(30);
PRalpha_2=fb(31);
 HC3alpha_1=fb(32);      HC3alpha_2=fb(33);       HC5alpha_1=fb(34);
HC5alpha_2=fb(35);
 HC7alpha_1=fb(36);      HC7alpha_2=fb(37);

 Ibeta_PRHC_1=fb(38);    Ibeta_PRHC_2=fb(39);       PRbeta_1=fb(40);
PRbeta_2=fb(41);
 HC3beta_1=fb(42);       HC3beta_2=fb(43);          HC5beta_1=fb(44);
HC5beta_2=fb(45);
 HC7beta_1=fb(46);       HC7_2beta=fb(47);

 Izero_PRHC_1=fb(48);    Izero_PRHC_2=fb(49);         PRzero_1=fb(50);
PRzero_2=fb(51);
 HC3zero_1=fb(52);       HC3zero_2=fb(53);            HC5zero_1=fb(54);
HC5zero_2=fb(55);
 HC7zero_1=fb(56);       HC7zero_2=fb(57);

v_A= Vabc(1);
v_B= Vabc(2);
v_C= Vabc(3);

 V_Alpha= 1/3*(v_A-0.5*(v_B+v_C));
 V_Beta = 0.5*(v_B-v_C)/sqrt(3);

  n21=M1*SQRT2*w;
  d21=M1^2+M1*SQRT2*w+w^2;
  d11=2*w^2-2*M1^2;
  d01=M1^2-M1*SQRT2*w+w^2;
  n22=SQRT2*w^2;
  npi2=ki/M1+kp;
  npi1=ki/M1-kp;

 VdAlpha = -(d11/d21)*VdAlpha_1-(d01/d21)*VdAlpha_2  +(n21/d21)*(V_Alpha-
V_Alpha_2);
 QVdAlpha= -(d11/d21)*QVdAlpha_1-(d01/d21)*QVdAlpha_2
+(n22/d21)*(V_Alpha+2*V_Alpha_1+V_Alpha_2);

 VdBeta=  -(d11/d21)*VdBeta_1-(d01/d21)*VdBeta_2  +(n21/d21)*(V_Beta-
V_Beta_2);
 QVdBeta= -(d11/d21)*QVdBeta_1-(d01/d21)*QVdBeta_2
+(n22/d21)*(V_Beta+2*V_Beta_1+V_Beta_2);

 V_Alpha_2=V_Alpha_1;
 V_Alpha_1=V_Alpha;
 VdAlpha_2=VdAlpha_1;
 VdAlpha_1=VdAlpha;
 QVdAlpha_2=QVdAlpha_1;
 QVdAlpha_1=QVdAlpha;

 V_Beta_2=V_Beta_1;
 V_Beta_1=V_Beta;
 VdBeta_2=VdBeta_1;
 VdBeta_1=VdBeta;
```

```
 QVdBeta_2=QVdBeta_1;
 QVdBeta_1=QVdBeta;

 Alpha_plus= VdAlpha-QVdBeta;

 Beta_plus = QVdAlpha +  VdBeta;

 Vpccd = Alpha_plus*cos (Theta)+ Beta_plus*sin (Theta); %%%*(t(n)-k)
 Vpccq = Alpha_plus*sin (Theta)- Beta_plus*cos (Theta);
 errorVq = -Vpccq;

 int_Vq =int_Vq_1+npi2*errorVq+npi1*error_theat_1;
 int_Vq_1=int_Vq;
 error_theat_1=errorVq;
 iqplusw=int_Vq +2*pi*50;

 int_w =int_w_1+iqplusw*Ts;
 int_w_1=int_w;

 Theta= mod (int_w,2*pi);
%  w1= Theta;
 wo=iqplusw;
 if (wo>330 || wo<300)
     wo=2*pi*50;
 end
  %%%%%%%%%%%%%%%%%%%%%%%%%%%%%%%%%%%%%%%%%%%%%%%%%%%%%%%%%%%%%%%%%%%%%%%%
ila= Ilabc(1);
ilb= Ilabc(2);
ilc= Ilabc(3);

Zero_seq=(ila+ilb+ilc)/3;
ila1=ila-Zero_seq;
ilb1=ilb-Zero_seq;
ilc1=ilc-Zero_seq;

ild =  (2/3)*(cos(Theta)*ila1+cos(Theta-
2*pi/3)*ilb1+cos(Theta+2*pi/3)*ilc1);
ilq =  -(2/3)*(sin(Theta)*ila1+sin(Theta-
2*pi/3)*ilb1+sin(Theta+2*pi/3)*ilc1);

 ild_DC = -den*ild_DC_1+num*(ild+ild_1);
 ilq_DC = -den*ilq_DC_1+num*(ilq+ilq_1);

 ild_1=ild;
 ilq_1=ilq;
 ild_DC_1=ild_DC;
 ilq_DC_1=ilq_DC;


 ila2= ild_DC*cos(Theta)-ilq_DC*sin(Theta);
 ilb2= ild_DC*cos(Theta-2*pi/3)-ilq_DC*sin(Theta-2*pi/3);
 ilc2= ild_DC*cos(Theta+2*pi/3)-ilq_DC*sin(Theta+2*pi/3);

 Ilar=ila-ila2;
 Ilbr=ilb-ilb2;
 Ilcr=ilc-ilc2;

ifa= Ifabc(1);
```

```
ifb= Ifabc(2);
ifc= Ifabc(3);

%%%%%%%%%%%%%%%%%%%%%%%%%%%%%%%%%%%%%%%%%%%%%%%%%%%%%%%%%%%%%%%%%%%%%%%%%%%%%%%%
Iga= ila-ifa;
Igb= ilb-ifb;
Igc= ilc-ifc;

Zero_seq=(Iga+Igb+Igc)/3;
Iga1=Iga-Zero_seq;
Igb1=Igb-Zero_seq;
Igc1=Igc-Zero_seq;

Igd =  (2/3)*(cos(Theta)*Iga1+cos(Theta-
2*pi/3)*Igb1+cos(Theta+2*pi/3)*Igc1);
Igq =  -(2/3)*(sin(Theta)*Iga1+sin(Theta-
2*pi/3)*Igb1+sin(Theta+2*pi/3)*Igc1);

 Igd_DC = -den*Igd_DC_1+num*(Igd+Igd_1);
 Igq_DC = -den*Igq_DC_1+num*(Igq+Igq_1);

 Igd_1=Igd;
 Igq_1=Igq;
 Igd_DC_1=Igd_DC;
 Igq_DC_1=Igq_DC;


 Iga2= Igd_DC*cos(Theta)-Igq_DC*sin(Theta);
 Igb2= Igd_DC*cos(Theta-2*pi/3)-Igq_DC*sin(Theta-2*pi/3);
 Igc2= Igd_DC*cos(Theta+2*pi/3)-Igq_DC*sin(Theta+2*pi/3);

 Igar=Iga-Iga2;
 Igbr=Igb-Igb2;
 Igcr=Igc-Igc2;

 Iar = Ilar+0.65*Igar;
 Ibr = Ilbr+0.65*Igbr;
 Icr = Ilcr+0.65*Igcr;
 %%%%%%%%%%%%%%%%%%%%%%%%%%%%%%%%%%%%%%%%%%%%%%%%%%%%%%%%%%%%%%%%%%%%%%%%%%%%%%%%
error_DC_link= 730-Vdc;
PIDC=PIDC_1+(kp_DC+ki_DC/M1)*error_DC_link+(ki_DC/M1-
kp_DC)*error_DC_link_1;

PIDC_1= PIDC;
error_DC_link_1 = error_DC_link;
d_DC_link= PIDC;
q_DC_link = 0;    %% when q=0 => no fundametal in filter

 A_DC_link= d_DC_link*cos(Theta)-q_DC_link*sin(Theta);
 B_DC_link= d_DC_link*cos(Theta-2*pi/3)-q_DC_link*sin(Theta-2*pi/3);
 C_DC_link= d_DC_link*cos(Theta+2*pi/3)-q_DC_link*sin(Theta+2*pi/3);

Alpha_DC_link = 2/3*(A_DC_link-0.5*(B_DC_link+C_DC_link));
Beta_DC_link = (B_DC_link-C_DC_link)/sqrt(3);
%%%%%%%%%%%%%%%%%%%%%%%%%%%%%%%%%%%%%%%%%%%%%%%%%%%%%%%%%%%%%%%%%%%%%%%%%%%%%%%%
%%%%%

Alfa_ref = 2/3*(Iar-0.5*(Ibr+Icr));
```

```
Beta_ref = (Ibr-Icr)/sqrt(3);
Zero_ref = (Iar+Ibr+Icr)/3;
Alfa_filter= 2/3*(ifa-0.5*(ifb+ifc));
Beta_filter = (ifb-ifc)/sqrt(3);
Zero_filter = (ifa+ifb+ifc)/3;

Ialpha_PRHC = Alfa_ref - Alfa_filter - Alpha_DC_link;
Ibeta_PRHC  = Beta_ref - Beta_filter - Beta_DC_link;
Izero_PRHC = Zero_ref- Zero_filter;

 PR_alpha=-(B1/B2)*PRalpha_1-
(B0/B2)*PRalpha_2+(A2/B2)*Ialpha_PRHC+(A1/B2)*Ialpha_PRHC_1+(A0/B2)*Ialpha_
PRHC_2;
 HC3_alpha=-(B31/B32)*HC3alpha_1-
(B30/B32)*HC3alpha_2+(A32/B32)*(Ialpha_PRHC-Ialpha_PRHC_2);
 HC5_alpha=-(B51/B52)*HC5alpha_1-
(B50/B52)*HC5alpha_2+(A52/B52)*(Ialpha_PRHC-Ialpha_PRHC_2);
 HC7_alpha=-(B71/B72)*HC7alpha_1-
(B70/B72)*HC7alpha_2+(A72/B72)*(Ialpha_PRHC-Ialpha_PRHC_2);



 Ialpha_PRHC_2=Ialpha_PRHC_1;
 Ialpha_PRHC_1=Ialpha_PRHC;
 PRalpha_2=PRalpha_1;
 PRalpha_1=PR_alpha;
 HC3alpha_2=HC3alpha_1;
 HC3alpha_1=HC3_alpha;
 HC5alpha_2=HC5alpha_1;
 HC5alpha_1=HC5_alpha;
 HC7alpha_2=HC7alpha_1;
 HC7alpha_1=HC7_alpha;

 PR_beta=-(B1/B2)*PRbeta_1-
(B0/B2)*PRbeta_2+(A2/B2)*Ibeta_PRHC+(A1/B2)*Ibeta_PRHC_1+(A0/B2)*Ibeta_PRHC
_2;
 HC3_beta=-(B31/B32)*HC3beta_1-(B30/B32)*HC3beta_2+(A32/B32)*(Ibeta_PRHC-
Ibeta_PRHC_2);
 HC5_beta=-(B51/B52)*HC5beta_1-(B50/B52)*HC5beta_2+(A52/B52)*(Ibeta_PRHC-
Ibeta_PRHC_2);
 HC7_beta=-(B71/B72)*HC7beta_1-(B70/B72)*HC7_2beta+(A72/B72)*(Ibeta_PRHC-
Ibeta_PRHC_2);



 Ibeta_PRHC_2=Ibeta_PRHC_1;
 Ibeta_PRHC_1=Ibeta_PRHC;
 PRbeta_2=PRbeta_1;
 PRbeta_1=PR_beta;
 HC3beta_2=HC3beta_1;
 HC3beta_1=HC3_beta;
 HC5beta_2=HC5beta_1;
 HC5beta_1=HC5_beta;
 HC7_2beta=HC7beta_1;
 HC7beta_1=HC7_beta;

PR_zero=-(B1/B2)*PRzero_1-
(B0/B2)*PRzero_2+(A2/B2)*Izero_PRHC+(A1/B2)*Izero_PRHC_1+(A0/B2)*Izero_PRHC
_2;
 HC3_zero=-(B31/B32)*HC3zero_1-(B30/B32)*HC3zero_2+(A32/B32)*(Izero_PRHC-
Izero_PRHC_2);
```

```
 HC5_zero=-(B51/B52)*HC5zero_1-(B50/B52)*HC5zero_2+(A52/B52)*(Izero_PRHC-
Izero_PRHC_2);
 HC7_zero=-(B71/B72)*HC7zero_1-(B70/B72)*HC7zero_2+(A72/B72)*(Izero_PRHC-
Izero_PRHC_2);


 Izero_PRHC_2=Izero_PRHC_1;
 Izero_PRHC_1=Izero_PRHC;
 PRzero_2=PRzero_1;
 PRzero_1=PR_zero;
 HC3zero_2=HC3zero_1;
 HC3zero_1=HC3_zero;
 HC5zero_2=HC5zero_1;
 HC5zero_1=HC5_zero;
 HC7zero_2=HC7zero_1;
 HC7zero_1=HC7_zero;

Valpha_ref =PR_alpha+HC3_alpha+HC5_alpha+HC7_alpha;
Vbeta_ref  =PR_beta+HC3_beta+HC5_beta+HC7_beta;
Vzero_ref  =PR_zero+HC3_zero+HC5_zero+HC7_zero;

Va_ref= Valpha_ref + Vzero_ref;
Vb_ref= -0.5*Valpha_ref + sqrt(3)/2*Vbeta_ref + Vzero_ref;
Vc_ref= -0.5*Valpha_ref - sqrt(3)/2*Vbeta_ref + Vzero_ref;
Vn_ref= -3*Vzero_ref;
if Va_ref >= 240*sqrt(2)
    Va_ref=240*sqrt(2);
end
if Va_ref <= -240*sqrt(2)
    Va_ref=-240*sqrt(2);
end

if Vb_ref >= 240*sqrt(2)
    Vb_ref=240*sqrt(2);
end
if Vb_ref <= -240*sqrt(2)
    Vb_ref=-240*sqrt(2);
end

if Vc_ref >= 240*sqrt(2)
    Vc_ref=240*sqrt(2);
end
if Vc_ref <= -240*sqrt(2)
    Vc_ref=-240*sqrt(2);
end
if Vn_ref <= -240*sqrt(2)
    Vn_ref=-240*sqrt(2);
end
if Vn_ref >= 240*sqrt(2)
    Vn_ref = 240*sqrt(2);
end
Va_ref_pu=Va_ref/(240*sqrt(2)); %Vd*sqrt(2)
Vb_ref_pu=Vb_ref/(240*sqrt(2));
Vc_ref_pu=Vc_ref/(240*sqrt(2));
Vn_ref_pu=Vn_ref/(240*sqrt(2));

Va_ref_scaled =(Va_ref_pu+1)*Up_lim*0.5;
Vb_ref_scaled =(Vb_ref_pu+1)*Up_lim*0.5;
Vc_ref_scaled =(Vc_ref_pu+1)*Up_lim*0.5;
```

```
Vn_ref_scaled =(Vn_ref_pu+1)*Up_lim*0.5;

Vabc_ref =[ Va_ref_scaled Vb_ref_scaled Vc_ref_scaled Vn_ref_scaled];

y1= [VdAlpha_1 VdAlpha_2 QVdAlpha_1 QVdAlpha_2 V_Alpha_1 V_Alpha_2 VdBeta_1
VdBeta_2 QVdBeta_1 QVdBeta_2 V_Beta_1 V_Beta_2 Theta...
     error_theat_1 int_Vq_1 int_w_1 wo ...
     ild_1 ilq_1 ild_DC_1 ilq_DC_1 ...
     Igd_1 Igq_1 Igd_DC_1 Igq_DC_1 ...
     error_DC_link_1 PIDC_1...
     Ialpha_PRHC_1 Ialpha_PRHC_2 PRalpha_1 PRalpha_2 HC3alpha_1 HC3alpha_2
HC5alpha_1 HC5alpha_2 HC7alpha_1 HC7alpha_2 ...
     Ibeta_PRHC_1 Ibeta_PRHC_2 PRbeta_1 PRbeta_2 HC3beta_1 HC3beta_2
HC5beta_1 HC5beta_2 HC7beta_1 HC7_2beta ...
     Izero_PRHC_1 Izero_PRHC_2 PRzero_1 PRzero_2 HC3zero_1 HC3zero_2
HC5zero_1 HC5zero_2 HC7zero_1 HC7zero_2];
```